Gruppo Nazionale per la Fisica Matematica

CENTRO INTERDIPARTIMENTALE DI MATEMATICA PER LA TECNOLOGIA "A. M. ANILE"

UNIVERSITÀ degli STUDI di CATANIA

DIPARTIMENTO DI MATEMATICA E INFORMATICA

associazione angelo marcello anile

SCEE 2018

THE 12TH INTERNATIONAL CONFERENCE ON SCIENTIFIC COMPUTING IN ELECTRICAL ENGINEERING

September 23-27, 2018 – Taormina, Sicily, Italy

Programme and abstracts

Chairs

Giuseppe Nicosia, University of Catania, Italy
Vittorio Romano, University of Catania, Italy

Scientific Committee

Gabriela Ciuprina, Politehnica University of Bucharest, Romania
Herbert De Gersem, TU Darmstadt, Germany
Georg Denk, Infineon, Germany
Michael Günther, University of Wuppertal, Germany
Ulrich Langer, Johannes Kepler University Linz, Austria
Jan ter Maten, University of Wuppertal, Germany
Jörg Ostrowski, ABB, Switzerland
Ursula van Rienen, University of Rostock, Germany
Vittorio Romano, University of Catania, Italy
Ruth Sabariego, KU Leuven, Belgium
Wil Schilders, TU Eindhoven, Netherlands
Caren Tischendorf, Humboldt University of Berlin, Germany

Local Organizing Committee

Salvatore Alfonzetti, University of Catania, Italy
Armando Majorana, University of Catania, Italy
Orazio Muscato, University of Catania, Italy
Giuseppe Nicosia, University of Catania, Italy
Vittorio Romano, University of Catania, Italy
Rita Tracinà, University of Catania, Italy
Marco Coco, University of Catania, Italy
Liliana Luca, University of Catania, Italy
Giovanni Nastasi, University of Catania, Italy

Contents

Part I

Program

Sunday, September 23

18:30 – 19:30 Registration

19:30 – 20:30 Welcome cocktail

Monday, September 24 – Morning

8:30 – 9:00 ***Registration***

9:00 – 9:20 ***Opening***

Session 1

9:20 – 10:10 IT: **Matthias Auf der Maur**
Current developments in device simulation: degeneracy, arbitrary density of states and multi-particle drift-diffusion

10:10 – 10:35 CT: René Pinnau
Semiconductor Optimization, Model Hierarchies & Asymptotic Analysis

10:35 – 11:00 CT: Marco Coco and Vittorio Romano
Charge and phonon transport in suspended monolayer graphene

11:00 – 11:20 ***Coffee break***

Session 2

11:20 – 12:10 IT: **Tudor Ionescu**
Model reduction for nonlinear systems – a time-domain moment matching perspective

12:10 – 12:35 CT: Jan Kühn, Andreas Bartel and Piotr Putek
A Thermal Extension of Tellinen's Scalar Hysteresis Model

12:35 – 13:00 CT: Armin Fohler and Walter Zulehner
Adaptive Mesh Refinement for Rotating Electrical Machines Taking into Account Boundary Approximation Errors

13:00 – 15:00 ***Lunch***

Monday, September 24 – Afternoon

Session 3

15:00 – 15:50 IT: **Sara Grundel**
Simulation and Model Order Reduction of Power Systems

15:50 – 16:15 CT: Onkar Jadhav, Evgenii Rudnyi and Tamara Bechtold
Load Snapshot Based Nonlinear-Input Model Order Reduction of a Thermal Human Tissue Model

16:15 – 16:40 CT: Roland Pulch
Frequency-domain integrals for stability preservation in model order reduction

16:40 – 17:05 CT: Ruxandra Barbulescu, Daniel Ioan, Gabriela Ciuprina, Aurel Sorin Lup and Mihai Popescu
Reduced Order Models for the Simulation of the Saltatory Conduction

17:05 – 17:25 Coffee break

17:25 – 17:50 CT: Orazio Muscato
Direct Simulation Monte Carlo of the Wigner transport equation

17:50 – 18:15 CT: Piotr Putek, E. Jan W. ter Maten and Michael Günther
Shape optimization of a permanent magnet synchronous machine under probabilistic constraints

18:15 – 18:40 CT: G. Aiello, S. Alfonzetti, S.A. Rizzo, N. Salerno
Shape optimization of an induction heating device

Tuesday, September 25

Session 5

9:00 – 9:50 IT: **Omar Morandi**

Description of the trajectories of quantum particles by a Quantum Lagrangian approach

9:50 – 10:15 CT: Karthik V. Aadithya, Eric R. Keiter and Ting Mei

Predictor/Corrector Newton-Raphson (PCNR): A Simple, Flexible, Scalable, Modular, and Consistent Replacement for Limiting in Circuit Simulation

10:15 – 10:40 CT: Kai Bittner, Hans G. Brachtendorf and Wim Schoenmaker

LinzFrame – A Modular Mixed-Level Simulator with Emphasis on Radio Frequency Circuits

10:40 – 11:00 Coffee break

Session 6

11:00 – 11:25 CT: Giovanni Nastasi and Vittorio Romano

Simulation of double gate graphene field effect tansistors

11:25 – 11:50 CT: Giovanni Mascali and Vittorio Romano

A hydrodynamic model for 2D-3D electron transport in silicon devices

11:50 – 12:15 CT: Jeroen Tant and Johan Driesen

Analysis and Numerical Solution of Piecewise Smooth Differential Algebraic Equations for Power Electronic Circuit Simulation

12:15 – 12:40 CT: Pasquale Claudio Africa, Carlo de Falco and Dario Natali

Scalable Adaptive Numerical Simulation for Organic Thin Film Transistors

13:00 – 15:00 Lunch

15:00 – 17:00 Social tour

20:00 Social dinner

Wednesday, September 26 – Morning

Session 7

9:15 – 9:45 IS: **Mario Saggio**

Title tba

9:45 – 10:15 IS: **Tonio Biondi**

Data Center Power

10:15 – 10:40 CT: Andreas Blaszczyk, Thomas Christen, Hans K. Meyer and Michael Schüller

Surface Charging Formulations for Engineering Applications. Validation by Experiments and Transient Models

10:40 – 11:00 Coffee break

Session 8

11:00 – 11:50 IT: **P. Gangl**

Topology and Shape Optimization of Electrical Machines

11:50 – 12:15 CT: Julius Zimmermann and Ursula van Rienen

Electromagnetic stimulation chambers for cartilage regeneration

12:15 – 12:40 CT: Konstantin Butenko, Andrea Böhme and Ursula van Rienen

Open Source Simulation Platform for Deep Brain Stimulation

12:40 – 14:40 Lunch

Wednesday, September 26 – Afternoon

Session 9

14:40 – 15:30 IT: **Jay Gopalakrishnan**

Techniques for modeling fiber laser amplifiers

15:30 – 15:55 CT: Nicolas Marsic and Herbert De Gersem

Optimized Schwarz methods for Helmholtz problems in a closed domain

15:55 – 16:20 CT: Peter Gangl, Ulrich Langer, Angelos Mantzaflaris and Rainer Schneckenleitner

Isogeometric Simulation and Shape Optimization with Applications to Electrical Machines

16:20 – 16:40 Coffee break

16:40 – 17:20 Poster shot gun presentation

17:20 – 19:00 Poster session

Thursday, September 27

Session 10

9:00 – 9:50 IT: **Bilen Emek Abali**

Modeling mechanochemistry in Li-ion batteries

9:50 – 10:15 CT: Ioannis Deretzis and Antonino La Magna

Multiscale atomistic modeling for materials science applications

10:15 – 10:40 CT: A. Bermúdez, D. Gómez and D. González-Peñas

Thermo-electrical analysis of indirect resistance heating furnaces combining numerical simulation and lumped models

10:40 – 11:00 Coffee break

Session 11

11:00 – 11:50 IT: **Steffen Börm**

GCA-H^2 matrix compression for electrostatic simulations

11:50 – 12:15 CT: Siyang Hu, Chengdong Yuan and Tamara Bechtold

Quasi-Schur Transformation for the Stable Compact Modeling of Piezoelectric Energy Harvester Devices

12:15 – 12:40 CT: A.K. Tyagi, X. Jonsson, T.G.J. Beelen and W.H.A. Schilders

An Unbiased Hybrid Importance Sampling Monte Carlo Approach for Yield estimation in Electronic Circuit Design

12:40 – 13:05 CT: Herbert Egger, Bogdan Radu

A mass-lumped mixed finite element method for Maxwell's equations

13:05 Closing

Part II

Abstracts of Invited Talks

Modeling mechanochemistry in Li-ion batteries

B. Emek Abali[1]

Technische Universität Berlin, Einsteinufer 5, 10587 Berlin, Germany bilenemek@abali.org

Summary. Mechanoschemistry in Li-ion batteries involve interaction of ions migrating in a cell with mechanical stresses as well as electromagnetic fields. We aim at modeling this multiphysics in a battery cell by involving balance equations and MAXWELL equations. Before applying specific assumptions relevant for Li-ion batteries, we address developing a complete theory by using continuum mechanics and thermodynamics.

1 Objective of this study

Consider a battery cell composed of electrodes, binder, polymer, and ions diffusing between as well as intercalating into the electrodes during charge and discharge. At any given point all constituents build the bulk. Basically, we have different constituents denoted by α and their corresponding mass and momentum equations need to be fulfilled. Technically, it is challenging to measure velocity of every constituent, $\boldsymbol{v}^\alpha$, accurately. Therefore, constitutive relations involving this quantity fail to be feasible. In order to overcome this restriction, we introduce a diffusion flux $\boldsymbol{J}^\alpha = \rho^\alpha(\boldsymbol{v}^\alpha - \boldsymbol{v})$ as the relative velocity of a constituent with the partial mass density ρ^α with respect to the bulk velocity $\boldsymbol{v}$. The partial mass density, $\rho^\alpha = M^\alpha c^\alpha$, is given by the molar mass, M^α, and the concentration, c^α, which is the molar density. Then we find a constitutive equation relating the diffusion flux to other measurable quantities like concentration such that the constituents' velocities never occur in the formulation. In this setting, we have the following mass and momentum equations for the bulk as well as for the constituents

$$\begin{aligned} \frac{\partial \rho}{\partial t} + \frac{\partial \rho v_i}{\partial x_i} &= 0 \,, \\ \frac{\partial \rho^\alpha}{\partial t} + \frac{\partial}{\partial x_i}\left(\rho^\alpha v_i + J_i^\alpha\right) &= k^\alpha \,, \\ \frac{\partial \rho v_i}{\partial t} + \frac{\partial}{\partial x_j}\left(v_j \rho v_i + \sigma_{ji}\right) &= \mathcal{F}_i \,, \end{aligned} \tag{1}$$

where we employ EINSTEIN's summation convention over repeated indices. Apart from the constitutive equations for CAUCHY's stress of the bulk, $\boldsymbol{\sigma}$, and for the diffusion flux of each constituent, $\boldsymbol{J}^\alpha$, subject to a chemical reaction given by the rate k^α; we need to define the interaction between mechanics and electromagnetism by defining the electromagnetic (ponderomotive) force density, $\boldsymbol{\mathcal{F}}$. Especially the definition of this quantity is very challenging and there exists no consensus between the scientific community, see for example [4, 6, 12, 13]. We follow the method of derivation used in [10, Eq. (15)], [9, Chap. 1], [8, Chap. XIV], [7, Chap. 8], [11, Sect. 3.3] in the following and introduce a very general identity,

$$\frac{\partial \mathcal{G}_i}{\partial t} = \frac{\partial m_{ji}}{\partial x_j} - \mathcal{F}_i \,, \tag{2}$$

between the electromagnetic momentum density, $\boldsymbol{\mathcal{G}}$, electromagnetic stress, $\boldsymbol{m}$, and the electromagnetic force density, $\boldsymbol{\mathcal{F}}$. This relation is in analogy with the balance of momentum such that the names stress and momentum are justified. If the electromagnetic momentum, $\boldsymbol{\mathcal{G}}$, is defined, as a consequence of the latter relation we can propose the electromagnetic stress and the electromagnetic force density. By following [3] we emphasize that different choices are perfectly appropriate.

The measurable electromagnetic fields are the electric field $\boldsymbol{E}$ and the magnetic flux (area density) $\boldsymbol{B}$ defined by solving two of four MAXWELL equations as follows:

$$E_i = -\frac{\partial \phi}{\partial x_i} - \frac{\partial A_i}{\partial t} \,, \quad B_i = \varepsilon_{ijk}\frac{\partial A_k}{\partial x_j} \,, \tag{3}$$

where the electromagnetic potentials ϕ, $\boldsymbol{A}$ are sought after, ε_{ijk} is the LEVI-CIVITA symbol. In order to solve the scalar (electric) potential, ϕ, we use the balance of electric charge combined by one MAXWELL equation,

$$\frac{\partial \rho z}{\partial t} + \frac{\partial J_i}{\partial x_i} = 0 \,, \quad \rho z = \frac{\partial D_i}{\partial x_i} \,, \tag{4}$$

respectively, where the specific charge, z, is related to the total charge potential, $\boldsymbol{D}$, and the electric current, $\boldsymbol{J}$, of the total charge reads

$$J_i = J_i^{\text{fr.}} + \frac{\partial P_i}{\partial t} + \varepsilon_{ijk}\frac{\partial \mathcal{M}_k}{\partial x_j} \,, \tag{5}$$

with the electric current of free charges, $\boldsymbol{J}^{\text{fr.}}$, electric polarization, $\boldsymbol{P}$, and magnetic polarization, $\boldsymbol{\mathcal{M}}$, all to be given by constitutive equations. In order to solve the vector (magnetic) potential, $\boldsymbol{A}$, we use the final MAXWELL equation augmented by the LORENZ gauge,

$$-\frac{\partial D_i}{\partial t}+\varepsilon_{ijk}\frac{\partial H_k}{\partial x_j}=J_i\ ,\ \ \frac{\partial \phi}{\partial t}+\frac{1}{\varepsilon_0\mu_0}\frac{\partial A_i}{\partial x_i}=0\ , \quad (6)$$

respectively, where the LORENZ gauge is an appropriate choice for numerical solutions, see [2] for implementation and applications. The universal constants:

$$\begin{aligned}\varepsilon_0 &= 8.85\cdot 10^{-12}\,\mathrm{A\,s/(V\,m)}\ ,\\ \mu_0 &= 12.6\cdot 10^{-7}\,\mathrm{V\,s/(A\,m)}\ ,\end{aligned} \quad (7)$$

and the MAXWELL–LORENTZ aether relations:

$$D_i=\varepsilon_0 E_i\ ,\ \ H_i=\frac{1}{\mu_0}B_i\ , \quad (8)$$

are used to combine the electromagnetic fields with the (total) charge potential, $\boldsymbol{D}$, and the (total) current potential, $\boldsymbol{H}$.

For the interaction between mechanics and electromagnetism, we can choose one of the existing electromagnetic momenta, see [5, 14] for different possibilities. Herein, we choose the POYNTING vector:

$$\mathcal{G}_i=(\boldsymbol{D}\times\boldsymbol{B})_i\ , \quad (9)$$

leading to the following electromagnetic stress and force

$$\begin{aligned}m_{ji} &= -\frac{1}{2}\delta_{ji}(H_kB_k+D_kE_k)+H_iB_j+D_jE_i\ ,\\ \mathcal{F}_i &= \rho z E_i+\varepsilon_{ijk}J_jB_k\ ,\end{aligned} \quad (10)$$

where in this setting $\boldsymbol{m}$ is called MAXWELL stress and $\boldsymbol{\mathcal{F}}$ is named after LORENTZ.

We have briefly presented the governing equations modeling mechanochemistry in a battery cell. We aim at solving mass density, ρ, and velocity, $\boldsymbol{v}$, of the bulk as well as concentrations, c^α, of all constituents taking part in the chemical reaction called intercalation at the electrode by satisfying Eq. (1). Moreover, we need to solve Eqs. (4), (6) in order to obtain electromagnetic fields, $\boldsymbol{E}$, $\boldsymbol{B}$, by using Eq. (3). For being able to solve the governing equations, we have to close them by defining $\boldsymbol{J}^\alpha$, k^α, $\boldsymbol{\sigma}$, $\boldsymbol{P}$, $\boldsymbol{\mathcal{M}}$, $\boldsymbol{J}^{\mathrm{fr.}}$ as constitutive equations depending on $\{\rho,\boldsymbol{v},c^\alpha,\boldsymbol{E},\boldsymbol{B}\}$. We suggest to follow [1, Chap. 3] for deriving the constitutive equations by using principle of thermodynamics as well as for generating the weak form. The weak form is the necessary input for a computational simulation in multiphysics.

Acknowledgement. B. E. Abali acknowledges the Daimler and Benz Foundation Postdoctoral Scholarship 2018.

References

1. B E Abali. *Computational Reality, Solving Nonlinear and Coupled Problems in Continuum Mechanics*. Advanced Structured Materials. Springer, 2016.
2. B E Abali and F A Reich. Thermodynamically consistent derivation and computation of electro-thermomechanical systems for solid bodies. *Computer Methods in Applied Mechanics and Engineering*, 319:567–595, 2017.
3. S M Barnett. Resolution of the Abraham–Minkowski dilemma. *Physical Review Letters*, 104(7):070401, 2010.
4. M Bethune-Waddell and K J Chau. Simulations of radiation pressure experiments narrow down the energy and momentum of light in matter. *Reports on Progress in Physics*, 78(12):122401, 2015.
5. A R Felix. *Coupling of Continuum Mechanics and electrodynamics: An Investigation of Electromagnetic Force Models by Means of Experiments and Selected Problems*. PhD thesis, TU Berlin, 2017.
6. D J Griffiths. Resource letter em-1: Electromagnetic momentum. *American Journal of Physics*, 80(1):7–18, 2012.
7. D J Griffiths and R College. *Introduction to electrodynamics*, volume 3. prentice Hall Upper Saddle River, NJ, 1999.
8. S R Groot and P Mazur. Non-equilibrium thermodynamics, 1984.
9. D S Jones. *The Theory of Electromagnetism*. Pergamon, 1964.
10. H A Lorentz. Versuch einer Theorie der elektrischen und optischen Erscheinungen in bewegten Körpern. *Zittungsverlagen Akad. van Wettenschappen 1, 74 (Nov. 26, 1892); Proc. Acad. Sci.(Amsterdam)(Engl. version)*, 6:809, 1904.
11. F E Low. *Classical field theory: electromagnetism and gravitation*. Wiley-VCH Verlag, 2004.
12. M Mansuripur. Resolution of the Abraham–Minkowski controversy. *Optics Communications*, 283(10):1997–2005, 2010.
13. Y N Obukhov. Electromagnetic energy and momentum in moving media. *Annalen der Physik*, 17(9-10):830–851, 2008.
14. F A Reich, W Rickert, and W H Müller. An investigation into electromagnetic force models: differences in global and local effects demonstrated by selected problems. *Continuum Mechanics and Thermodynamics*, 30(2):233–266, 2018.

Current developments in device simulation: degeneracy, arbitrary density of states and multi-particle drift-diffusion

Matthias Auf der Maur[1]

Dept. Electronics Engineering, University of Rome Tor Vergata, Via Politecnico 1, 00133 Rome, Italy
auf.der.maur@ing.uniroma2.it

Summary. In recent years the well established drift-diffusion model for semiconductors has returned into focus in relation with the development of new devices and materials. The standard formulation of the model and its discretization are based on a number of assumptions, which are not always valid and require modifications for certain device types and materials currently of interest. We will show that, while still remaining in the framework of drift-diffusion, we can formulate more generalized schemes allowing to simulate a larger class of devices and physical effects.

1 Introduction

The drift-diffusion model, also known as the van Roosbroeck system [5], has been the work horse of electronic device simulation during the last 50 years. This well known model in its usual formulation [6] is based on a set of three partial differential equations, namely two continuity equations for the electron and hole flow, and the Poisson equation for the calculation of the mean electrostatic field:

$$\frac{\partial n}{\partial t} + \nabla j_n = -R + G \tag{1a}$$

$$\frac{\partial p}{\partial t} + \nabla j_p = -R + G \tag{1b}$$

$$-\nabla(\varepsilon \nabla \varphi) = -e(n - p + C). \tag{1c}$$

Here, n and p are the electron and hole densities, respectively. R and G are the recombination and generation rates, j_n and j_p are the electron and hole fluxes. In the Poisson equation (1c) ε denotes the permittivity, while e is the elementary charge and C is the net charge density due to e.g. dopants. φ is the electrostatic potential. Two constitutive equations connect the carrier fluxes with the densities and the electrostatic potential, most often written in the drift-diffusion form

$$j_n = -D_n \nabla n + \mu_n n \nabla \varphi \tag{2a}$$

$$j_p = -D_p \nabla p - \mu_p p \nabla \varphi, \tag{2b}$$

where $D_{n,p}$ are the diffusion constants and $\mu_{n,p}$ the mobilities. The most important basic assumption of the model (1) is that electrons and holes are in a local thermal quasi equilibrium, so that their densities can be written in terms of a quasi Fermi level or electrochemical potential as e.g. for electrons

$$n = \int_{-\infty}^{\infty} D(E) f(E - E_{F,n}) \, \mathrm{d}E \,, \tag{3}$$

where $D(E)$ is the density of states and $f(x)$ is the Fermi-Dirac distribution. In many practical implementations the Boltzmann approximation is used to get the familiar expression $n = N_c \exp\left(\frac{E_{F,n} - E_c}{k_B T}\right)$.

While this model has been developed for the description of electron and hole transport in inorganic semiconductors like silicon and gallium arsenide, it has been subsequently applied to other materials, in particular organics, electrochemical systems and novel materials like Perovskites. Moreover, it is often applied in device structures where some of the basic assumptions and approximations may be globally or locally violated, like quantum confined structures, heterostructures or transistors with short gates.

To some extent, the standard drift-diffusion model as given in (1) can be adjusted to give reasonable results even in such situations by carefully designing models for the mobility and the recombination terms, for example, or by resorting to Schrödinger/Poisson type of setups, or multiphysics/multiscale coupling to more involved models [2]. Other cases, however, require modifications of the model formulation or the discretization scheme.

Here we show some examples of situations, where a reformulation of the model can lead to a more sound description of the device physics, without however sacrificing important advantages of the drift-diffusion model like its computational effectiveness.

2 Degeneracy and arbitrary density of states

Today, in a large number of device structures the validity of the Boltzmann approximation or the assumption of the density having an exponential or Fermi integral type of dependency on the potentials do not hold. Especially, in organic electronics the density of states (DOS) is completely different from that of inorganic cristalline semiconductors. In fact, the macroscopic DOS in the latter is in most cases due to a

disordered spatial and energetic distribution of energy levels of localized states [1]. Although still an approximation, often a gaussian density of states is assumed for organic materials, to be used in (3). This clearly modifies the functional dependency of the density on the potentials, and reduces the range of validity of the Boltzmann approximation. Similarly, in quantum confined structures the local DOS obtained from a quantum mechanical model can be used. Hoever, any deviation from a Boltzmann form of the densities requires a subtle modification in the transport equations. In fact, the diffusion constants and mobilities are not independent, but they are related by means of an Einstein relation of the form $D_n = q^{-1} n \left(\partial n / \partial E_{F,n}\right)^{-1} \mu_n$, which in Boltzmann approximation reduces to $D_n = k_B T / q \mu_n$. This is well known, and usually called *diffusion enhancement* [3]. Note that this could have measurable effects on device performance. As an example, we report in Fig. 1 the predicted dependancy of the rate of change of the open circuit voltage of a solar cell with light intensity, for different DOS [1]. Unfortunately, this not only leads to a nonlinear diffusion, but it also affects the discretization. In fact, it is well known that standard discretization approaches like finite differences or finite elements of (1) and (2) lead to an unstable scheme. The state of the art solution is to use the Scharfetter-Gummel (SG) approach in conjunction with a finite volume discretization [3]. However, the SG scheme is strictly valid only in the Boltzmann approximation and must be adapted if this is not the case. Therefore, discretization schemes for the drift-diffusion equations have regained interest in the last years.

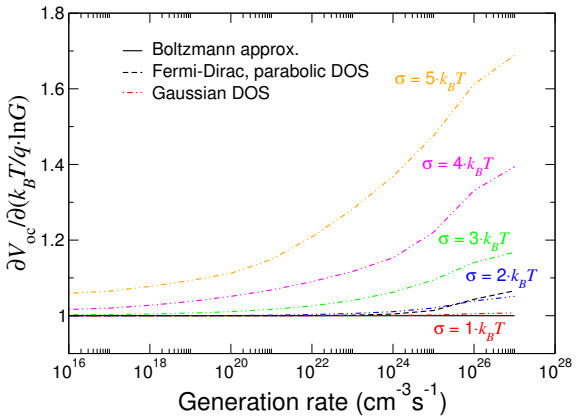

Fig. 1. Effect of the diffusion enhancement on the dependency of the solar cell open circuit voltage on the optical generation rate.

3 Multi-particle drift-diffusion

One of the limitations of the drift-diffusion model is the assumption of two equilibrium populations. In a series of devices one could define sub-populations which are individually in quasi equilibrium. For example, in multi quantum well structures as used for light emitting diodes (LEDs) the quantum confined carrier populations are coupled by thermal emission and capture processes to the free carriers, which can be assumed to be much slower than typical intraband relaxation. In such a situation, we can formally split the populations and couple them explicitly by suitable generation-recombination terms describing emission and capture. Similarly, the intermediate band (IB) concept is of interest in the field of photovoltaics [4], where a small band formed e.g. from quantum dot states inside the gap of a semiconductor theoretically allows to increase device efficiency. This can only be simulated by introducing a third carrier population with a finite width DOS, having its own quasi Fermi level.

We have implemented such a multi-particle drift-diffusion model, and made preliminary tests with several device types, like organic LEDs, IB solar cells and multi quantum wells. The model also allows to include mobile ions, of interest e.g. for the simulation of Perovskite devices.

Acknowledgement. The author acknowledges the support of EU-H2020 project “MOSTOPHOS” (n. 646259) and of the COST Action MP1406 “MultiscaleSolar”.

References

1. M Auf der Maur, A Gagliardi, and Tim Albes. Thin film solar cells. In J. Piprek, editor, *Handbook of Optoelectronic Device Modeling & Simulation*, chapter 43, pages 497–538. CRC Press, Taylor & Francis Group, Boca Raton, 2017.
2. M. Auf der Maur, G. Penazzi, G. Romano, F. Sacconi, A. Pecchia, and A. Di Carlo. The multiscale paradigm in electronic device simulation. *IEEE Transactions on Electron Devices*, 58(5):1425–1432, May 2011.
3. Thomas Koprucki, Nella Rotundo, Patricio Farrell, Duy Hai Doan, and Jürgen Fuhrmann. On thermodynamic consistency of a scharfetter–gummel scheme based on a modified thermal voltage for drift-diffusion equations with diffusion enhancement. *Optical and Quantum Electronics*, 47(6):1327–1332, 2015.
4. Antonio Luque and Antonio Martí. The intermediate band solar cell: Progress toward the realization of an attractive concept. *Advanced Materials*, 22(2):160–174, 2010.
5. W van Roosbroeck. Theory of the flow of electrons and holes in germanium and other semiconductors. *Bell Labs Technical Journal*, 29(4):560–607, 1950.
6. Siegfried Selberherr. *Analysis and Simulation of Semiconductor Devices*. Springer-Verlag Wien New York, 1st edition, 1984.

Data Center Power

Tonio Biondi[1]

[1] Maxim Integrated

Summary: During the last decade, the growing demand for internet-related services has fostered the proliferation of data centers all over the world. At the same time, the increasing requirements in data storage, processing capability and transmission rates have pushed energy consumption of data centers to a higher level. Therefore, optimizing energy usage and improving power efficiency became imperative to minimize environmental, economic and energy supply security impact. In this work, the topic of powering data centers is analyzed at different levels from infrastructure to architecture to building blocks. The consolidated trend towards 48V power architectures, as a replacement of the commoditized 12V architectures, is discussed with special emphasis on power efficiency benefits. Design challenges and methodologies are described with a focus on power integration.

GCA-$\mathscr{H}^2$ matrix compression for electrostatic simulations

Steffen Börm[1] and Sven Christophersen[1]

Department of Mathematics, University of Kiel, 24118 Kiel, Germany
boerm@math.uni-kiel.de, christophersen@math.uni-kiel.de

Summary. We consider a compression method for boundary element matrices arising in the context of the computation of electrostatic fields. Green cross approximation combines an analytic approximation of the kernel function based on Green's representation formula and quadrature with an algebraic cross approximation scheme in order to obtain both the robustness of analytic methods and the efficiency of algebraic ones. One particularly attractive property of the new method is that it is well-suited for acceleration via general-purpose graphics processors (GPGPUs).

Boundary integral formulations for electrostatic field problems typically lead to equations of the form

$$\int_{\partial\Omega} g(x,y)u(y)\,dy = \lambda u(x) + \int_{\partial\Omega} \frac{\partial g}{\partial n_y}(x,y)v(y)\,dy$$

for all $x \in \partial\Omega$, where $\Omega \subseteq \mathbb{R}^3$ is a domain, $\lambda \in \mathbb{R}$, u and v are scalar functions on the boundary $\partial\Omega$, and

$$g(x,y) = \frac{1}{4\pi\|x-y\|}$$

is the fundamental solution of Laplace's equation.

Discretization by Galerkin's method with basis functions $(\varphi_i)_{i\in\mathscr{I}}$ leads to a matrix $G \in \mathbb{R}^{\mathscr{I}\times\mathscr{I}}$ given by

$$g_{ij} = \int_{\partial\Omega} \varphi_i(x) \int_{\partial\Omega} g(x,y)\varphi_j(y)\,dy\,dx \qquad (1)$$

for all $i,j \in \mathscr{I}$, and all of these coefficients are typically non-zero. In order to find a data-sparse approximation of G, we consider a domain $\tau \subseteq \mathbb{R}^3$ and a superset $\omega \subseteq \mathbb{R}^3$ such that the distance from τ to the boundary $\partial\omega$ of ω is non-zero. For any $y \in \mathbb{R}^3 \setminus \overline{\omega}$, the function $x \mapsto g(\cdot,y)$ is harmonic in ω, so we can apply Green's third identity to obtain

$$g(x,y) = \int_{\partial\omega} g(x,z)\frac{\partial g}{\partial n_z}(z,y) - \frac{\partial g}{\partial n_z}(x,z)g(z,y)\,dz$$

for all $x \in \tau$ and $y \in \mathbb{R}^3 \setminus \overline{\omega}$. If the distances between $\partial\omega$ and τ and between $\partial\omega$ and y are sufficiently large, the integrand is smooth, and we can approximate the integral by a quadrature rule to find

$$g(x,y) \approx \sum_{\nu=1}^{k} w_\nu g(x,z_\nu)\frac{\partial g}{\partial n_z}(z_\nu,y) - w_\nu \frac{\partial g}{\partial n_z}(x,z_\nu)g(z_\nu,y) \qquad (2)$$

with weights w_ν and quadrature points z_ν, and in this approximation the variables x and y are separated.

This gives rise to a first low-rank approximation of G: given subsets $\widehat{\tau},\widehat{\sigma} \subseteq \mathscr{I}$ of the index set, we can introduce the corresponding supports

$$\tau := \bigcup_{i\in\widehat{\tau}} \operatorname{supp}\varphi_i, \qquad \sigma := \bigcup_{j\in\widehat{\sigma}} \operatorname{supp}\varphi_j,$$

and if these sets are well-separated, we can find a superset ω of τ such that its boundary $\partial\omega$ is sufficiently far from both τ and σ. Replacing g in (1) by the quadrature-based approximation leads to a factorized approximation

$$G|_{\widehat{\tau}\times\widehat{\sigma}} \approx A_{\tau,\sigma}B_{\tau,\sigma}^*,$$

with $A_{\tau,\sigma} \in \mathbb{R}^{\widehat{\tau}\times 2k}$ and $B_{\tau,\sigma} \in \mathbb{R}^{\widehat{\sigma}\times 2k}$, so the rank of the approximation is bounded by $2k$.

In order to make the approximation more efficient, we can apply adaptive cross approximation [1] to derive the algebraic counterpart of interpolation: this technique provides us with a small subset $\tilde{\tau} \subseteq \widehat{\tau}$ and a matrix $V_\tau \in \mathbb{R}^{\widehat{\tau}\times\tilde{\tau}}$ such that

$$V_\tau A_{\tau,\sigma}|_{\tilde{\tau}\times 2k} \approx A_{\tau,\sigma},$$

i.e., we can reconstruct $A_{\tau,\sigma}$ using only a few of its rows. Since $A_{\tau,\sigma}$ is a thin matrix, we can afford to use reliable pivoting strategies and do not have to rely on heuristics. We conclude

$$V_\tau G|_{\tilde{\tau}\times\widehat{\sigma}} \approx V_\tau A_{\tau,\sigma}|_{\tilde{\tau}\times 2k}B_{\tau,\sigma}^* \approx A_{\tau,\sigma}B_{\tau,\sigma}^* \approx G|_{\widehat{\tau}\times\widehat{\sigma}},$$

i.e., the algebraic interpolation can also be applied directly to the original matrix G instead of the low-rank approximation. This is called a *Green cross approximation* (GCA).

We can apply the same reasoning to the columns to obtain $\tilde{\sigma} \subseteq \widehat{\sigma}$ and $V_\sigma \in \mathbb{R}^{\widehat{\sigma}\times\tilde{\sigma}}$ with

$$G|_{\widehat{\tau}\times\widehat{\sigma}} \approx V_\tau G|_{\tilde{\tau}\times\tilde{\sigma}}V_\sigma^*,$$

and this turns out to be a very efficient approximation of the matrix block, since $G|_{\tilde{\tau}\times\tilde{\sigma}}$ is usually significantly smaller than $G|_{\widehat{\tau}\times\widehat{\sigma}}$.

We can improve the construction further by representing the *basis matrices* V_τ and V_σ in a hierarchy: assume that $\widehat{\tau}$ is subdivided into disjoint subsets $\widehat{\tau}_1$ and $\widehat{\tau}_2$ and that matrices V_{τ_1}, V_{τ_2} and subsets

$\tilde{\tau}_1 \subseteq \hat{\tau}_1, \tilde{\tau}_2 \subseteq \hat{\tau}_2$ have already been constructed. We let $\tilde{\tau}_{1,2} := \tilde{\tau}_1 \cup \tilde{\tau}_2$ and observe

$$A_{\tau,\sigma} = \begin{pmatrix} A_{\tau,\sigma}|_{\hat{\tau}_1 \times 2k} \\ A_{\tau,\sigma}|_{\hat{\tau}_2 \times 2k} \end{pmatrix} \approx \begin{pmatrix} V_{\tau_1} A_{\tau,\sigma}|_{\tilde{\tau}_1 \times 2k} \\ V_{\tau_2} A_{\tau,\sigma}|_{\tilde{\tau}_2 \times 2k} \end{pmatrix} = \begin{pmatrix} V_{\tau_1} & \\ & V_{\tau_2} \end{pmatrix} A_{\tau,\sigma}|_{\tilde{\tau}_{1,2} \times 2k},$$

and applying cross approximation to the right factor allows us to express V_τ recursively in terms of V_{τ_1} and V_{τ_2}. Since $\tilde{\tau}_{1,2}$ is usually significantly smaller than $\hat{\tau}$, this construction is more efficient than the straightforward GCA approach. The resulting GCA-$\mathscr{H}^2$-matrix compression algorithm can be proven to have almost optimal complexity [3]. Its result is a special case of the more general $\mathscr{H}^2$-matrix structure [2, 4].

Once the sets $\tilde{\tau}$ and $\tilde{\sigma}$ are known, the entries of the matrix $G|_{\tilde{\tau}\times\tilde{\sigma}}$ can be constructed independently, and this property makes this part of the algorithm very attractive for general-purpose graphics processors (GPGPUs).

n	V_τ(CPU)	$G\|_{\tilde{\tau}\times\tilde{\sigma}}$(GPU)
8 192	0.1s	0.2s
32 768	0.4s	0.7s
131 072	1.5s	2.7s
524 288	6.2s	11.8s
2 097 152	62.0s	64.1s

Fig. 1. Run-times for the setup of the GCA-$\mathscr{H}^2$ matrix for the single layer integral operator

Compressing the single layer integral operator on a unit sphere approximated by n triangles using piecewise constant basis functions with an error tolerance that ensures that the solution of the integral equation is approximated at full accuracy yields the run-times given in Figure 1.

The column "V_τ" corresponds to the time for the row and the column basis, although both are identical for the symmetric matrix considered here. Since the basis construction is an adaptive process, we use a general-purpose processor, in this case an Intel Core i7-3820 with four cores, to handle this part of the algorithm.

The column "$G|_{\tilde{\tau}\times\tilde{\sigma}}$" gives the time for both farfield matrices, i.e., matrices handled by the GCA-$\mathscr{H}^2$ approximation, and nearfield matrices that are computed by the well-known Sauter-Schwab quadrature technique [5]. This task is well-suited for massively parallel computing, and we employ an NVIDIA GeForce GTX 680 card.

For the last line we had to increase the order of the Green quadrature in (2) to preserve the full discretization accuracy, this explains the larger increase in run-time compared to the previous lines. We can conclude that our approach allows us to discretize geometries with more than two million degrees of freedom on a standard (if a little outdated) workstation in approximately two minutes.

References

1. M. Bebendorf. Approximation of boundary element matrices. *Numer. Math.*, 86(4):565–589, 2000.
2. S. Börm. *Efficient Numerical Methods for Non-local Operators: $\mathscr{H}^2$-Matrix Compression, Algorithms and Analysis*, volume 14 of *EMS Tracts in Mathematics*. EMS, 2010.
3. S. Börm and S. Christophersen. Approximation of integral operators by Green quadrature and nested cross approximation. *Numer. Math.*, 133(3):409–442, 2016.
4. W. Hackbusch, B. N. Khoromskij, and S. A. Sauter. On $\mathscr{H}^2$-matrices. In H. Bungartz, R. Hoppe, and C. Zenger, editors, *Lectures on Applied Mathematics*, pages 9–29. Springer-Verlag, Berlin, 2000.
5. S. A. Sauter and C. Schwab. *Boundary Element Methods*. Springer, 2011.

Topology and Shape Optimization of Electrical Machines

Peter Gangl[1], Samuel Amstutz[2], and Ulrich Langer[3]

[1] Institute of Applied Mathematics, TU Graz, Steyrergasse 30, 8010 Graz, Austria gangl@math.tugraz.at,
[2] UFR-ip Sciences Technologie Sant - 301 rue Baruch de Spinoza - BP 21239 - 84916 Avignon Cedex 9
samuel.amstutz@univ-avignon.fr
[3] RICAM Linz, Austrian Academy of Sciences, Altenbergerstraße 69, 4040 Linz, Austria
ulrich.langer@ricam.oeaw.ac.at

Summary. We perform design optimization of electrical machines by means of the topological derivative and the shape derivative for two-dimensional nonlinear magnetostatics. In order to control the complexity of the arising structure and ensure manufacturability, we include a bound on the perimeter of the design. We show results for the optimization with respect to two materials (iron, air) as well as an extension to also include a third material (permanent magnet) into the optimization.

1 Problem Description

For the design optimization of an electric motor, we consider its two-dimensional cross-section, see Fig. 1 for a model problem. The computational domain D comprises areas of ferromagnetic material (Ω_f; brown), air regions (Ω_air; dark blue), coil areas (Ω_c; light blue), and permanent magnets (Ω_mag; orange) which are magnetized in the indicated directions.

Our goal is to determine the optimal material distribution inside a fixed design subdomain Ω^d of the electric motor such that a given objective function is minimized. On the one hand, we consider the distribution of two materials (ferromagnetic material and air) and, on the other hand, also the optimization with respect to three materials (ferromagnetic material, air and permanent magnet). In the case of two materials, we are facing the following problem:

$$\min_{\Omega} \mathscr{J}(u) \tag{1a}$$

$$\text{s.t.} -\operatorname{div}(\nu_\Omega(x,|\nabla u|)\nabla u) = F(x) \quad \text{in } D, \tag{1b}$$

$$u = 0 \quad \text{on } \partial D, \tag{1c}$$

where the optimization variable Ω denotes the variable ferromagnetic subset of the design subdomain. The state variable u is the third component of the magnetic vector potential of the magnetic flux density, $\mathbf{B} = \operatorname{curl}(0,0,u)$. The magnetic recluctivity ν_Ω is a nonlinear function depending on $|\nabla u|$ in the ferromagnetic subdomains and piecewise constant elsewhere,

$$\nu_\Omega(x,|\nabla u|) = \begin{cases} \hat{\nu}(|\nabla u|) & x \in \Omega_\mathrm{f}, \\ \nu_0 & x \in \Omega_\mathrm{air} \cup \Omega_c, \\ \nu_\mathrm{mag} & x \in \Omega_\mathrm{mag}. \end{cases}$$

The right hand side F comprises the impressed current density in the coils as well as the permanent magnetization,

$$F(x) = \chi_{\Omega_\mathrm{c}}(x) J_\mathrm{i}(x) - \chi_{\Omega_\mathrm{mag}}(x) \nu_\mathrm{mag} \operatorname{div} M^\perp(x).$$

We consider different objective functionals $\mathscr{J}$. For instance, we maximize the average torque over different rotor positions, or we minimize a functional which yields a smooth rotation of the rotor.

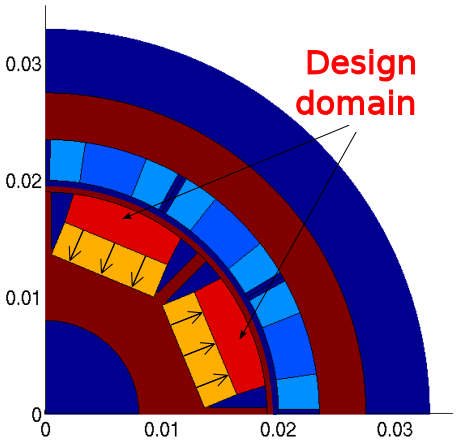

Fig. 1. Model problem with design area Ω^d

2 Design Optimization

We approach the design optimization problem (1) by means of a two-stage algorithm: in the first stage, the topology is optimized using the topological derivative concept, and in the second stage shape optimization is performed as post-processing.

2.1 Stage I: Topology Optimization

We employ the level set algorithm [1] in which the evolution of the design is guided by the *topological derivative*. Therefore, topological changes of the geometry can easily be achieved.

The topological derivative of a domain-dependent functional $J = J(\Omega)$ denotes the functional's sensitivity with respect to a local change of material around an interior point. The topological derivative of the optimization problem (1), which is constrained by a quasilinear partial differential equation, was derived in [2].

2.2 Stage II: Shape Optimization

The *shape derivative* denotes the sensitivity of a domain-dependent objective function with respect to smooth perturbations of the boundary of a domain or of a material interface. As a post-processing of the final design obtained in Stage I, we perform a gradient-based shape optimization algorithm based on the shape derivative of problem (1), see also [4].

3 Interface Handling

In the course of the optimization algorithm of Section 2, the material interface between ferromagnetic material and air inside the design area Ω^d evolves. However, in each step of the optimization algorithms, the state equation (1b)–(1c) as well as an adjoint equation have to be solved, which is done by the finite element method. In order to ensure accurate approximate solutions, we employ a local mesh adaptation strategy in order to resolve the material interfaces. We show optimal order of convergence and introduce a preconditioner for which optimal conditioning of the preconditioned system can be observed.

4 Manufacturability

Problem (1) only accounts for the optimization of the electromagnetic performance of the electric motor and does not take into account important other aspects such as the manufacturability of the design or its mechanical stability when rotating with high speed.

We can restrict the complexity of the designs arising in the optimization by controlling the perimeter of the design Ω, e.g., by replacing the objective function in (1a) by

$$\tilde{\mathscr{J}}(u,\Omega) := \mathscr{J}(u) + \beta \operatorname{Per}(\Omega)$$

with $\beta > 0$.

For the perimeter functional $\operatorname{Per}(\Omega)$, the topological derivative cannot be computed [3]. However it can be approximated by a quantity $\operatorname{Per}_\delta(\Omega)$, which converges to $\operatorname{Per}(\Omega)$ as δ approaches zero, for which the topological derivative was derived in [3].

In order to incorporate a bound on the complexity of the structure, we consider the regularized design optimization problem

$$\begin{aligned} min\, \mathscr{J}(u) + \beta \operatorname{Per}_\delta(\Omega) \\ \text{s.t. (1b)} - \text{(1c)} \end{aligned} \tag{2}$$

an solve this problem for a decreasing sequence $(\delta_n)_n$. Here, the complexity can be controlled by choosing different weights β, see Fig. 2.

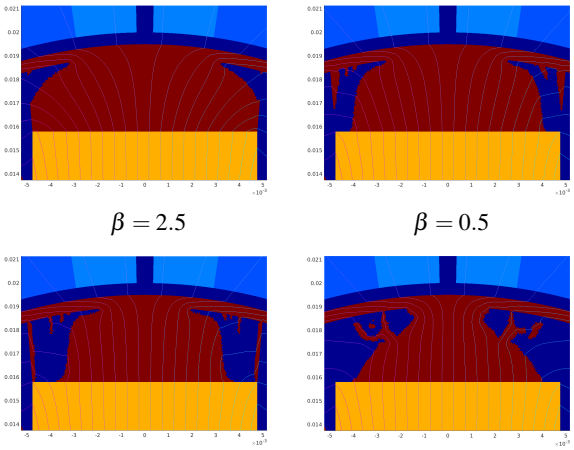

Fig. 2. Optimization results for (2) for different values of β.

5 Multi-material Optimization

We also consider the case, where the design area Ω^d may be occupied by not only two, but three different materials, namely by ferromagnetic material, air and permanent magnet material. For this purpose, we extend the level set algorithm [1] to the case of three materials by introducing an $\mathbb{R}^2$-valued level set function. We include a penalization of the permanent magnet volume on the one hand, and of the perimeter of the design on the other hand.

References

1. Amstutz, S. and Andrä, H. (2006) A new algorithm for topology optimization using a level-set method. Journal of Computational Physics, 216(2):573–588.
2. Gangl, P. (2017) Sensitivity-based topology and shape optimization with application to electrical machines. PhD thesis, JKU Linz, 2016.
3. Amstutz, S. (2013) Regularized perimeter for topology optimization. SIAM Journal on Control and Optimization, 51(3): 2176–2199.
4. Gangl, P., Langer, U., Laurain, A., Meftahi, H. and Sturm, K. (2015) Shape optimization of an electric motor subject to nonlinear magnetostatics. SIAM Journal on Scientific Computing, 37(6): B1002–B1025.

Techniques for modeling fiber laser amplifiers

Jay Gopalakrishnan[1], Tathagata Goswami[1], and Jacob Grosek[2]

[1] Portland State University, PO Box 751, Portland, OR 97207-0751, USA, gjay@pdx.edu, tgoswami@pdx.edu
[2] Air Force Research Laboratory, 3550 Aberdeen Ave SE, Kirtland Air Force Base, NM 87117, USA, jacob.grosek.1@us.af.mil

Summary. Numerical techniques for simulation of electromagnetic wave propagation within fiber amplifiers are discussed. Since a full-featured simulation using the Maxwell system on a realistic fiber is beyond reach, simplified models form the state of the art. This work presents a novel concept of equivalent short fiber, an artificial fiber, which while imitating a longer fiber in certain aspects, requires only a fraction of the computational resources needed to simulate the full length fiber.

1 Fiber amplifiers

Fiber amplifiers are typically circularly symmetric double-clad step-index fibers. They have a core that is usually doped with lanthanide rare-earth metallic elements like Thulium or Ytterbium. They are used to amplify input signal light by transferring energy from pump light. Pump light energizes dopant ions to excited radiative states. Stimulated emission of signal photons follows.

The ability of solid-state fiber laser amplifiers to deliver high output power has been exploited and studied over the last few decades [1]. The rate of increase in average output power realized over these years seems to have hit a roadblock when transverse modal instabilities (TMI) were experimentally observed found at high powers. These observations have led to intensive speculations on the cause of TMI, the prevailing theory being that the cause is a temperature-induced grating. Reliable numerical simulation of TMI and other nonlinear optical effects within fibers can provide important insights for validating or rejecting various physical hypothesis put forth to explain these effects. These techniques must however be able to numerically solve the field propagation within a long fiber a vast number of times.

2 Hierarchy of models

Starting from first principles, we introduce gain terms through polarization. It can be seen, by mathematically comparing with the familiar conductivity terms, that such gain terms must cause light amplification.

We then outline a hierarchy of models for numerical simulation, ranging from the most-expensive but full-fidelity Maxwell system, to the quicker but low-fidelity approaches such as the Couple Mode Theory (CMT) model. The CMT model uses an electric field ansatz based on the transverse guided modes of the fiber, which can be approximated by finite elements. Although the field problem is reduced to one that can be sent to an ordinary differential equation (ODE) system solver, even the CMT model is computationally demanding due to the many transverse finite element integrations required along a long fiber. With this perspective, we review the significant contributions made so far in the optics community [1–3] in the numerical modeling of fiber laser amplifiers.

3 Equivalent short fiber

We present a new equivalent short fiber concept. In various fields of study, physical or numerical scale models of an object have been used – they preserve some of the important properties of the object while not preserving the original dimensions of the object. In the context of fiber amplifiers, its natural to seek a miniature scale model that reduces fiber length while preserving the remaining dimensions. By reducing the number of transverse integrations required within the ODE solver, an equivalent shorter fiber can bring about drastic reductions in computational cost. We show that this is indeed feasible under certain conditions.

Acknowledgement. This work was supported in part by AFOSR grant FA9550-17-1-0090.

References

1. C. Jauregui, J. Limpert, and A. Tünnermann. High-power fibre lasers. *Nature Photonics*, 7(11):861–867, 2013.
2. S. Naderi, I. Dajani, T. Madden, and C. Robin. Investigations of modal instabilities in fiber amplifiers through detailed numerical simulations. *Optics Express*, 21(13):16111–16129, 2013.
3. A. V. Smith and J. J. Smith. Mode instability in high power fiber amplifiers. *Optics Express*, 19(11):10180–10192, 2011.

Model reduction for nonlinear systems – a time-domain moment matching perspective

Tudor C. Ionescu[1]

Dept. of Automatic Control and Systems Eng., Politehnica Univ. of Bucharest, 060042 Bucharest, Romania and "G. Mihoc-C. Iacob" Institute of Mathematical Statistics and Appl. Math. of the Romanian Academy, 050711 Bucharest, Romania. tudor.ionescu@acse.pub.ro

Summary. For nonlinear systems, high dimension and complexity are two major issues in dealing with models suitable for (nonlinear) analysis, simulation and control. Even if the high dimension is reduced, complexity may increase as opposed to linear systems where these notions are identical. Therefore, suitable model reduction is called for. This has been studied recently in the time-domain moment matching framework, where suitable notions of moment have been introduced and families of parameterized reduced order models have been developed. The degrees of freedom are used to enforce/preserve properties or topology, increase accuracy, etc. Same ideas apply to the case of infinite-dimensional systems such as, e.g., time-delayed systems, PDE-based models, etc. where families of finite-dimensional systems can be achieved based on moment matching.

1 Introduction

Nowadays we are living in a more complex and interconnected world in all areas. Mathematical tools yield complex and highly dimensional dynamical models (e.g., from partial-differential equations, networks of large numbers of subsystems, etc), gathered under the name of large-scale systems. Hence, for purposes such as simulation and control design, scientists and engineers need tweaking of such models rendering them simpler and useful. To this end, model reduction is called for. The main idea of model order reduction is to find a low-order mathematical model that approximates the given large-scale dynamical system. The approximation is accurate if the *approximation error* is *small* and if the most important physical structure/properties, such as stability or energy dissipation, of the given system are preserved.

Typically, the model reduction problem is formulated as follows. Given a dynamical system

$$\dot{x} = f(x,u,t),\ x(0) = x_0,\ y = h(x,u,t). \qquad (1)$$

where $x(t) \in \mathbb{R}^n$, is the state of the system, $u(t) \in \mathbb{R}^m$ is the input and $y(t) \in \mathbb{R}^p$ represents the output of the system. $t \in \mathbb{R}$ represents the time. By reducing this system, we mean to find a system

$$\dot{\hat{x}} = \hat{f}(\hat{x},u,t),\ \hat{y} = \hat{h}(\hat{x},u,t), \qquad (2)$$

with $\hat{x}(t) \in \mathbb{R}^r$, $\hat{y}(t) \in \mathbb{R}^p$ such that

- $r < n$,
- system (2) preserves the properties/structure of system (1) for certain analysis/control purposes,
- system (2) approximates system (1) under certain criteria and within an error bound,
- system (2) is easy to compute.

A category of computationally-efficient model reduction techniques are based on moment matching, see, e.g., [2, 5] and [1] for an overview for linear systems. In such techniques the (reduced order) model is obtained by constructing a lower degree rational function that approximates the original transfer function. The low degree function matches the original transfer function and its derivatives at various points in the complex plane. The low order system is computed employing Krylov projections yielding numerically efficient algorithms (see e.g., [1, 6, 8]).

More recently, in [3, 4, 12] new definitions of moments in a time-domain framework have been given. This equivalent definition of moments is in the relation with the steady-state response (if it exists) of the system driven by a signal generator (a novel interpretation of the results in [7]). The moments of a linear system are defined in terms of the solution of a Sylvester equation. The reduced order model that achieves moment matching at ν points is a parametric model, the degree of freedom being used such that certain properties are preserved. Based on the dual Sylvester equation, a new definition of moment dual to the previous one is obtained. The reduced order model that achieves moment matching at ν points is also a parametric one.

Based on this time-domain notion of moment matching, several goals have been achieved, leading to a nice and fruitful theory of moment matching for nonlinear systems (also adapted to infinite-dimensional systems). We present some of the main results of the past eight years and very recently obtained in this direction. The results are mainly ideas of how to use the degrees of freedom to achieve specific goals, as well as extensions of well-known ideas of moment matching to the nonlinear case.

2 Main time-domain moment matching results

2.1 Nonlinear moment matching - system driven by a signal generator [4]

Consider the single-input, single-output,

$$\dot{x} = f(x,u),\ y = h(x), \tag{3}$$

where $x(t) \in \mathbb{R}^n$, $u(t) \in \mathbb{R}$, $y(t) \in \mathbb{R}$ and f and h are smooth mappings, such that $f(0,0) = 0$ and $h(0) = 0$ and the signal generator $\dot{\omega} = s(\omega), \eta = l(\omega)$. Consider the interconnected system

$$\dot{\omega} = s(\omega),\ \dot{x} = f(x,l(\omega)),\ y = h(x). \tag{4}$$

A family of reduced order models, all achieving moment matching at $\{s,l\}$, is described by

$$\Sigma_{\delta(\xi)} : \begin{cases} \dot{\xi} = s(\xi) - \delta(\xi) l(\xi) + \delta(\xi) u, \\ \psi = h(\pi(\xi)), \end{cases} \tag{5}$$

with $\xi(t) \in \mathbb{R}^\nu$, where δ is a free parameter.

3 Nonlinear moment matching, a new approach - the signal generator driven by the system [11]

In this section we present a new general framework for nonlinear moment matching based on "swapping" the interconnection between the system and the (generalized) signal generator.

Consider the nonlinear system $\dot{\xi} = \varphi(\xi,u), \eta = \psi(\xi)$ and the signal generator $\dot{\varpi} = q(\varpi,v),\ \varpi(0) = 0,\ d = \mathbf{v}(\varpi,x)$. Assume there exists γ such that $\chi(\gamma(\xi),\xi) = 0$. Then the system matches the moments of (3) at q, if and only if

$$\left(\frac{\partial \chi(\varpi,\xi)}{\partial \varpi} q(\varpi - \zeta, \psi(\xi)) + \frac{\partial \chi(\varpi,\xi)}{\partial \xi} \varphi(\xi,u)\right)\Big|_{\varpi=\gamma(\xi)} = \frac{\partial \mathbf{v}(\varpi,x)}{\partial x}[f(x,u) - f(x,0)]\Big|_{\varpi=\rho(x),x=\alpha(\xi)}. \tag{6}$$

A family of models $\dot{\xi} = \varphi(\xi,u), \eta = \psi(\xi)$ parametrized in ψ that achieves moment matching is characterized by a mapping φ satisfying

$$\frac{\partial \chi(\varpi,\xi)}{\partial \xi}\Big|_{\varpi=\gamma(\xi)} \varphi(\xi,0) + \frac{\partial \chi(\varpi,\xi)}{\partial \varpi} q(\varpi - \zeta, \psi(\xi))\Big|_{\varpi=\gamma(\xi)} = 0, \tag{7}$$

under certain assumptions.

3.1 Two-sided moment matching [9, 11]

In this section we give the nonlinear counterpart of [10, Proposition 1], *i.e.*, we compute the subfamily of models of order ν that match the moments at $\{s,l\}$ and the moments at $\{\bar{q},r\}$ (a more explicit form of the generalized signal generator), of a given nonlinear system, simultaneously.

Indeed, under mild assumptions, there exists a subfamily of models that match both nonlinear moments simultaneously. In the linear case, the families of models Σ_G and Σ_H that match the moments at two sets of different moments at distinct interpolation points have a unique model in common that matches the moments form both sets simultaneously.

Furthermore, in the linear case, if the interpolation points are not distinct, there exists one model that matches the moments of the transfer function and its derivative simultaneously at the set of interpolation points chosen. Simulations illustrate that indeed, matching the moments of the transfer function and its derivative lead to a decrease of the H_2-norm of the approximation error. Other significant results are presented, including approximation of time-delay systems, port-Hamiltonian systems etc.

References

1. A. C. Antoulas. *Approximation of large-scale dynamical systems*. SIAM, Philadelphia, 2005.
2. A. C. Antoulas, J. A. Ball, J. Kang, and J. C. Willems. On the solution of the minimal rational interpolation problem. *Linear Algebra & its Applications*, 137/138:511–573, 1990.
3. A. Astolfi. A new look at model reduction by moment matching for linear systems. In *Proc. 46th IEEE Conf. on Decision and Control*, pages 4361–4366, 2007.
4. A. Astolfi. Model reduction by moment matching for linear and nonlinear systems. *IEEE Trans. Autom. Contr.*, 50(10):2321–2336, 2010.
5. C. de Villemagne and R. E. Skelton. Model reductions using a projection formulation. *Int. J. Control*, 46:2141–2169, 1987.
6. K. Gallivan and P. Van Dooren. Rational approximations of pre-filtered transfer functions via the Lanczos algorithm. *Numerical Algorithms*, 20:331–342, 1999.
7. K. Gallivan, A. Vandendorpe, and P. Van Dooren. Sylvester equations and projection based model reduction. *J. Comp. Appl. Math.*, 162:213–229, 2004.
8. W. B. Gragg and A. Lindquist. On the partial realization problem. *Linear Algebra & its Applications*, 50:277–319, 1983.
9. T. C. Ionescu. Two-sided time-domain moment matching for linear systems. *IEEE Trans. Autom. Contr.*, 61(9):2632–2637, 2016.
10. T. C. Ionescu and A. Astolfi. Families of reduced order models that achieve nonlinear moment matching. In *Proc. American Control Conference*, pages 5518–5523, 2013.
11. T. C. Ionescu and A. Astolfi. Nonlinear moment matching-based model order reduction. *IEEE Trans. Autom. Contr.*, 61(10):2837–2847, 2016.
12. T. C. Ionescu, A. Astolfi, and P. Colaneri. Families of moment matching based, low order approximations for linear systems. *Systems & Control Letters*, 64:47–56, 2014.

Description of the trajectories of quantum particles by a Quantum Lagrangian approach.

Omar Morandi[1]

Università degli Studi di Firenze, Florence, Italy. omar.morandi@unifi.it

Summary. A quantum model based on a Euler-Lagrange variational approach is proposed. In analogy with the classical transport, our approach maintain the description of the particle motion in terms of trajectories in a configuration space. Our method is designed to describe correction to the motion of nearly localized particles due to quantum phenomenas. We focus on the simulation of the motion of light nuclei in ab initio calculations. We discuss the connection of our results with the Bohm trajectories approach.

1 Introduction

During the last decade, the dynamics of molecules and the optical properties of nanostructures have been extensively investigated. Numerical methods based on ab initio approaches constitute a very important tool to understand the dynamics the optical properties of nanostructures.

New concepts such as the deterministic and the stochastic quantum trajectories have been proposed to develop new ab initio methods that go beyond the classical description of the atomic nuclei. One of the major advantages of developing a method that extends the concept of classical trajectory to the quantum mechanical context, is that the molecular dynamics solvers already developed my be easily extended to integrate such a new theory.

We derive the motion of a quantum particle by using a integral formulation of the equation of motion. We assume that the particle is described by a Gaussian-like wave packet parametrized by a set of numbers that depend on time. We formulate the dynamics of the particle wave function in terms of a variational Euler-Lagrange problem. By minimizing the action of the quantum Lagrangian of the particle, we derive the evolution equations for the parameters.

Our approach is particularly suited to describe the motion of heavy particles that have a quasi-classical behavior as for example the neutrons and the protons. We will discuss the application of our Lagrangian method to describe the quantum correction to the 2D motion of heavy particles in the presence of confining non harmonic potentials. In particular, the connection with the Bohm interpretation of the quantum mechanics will be presented.

2 Model

Our model is based on the quantum Lagrangian formulation of the evolution equation of a $d-$dimensional quantum system. The motion is formulated in terms of a system of coupled ODE obtained by the Euler-Lagrange equation related to the following Lagrangian

$$L = \int_{\mathbb{R}^d} \left[\mathrm{Im}\left(\psi^\dagger \partial_t \psi\right) - \frac{1}{2}|\nabla\psi|^2 - U|\psi|^2 \right] \prod dx_i \tag{1}$$

where ψ is the quantum wave function of the system and U is the potential. In order to obtain a treatable system, we expand the solution over a complete set of Hermite polynomials. Details of the model are given in [1]. Our method is adapted to treat nearly localized quantum particles. In order to illustrate our results, in Fig. 1 we depict the evolution of the variance of a single particle system in the presence of an external double well potential. In particular, we compare the results obtained with our approach with the direct solution of the Schrödinger equation and with the popular Gaussian beam approximation that shares close similarities with our method.

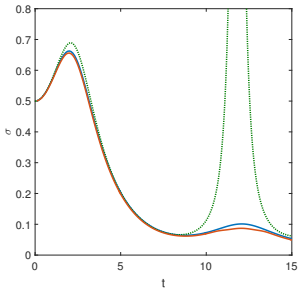

Fig. 1. Time evolution of the variance of the wave function. The red solid curve is obtained by using the Euler-Lagrange method, the blue solid curve is obtained by solving the Schrödinger equation and the green dotted curve is obtained by taking the standard Gaussian approximation

2

References

1. O. Morandi Quantum motion with trajectories: beyond the Gaussian beam approximation. *J. Phys. A: Math. Theor*, 51, 255301, 2018.

Part III

Abstracts of Contributed Talks

Predictor/Corrector Newton-Raphson (PCNR): A Simple, Flexible, Scalable, Modular, and Consistent Replacement for Limiting in Circuit Simulation

Karthik V. Aadithya, Eric R. Keiter, and Ting Mei

Sandia National Laboratories, Albuquerque, New Mexico, USA. Email: {kvaadit,erkeite,tmei}@sandia.gov

Summary. Limiting (the practice of improving the convergence of Newton-Raphson (NR) solves by preventing some quantities (*e.g.*, the voltages across diodes) from changing too much between successive iterations) has become indispensable in circuit simulation. But its implementation tends to be inflexible, non-modular, inconsistent, and confusing. We propose PCNR, a replacement for limiting that overcomes these disadvantages. The key ideas behind PCNR are, (1) to add each limited quantity as an extra unknown to the circuit's Modified Nodal Analysis (MNA) system of equations, (2) to split each NR iteration into a "prediction" phase followed by a "correction" phase, and (3) to mitigate the computational cost of the extra unknowns by eliminating them from all $Ax = b$ solves using a Schur complement based technique.

1 An illustrative example

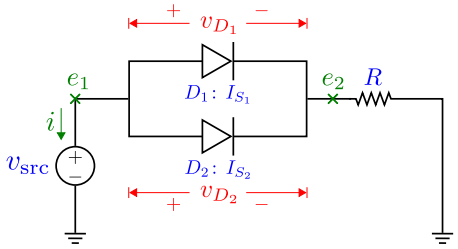

Fig. 1. The circuit we use to illustrate key ideas in this abstract.

Consider the circuit in Fig. 1; it contains two parallel diodes D_1 and D_2 (with saturation currents I_{S_1} and I_{S_2} respectively), in series with a resistor R, driven by a DC voltage source v_{src}. In Sect. 2, we use this circuit to highlight the problems with existing limiting implementations. Then, in Sect. 3, we use the same circuit to introduce the key ideas behind PCNR, which we then generalize into a powerful replacement for limiting that works for all circuits.

2 Problems with traditional limiting

The MNA equations [1, 2] for the circuit in Fig. 1 are:

$$\mathbf{g}\left(\underbrace{\begin{bmatrix} e_1 \\ e_2 \\ i \end{bmatrix}}_{\mathbf{x}}\right) = \begin{bmatrix} \underbrace{i + I_{S_1}\left(\mathrm{e}^{\frac{e_1-e_2}{V_T}} - 1\right)}_{D_1} + \underbrace{I_{S_2}\left(\mathrm{e}^{\frac{e_1-e_2}{V_T}} - 1\right)}_{D_2} \\ \underbrace{-I_{S_1}\left(\mathrm{e}^{\frac{e_1-e_2}{V_T}} - 1\right)}_{D_1} \underbrace{-I_{S_2}\left(\mathrm{e}^{\frac{e_1-e_2}{V_T}} - 1\right)}_{D_2} + \frac{e_2}{R} \\ e_1 - v_{\text{src}} \end{bmatrix} = \mathbf{0}, \quad (1)$$

where V_T is the thermal voltage.

The equations take the form $\mathbf{g}(\mathbf{x}) = \mathbf{0}$,[1] where $\mathbf{x}$ is the vector of unknowns the simulator has to solve for. This is normally done by NR iteration [1, 3, 4]; the simulator starts with an initial guess $\mathbf{x_0}$, and repeatedly refines it (into successively better guesses $\mathbf{x_1}$, $\mathbf{x_2}$, *etc.*) until a close enough approximate solution is found. Each iteration requires computing $\mathbf{g}$, as well as its Jacobian with respect to $\mathbf{x}$, at a new guess $\mathbf{x_i}$. The simulator does this by calling each device in the circuit, requesting it to calculate its branch currents and charges at $\mathbf{x_i}$, and then assembling these into vectors/matrices according to the circuit's topology [1, 2, 5]. For example, (1) shows the values calculated by the diodes D_1 and D_2. However, the exponentials in these calculations often adversely affect NR convergence. So, it is necessary to prevent the diode voltages from changing too much between successive iterations. This idea is called limiting [1, 5, 6]. To implement limiting, each diode keeps track of both the current guess $\mathbf{x_i}$ and the previous guess $\mathbf{x_{i-1}}$; when called by the simulator, instead of doing calculations at $\mathbf{x_i}$ as requested, each diode computes an intermediate point $\hat{\mathbf{x}}_\mathbf{i}$ between $\mathbf{x_{i-1}}$ and $\mathbf{x_i}$ (using a method like `pnjlim` [1, 7]), and does all calculations at $\hat{\mathbf{x}}_\mathbf{i}$ [1, 5, 6].

There are several problems with this approach. First, $\mathbf{g}$ and its Jacobian are no longer functions of just $\mathbf{x}$; they also depend on the history of $\mathbf{x}$. This adds confusion and breaks the clean mathematical abstractions underlying circuit simulation theory [5]. For example, evaluating $\mathbf{g}$ twice on the same $\mathbf{x}$ can result in two completely different answers. Second, this approach is fundamentally inconsistent. For example, the diodes D_1 and D_2 above would assume very different values for the *same* branch voltage $e_1 - e_2$, making both $\mathbf{g}$ and its Jacobian inconsistent, and hence difficult to analyze mathematically [1, 5]. Third, by requiring each device to know about previous iterations and other analysis-specific context information, this approach increases code complexity and reduces modularity; we believe it is the simulator's (and not the devices') responsibility to keep track of the analysis context, NR iterations, *etc.*

3 PCNR: Our replacement for limiting

In Sect. 2, we saw that *different* devices in a circuit may try to limit the *same* branch voltage, leading to inconsistencies in the evaluation of $\mathbf{g}$ and its Jacobian. For example, the diodes D_1 and D_2 from Fig. 1 both try to limit the same branch voltage $e_1 - e_2$. The root cause of this problem is that traditional MNA only treats node voltages (like e_1 and e_2), and *not* branch voltages (like v_{D_1} and v_{D_2} from Fig. 1) as unknowns [1, 2, 5]. This creates "clashes" between limiting devices that share node connections. Instead, if we treat limited quantities as unknowns in their own right, we can eliminate these clashes (and the inconsistencies they induce) by making sure that each device "owns" all the solution variables that it limits. This is our first key insight: in PCNR, we treat each limited quantity as a circuit unknown; this increases system size, but as we show below, the extra computational burden can be quite effectively mitigated.

Figure 2 shows the PCNR flow. At the top, we see that the PCNR vector $\mathbf{x}$ of unknowns contains all the original MNA unknowns ($\mathbf{x}_{\text{MNA}}$), as well as all the limited quantities ($\mathbf{x}_{\text{lim}}$).

[1] PCNR works for differential-algebraic equations as well, but for simplicity, we only consider algebraic equations in this abstract.

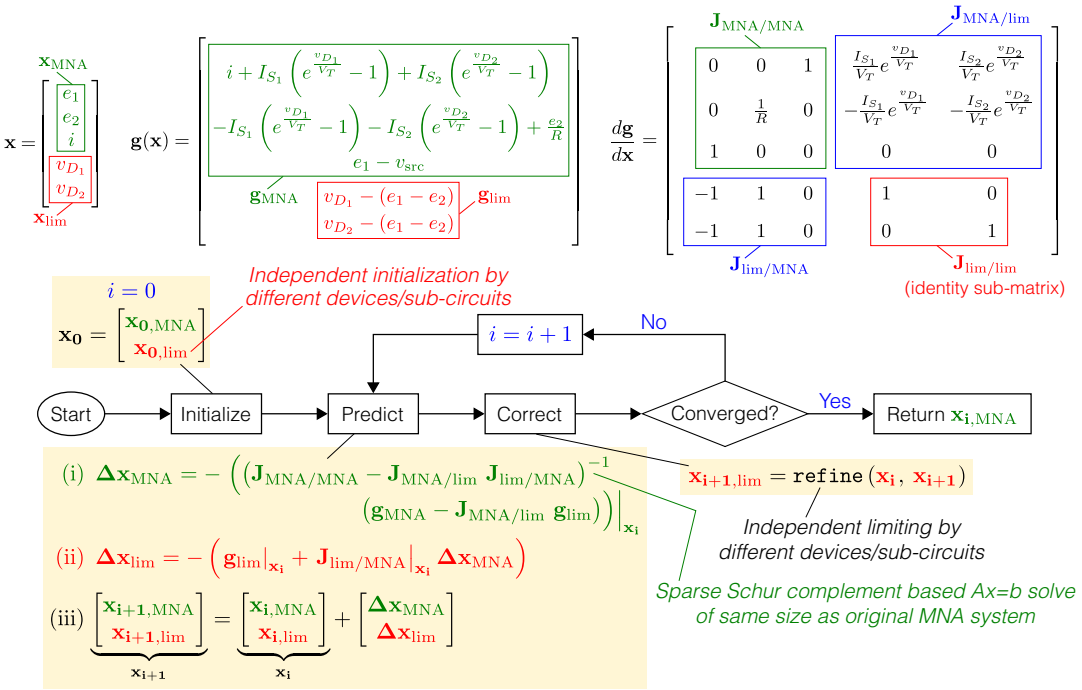

Fig. 2. The generalized PCNR flow that replaces limiting, and its application to the circuit shown in Fig. 1.

For example, when PCNR is applied to the circuit of Fig. 1, the limited branch voltages v_{D_1} and v_{D_2} become additional unknowns, owned by the diodes D_1 and D_2 respectively.

Thus, the diode D_1 (D_2), when called by the simulator, can simply do all its calculations at the current iteration's v_{D_1} (v_{D_2}), instead of having to keep track of the evolution of the branch voltage $e_1 - e_2$ between the previous iteration and this one. This is shown in $\mathbf{g}_{\text{MNA}}$, the top part of $\mathbf{g}$, as depicted in Fig. 2. The bottom part of $\mathbf{g}$ (denoted $\mathbf{g}_{\text{lim}}$) is obtained by simply writing equations expressing the limited quantities $\mathbf{x}_{\text{lim}}$ in terms of the original MNA unknowns $\mathbf{x}_{\text{MNA}}$; in our circuit, this means equating both the limited voltages v_{D_1} and v_{D_2} to $e_1 - e_2$ (Fig. 2). In similar fashion, as the top right of Fig. 2 shows, we split the Jacobian $d\mathbf{g}/d\mathbf{x}$ into four block sub-matrices, of which the bottom right sub-matrix ($\mathbf{J}_{\text{lim/lim}}$) is guaranteed to be identity. Thus, in PCNR, both $\mathbf{g}$ and its Jacobian are functions of just $\mathbf{x}$ (and not the history of $\mathbf{x}$), which ensures simplicity and consistency.

The bottom half of Fig. 2 shows a flowchart for solving circuits using PCNR. This brings us to our second key insight: in PCNR, each NR iteration is split into two phases – a "prediction" phase followed by a "correction" phase. The prediction phase is identical to traditional NR (without limiting); at the i^{th} iteration, the following update is applied:

$$\mathbf{x_{i+1}} = \mathbf{x_i} - \left(\left. \frac{d\mathbf{g}}{d\mathbf{x}} \right|_{\mathbf{x_i}} \right)^{-1} \mathbf{g}(\mathbf{x_i}), \text{ for } i \geq 0.$$

The naïve way to apply the above involves solving a sparse $Ax = b$ problem of size $|\mathbf{x}_{\text{MNA}}| + |\mathbf{x}_{\text{lim}}|$. But we can reduce the size to just $|\mathbf{x}_{\text{MNA}}|$, by exploiting the identity sub-matrix structure above to efficiently eliminate the limited quantities using the Schur complement $(d\mathbf{g}/d\mathbf{x})/\mathbf{J}_{\text{lim/lim}}$ [8] (Fig. 2 shows the equations involved). This is our third key insight; it enables us to effectively mitigate the computational cost of the extra unknowns introduced by PCNR. Also, it can be shown that PCNR never takes more iterations than traditional limiting, which ensures scalability. Finally, in the correction phase, the updates computed during the prediction phase are limited, by requesting each device/sub-circuit to limit the solution variables it owns. So, in PCNR, limiting is *explicitly* invoked by the simulator, rather than being *implicitly* done by the devices without the simulator's knowledge. This increases both modularity and flexibility.

Thus, PCNR is a simple, scalable, and easy-to-understand replacement for limiting. It allows device models to use a stateless API to communicate with circuit simulators, and frees them from cumbersome bookkeeping, which is especially attractive for next-generation CPU + GPU architectures. Also, since PCNR reduces code complexity and increases modularity and flexibility, we believe that it can be used to rapidly develop and test robust limiting strategies at the device, sub-circuit, and circuit levels – for mainstream as well as newly emerging devices. Finally, we believe that PCNR's generic predictor/corrector flow opens the door to developing limiting-inspired heuristics to accelerate NR convergence in domains outside circuit simulation.

References

1. L. W. Nagel. *SPICE2: A computer program to simulate semiconductor circuits*. PhD thesis, The University of California at Berkeley, 1975.
2. C. W. Ho, A. Ruehli, and P. Brennan. The modified nodal approach to network analysis. *IEEE Transactions on Circuits and Systems*, 22(6):504–509, 1975.
3. J. Roychowdhury. Numerical simulation and modelling of electronic and biochemical systems. *Foundations and Trends in Electronic Design Automation*, 3(2–3):97–303, 2009.
4. A. L. Sangiovanni-Vincentelli. *Computer Design Aids for VLSI Circuits*, chapter Circuit Simulation, pages 19–112. Springer, Netherlands, 1984.
5. E. R. Keiter, S. A. Hutchinson, R. J. Hoekstra, T. V. Russo, and L. J. Waters. Xyce® parallel electronic simulator design: Mathematical formulation. Technical Report SAND2004-2283, Sandia National Laboratories, Albuquerque, NM, USA, 2004.
6. W. H. Kao. Comparison of quasi-Newton methods for the DC analysis of electronic circuits. Master's thesis, The University of Illinois at Urbana-Champaign, 1972.
7. T. Wang and J. Roychowdhury. Well-posed models of memristive devices. *ArXiv e-prints*, May 2016.
8. https://en.wikipedia.org/wiki/Schur_complement.

Scalable Adaptive Numerical Simulation for Organic Thin Film Transistors

Pasquale Claudio Africa[1], Carlo de Falco[1], and Dario Natali[2,3]

[1] MOX Modeling and Scientific Computing, Dipartimento di Matematica, Politecnico di Milano, Piazza L. da Vinci 32, 20133, Milano, Italy carlo.defalco@polimi.it, pasqualeclaudio.africa@polimi.it
[2] Dipartimento di Elettronica, Informazione e Bioingegneria, Politecnico di Milano, Piazza L. da Vinci 32, 20133, Milano, Italy dario.natali@polimi.it
[3] Center for Nano Science and Technology, Istituto Italiano di Tecnologia, via Pascoli 70/3, 20133 Milano, Italy

Summary. We present a step-by-step procedure enabling to determine critical model parameters – such as the density of states width, the carrier mobility and the injection barrier – by fitting experimental data from a sequence of relatively simple measurements to 2D and 3D numerical simulations under different regimes.

1 Introduction

The accurate knowledge of relevant physical parameters is crucial to determine the predictive accuracy of numerical models for organic semiconductor devices. We present a step-by-step procedure enabling to determine critical model parameters – such as the density of states width, the carrier mobility and the injection barrier – by fitting experimental data from a sequence of relatively simple measurements to 2D and 3D numerical simulations under different regimes.

The current presentation extends the results of [**?**, **?**] where 1D models were used both for transient simulation of Metal-Insulator-Semiconductor (MIS) capacitors and for the estimating the DC transfer characteristics of Organic Thin-Film Transistors in the linear regime. The newly developed multi-dimensional simulator allows to account in a more natural way for a set of inherently 2D and 3D phenomena, such as: the non-planarity of the semiconductor/insulator interface (due to the solution processing of materials); parasitic capacitances due to coupling between metal layers; the boundary condition at the semiconductor/substrate interface; contact resistance due to current-crowding effects. The devices being considered in this study are shown in figure 1.

2 Numerical methods for 2D and 3D simulation

In order to deal with the increased complexity of numerical simulations in the new geometrical setting efficient numerical methods based on a hierarchically refined oct- and quad-tree meshes [**?**] have been implemented. The use of such meshes allows, on the one hand, for the straightforward definition of robust monotone discretization schemes and, on the other hand it allows for an efficient and highly scalable implementation. Furthermore, by using a suitable recently developed recovery-based a-posteriori error estimator to drive adaptive mesh refinement [**?**] (see figures 2 and 3) the simulation efficiency is highly improved.

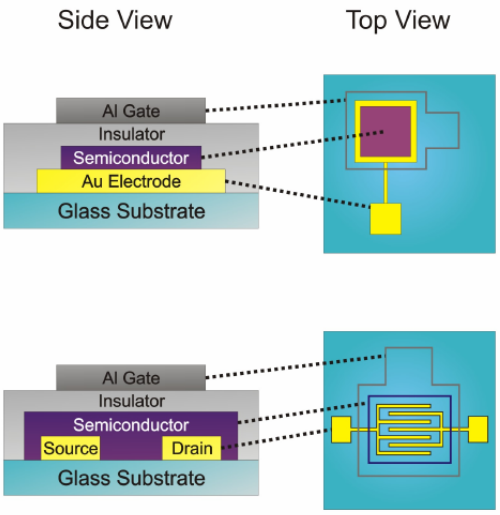

Fig. 1. Top and side view of the devices used: the MIS capacitor at the top and the OTFT at the bottom. Reprinted with permission from [**?**]. Copyright Elsevier 2015.

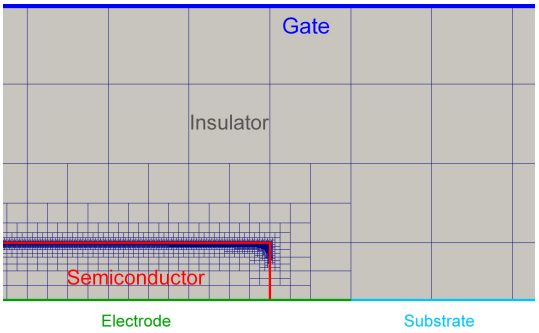

Fig. 2. Example of an *a posteriori* estimator driven mesh adaptation at the semiconductor/insulator interface in a benchmark MIS structure.

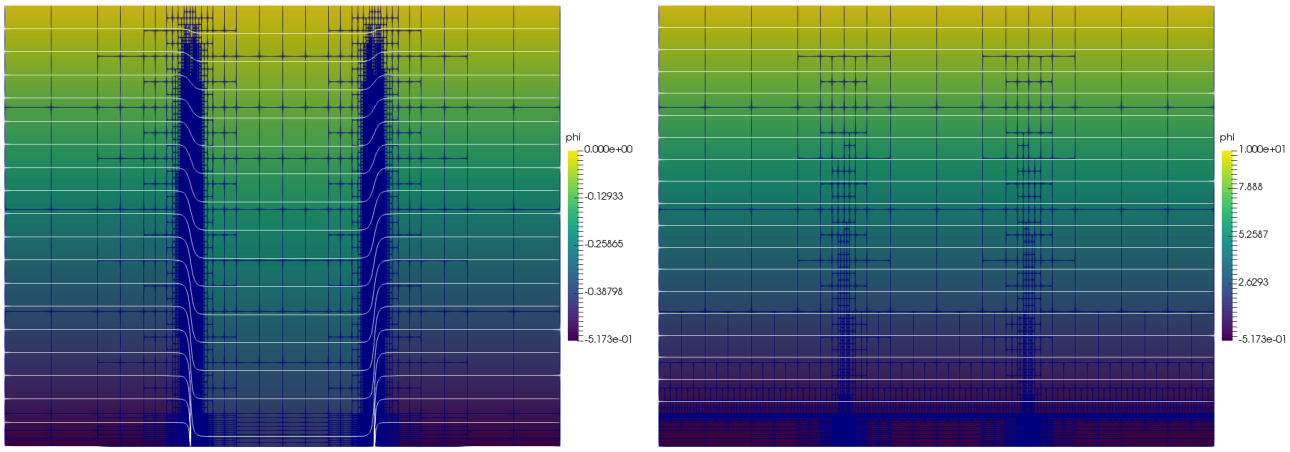

(a) $V_g = 0\,V$ (b) $V_g = 20\,V$

Fig. 3. Example of an *a posteriori* estimator driven mesh adaptation at the semiconductor/insulator interface in a benchmark FET structure at different gate biases. Electric field distribution in the device and electric field isolines are shown.

Shape optimization of an induction heating device

G. Aiello, S. Alfonzetti, S.A. Rizzo, and N. Salerno

Dipartimento di Ingegneria Elettrica Elettronica e Informatica - Università degli Studi di Catania, Viale Andrea Doria, 6 - I-95125 Catania - Italy. alfo@dieei.unict.it

Abstract The optimization of the cross section of an axisymmetric induction heating device is performed by means of stochastic methods. The formulation of the problems takes into account skin and proximity effects in the source currents. The hybrid FEM - DBCI method is used to deal with the unbounded nature of the field.

1 Introduction

Shape optimization of electromagnetic devices through the use of stochastic methods, such as Simulated Annealing (SA) and Genetic Algorithms (GA), implies numerous FEM (Finite Element Method) solutions with different geometries. This leads to high computational cost, especially if the basic problem is complicated by non-linearities and/or open boundary domains. In this paper the optimization of the shape of an axisymmetric induction heating device in open boundaries and in the presence of skin and proximity is addressed. It will be shown how the use of the hybrid FEM-DBCI (Dirichlet Boundary Condition Iteration method [1–3] for the solution of the unbounded field problem allows us to reduce substantially the computing time of the whole optimization process.

2 FEM-DBCI formulation

Consider the axisymmetric device shown in Fig. 1, in which a massive copper coil with a given time-harmonic source current I heats a passive circular metallic cylinder of radius R (half the system is depicted in Fig.1, the r-axis being a symmetry axis). In the coil the following equation holds [4]:

$$r^2\left(\frac{\partial^2 V}{\partial r^2}+\frac{\partial^2 V}{\partial z^2}\right)+3r\frac{\partial V}{\partial r}-\frac{\mathrm{j}\kappa}{\nu_0}(r^2V-\Phi)=\frac{-I}{\beta\nu_0} \quad (1)$$

where r, z are the cylindrical coordinates, $V=\frac{A}{r}$ is the modified magnetic vector potential, ν_0 is the vacuum reluctivity, $\kappa=\omega\sigma$ with σ the conductivity and ω the angular frequency of the source current, and:

$$\beta=\int_S\frac{1}{r}\,dS \qquad \Phi=\frac{1}{\beta}\int_S rV\,dS \quad (2)$$

S being the coil cross section. Equation (1) simplifies in the cylinder, where I=0 and $\Phi=0$, and in the air where $\sigma=0$ also.

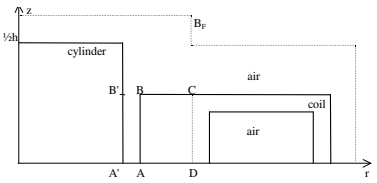

Figure 1. Geometry of the problem.

In order to solve the unbounded problem, FEM-DBCI is applied by introducing a fictitious truncation boundary Γ_F (see the dotted line in Fig.1) on which the unknown Dirichlet condition is expressed through the integral relation:

$$V(P_F)=-\frac{1}{r_F}\int_{\Gamma_M}\left(\frac{\partial rV}{\partial n}g-rVg'\right)dS \quad (3)$$

where Γ_M is a closed surface external to the conductors but enclosed by Γ_F, n is the unit vector normal to Γ_F, P_F is a node on Γ_F, r_F is its r-coordinate and g and g' are two influence functions given by ($\bar{r}=r/4\pi$):

$$g=\bar{r}\int_0^{2\pi}\frac{\cos\theta}{r_{P'P_F}}d\theta \qquad g'=\bar{r}\int_0^{2\pi}\frac{\partial}{\partial n'}\frac{\cos\theta}{r_{P'P_F}}d\theta \quad (4)$$

which can be evaluated by elliptic integrals [4]. Application of the FEM leads to the algebraic system [4]:

$$\mathbf{MV}=\mathbf{D}-\mathbf{M_F}\mathbf{V_F} \quad (5)$$

$$\mathbf{V_F}=\mathbf{HV} \quad (6)$$

where $\mathbf{V}$ and $\mathbf{V_F}$ are the arrays of the values of the potential V at the internal and boundary nodes, respectively, $\mathbf{M}$ is a square symmetric matrix of coefficients, $\mathbf{M_F}$ is a rectangular matrix, $\mathbf{D}$ is the known term array due to the source current I, and $\mathbf{H}$ comes from the discretization of (4). The hybrid system (5)-(6) is conveniently solved by iteration: starting from an initial guess for $\mathbf{V_F}$, (5) is solved for $\mathbf{V}$, which is used in (6) to improve $\mathbf{V_F}$. The procedure is iterated until convergence takes places. Once the system(5)-(6) is solved, the current density in the passive cylinder is computed as: $J=-\mathrm{j}\omega\sigma rV$.

3 Reducing the optimization time

Assume that uniform heating is desired on the cylinder surface (the segment A'B' in Fig.1), as required in

the quenching of steel manufactures. The following objective function to be minimized can be selected:

$$f = \frac{1}{|I|^2}\sum_n (|J_n| - J_0)^2 = (\frac{\omega\sigma R}{|I|})^2 \sum_n (|V_n| - V_0)^2 \quad (7)$$

where the summation is extended to the nodes in A'B' and J_0 and V_0 are the mean absolute values of the current density J and of the magnetic potential V in A'B'. The optimization of the device is achieved by modifying the profile AB of the coil in front of the cylinder. In order to reduce the computing time of the whole optimization, a convenient approach is to foresee a regular mesh of $2 \cdot M \cdot N$ triangles (M subdivisions along r, N along z) in the ABCD rectangle, which constitutes the admissible region for the profile (a total of $(M+1)^N$ possible configurations). In this way the mesh is the same for all the analyses in the optimization; only the conductivity of some finite elements changes from σ to zero or vice versa from one analysis to the next. This allows us to avoid a full preprocessing session for each analysis. Post-processing can also be avoided since the objective function (7) can be evaluated from the nodal field values directly without any further manipulation. In addition the algebraic systems (5)-(6) in the optimization can be built in an economic way if the first analysis is led for the maximum coil section (that is, for the case in which the profile of the coil coincides with AB), as explained in the following. Matrix $\mathbf{M_F}$ remains unchanged. Matrix $\mathbf{H}$ does not change either if Γ_M is selected to include the cylinder-coil air gap: a good choice is to select the conductor surfaces linked by the segment BB'. As far as matrix $\mathbf{M}$ is concerned, it can be built by decomposing the one in the first analysis $\mathbf{M^{(1)}}$, into two parts, $\mathbf{M_d^{(1)}}$ and $\mathbf{M_i^{(1)}}$, which refer to the differential and integral terms on the left hand side in (1), respectively. So the actual matrix $\mathbf{M}$ is first initialized to $\mathbf{M_d^{(1)}}$, and then all the air elements in ABCD are processed for the contributions of the $-\mathrm{j}\omega\sigma r^2 V$ term which are assembled with a change of sign. The contribution of the integral term is obtained in a similar way from the value of $\beta^{(1)}$ and of the auxiliary expansion:

$$\Psi^{(1)} = \int_S r V \, dS = \sum_i \Psi_i V_i \quad (8)$$

where the integral is extended to the maximum cross section of the coil and the summation to its nodes. Processing all the air elements in ABCD by subtracting their contributions from β and Ψ, their correct values are obtained and from these the contribution of the integral term. Analogously, after having set the current I numerically equal to β (this choice is always possible due to the linearity of equation (1) and implies that the known term of (1) is in all cases equal to $-1/\nu_0$), the actual array $\mathbf{D}$ can be built from that of the first analysis $\mathbf{D^{(1)}}$, by processing only the elements in ABCD whose constitutive parameters have been changed and by subtracting their contributions from the above array.

4 Optimization by GAs

Optimizations of the device in Fig.1 is addressed with the following data: cylinder radius R=12 mm, cylinder height h=28 mm, frequency f=100 kHz, AB=8 mm, AD=4.55 mm, AA'=2 mm, $\mu_0 = 4\pi \cdot 10^{-7}\,\mathrm{H/m}$, $\sigma = 3.14 \cdot 10^6\,\mathrm{S/m}$ both for the coil and the cylinder. The domain is discretized by means of 808 second-order triangular finite elements and 1693 nodes, 17 of which lie on A'B'. In particular M=7, N=8, are set for a total of $8^8 = 16,777,216$ different coil shapes. The end-iteration tolerance is set to $\delta_0 = 1.0\%$. The biconjugate gradient is used to solve the non-symmetric system (6). In this paper GAs are used with the characteristics described in [5]. In Fig.2 the contours of the magnitude of the current density J for the best configuration are plotted. The optimization of the device by means of SA will be provided in the full paper.

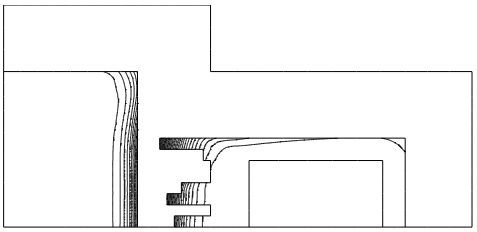

Figure 2. Magnitude of current density for the optimum.

References

1. G. Aiello, S. Alfonzetti, N. Salerno. Solution of skin effect problems by means of the DBCI-GMRES method. *COMPEL, vol. 21, no. 3*, pp 474-475, 2002.
2. G. Aiello, S. Alfonzetti, E. Dilettoso. Finite element solution of eddy current problems in unbounded domains by means of the hybrid FEM-DBCI method. *IEEE Trans. on Mag., vol. 39, no. 3*, pp. 1409-1412, May 2003.
3. G. Aiello, S. Alfonzetti, E. Dilettoso. Improved Selection of the Integration Surface in the Hybrid FEM-DBCI Method. *IEEE Trans. on Mag., vol. 46, n. 8*, pp. 3357-3360, August 2010.
4. G. Aiello, S. Alfonzetti. Finite element computation of axisymmetric eddy currents in an infinite domain. *COMPEL, vol. 19, n. 2*, 2000, pp. 167 - 172.
5. S. Alfonzetti, E. Dilettoso, N. Salerno. A proposal for a universal parameter configuration for genetic algorithm optimization of electromagnetic devices. *IEEE Trans. on Mag., vol. 37, n. 5*, pp. 3208-3211, September 2001.

Reduced Order Models for the Simulation of the Saltatory Conduction

Ruxandra Barbulescu, Daniel Ioan, Gabriela Ciuprina, Aurel Sorin Lup, and Mihai Popescu

Politehnica University of Bucharest, Spl. Independentei 313, 060042, Bucharest, Romania gabriela@lmn.pub.ro

Summary. The paper deals with phenomena occurring in the transmission of neuronal signals along myelinated axons. Myelinated sections alternate with Ranvier nodes able to regenerate the transmitted signals, phenomenon known as *saltatory conduction*. From the modeling point of view, the myelinated sections are linear systems, whereas the Ranvier nodes have a nonlinear behavior. Our aim is to investigate various ways to obtain reduced models able to catch this dynamic phenomenon. Models of the linear parts, obtained after electromagnetic field modeling and order reduction are coupled with nonlinear models of the the Ranvier nodes.

1 Neuron models

Efficient models of myelinated axons are needed in the simulation of large scale neuronal circuits. A myelinated axon (Fig. 1) consists of myelinated sections through which the signal is transmitted, which alternate with Ranvier nodes where the signal is regenerated, phenomenon known as *saltatory conduction* [1].

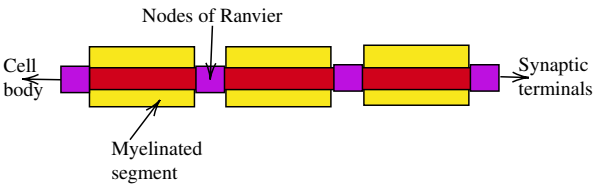

Fig. 1. The neuronal signal is transmitted along myelinated axons and regenerated in the Ranvier nodes.

In order to model the transmission of signals through this chain, the phenomena occurring in the myelinated sections have to be coupled with the phenomena occurring in the Ranvier nodes. This coupling can be carried out by means of electric terminals that can be defined both for the myelinated sections [2] and for the Ranvier nodes. Consequently, in order to obtain a reduced model for the axon, both components (called *nodes* and *internodes*) can be modeled separately.

The phenomena occurring in a node is very well described by the Hodgkin-Huxley (HH) model [3]. Its mathematical description consists of four nonlinear ordinary differential equations (1), in which one describes the capacitive effect, having as state quantity the membrane voltage V, and the other three describe the degree of ion channels opening, quantified in 3 *gating variables* denoted by n for the potassium ions and m and h for the sodium channels. $i(t)$ is the input signal that travels and reaches the node thus described by a zero-dimensional model, involving no space variables [4].

$$\begin{cases} C\frac{dV}{dt} = -G_K(V-E_K) - G_{Na}(V-E_{Na}) + i(t) \\ \frac{dn}{dt} = \alpha_n(V)(1-n) - \beta_n(V)n \\ \frac{dm}{dt} = \alpha_m(V)(1-m) - \beta_m(V)n \\ \frac{dh}{dt} = \alpha_h(V)(1-h) - \beta_h(V)h \end{cases} \quad (1)$$

The parameters of (1) have been fitted from experimental data.

- The quantity C is a constant value representing the capacitance of the node, the corresponding capacitor being initially charged at a *resting potential* of a typical value of -62.5 mV.
- G_K and G_{Na} are the conductances of the potassium and sodium channels respectively and they depend nonlinearly with respect to the node potential and the gating variables: $G_K = \overline{G_K} n^4$, $G_{Na} = \overline{G_{Na}} m^3 h$, where $\overline{G_K}$ and $\overline{G_{Na}}$ are constants.
- Coefficients α_* and β_* have known dependencies with respect to the node voltage.
- Each ion species has an equilibrium potential known as *batery potential* and denoted by E_K and E_{Na} in (1).
- The initial values of the gating variables are also known, they correspond to a resting state of the node, in which no signal is traveling.

The phenomena that describe the myelinated sections are based on a combination of electroquasistatic and electric conduction field regimes (Fig. 2) that are responsible for the transmission of the neural signal along the axon [2].

2 Coupling of sub-models

The coupling between the node and the internode models can be done easily if they are described as circuit netlist and circuit simulators are used. This is the approach used in [5], where simple models were used for the internodes. Improvements are obtained if the internode models are refined. In a such approach, the

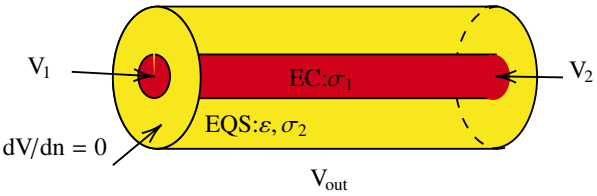

Fig. 2. The myelinated axons can be modeled with a combination of electroquasistatic (EQS) and electric conduction (EC) regimes.

success of the solving method is restricted by the facilities offered by the circuit simulator.

For instance, assuming an impulse input signal $i(t)$ of 6 nA and a chain connection of the reduced netlist models of 6 nodes separated by 5 myelinated axons, the voltages of the nodes are shown in Fig. 3. The figure illustrates the saltatory conduction, in this example the extracted conduction velocity being of 54.76 m/s.

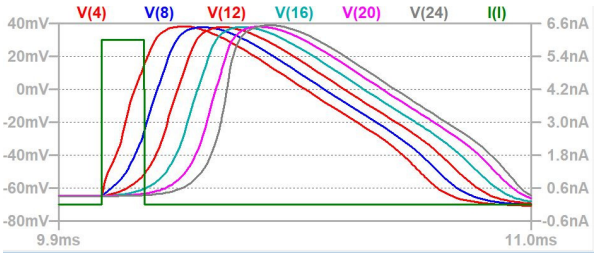

Fig. 3. Saltatory conduction - as a response to an impulse current excitation.

The approach we investigate in this paper is based on the systemic coupling of the node and internode models.

This has two advantages. On the one hand one could use directly the reduced order models obtained from model order reduction procedures, without a need to realize them as circuits and thus increase artificially the degrees of freedom of the circuit model since, usually, this realisation includes a lot of controlled sources. On the other hand, in such an approach the user can use robust nonlinear ODE solvers that are already available. In this approach procedures to couple the models are required and they have to be tailored for the specific significance of the input/output signals that are considered for each constitutive part.

Our final goal is not only to obtain a neuron model model able to reproduce the saltatory conduction with acceptable accuracy, but also to obtain the most appropriate global model so that it can be included in large scale neuronal circuits.

Acknowledgment

This work has been funded by University Politehnica of Bucharest, through the Excellence Research Grants Program, UPB GEX 2017. Ctr. No. 05/25.09.2017.

References

1. A. Huxley, R. Stampeli. Evidence for saltatory conduction in peripheral myelinated nerve fibres. The Journal of physiology 108(3): 315-339, 1949.
2. Daniel Ioan, Ruxandra Barbulescu, Luis Miguel Silveira, Gabriela Ciuprina Reduced Order Models of Myelinated Axonal Compartments, *under review*
3. A.L. Hodgkin A quantitative description of membrane current and its application to conduction and excitation in nerve. The Journal of physiology 117(4): 500-544, 1952
4. Robert B. Szlavik, Abuhanif K. Bhuiyan, Anthony Carver, and Frank Jenkins NeuralElectronic Inhibition Simulated With a Neuron Model Implemented in SPICE IEEE Transactions on Neural Systems and Rehabilitation Engineering, 14(1): 109-115, 2006.
5. N. Angel Equivalent circuit implementation of demyelinated human neuron in SPICE MSc. Thesis, Faculty of California Polytechnic State University, 2011.

Thermo-electrical analysis of indirect resistance heating furnaces combining numerical simulation and lumped models

A. Bermúdez[1], D. Gómez[1], and D. González-Peñas[1]

Departamento de Matemática Aplicada & Instituto Tecnológico de Matemática Industrial (ITMATI). Universidade de Santiago de Compostela, Spain alfredo.bermudez@usc.es, mdolores.gomez@usc.es, david.gonzalez.penas@usc.es

Summary. This work proposes a methodology to analyze the thermo-electrical behaviour of indirect heating resistance furnaces at the design stage. More precisely, carrying out a single 3D numerical simulation of the furnace combined with some subsequent computations on an equivalent lumped circuit model allow to obtain the power dissipation in the device (and, as a consequence, the thermal dissipation) as a function of the current supplied to the system. The method has been validated in an industrial resistance furnace devoted to metal purification.

1 Introduction

Indirect resistance heating has an extending application in different metallurgical processes. One of its main advantages is to produce uniform energy distribution over the workpiece, which is essential in many metal purification processes.

The prediction of the current distribution inside the resistor of the furnace and the computation of the power dissipated by Joule effect, is and important and non trivial matter, which in most cases can be only performed by numerical computations of the underlying electromagnetic models ([2], [3] or [4]). Contrary to other technologies, in this case the bibliography relative to the physical and mathematical modeling of industrial examples. On the other hand, at the design stage, it is in general mandatory to know the response to different inputs so a single simulation is not enough.

In this work we propose a mathematical model for a quite general case of resistance furnace devoted to metal refining. In particular, we show how to obtain an equivalent lumped model by using a single 3D numerical simulation and how to apply it to improve the design of the device.

2 Numerical simulation

We consider a resistance furnace consisting of a stainless steel chamber enclosing an hemispherical crucible containing the metal to be treated and a heater located under the crucible. Both the crucible and the resistor are surrounded by isolated materials (see Fig. 1).

The furnace is fed with a well balanced 3-phase system of alternating currents which are supplied to the resistor through three electrodes. The current magnitudes are supposed to be the known input data.

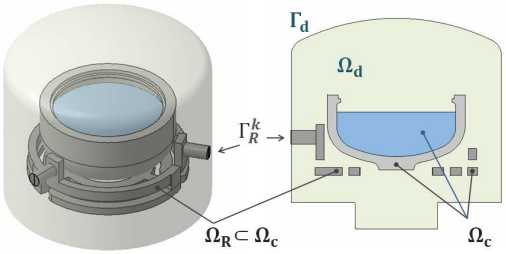

Fig. 1. Computational domain and notations. Isometric view (left) and section (right)

The electromagnetic model is based on the well-know time-harmonic eddy current model (see, for instance, [1]:

$$\mathbf{curl}\mathbf{H} = \mathbf{J}, \tag{1}$$

$$i\omega\mathbf{B} + \mathbf{curl}\mathbf{E} = \mathbf{0}, \tag{2}$$

$$\mathrm{div}\mathbf{B} = 0, \tag{3}$$

where $\mathbf{H}$, $\mathbf{J}$ and $\mathbf{E}$ are the complex amplitudes associated with the magnetic field, the current density and the electric field, respectively. The system is closed by adding the constitutive law $\mathbf{B} = \mu\mathbf{H}$ and the Ohm's law, $\mathbf{J} = \sigma\mathbf{E}$; μ and σ being the magnetic permeability and the electric conductivity, respectively. The model is completed with suitable boundary conditions

$$\mathbf{E} \times \mathbf{n} = \mathbf{0} \quad \text{on } \Gamma_{\mathrm{R}}, \tag{4}$$

$$\mu\mathbf{H} \cdot \mathbf{n} = 0 \quad \text{on } \Gamma_{\mathrm{d}}, \tag{5}$$

and the input data

$$\int_{\Gamma_{\mathrm{R}}^k} \mathbf{J} \cdot \mathbf{n}\, \mathrm{dS} = -I_K \quad K = 1,2, \tag{6}$$

$$V_3 = 0 \quad \text{on } \Gamma_{\mathrm{R}}^3. \tag{7}$$

This model is numerically solved by using a finite element method. The heat released by the heater due to Joule effect, P^{h}, is computed as

$$P^{\mathrm{h}} = \int_{\Omega_{\mathrm{R}}} \frac{|\mathbf{Jx}|^2}{2\sigma}\, \mathrm{dV}. \tag{8}$$

3 Equivalent lumped model

By assuming that the resistor is a single body, perfectly isolated inside the chamber, and without any more external contacts than the electrode terminals, the circuit sketched in Fig. 2 applies.

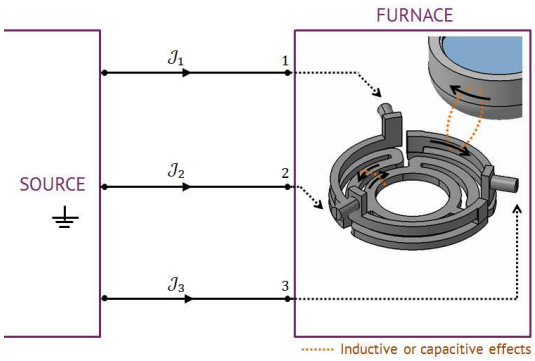

Fig. 2. Electrical circuit of the furnace.

If we combine all the passive elements of the circuit within the same block and forget about its particular topology, it is possible to replace it by a multiterminal connected network with six accessible variables ($\mathrm{I_k}$, $\mathrm{V_k}$; $\mathrm{k} = 1,2,3$). By applying Tellegen's Theorem on the multi terminal network (see [5]), we can deduce a relation between the Joule dissipation P^{h} and the lumped circuit parameters

$$P^{\mathrm{h}} = \mathrm{Re}\left(\frac{1}{2}\sum_{\mathrm{k}=1}^{3} \mathrm{V_k}\bar{\mathrm{I}}_{\mathrm{k}}\right) \tag{9}$$

By applying Kirchhoff's current law and performing some formal computations, last expression can be rewritten as

$$P^{\mathrm{h}} = \mathrm{Re}\left(\mathrm{Z}^{\mathrm{R}}\left|\mathrm{I}^{\mathrm{R}}\right|^2\right) \tag{10}$$

where $\mathrm{Z}^{\mathrm{R}} = \mathrm{V}^{\mathrm{R}}/\mathrm{I}^{\mathrm{R}}$ represents an equivalent reduced impedance for the furnace; I^{R} and V^{R} denote, respectively, the reduced current and reduced voltage drop, which are given by

$$\mathrm{I}^{\mathrm{R}} = \mathrm{I}_1, \tag{11}$$

$$\mathrm{V}^{\mathrm{R}} = (\mathrm{V}_1 - \mathrm{V}_3) + (\mathrm{V}_2 - \mathrm{V}_3)\mathrm{e}^{-\mathrm{i}(2\pi/3)}. \tag{12}$$

4 Numerical results

A combination of the both distributed and lumped models described in previous section was employed during the designing process of an indirect resistance furnace devoted to Solar Grade Silicon (SoG) purification.

As post-processing result, we obtain the output voltage on each terminal and from (8) we compute the Joule effect on the heater. Finally, the reduced equivalent impedance of the furnace $\mathrm{Z}^{\mathrm{R}} = \mathrm{V}^{\mathrm{R}}/\mathrm{I}^{\mathrm{R}}$ is obtained after replacing these voltages in (12).

Once Z^{R} has been obtained, it is easy to compute the current input signal which is required to get a target Joule effect by just applying (10). In this particular case, the curve represented in Fig. 3 has been obtained. The values attained has been compared with in plant measurements and the results show a good agreement of the results.

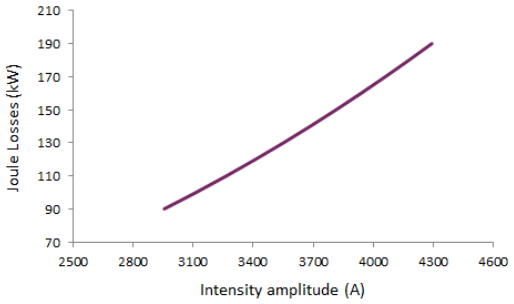

Fig. 3. Characteristic curve estimated for the projected furnace

References

1. A.Bermúdez, D. Gómez and P. Salgado. *Mathematical Models and Numerical Simulation in Electromagnetism*. Springer International, 2014.
2. A.Bermúdez, D. Gómez, M. Muñiz and P. Salgado. Transient numerical simulation of a thermoelectrical problem in cylindrical induction heating furnaces. *Advances in Computational Mathematics*, 26:39–62, 2007.
3. M.Ramírez, J.Garduño-Esquivel and G.Trapaga. Mathematical modeling of a direct current electric arc. *Metallurgical and Materials Transactions B*, 35:373–380, 2004.
4. Y.Tan, S.Wen, S.Shi, D.Jiang, W.Dong, and X.Guo. Numerical simulation for parameter optimization of silicon purification by electron beam melting. *Vacuum*, 95:18–24, 2013.
5. R.C.Redondo, N.R.Melchor, M.Redondo, and F.R.Quintela. Electrical Power and Energy Systems Instantaneous active and reactive powers in electrical network theory. *INT J ELEC POWER*, 53:548–552, 2013.

LinzFrame - A Modular Mixed-Level Simulator with Emphasis on Radio Frequency Circuits

Kai Bittner[1], Hans Georg Brachtendorf[1] and Wim Schoenmaker[2]

[1] University of Applied Sciences of Upper Austria Kai.Bittner, brachtd@fh-hagenberg.at,
[2] MAGWEL N.V., Leuven, Belgium wim.schoenmaker@magwel.com

Abstract. The modular simulator LinzFrame is a mixed-level simulator, combining device, circuit and analog/mixed signal simulation in one tool as depicted in Fig. 2. It is a general tool to solve ordinary differential algebraic equations (DAEs) and partial differential equations (PDEs) resulting from electronic, mechanical, physical and other problems. However, the simulator is optimized for radio frequency (RF) simulation. In a current research project the simulator is employed for the development of novel signal sources in the THz range, investigating the physical origin of plasma waves in quasi 2D electron gases.

For mixed-level simulation interfaces exist to the field and device simulator devEM from MAGWEL N.V., Leuven, [6] to Octave/Matlab for analog mixed signal simulation and the device simulator from RWTH ITHE. The latter is an R&D simulator for modeling novel semiconductor devices in the THz range [4].

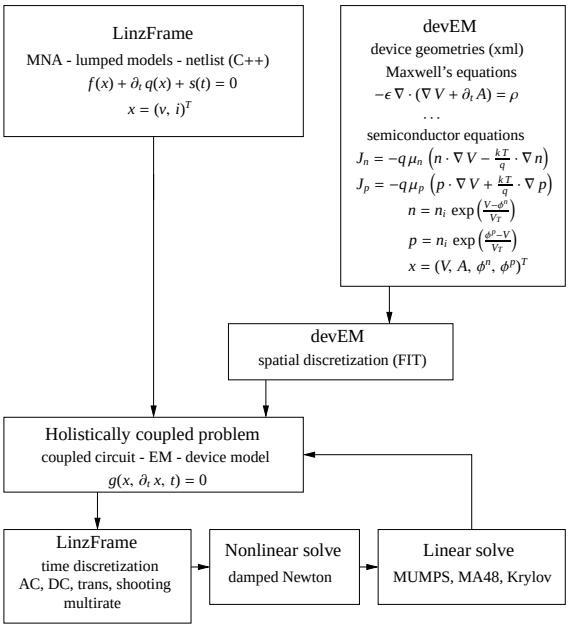

Fig. 1. Coupled circuit and device simulation.

In RF circuitry the lumped model assumption is often not valid anymore. Moreover critical devices are to be optimized w.r.t. geometry and - in the case of semiconductors - doping profile. Therefore, LinzFrame has been coupled with the EM field/device simulator devEM [2,6]. Critical RF devices are simulated in full 3D, whereas for the remaining circuit lumped device models are employed.

The simulator devEM is a technology CAD (TCAD) simulator with the scalar and vector potentials V, A as unknowns, as depicted in Fig. 1. The TCAD simulator employs the Finite Integration Technique (FIT) for spatially discretizing the partial differential equations resulting from Maxwell's equations and the device constitutive equations such as the drift diffusion equations for semiconductors. The simulator LinzFrame serves as the master simulator, providing the numerical techniques for time integration, i.e. the multistep BDF methods, shooting, Harmonic Balance or envelope techniques. The device simulator devEM provides the functional evaluations of the scalar and vector potentials on the spatial grid and their partial derivatives in a sparse matrix format, both for the algebraic and dynamic parts separately. Hence a full Newton method can be applied on both the lumped and TCAD models, which we refer to as strong or holistic coupling [2]. Since full Newton techniques can be employed in contrary to relaxation methods or a weak coupling of the two simulators, the convergence is guaranteed in nearly all practical applications.

After spatial discretization ene obtains a system of differential-algebraic equations (DAEs) of the form

$$\frac{d}{dt} q\big(x(t)\big) + \underbrace{i\big(x(t)\big) + s(t)}_{f(x(t),t)} = 0 \qquad (1)$$

LinzFrame follows a strict modular concept with clear interfaces for the topological setup of the PDEs/DAEs, model libraries and several analysis toolboxes Fig. 2. The model libraries for the device constitutive equations cover most of the industry standards of semiconductor device models and various signal sources. The analysis toolboxes comprise AC, DC, transient, envelope [3, 7, 8] and steady state techniques including Harmonic Balance and a spline-wavelet simulation engine [1]. The simulator is therefore highly flexible and renders simulation techniques for varous kinds of problems. Moreover, the Automatic Differential Suite (ADS) [5] facilates rapid prototyping of novel device models, since the ADS tool makes the calculation by hand of the partial derivatives unnecessary. Furthermore, an interface to MATLAB enables a rapid prototyping of novel algorithms. Clear interfaces to both linear and nonlinear iterative and moreover direct solvers from third parties complete the toolbox. A graphical user interface (GUI) and netlist parsers for SpectreRF and Spice are available.

In Radio Frequency (RF) circuits one observes on the one hand slowly varying baseband signals and on the other modulated or bandpass signals. The spectra of bandpass signals are centered around a carrier frequency, typically in the GHz range. The baseband is the envelope of bandpass signals and covers a spectrum of typically a few MHz.

Communication engineers are mainly interested in distortions of the baseband signals during transmission, since the information is coded in the envelope. The signal source library of LinzFrame covers the most relevant digital communication methods including PSK, QAM and OFDM.

System simulators for communication systems consider only the baseband signals, referred to as Equivalent Complex Baseband method. This technique is however not applicable for nonlinear circuits. Circuits are described by the Modified Nodal Analysis (MNA) and device constitutive equations, resulting often in huge systems of nonlinear ordinary differential algebraic equations (DAEs). Standard

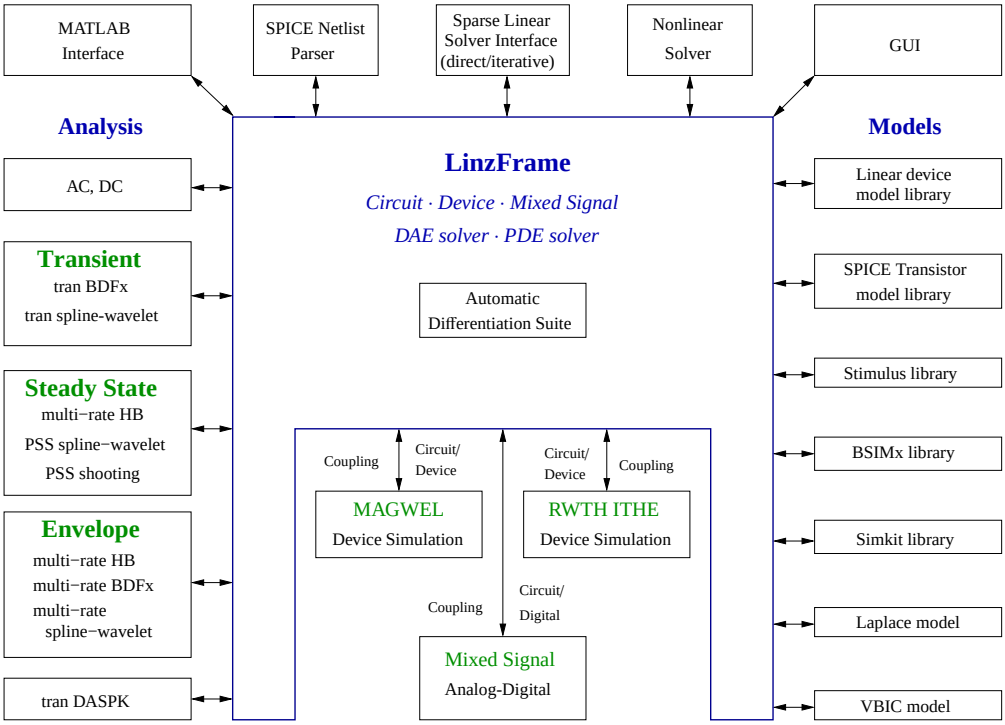

Fig. 2. Overview on the LinzFrame toolbox.

DAE solvers employing Backward Differentiation Formulas (BDF) are prohibitively slow since the time-steps for numerical integration must be much smaller than the reciprocal of the highest relevant frequency of the spectrum. The Multirate PDE (MPDE) reformulates the system of ordinary DAEs as a system of suitable partial differential equations (PDEs) with mixed boundary/initial value conditions. The baseband and bandpass signals have then appropriate time-steps, circumventing the restriction of the sampling theorem. The solution of the ordinary DAE is obtained along a characteristic curve of the PDE.

The boundary/initial value problem can be solved by standard techniques such as the well known Harmonic Balance (HB) method based on trigonometric basis functions, multistep integration formulas (e.g. BDF methods) etc. On the one hand, trigonometric basis functions are not compact and do not permit local refinements. BDF methods exhibit, on the other hand, a numerical damping, leading to erroneous results, e.g., for oscillator circuits. In recent research projects spline/wavelet methods [1] with adaptive grids have been developed as an alternative. Due to their compactness, B-splines lead to highly sparse systems, making the solution run-time efficient. Moreover the Gibb's phenomenon is avoided. Trigonometric B-splines moreover avoid the numerical damping.

Acknowledgment

This project has been co-financed by the European Union using financial means of the European Regional Development Fund (EFRE). Further information to IWB/EFRE is available at www.efre.gv.at.

References

1. K. Bittner and H.-G. Brachtendorf. Fast algorithms for grid adaptation using non-uniform biorthogonal spline wavelets. *SIAM J. Scient. Computing*, 37(2):283–304, 2015.
2. K. Bittner, H. G. Brachtendorf, W. Schoenmaker, and P. Reynier. Coupled circuit/em simulation for radio frequency. In *54th ACM/EDAC/IEEE Design Automation Conference, Austin, TX, June 18-22, 2017*, pages 1–6, June 2017.
3. H. G. Brachtendorf. *Theorie und Analyse von autonomen und quasiperiodisch angeregten elektrischen Netzwerken. Eine algorithmisch orientierte Betrachtung*. PhD thesis, 2001. Habilitationsschrift.
4. C. Jungemann, K. Bittner, and H. G. Brachtendorf. Simulation of plasma resonances in mosfets for thz-signal detection. In *2016 Joint International EUROSOI Workshop and International Conference on Ultimate Integration on Silicon (EUROSOI-ULIS)*, pages 48–51, Jan 2016.
5. Robert Melville, Shahriar Moinian, Peter Feldmann, and Layne Watson. Sframe: An efficient system for detailed dc simulation of bipolar analog integrated circuits using continuation methods. *Analog Integrated Circuits and Signal Processing*, 3(3):163–180, 1993.
6. P. Meuris, W. Schoenmaker, and W. Magnus. Strategy for electromagnetic interconnect modeling. *IEEE Transactions on Computer-Aided Design of Integrated Circuits and Systems*, 20(6):753–762, Jun 2001.
7. Roland Pulch. *PDAE Methoden zur numerischen Simulation quasiperiodischer Grenzzyklen von Oszillatorschaltungen*. PhD thesis, Universität Wuppertal, 2003.
8. J. Roychowdhury. Analyzing circuits with widely separated time scales using numerical pde methods. *Circuits and Systems I: Fundamental Theory and Applications, IEEE Transactions on*, 48(5):578 –594, may 2001.

Surface Charging Formulations for Engineering Applications. Validation by Experiments and Transient Models

Andreas Blaszczyk[1], Thomas Christen[1], Hans Kristian Meyer[2], and Michael Schüller[3]

[1] ABB Corporate Research 5405 Baden-Dättwil, Switzerland Andreas.Blaszczyk@ch.abb.com, Thomas.Christen@ch.abb.com
[2] Norwegian University of Science and Technology (NTNU), Trondheim, Norway hans.meyer@ntnu.no
[3] University of Applied Sciences Rapperswil, Switzerland michael.schueller@hsr.ch

Summary. Electrostatic BEM (Boundary Element Method) formulations are presented for the calculation of dielectric surface charging, including saturation and restrike phenomena. The simulation results turn out to be in agreement with surface potential measurements in a simple rod-barrier-plane configuration, where lightning impulses initiate streamers and charge accumulation on the barrier. The usefulness of the given BEM-formulation is additionally supported by transient charging simulations in the framework of an electric carrier drift model.

1 Introduction

Surface charges (SC) on solid insulator surfaces can significantly influence the dielectric performance of medium and high voltage power devices. They can mitigate discharge inception effects during a lightning impulse test, as well as enhance them for applied voltages with reversed polarity. Unfortunately, the simulation of the intrinsically transient charging, which may occur via a zoo of different gas discharge processes like streamers, leaders, ion motion and combinations thereof, is a complex task and thus requires simplified approaches for application to real devices.

Recently a simplified engineering approach based on the saturation-charge boundary-condition has been proposed [1]. It works because saturation is a rather robust extremal stage of SC accumulation that allows assessment of possible changes in field distribution without performing the full analysis of the charging process. By neglecting the influence of the space charge, a simple electrostatic computation based on integral approach is possible (without meshing the gas volume).

In this paper we present a new formulation of the saturated SC for the 3D boundary element method (BEM), which can be efficiently applied in an industrial design environment. In addition to the saturation stage, computational models for modification of the accumulated charge due to restrikes (back discharges after changes of electrode potentials) are considered. The new formulation has been validated based on experiments and transient models. We present results for an example of a rod-barrier-plane arrangement in atmospheric air.

2 BEM Formulation

We assume that the saturation stage at the dielectric boundary is achieved when the amount of accumulated SC is so large that the normal component of the electric field in the gas is zero. In order to fulfill the Gauss law, the saturation charge density must be then equal to the flux density on the solid insulation side. In the traditional BEM formulation [2], both relationships can be expressed for a collocation point i on a dielectric surface as follows:

$$E_{ni}^{-} + \frac{\sigma_i}{2\varepsilon_0} = 0 \tag{1}$$

$$E_{ni}^{-} - \frac{\sigma_i}{2\varepsilon_0} - \frac{\sigma_{sati}}{\varepsilon_0 \varepsilon_{r,Ins}} = 0 \tag{2}$$

where σ_i and σ_{sati} are unknown densities of the virtual and saturation charges, $\varepsilon_{r,Ins}$ is the relative permittivity of the solid insulation, and E_{ni}^{-} is based on Green's function integration over all surfaces of the model:

$$E_{ni}^{-} = \frac{1}{4\pi\varepsilon_o} \sum_j \int_{S_j} \frac{\mathbf{n_{iK}} \cdot \mathbf{r_{ij}}}{r_{ij}^3} \sigma_j dS \tag{3}$$

An example of a σ_{sati} computation is shown in Fig. 1. More details on saturation and "restrike"-formulations will be presented in the full paper.

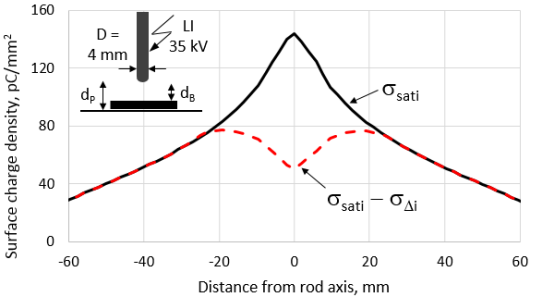

Fig. 1. Charge density-distributions calculated for a rod-barrier-plane configuration (d_P=10 mm, d_B=5 mm). The bell-shaped curve corresponds to σ_{sati} calculated with (1) - (3). The volcano-shaped distribution has been calculated after removing some of charge due to restriking.

3 Experimental Validation

The experimental test arrangement includes a HV rod with diameter D=7 mm (or 4 mm), a dielectric barrier 600x600x5 mm with $\varepsilon_{r,Ins}$=3, and a grounded plate electrode. The rod-barrier distance, d_B, and rod-plate distance, d_p, vary between 0 and 100 mm. A standard lightning voltage impulse (LI) with 1.2/50 μs and a peak value in the range between 20 and 100 kV is applied to the rod. The positive streamer discharge initiated at the spherical rod tip deposes SC at the barrier surface. After the impulse and a possible restrike the barrier together with the grounded plane are moved to another location where the surface potential due to accumulated charge is scanned by a robot-driven measurement probe. Before applying the next impulse the barrier is cleaned with alcohol in order to remove the SC. Results of surface potential distributions measured for two selected configurations and calculated with the above mentioned BEM method are compared to each other in Fig. 2 and show reasonable agreement. More experimental results are included in [3].

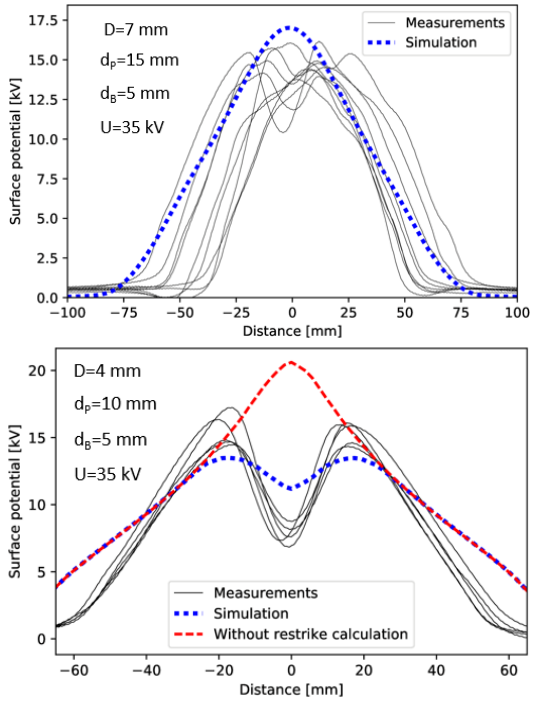

Fig. 2. Surface potential distribution measured and calculated for 2 rod-barrier-plane configurations: without and with a restrike.

4 Transient Model

The real charging dynamics may consist of different phases, starting with very fast (positive) streamer(s) leaving behind a column of ionized air with subsequent ion drift towards the insulator surface. Nevertheless, we used a simple charge-density drift-diffusion model with a field-dependent injection condition at the high field electrode (see, e.g., [4]), and calculated the transient SC accumulation for testing the normal-field nullification assumption. The results (cf. Fig. 3 for an example geometry similar to the above ones) indicate that the assumption is sufficiently confirmed for practical purposes. Deviations are second order effects that can be explained by simple physical arguments, as will be mentioned in the full paper, like global dynamic field distortion and suppression of inception if the surface-electrode distance is too short.

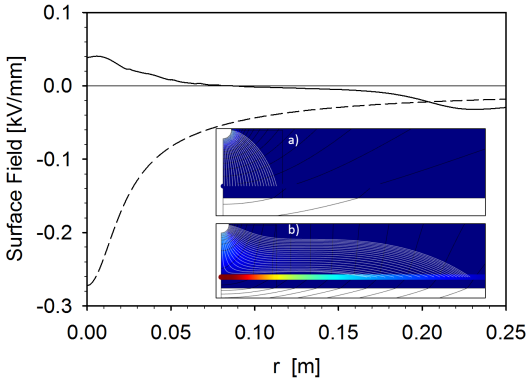

Fig. 3. Initial (dashed) and SC-saturated (solid) normal electric surface field. Insets: flow lines (white), equipotential lines (black), and SC (color) of initial (a) and saturated (b) states.

5 Conclusion

A comparison with experiments and transient modelling indicates that the numerically efficient steady-state surface charging model based on the discussed saturation concept can be used for a reasonable prediction of electric fields during high voltage tests.

References

1. A. Blaszczyk, J. Ekeberg, S. Pancheshnyi, and M. Saxegaard. Virtual High Voltage Lab. SCEE 2016, Springer ser. Mathematics in Industry, Heidelberg 2018.
2. N. De Kock, M. Mendik, Z. Andjelic and A. Blaszczyk. Application of 3D boundary element method in the design of EHV GIS components. *IEEE Mag. on Electrical Insulation*, Vol.14, No. 3, pp. 1722, May/June 1998.
3. H.K. Meyer, A. Blaszczyk, M. Schüller, F. Mauseth, A. Pedersen. Streamer inception and propagation for air insulated rod-plane gaps with barrierrs. submitted to *IEEE Conf. on High Voltage Engineering and Application,* . ICHVE September 2018, Athens, Greece.
4. T. Christen. FEM Simulation of Space Charge, Interface and Surface Charge Formation in Insulating Media. *XVth International Symposium on High Voltage Engineering*, Ljubliana, Slovenia, 2007, 7, T8-54, 2007.

Open Source Simulation Platform for Deep Brain Stimulation

Konstantin Butenko, Andrea Böhme, and Ursula van Rienen

Universität Rostock, Institut für Allgemeine Elektrotechnik, Albert-Einstein-Str. 2, Rostock, Germany
konstantin.butenko@uni-rostock.de, andrea.boehme@uni-rostock.de
ursula.van-rienen@uni-rostock.de

Summary. The application of numerical models for Deep Brain Stimulation (DBS) has improved the understanding of the mechanisms behind the neurosurgical treatment. Currently, the evaluation of the induced electric field in the corresponding volume conductor models predominantly relies on commercial software. In this study, we propose a new open source simulation platform, which comprises CAD and CAE tools for solving the electro-quasistatic formulation of Laplace′s equation.

1 Introduction

Disruption of excessive neuronal synchronization in $\beta-$ and $\gamma-$band frequencies, observed in patients with Parkinson′s disease and dystonia, can be achieved by Deep Brain Stimulation (DBS). The basic principle of the therapy is to deliver electric pulses into deep brain areas via an electrode. A rectangular shaped signal of 130 Hz with pulse duration of 60-90 µs is the conventional stimulation protocol, though its numerous modifications were suggested. The therapeutic effect arises from the regularization of the pathological neural pattern [5], but the source of the regularization is still debatable. The response of neural networks to DBS requires further investigation in order to increase efficiency of the treatment.

Accurate estimation of the electric field distribution is an essential step in DBS optimization, which will define an optimal electrode geometry, its location and a stimulation protocol. The open source simulation platform, proposed in this work, will simplify the process of numerous field computations, required by an optimization algorithm. Moreover, it will also allow fast reproducibility of the results by other research groups: the combination of open source CAD and CAE modules, connected and controlled via a Python interface, facilitates quick prototyping.

2 Methods

2.1 Setting up a Discretized Model

Designing and discretizing of the computational domain was conducted in the open source software SALOME (www.salome-platform.org, vers. 8.3.0) with the Netgen module. Apart from its GUI, SALOME allows to export and import Python scripts, which provides its integration to a Python-based simulation platform. Using only the surface of the brain (or its approximation) as a CAD model in the first step avoids modeling of the interior structures with its process complexity and the risk of instability of imported assemblies. Nevertheless, the developed platform supports explicit definition of subdomains (i.e. inner structures) and it was utilized to model the encapsulation layer (Fig. 1) as well, which is built up due to the inflammatory response. Further, an efficient discretization of the computational domain requires the definition of sub-meshes: boundary conditions and the region of interest (ROI) demand a highly refined mesh, while the field elsewhere can be computed with a rather rough discretization. It is also

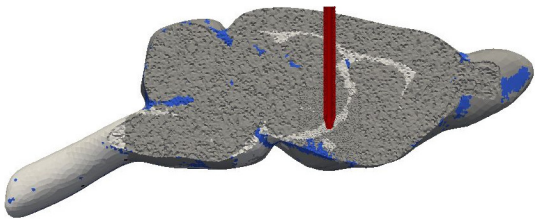

Fig. 1. Distribution of tissues in the rat brain, mapped onto tetrahedral mesh (sagittal plane). Grey and white matter are depicted with corresponding colors, cerebrospinal fluid is shown in blue and the encapsulation layer (surrounding the electrode) in red. The electrode is considered as a perfect conductor and subtracted from the computational domain.

important to take heterogeneity of the brain tissues into account as it influences the current spread [4]. Our platform supports the incorporation of voxelized MRI data by mapping it onto the generated mesh: the algorithm defines to which voxel the midpoint of a mesh cell belongs and assigns the corresponding tissue marker. Obviously, the accuracy of the mapping depends on the level of discretization, introducing additional criteria for refinement. Furthermore, the targets of DBS reside near fiber tracts, which have highly anisotropic properties and thus considerable effect on the electric field distribution [2]. In the simulation platform, anisotropy is implemented analogously to heterogeneity, using conductivity tensors, obtained from voxelized Diffusion Tensor Imaging (DTI) data.

2.2 FEniCS Model

The discretized model is then to be exported to the free software FEniCS (www.fenicsproject.org, vers. 2017.2.0) [1], which contains programming and mathematical tools for solving differential equations with the Finite Element Method (FEM). FEniCS uses C++ classes for the assembly of systems and offers a Python interface, providing computational and prototyping efficiency.

After the model is imported, we solve the electroquasistatic (EQS) problem [7]

$$\nabla\cdot\Big((\sigma(r)+\mathrm{j}\omega\varepsilon(r))\nabla\phi(r)\Big)=0, \qquad (1)$$

with FEniCS. The approximation is valid for the electric fields of relatively low frequencies in the absence of the magnetic induction [8]. Here, ϕ is the electric potential, ε and σ are the permittivity and conductivity of the material, ω denotes the angular frequency and j is the imaginary unit. The frequencies are defined by Fourier transform of the stimulation signal, and the dispersive nature of brain tissues is taken into account using a 4-term Cole-Cole model with parameters from [3]. Accurate signal reproduction might require a multitude of calculations; therefore a multiprocessing algorithm was implemented.

3 Numerical Results

We constructed a geometric model of the Sprague Dawley rat brain's exterior surface basing on the Waxholm Space atlas [6]. Using the approach described in Sect. 2, we created a FEM model and carried out numerical investigations within the developed platform. We employed a concentric bipolar electrode CEAX-200 (microprobes.com) and defined Dirichlet boundary conditions (b.c.): we assigned 1 V to the surface of the core contact and set the outer contact to ground. The rest of the outer surface was considered isolated, i.e. Neumann b.c. was applied. While heterogeneity, dispersion and the encapsulation layer were considered, anisotropic properties were neglected in the preliminary model as well as the electrical double layer.

Solution of (1) was performed by the MUltifrontal Massively Parallel sparse direct Solver (MUMPS) with incomplete LU factorization on redundant computational resources. The mesh optimization was conducted in two steps: first, integrals of the potential at the contact surfaces (i.e. Dirichlet b.c. with manually defined values) were set as goal functions; afterwards, the sub-meshes were refined, basing on the relative error in the electric potential with stricter requirements in the ROI. The results on the optimized mesh were compared to an analogous model, designed in COMSOL Multiphysics® (vers. 5.3a). Though the electric potential is the same near the electrode, values outside this area reveal a scaling factor (≈ 0.96). Studies are ongoing to find the origin of the scaling. Using the relation $\mathbf{E}=-\nabla\phi$, the electric field distribution was obtained (Fig. 2), clearly demonstrating the influence of heterogeneity. In the full paper, a thorough comparison of the models will be conducted, basing on the results of simulations for the conventional DBS signal.

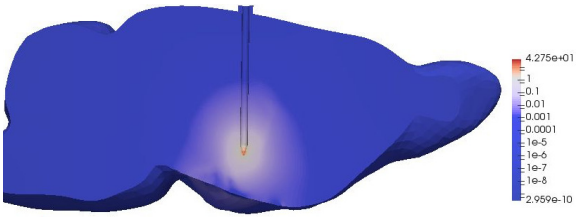

Fig. 2. Magnitude of the electric field at 130 Hz and 1 V bipolar stimulation, the scale is in V/mm.

Acknowledgement. This research was supported by the German Research Foundation (Deutsche Forschungsgemeinschaft, DFG) within the Collaborative Research Centre 1270 ELAINE. The authors wish to acknowledge Dr. C. Schmidt, whose Python package FanPy was partially adapted for the proposed platform.

References

1. M. Alnæs et al. The fenics project version 1.5. *Archive of Numerical Software*, 3(100), 2015.
2. A. Böhme and U. van Rienen. A comparative study of approaches to compute the field distribution of deep brain stimulation in the hemiparkinson rat model. In *Annual International Conference of the IEEE Engineering in Medicine and Biology Society*, volume 2016, pages 5821–5824. 2016.
3. S. Gabriel, R.W. Lau, and C. Gabriel. The dielectric properties of biological tissues: Iii parametric models for the dielectric spectrum of tissues. *Phys Med Biol*, 41(11):2271–2293, 1996.
4. B. Howell and C.C. McIntyre. Role of soft-tissue heterogeneity in computational models of deep brain stimulation. *Brain Stimulation*, 10(1):46 – 50, 2017.
5. M.D. Johnson, S. Miocinovic, C.C. McIntyre, and J.L. Vitek. Mechanisms and targets of deep brain stimulation in movement disorders. *Neurotherapeutics*, 5(2):294–308, 2008.
6. E.A. Papp, T.B. Leergaard, E. Calabrese, G.A. Johnson, and J.G. Bjaalie. Waxholm space atlas of the sprague dawley rat brain. *NeuroImage*, 97:374–386, 2014.
7. R. Plonsey and D.B. Heppner. *Considerations of quasi-stationarity in electrophysiological systems*, volume 29. The Bulletin of Mathematical Biophysics, 1967.
8. U. van Rienen. *Numerical Methods in Computational Electrodynamics*. Lecture Notes in Computational Science and Engineering. Springer-Verlag Berlin Heidelberg, 2001.

Charge and phonon transport in suspended monolayer graphene

Marco Coco[1] and Vittorio Romano[2]

[1] Università degli Studi di Catania, Dipartimento di Matematica e Informatica mcoco@dmi.unict.it,
[2] Università degli Studi di Catania, Dipartimento di Matematica e Informatica romano@dmi.unict.it

Summary. Thermal effects in monolayer graphene due to an electron flow are investigated with a Direct Simulation Monte Carlo (DSMC) analysis [1,2]. The crystal heating is described by simulating the phonon dynamics of the several relevant branches, acoustic, optical, K and Z phonons. In particular, it is shown that the Z phonons, although they do not enter the scattering with electrons, play a non-negligible role in the determination of the crystal temperature. Moreover, a significant influence of the lattice temperature on the characteristic curves is observed only for long times [3,4].

1 The mathematical model

In a semiclassical kinetic setting, the charge transport in graphene is described by four Boltzmann equations, one for electrons in the valence band (π) and one for electrons in the conduction band (π^*), that in turn can belong to the K or K' valley,

$$\frac{\partial f_{\ell,s}(t,\mathbf{x},\mathbf{k})}{\partial t} + \mathbf{v}_{\ell,s}\cdot\nabla_{\mathbf{x}} f_{\ell,s}(t,\mathbf{x},\mathbf{k}) + \\ -\frac{e}{\hbar}\mathbf{E}\cdot\nabla_{\mathbf{k}} f_{\ell,s}(t,\mathbf{x},\mathbf{k}) = \left.\frac{df_{\ell,s}}{dt}(t,\mathbf{x},\mathbf{k})\right|_{e-ph} \quad (1)$$

where $f_{\ell,s}(t,\mathbf{x},\mathbf{k})$ represents the distribution function of charge carriers, in the band π or π^* ($s=-1$ or $s=1$) and valley ℓ (K or K'), at position $\mathbf{x}$, time t, and with wave-vector $\mathbf{k}$. We denote by $\nabla_{\mathbf{x}}$ and $\nabla_{\mathbf{k}}$ the gradients with respect to the position and the wave-vector, respectively. The group velocity $\mathbf{v}_{\ell,s}$ is related to the band energy $\varepsilon_{\ell,s}$ by

$$\mathbf{v}_{\ell,s} = \frac{1}{\hbar}\nabla_{\mathbf{k}}\,\varepsilon_{\ell,s}\,.$$

With a very good approximation, a linear dispersion relation holds for the band energies $\varepsilon_{\ell,s}$ around the equivalent Dirac points, so that

$$\varepsilon_{\ell,s} = s\hbar\, v_F\,|\mathbf{k}-\mathbf{k}_\ell|\,, \quad (2)$$

where v_F is the (constant) Fermi velocity, $\hbar$ the Planck constant divided by 2π, and $\mathbf{k}_\ell$ is the position of the Dirac point ℓ. The elementary (positive) charge is denoted by e, and $\mathbf{E}$ is the electric field, here considered as an external field. The right hand side of (1) is the collision term representing the interactions of electrons with acoustic, optical and K phonons. Acoustic phonon scattering is intra-valley and intra-band and can be longitudinal (LA) or transversal (TA). Optical phonon scattering is intra-valley and can be longitudinal (LO) and transversal (TO); it can be intra-band, leaving the electrons in the same band, or inter-band, pushing the electrons from the initial band toward another one. Scattering with phonons of K-type pushes electrons from a valley to a nearby one (inter-valley scattering). The general form of the collision term can be written as

$$\left.\frac{df_{\ell,s}}{dt}(t,\mathbf{x},\mathbf{k})\right|_{e-ph} = \\ = \sum_{\ell',s'}\left[\int_{\mathscr{B}} S_{\ell',s',\ell,s}(\mathbf{k}',\mathbf{k})\, f_{\ell',s'}(t,\mathbf{x},\mathbf{k}')\left(1-f_{\ell,s}(t,\mathbf{x},\mathbf{k})\right)d\mathbf{k}'\right. \\ \left. - \int_{\mathscr{B}} S_{\ell,s,\ell',s'}(\mathbf{k},\mathbf{k}')\, f_{\ell,s}(t,\mathbf{x},\mathbf{k})\left(1-f_{\ell',s'}(t,\mathbf{x},\mathbf{k}')\right)d\mathbf{k}'\right],$$

where the total transition rate $S_{\ell',s',\ell,s}(\mathbf{k}',\mathbf{k})$ is given by the sum of the contributions of the several types of scatterings. The evolutions of the phonon branches are governed by the following Boltzmann equations

$$\frac{\partial g_\mu(t,\mathbf{q})}{\partial t} = C_\mu^{p-e}(\mathbf{q}) - \frac{g_\mu - g_\mu^{LE}}{\tau_\mu}, \quad (3)$$

where $\mu = LA, TA, ZA, LO, TO, ZO, K$, g_μ is the phonon distribution function, C_μ^{p-e} describes the phonon-electron collisions and is equal to zero for ZO and ZA, $\tau_\mu = \tau_\mu(T_\mu)$ are the temperature dependent phonon relaxation times, g_μ^{LE}'s are the local equilibrium phonon distributions given by

$$g_\mu^{LE} = \left[e^{\hbar\omega_\mu/k_B T_{LE}} - 1\right]^{-1}. \quad (4)$$

The main aims of the paper is to calculate the actual phonon distributions and the graphene heating, by means of the deterimnation of the local equilibrium temperature T_{LE} The phonons distribution is a Bose-Einstein one for $t=0$ and it is updated at each time step using the scatterings dynamics. For this purpose, we need to know the production terms $C_\mu^{p-e}(\mathbf{q})$, that represent the rate of variation of the phonon populations per unit time and are proportional to the difference between the number of emission and absorption processes, $n^+(\mathbf{q})$ and $n^-(\mathbf{q})$ respectively, due to the electron-phonon scatterings. These are evaluated using the intermediate results of the DSMC part, counting them in each time window $[t_{n-1},t_n]$ and in each

elementary cell of the grid in the $\mathbf{q}$-space, being $\mathbf{q}$ the phonon wave-vector. The only relevant contributions come from the LO, TO and K phonons.

At each scattering event, we consider whether it is an absorption or an emission process, calculate the wave-vector $\mathbf{q}$, taking into account the momentum conservation $\mathbf{q}^{\pm} = \pm(\mathbf{k}' - \mathbf{k})$, and determine the cell to be updated. The values of the phonons distributions in the cell the wave-vector belong to are updated by augmenting or decreasing the number of phonons per unit cell by using the values $n^+$and n^- obtained from the MC simulation.

The crucial point is to define the suitable statistical weight, β_{scatt}, for each phonon population, in order to estimate the correct values of the production terms as $C_\eta^{p-e}(\mathbf{q}) = \dfrac{1}{\Delta t}\beta_{scatt}\,(n^+(\mathbf{q}) - n^-(\mathbf{q}))$, $\eta = LO, TO, K$ and it will be shown that

$$\beta_{scatt} = \frac{(2\pi)^2}{|C_\alpha|}\frac{\rho}{N_P}, \tag{5}$$

where ρ is electron density, N_P the number of the simulated particles and $|C_\alpha|$ the measure of the elementary cell of the grid. By introducing the average phonon energy densities as

$$W_\mu = \frac{1}{(2\pi)^2}\int_{\mathscr{B}} \hbar\omega_\mu\, g_\mu\, d\mathbf{q}, \tag{6}$$

from the general properties of the phonon collision operators, the relation

$$\sum_\mu \frac{W_\mu - W_\mu^{LE}}{\tau_\mu} = 0 \tag{7}$$

holds, where W_μ^{LE} are calculated by means of (4). T_{LE} is obtained by numerically solving the non linear relation arising from (7). The temperatures of each phonon branch are introduced according to

$$\int_{\mathscr{B}} \hbar\omega_\mu g_\mu(\mathbf{q}) d\mathbf{q} = \int_{\mathscr{B}} \hbar\omega_\mu \left[e^{\hbar\omega_\mu/k_B T_\eta} - 1\right]^{-1} d\mathbf{q}. \tag{8}$$

2 Numerical results

The physical situation we simulate is that of a strip of graphene which is infinitely long in the transversal direction with respect to that of the electric field. This allows us to look for solutions which are not depending on space and to avoid any effect related to the boundary conditions. $N_P = 10^4$ particles have been used. The time step has been set equal to $\Delta t = 2.5$ fs. Several Fermi energies have been considered in order to investigate the dependence of the rise in temperature also on the electron density and not only on the applied field.

In Fig. 1 the LO and TO phonon distributions are shown, in Fig. 2 the phonon temperatures for each branch and in Fig. 3 the local equlibrium temperature versus time, where the Z phonons influence is highlighted as well.

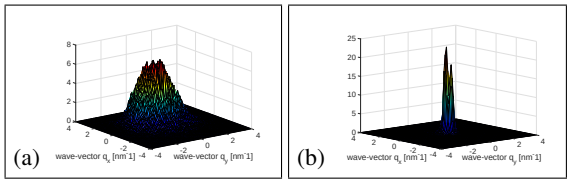

Fig. 1. LO (a) and TO (b) distribution after 10 ps in the case $\varepsilon_F = 0.6$ eV and $E = 20$ kV/cm.

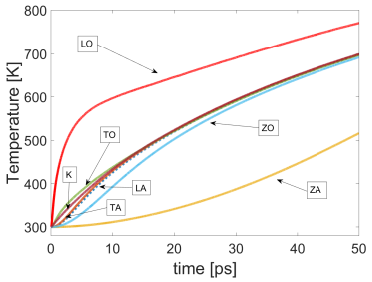

Fig. 2. Phonon branches temperatures versus time in the case $\varepsilon_F = 0.6$ eV when $E = 20$ kV/cm.

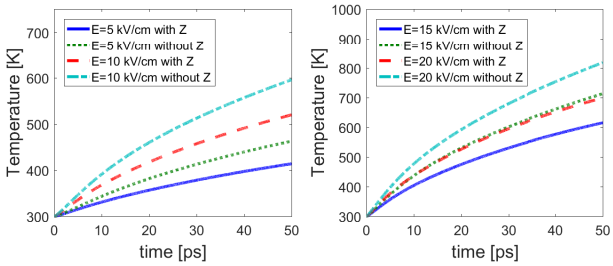

Fig. 3. Comparison of local equilibrium temperature versus time with and without the inclusion of Z phonons for $\varepsilon_F = 0.6$ at different values of the electric field.

References

1. V. Romano, A. Majorana, M. Coco. DSMC method consistent with the Pauli exclusion principle and comparison with deterministic solutions for charge transport in graphene. *Journal of Computational Physics*, 302, 267–284, 2015.
2. M. Coco, A. Majorana, V. Romano. Cross validation of discontinuous Galerkin method and Monte Carlo simulations of charge transport in graphene on substrate. *Ricerche Math.*, 66, 201–2020, 2017.
3. M. Coco, G. Mascali, V. Romano. Monte Carlo analysis of thermal effects in monolayer graphene. *J.Computational and Theoretical Transport*, 45 (7), 540–553, 2016.
4. M. Coco, V. Romano. Simulation of electron-phonon coupling and heating dynamics in suspended monolayer graphene including all the phonon branches. *J. Heat Transfer*, doi: 10.1115/1.4040082, 2018.

Multiscale atomistic modeling for materials science applications

Ioannis Deretzis and Antonino La Magna

CNR-IMM, Catania, Italy ioannis.deretzis@imm.cnr.it, antonino.lamagna@imm.cnr.it

Summary. Multiscale modeling is nowadays a general trend in computational physics and industrial mathematics, as it allows the numerical simulation of complex processes and phenomena that would be otherwise impossible to study solely by means of first principles approaches. Within this framework, a simplified problem is initially investigated through accurate calculations and appropriate parameters are extracted. Thereon, these parameters are used to calibrate theoretical models that are computationally less demanding whilst able to span in space- and time-scales that are comparable to those of real processes and experiments. In this paper we will discuss examples from our studies for such coupled numerical techniques, considering the case of graphene, other low-dimensional materials and hybrid perovskites.

1 Introduction

Multiscale modeling allows the computationally efficient numerical simulation of complex processes and phenomena. Within materials science, multiscale modeling often regards the simulation of mass and electron transport in nanoscale and mesosclale systems. The basic idea is to approach a simplified problem through accurate calculations, extracting appropriate parameters that can be successively used to calibrate theoretical models that are computationally less demanding. Often, the atomistic mechanisms and related parameters are investigated and calculated accurately in the quantum framework of the Density Functional Theory (DFT) and/or within DFT-based Molecular Dynamics (MD). Such *ab initio* approaches guarantee the theoretical evaluation of the atomic properties of materials specifying their constituents (atoms and electrons), without any relevant approximations. The integrated development of simulation codes supported by *ab initio* quantum calculations can significantly improve the quality of the transport models and the portability of their parameter calibration. The basis of the predictability potential for the mathematical model derives from the proper matching of the DFT/MD calculated "information" (e.g. material parameters, atomic configuration, migration/diffusion paths, energetics, electronic structure, etc.) in the simulation schemes. These calibrated simplified approaches can then efficiently simulate large systems for long times, i.e. at the scale of interest for the experimental studies. In this paper we will discuss examples from our studies for such coupled numerical techniques considering the case of low-dimensional materials [1,2], while expanding similar concepts for the case of hybrid perovskites [3].

2 Methodology

Quantum transport is calculated for two-terminal devices, i.e. devices that comprise of a channel of finite dimensions in contact with two semi-infinite leads.Here we consider ideal contacts, i.e. contacts made of the same material as the channel. Calculations are based on the nonequilibrium Green's function formalism [4]. The single-particle retarded Green's function matrix is

$$\mathscr{G}^r(\varepsilon) = [\varepsilon S - H - \Sigma_L - \Sigma_R]^{-1}, \tag{1}$$

where ε is the energy, H the real-space Hamiltonian and S the overlap matrix, which in the case of an orthonormal basis set is identical with the unitary matrix I. $\Sigma_{L,R}$ are self-energies that account for the effect of ideal semi-infinite contacts, which can be calculated as:

$$\Sigma_{L(R)} = \tau^{\dagger}_{L(R)} g_{L(R)} \tau_{L(R)} \tag{2}$$

Here $\tau_{L,R}$ are interaction Hamiltonians that describe the coupling between the contacts and the device and $g_{L,R}$ the surface Green functions of the contacts. The transmission probability of an incident Bloch state with energy ε can be computed as the trace of the following matrix product:

$$T(\varepsilon) = Tr\{\Gamma_L \mathscr{G}^r \Gamma_R [\mathscr{G}^r]^{\dagger}\}, \tag{3}$$

where

$$\Gamma_{L(R)} = i\{\Sigma_{L(R)} - [\Sigma_{L(R)}]^{\dagger}\} \tag{4}$$

are the spectral functions of the two contacts. The reflection coefficient of a single quantum channel can be defined as $R = 1 - T$. According to the Landauer-Buttiker theory [4], conductance can be calculated as:

$$G = \frac{2e^2}{h} T, \tag{5}$$

where $G_0 = 2e^2/h \approx 77.5 \mu S$ is the conductance quantum.

3 Results

The electronic structure of graphene can be easily calculated within a next-neighbor tight-binding (TB) model. Such a description accounts only for the linear combination of π atomic orbitals of graphene, which is however sufficient for the low-energy spectrum of the material. Hence, the next-neighbor TB Hamiltonian can be written as

$$H = -t \sum_{<i,j>,\sigma} c^{\dagger}_{i,\sigma} c_{j,\sigma} + H.c., \qquad (6)$$

where $c_i(c_i^{\dagger})$ is the annihilation (creation) operator for an electron with spin σ at site i, and t is the hopping integral with a typical value $t = 2.7eV$. In order to show the possibilities of multiscale modeling, here we will discuss the transport properties of defected graphene, considering the presence of a single type of defect, i.e. carbon vacancies. The simplest and most common method to include a vacancy in a site i of the graphene lattice is to remove its π electron from the model by switching to infinite the related on-site energy term ε_i in the Hamiltonian, or equivalently, by switching to zero the hopping t_{ij} terms between the defected and the neighboring sites (see Fig. 1). However, comparison with DFT calculations shows that such approach is quantitatively inaccurate, due to the missing structural reconstruction around the vacancy site in the TB formalism. A more accurate treatment of the defect states within the electronic spectrum has to take into account such local structural reorganization. A method to incorporate such information within the TB model is to perform calculations with methods of higher accuracy (e.g. the DFT) and calibrate the TB Hamiltonian in order to reproduce the *ab initio* results. Here, based on density functional theory calculations of defected graphene nanoribbons, the tuned values of the on-site energy of the defect site and the hopping integrals between this and neighboring sites have been set to ε_i=10 eV and t_{ij}=1.7 eV, respectively (Fig. 1). Such calibration can then allow for the calculation of electron transport in large-scale devices with the presence of a finite concentration of vacancy defects (Fig. 2). This example is a typical paradigm of the multiscale approach often used for conductance calculations in doped and defected graphene systems.

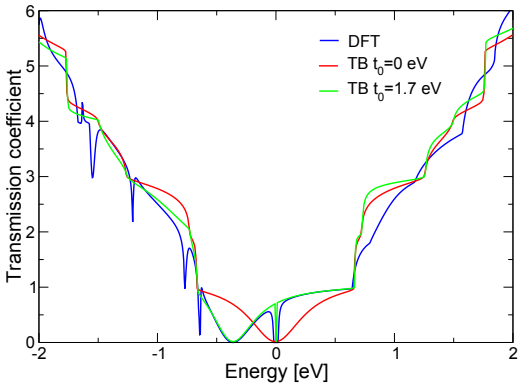

Fig. 1. Transmission coefficient as a function of energy for a graphene nanoribbon with 20 dimer lines having a single vacancy defect, calculated by means of (a) a DFT Hamiltonian, (b) a TB Hamiltonian with t_{ij}=0 eV and (c) a TB Hamiltonain with ε_i=10 eV and t_{ij}=1.7 eV.

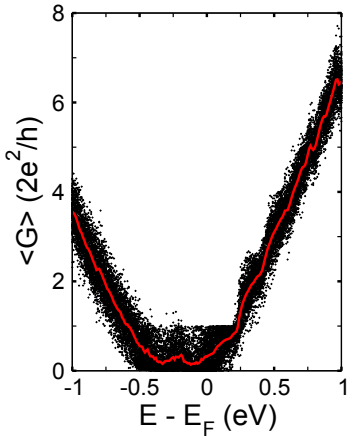

Fig. 2. Conductance distribution for a graphene nanoribbon with width W=9.88 nm, length L=20 nm and a fixed vacancy concentration of 0.5%. The solid line represents the mean conductance obtained from 100 different configurations of the system (shown as points).

References

1. I. Deretzis and A. La Magna. Interaction between hydrogen flux and carbon monolayer on SiC (0001): graphene formation kinetics. *Nanoscale*, 5(2), 671–680, 2013.
2. I. Deretzis, V. Romano and A. La Magna. Electron Quantum Transport in Disordered Graphene. *Scientific Computing in Electrical Engineering. Mathematics in Industry, vol 23. Springer, Cham*, 2016. pp. 3–12
3. I. Deretzis and A. La Magna. Exploring the orthorhombic-tetragonal phase transition in $CH_3NH_3PbI_3$: the role of atom kinetics. *Nanoscale*, 9(18), 5896–5903, 2017.
4. Datta, S.: Electronic Transport in Mesoscopic Systems. Cambridge University Press (1997)

A mass-lumped mixed finite element method for Maxwell's equations

Herbert Egger[1] and Bogdan Radu[2]

[1] AG Numerik, Mathematik, TU Darmstadt egger@mathematik.tu-darmstadt.de
[2] Graduate School for Computational Engineering, TU Darmstadt radu@gsc.tu-darmstadt.de

Summary. We consider the simulation of electromagnetic wave propagation problems by mixed finite elements with mass lumping. While the approximation order is formally reduced through the mass-lumping, we can establish superconvergence in one of the variables which allows to regain the full approximation order by post-processing. The overall method has a similar complexity to traditional finite-difference methods but can be applied also to problems with inhomogeneous parameters, curved geometries, and on unstructed grids. This is illustrated by numerical tests.

1 Introduction

The propagation of electromagnetic waves through a linear medium is described by Maxwell's equations

$$\varepsilon\partial_t \mathbf{E} - \nabla\times\mathbf{H} = \sigma \mathrm{e}, \tag{1}$$
$$\mu\partial_t \mathbf{H} + \nabla\times\mathbf{E} \;= 0. \tag{2}$$

Here $\mathbf{E}$ and $\mathbf{H}$ describe the electric and magnetic field densities and ε, μ denote, respectively, the permittivity and permeability of the medium. For the discreitzation of (1)–(2) we consider a mixed finite element method which is based the variational principle

$$(\varepsilon\partial_t \mathbf{E}_h(t), \mathbf{v}_h)_h - (\mathbf{H}_h(t), \nabla\times\mathbf{v}_h) = 0, \tag{3}$$
$$(\mu\partial_t \mathbf{H}_h(t), \mathbf{q}_h) + (\nabla\times\mathbf{E}_h(t), \mathbf{q}_h) = 0, \tag{4}$$

for all $\mathbf{v}_h \in \mathbf{V}_h$, $\mathbf{q}_h \in \mathbf{Q}_h$, and $t > 0$, and on the approximation of the electric and magnetic fields in the spaces $\mathbf{V}_h = P_1(T_h)^3 \cap H(curl)$ and $\mathbf{Q}_h = P_0(T_h)^3$ over some shape-regular simplicial mesh T_h. The first space consists of Nedelec finite elements of the second type. In the above formulation, $(\cdot,\cdot)$ denotes the L^2 scalar product and $(\cdot,\cdot)_h$ in (3) denotes an approximation obtained by numerical integration. Together with an appropriate choice of basis functions for $\mathbf{V}_h$, yields a mass-lumping strategy, i.e., the linear system

$$M\partial_t u(t) - B^\top p(t) = 0 \tag{5}$$
$$D\partial_t p(t) + Bu(t) = 0 \tag{6}$$

corresponding to (3)-(4) is governed by a diagonal matrix D and a block diagonal matrix M. This allows an efficient integration in by explicit single- and multi-step methods, e.g., the leapfrog scheme.

1.1 Previous work

Similar ideas were utilized by Elmkies and Joly in [4] for two-dimensional Maxwell's equations, by Cohen and Monk [2] on sructured grids, and by several authors for different applications; see [1] for further references. Our approach here is inspired by the work of Wheeler and Yotov [8] and our preliminary work [3] dealing with acoustic wave propagation.

2 Theoretical results

For approriate initial values $\mathbf{E}_h(0)$, $\mathbf{H}_h(0)$, one can show by standard arguments [6, 7] that (3)–(4) yields first order approximations

$$\|\mathbf{E}(t) - \mathbf{E}_h(t)\| \le Ch, \tag{7}$$
$$\|\mathbf{H}(t) - \mathbf{H}_h(t)\| \le Ch, \tag{8}$$

for the two field components, whenever the true solution $(\mathbf{E},\mathbf{H})$ is sufficiently smooth. This is optimal with respect to the approximation of $\mathbf{H}$ by piecewise constant functions, but sub-optimal with respect to the approximation of $\mathbf{E}$ by piecewise linear finite elements. In numerical tests, one can however observe superconvergence in the magnetic field, i.e.,

$$\|\pi_h^0\mathbf{H}(t) - \mathbf{H}_h(t)\| \le Ch^2, \tag{9}$$

where π_h^0 denotes the L^2-orthogonal projection onto piecewise constant functions in $\mathbf{Q}_h$. Based on the improved estimate (9), we are able to construct in a post-processing step piecewise linear improved approximations $(\widetilde{\mathbf{E}}_h, \widetilde{\mathbf{H}}_h)$ which satisfy

$$\|\mathbf{E}(t) - \widetilde{\mathbf{E}}_h(t)\| + \|\mathbf{H}(t) - \widetilde{\mathbf{H}}_h(t)\| \le Ch^2. \tag{10}$$

The overall method consisting of a mixed finite element approximation with mass-lumping and the post-processing strategy thus yields a second order approximation which can be computed efficiently by explicit time stepping schemes.

Remark. Using similar arguments as in [3,5], we can establish second order convergence for fully discrete approximations obtained by time-integration with the leap-frog scheme.

3 Numerical illustration

We now illustrate our theoretical results by a simple test problem which was also used in [6, 7].

Plane wave propagation. We consider a plane wave $(\mathbf{E} = (\mathbf{E}_x, \mathbf{E}_y, 0)$ and $\mathbf{H} = (0, 0, \mathbf{H}_z)$ with all fields depending only on the x and y coordinate. For our convergence study, we use a sequence $\{T_h\}$ of quasi-uniform but non-nested meshes T_h with decreasing mesh size $h = 2^{-k}$. In Table 1 and 2 we depict the errors obtained in our computational tests with the mixed-finite element method with mass-lumping and before and after post-processing. As error measure, we use $\|u\| = \max_{0\le t\le T} \|u(t)\|_{L^2)}$, where u stands for $\mathbf{E}$ and $\mathbf{H}$, respectively. The values of $\mathbf{E}(t)$ and $\mathbf{H}(t)$ are obtained by numerical integration of (3)–(4) by the leapfrog scheme with stepsize $\tau \le ch$.

h	$\|\mathbf{E}-\mathbf{E}_h\|$	eoc	$\|\mathbf{H}-\mathbf{H}_h\|$	eoc
2^{-3}	0.053047	—	0.069893	—
2^{-4}	0.020622	1.36	0.033095	1.08
2^{-5}	0.009977	1.05	0.016408	1.01
2^{-6}	0.004883	1.03	0.008114	1.02

Table 1. Errors and estimated order of convergence (eoc) for plane wave solution on a rectangular domain.

h	$\|\mathbf{E}-\widetilde{\mathbf{E}}_h\|$	eoc	$\|\mathbf{H}-\widetilde{\mathbf{H}}_h\|$	eoc
2^{-3}	0.051792	—	0.055946	—
2^{-4}	0.013486	1.94	0.013180	2.09
2^{-5}	0.003375	2.00	0.003220	2.03
2^{-6}	0.000836	2.01	0.000791	2.02

Table 2. Errors and estimated order of convergence (eoc) foir plane wave solution after post-processing.

As predicted in (7)–(8), we observe only first order convergence in both solution components by the mixed finite element method with mass-lumping. As can clearly be seen in Table 2, the full second order convergence for both solution components is obtained after post-processing.

Further visualization. To highlight the qualitative improvement obtained by the post-processing, we display in Figure 3 snapshots of the discrete solution components before and after post-processing. As can be seen from the illustrations, the post-processing not only reduces the error quantitatively, but it also leads to almost continuous approximations.

Acknowledgement. The authors are grateful for financial support by the "Excellence Initiative" of the German Federal and State Governments via the Graduate School of Computational Engineering GSC 233 at Technische Universitt Darmstadt and by the German Research Foundation (DFG) via grants IRTG 1529 and TRR 154.

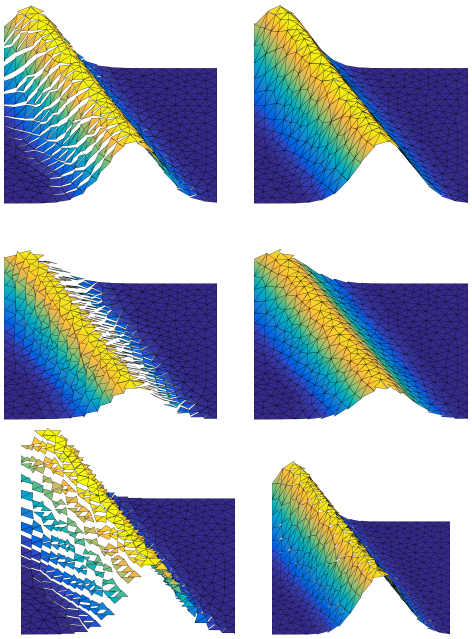

Fig. 1. Snapshots of the discrete approximations $\mathbf{E}_{\mathbf{x}h}$, $\mathbf{E}_{\mathbf{y}h}$, and $\mathbf{H}_{\mathbf{z}h}$ for the plane wave solution at time $t = 2$ (lect column) and corresponding approximations after post-processing (right column).

References

1. G. Cohen. *Higher-Order Numerical Methods for Transient Wave Equations*. Springer, Heidelberg, 2002.
2. G. Cohen and P. Monk. Gauss point mass lumping schemes for Maxwell's equations. *Numer. Meth. Part. Diff. Equat.*, 14:63–88, 1998.
3. H. Egger and B. Radu. A mass-lumped mixed finite element method for acoustic wave propagation. arXiv:1803.04238.
4. A. Elmkies and P. Joly. Finite elements and mass lumping for Maxwells equations: the 2D case. *Compt. Rend. Acad. Sci. Ser. 1*, 324:1287–1293, 1997.
5. P. Joly. Variational methods for time-dependent wave propagation problems. In *Topics in Computational Wave Propagation*, volume 31 of *LNCSE*, pages 201–264. Springer, 2003.
6. R. L. Lee and N. K. Madsen. A mixed finite element formulation for Maxwell's equations in the time domain. *J. Comput. Phys.*, 88(2):284–304, 1990.
7. P. Monk. A comparison of three mixed methods for the time-dependent Maxwell's equations. *SIAM J. Sci. Statist. Comput.*, 13:1097–1122, 1992.
8. M. F. Wheeler and I. Yotov. A multipoint flux mixed finite element method. *SIAM J. Numer. Anal.*, 44(5):2082–2106, 2006.
9. K. Yee. Numerical solution of initial boundary value problems involving Maxwells equations in isotropic media. *IEEE Trans. Antennas and Propagation*, AP-16:302–307, 1966.

Adaptive Mesh Refinement for Rotating Electrical Machines Taking into Account Boundary Approximation Errors

Armin Fohler[1] and Walter Zulehner[2]

[1] Linz Center of Mechatronics armin.fohler@lcm.at
[2] Johannes Kepler University Linz, Institute of Computational Mathematics zulehner@numa.uni-linz.ac.at

Summary. We will present an error estimator for the computation of the z-component of the vector potential of the magnetic field in the framework of rotating electrical machines. For the construction of the estimator we have to take care of the approximation errors of the curved domain by a polygonal mesh. Numerical results for the error reduction of the adaptive strategy in comparison with an uniform refinement will be presented.

1 Electrical Machines

This work focuses on the error analysis of a finite element scheme with linear elements in the framework of rotating electrical machines. We consider permanent-magnet synchronous machines (PMSM) that consist of two parts: an exterior part that is fixed – the stator; and in its interior a rotating part – the rotor. Each

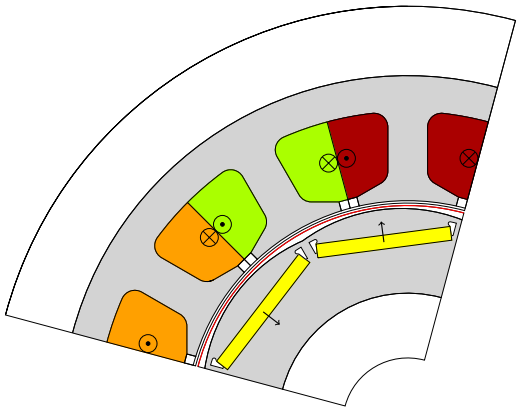

Fig. 1. Example: PMSM

of these parts is be further subdivided into different domains with distinct physical properties. In figure 1 a quarter of the cross-section of such a PMSM is shown. Magnets are depicted in yellow and their magnetization directions are indicated by the arrows. The machine has 12 slots with 4 pole-pairs. The scheme of the connection is shown by the different colors of the slots. Gray area symbolizes iron material, its nonlinear property described by the magnetic reluctivity $\nu(|\nabla u|)$.

2 Model Problem

We use the magnetostatic case of Maxwell's equations as a model problem and restrict the simulation to the 2d case because most of the flux is in the x-y plane.
When simulating an electrical machine we are not only interested in one rotor-to-stator position but in a whole rotation cycle. After meshing both motor parts once we rotate the rotor mesh for the simulation of the different rotor positions. To handle the rotation efficiently we use Nitsche coupling (NC) [2,3] as a domain decomposition method. The idea of this method is to insert an artificial interface Γ between the two separate parts. We introduce a new function λ on this interface that represents the solution on Γ and penalize the jump of the solution across this interface. With the notation $u_i := u\big|_{\Omega_i}$ the resulting variational formulation reads: Find $\mathbb{u} = (u, \lambda)$, $u : \overline{\Omega} \to \mathbb{R}$, $\lambda : \Gamma \to \mathbb{R}$ such that

$$a(\mathbb{u}, \mathbb{v}) = \langle f, \mathbb{v} \rangle \tag{1}$$

with

$$\begin{aligned} a(\mathbb{u}, \mathbb{v}) = \sum_i \Bigg(& \int_{\Omega_i} (\nu(|\nabla u_i|)\nabla u_i - M_\perp) \cdot \nabla v_i dx \\ & - \int_{\Gamma \cap \Omega_i} (\nu_0 \nabla u_i \cdot n_i)(v_i - \psi)\, dS \\ & + \beta \int_{\Gamma \cap \Omega_i} (\nu_0 \nabla v_i \cdot n_i)(u_i - \lambda)\, dS \\ & + \frac{\alpha}{|\Gamma|} \int_{\Gamma \cap \Omega_i} \nu_0 (u_i - \lambda)(v_i - \psi)\, dS \Bigg) \end{aligned}$$

and

$$\langle f, \mathbb{v} \rangle = \sum_i \int_{\Omega_i} J_3 \, v_i dx$$

$\forall \mathbb{v} = (v, \psi)$, $v : \overline{\Omega} \to \mathbb{R}, v\big|_{\partial\Omega} = 0$ and $\forall \psi : \Gamma \to \mathbb{R}$.
The functions ψ are the test-functions on the interface Γ.
J_3 is the current coming from the coils, $M_\perp$ is the magnetization in the permanent magnets.

3 Adaptive Mesh Refinement

For the optimization of an electrical motor many geometries have to be simulated to find a suitable topology. Thus the speed of the used solver is crucial. To accelerate the simulation time while retaining the accuracy of the simulation result we want to use adaptive meshes.
For the construction of an a posteriori error estimator in the framework of rotating electrical machines we have to take special care on the influence of the polygonal approximation of the curvilinear boundaries and interfaces.

3.1 Boundary approximation

For the case of pure Dirichlet conditions on a curvilinear boundary approximated by a polygonal mesh an error estimator was presented in the work by W. Dörfler and M. Rumpf [1]. In our problem we also have to deal with Neumann boundary conditions and interface conditions. This can not be treated by the same strategy. Instead we use ideas of hierachical basis error estimation. This gives us an estimate of the error contribution of the polygonal approximation.

3.2 Influence of Nitsche coupling

The error estimation will be done with respect to the NC-norm for our problem:

$$\|\mathfrak{u}\|_{NC}^2 = \sum_i \int_{\Omega_i} |\nabla u_i|^2 + \sum_i \frac{\alpha}{|\Gamma_{ij}|} \int_{\Gamma} |u_i - \lambda|^2$$

This norm is similar to the DG-norm used in the framework of discontinuous Galerkin methods. For the construction of the estimator we use a similar approach as it was used for a discontinuous Galerkin method in [4].

3.3 Numerical Results

Starting from an initial mesh with 562 degrees of freedom we compared the reduction of the error in the NC-norm using uniform refinement with our adaptive strategy for one rotation step and observed a reduction of the degrees of freedom by nearly $\frac{1}{3}$ after 4 adaptive refinement steps at a comparable size of the error (Fig. 2). Additionally we can observe the influence of the error terms estimating the effect of the boundary approximation.

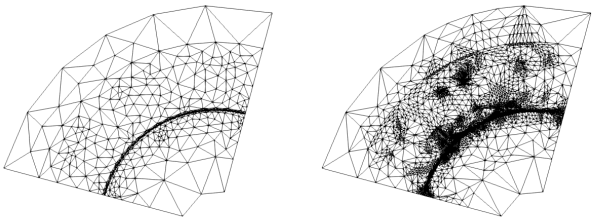

Initial Mesh (562 dof) 4 times refined Mesh (7692 dof)

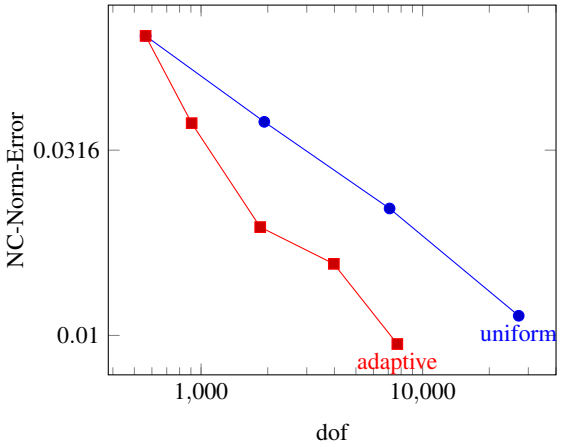

Fig. 2. Reduction in the NC-norm ($\varphi = 0, \alpha = 100$)

4 Future Goal

Using this ideas we get an refinement strategy for each rotor position. As already mentioned we are interested in the simulation of many different rotor-to-stator positions. This would result in a differently refined mesh for each position. However it is favourable to develop a refinement strategy for the original stator and rotor mesh independently of the rotation angle φ.

Acknowledgement. This work has been supported by the COMET-K2 Center for Symbiotic Mechatronics of the Linz Center of Mechatronics (LCM) funded by the Austrian federal government and the federal state of Upper Austria.

References

1. W. Dörfler and M. Rumpf. An adaptive strategy for elliptic problems including a posteriori controlled boundary approximation. *Mathematics of Computation*, 67(224):1361–1382, 1998.
2. H. Egger. A class of hybrid mortar finite element methods for interface problems with non-matching meshes. *preprint AICES-2009-2, Jan*, 2009.
3. K. Hollaus, D. Feldengut, J. Schöberl, M. Wabro, and D. Omeragic. Nitsche-type Mortaring for Maxwell's Equations. *Progress In Electromagnetics Research Symposium Proceedings*, pages 397–402, 2010.
4. P. Houston, E. Süli, and T. P. Wihler. A posteriori error analysis of hp-version discontinuous galerkin finite-element methods for second-order quasi-linear elliptic pdes. *IMA Journal of Numerical Analysis*, 28(2):245–273, 2008.

Isogeometric Simulation and Shape Optimization with Applications to Electrical Machines

Peter Gangl[1], Ulrich Langer[2,4], Angelos Mantzaflaris[3], and Rainer Schneckenleitner[4]

[1] Institute of Applied Mathematics, TU Graz, Austria gangl@math.tugraz.at,
[2] Institute of Computational Mathematics, JKU Linz, Austria ulanger@numa.uni-linz.ac.at
[3] Institute of Applied Geometry, JKU Linz, Austria angelos.mantzaflaris@jku.at
[4] RICAM, Austrian Academy of Sciences, Linz, Austria rainer.schneckenleitner@ricam.oeaw.ac.at

Summary. Future e-mobility calls for efficient electrical machines. For different areas of operations, these machines have to satisfy certain desired properties that often depend on their design. Here we investigate the use of Isogeometric Analysis (IgA) for the simulation and shape optimization problems subject to the partial differential equation (PDE) describing the electromagnetic behavior of the machine.

1 Simulation and Optimization

We investigate the simulation and shape optimization of an interior permanent magnet (IPM) electric motor by means of IgA. The IgA approach seems to be very attractive for such practical problem. The most beneficial aspect of IgA in the context of optimization is the fact that the same basis functions which are used to represent the geometry of the IPM electric motor are also exploited to solve the underlying PDEs. In the optimization procedure, we want to optimize the shape of the motor in order to maximize runout performance. An example of an IPM electric motor is given in Fig. 1 (left). One possible way to optimize the runout performance of an IPM electric motor is to minimize the squared L^2-distance between the radial component of the magnetic flux in the air gap and some desired reference function B_d. The resulting optimization problem is subject to the 2d magnetostatic PDE as constraint.

Mathematically, the arising optimization problem can be expressed as the minimization of the objective

$$J(u) := \int_\Gamma |B(u)\cdot n_\Gamma - B_\mathrm{d}|^2 ds = \int_\Gamma |\nabla u\cdot \tau_\Gamma - B_\mathrm{d}|^2 ds$$

over D subject to: find $u \in H^1_0(\Omega)$ such that

$$\int_\Omega \nu_\mathrm{D}(x)\nabla u\cdot\nabla\eta\, dx = \int_\Omega (J_3\eta + \nu_\mathrm{M} M^\perp\cdot\nabla\eta)\, dx \tag{1}$$

for all $\eta \in H^1_0(\Omega)$. The function J denotes the objective, while Γ is nothing but the midline of the airgap. Furthermore, Ω denotes the whole computational domain, and D is the domain of interest also called design domain. The variational problem (1) is the 2d linear magnetostatic problem and is well-posed. The involved physical quantities are the magnetic flux density B, the magnetic reluctivity ν which is nothing but the reciprocal of the magnetic permeability μ, the magnetization M as well as the third component of the impressed current density J_3. For simplicity, we assumed $J_3 = 0$ in our work. The involved expressions n_Γ and τ_Γ are the unit normal and the unit tangential vectors along the air gap, respectively.

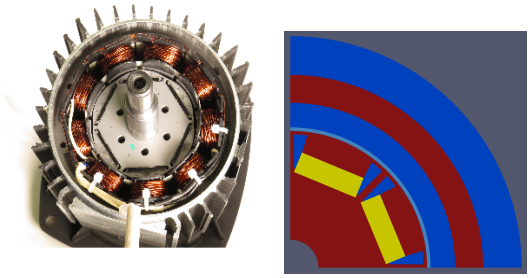

Fig. 1. IPM motor and a quarter of its cross section.

Figure 1 (right) shows a simplified quarter of a cross section of an IPM electric motor that is provided by CAD software. Hence, this geometry representation is suitable for IgA simulation. The red brown areas denote ferromagnetic material, the blue areas consist of air, the yellow areas are the permanent magnets, whereas the light blue area represents the air gap.

2 Numerical Computations

For the optimization problem introduced in Sect. 1, we consider gradient based shape optimization algorithms. For this purpose, we need the gradient with respect to the shape of the considered optimization problem.

2.1 Computation of the Shape Gradient

To compute the shape gradient, we solve the auxiliary problem: find $\nabla J \in H^1_0(\Omega,\mathbb{R}^2)$ such that

$$b(\nabla J,\psi) = -dJ(D)(\psi) \qquad \forall \psi \in H^1_0(\Omega,\mathbb{R}^2). \tag{2}$$

The expression on the right hand side of (2) is the shape derivative which is given by the relation

$$dJ(D)(\phi) = \int_\Omega \mathscr{S}(D,u,p) : \partial\phi \; dx, \quad \text{with}$$

$$\begin{aligned}\mathscr{S}(D,u,p) = (\nu_D(x)\nabla u\cdot\nabla p - \nu_M \nabla p\cdot M^\perp)\mathscr{I} \\ + \nu_M \nabla p \otimes M^\perp - \nu_D(x)\nabla p\otimes\nabla u \\ - \nu_D(x)\nabla u\otimes\nabla p,\end{aligned}$$

where $\mathscr{I}$ denotes the identity, the state u solves the constraint (1), and p solves the adjoint problem

$$\int_\Omega \nu_D \nabla p\cdot\nabla\eta \; dx = -2\int_\Gamma (B(u)\cdot n_\Gamma - B_d)(B(\eta)\cdot n_\Gamma)\, ds$$

for all $\eta \in H^1_0(\Omega)$, The expression $b(\cdot,\cdot)$ on the left hand side of (2) is some $H^1_0(\Omega,\mathbb{R}^2)$ - elliptic and bounded bilinear form that must be chosen appropriately; see [1,2,4] for more details.

2.2 First Numerical Results

For the numerical simulation, we used a continuous Galerkin approach which requires a suitable multi-patch representation of the domain from Fig. 1 such as presented in Fig. 2 (left). A first straightforward approach, which is entirely implemented in G+Smo, resulted in the optimal design presented in Fig. 2 (right). The objective drops approximately by a factor of two from $1.05863\cdot 10^{-4}$ down to $5.92351\cdot 10^{-5}$.

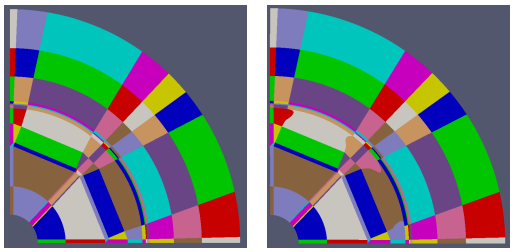

Fig. 2. Initial and final design of an IPM motor.

3 Numerical Improvements

Once the complexity of the problem grows, e.g., by refinements, solving the optimization problem in a standard straightforward way becomes computationally more and more demanding. Fortunately, G+Smo provides more sophisticated solution methods for PDEs, e.g., **D**ual-**P**rimal **I**sogeometric **T**earing and **I**nterconnecting (IETI-DP) that is a generalization of FETI-DP to IgA [3]. Numerical tests show that we get a pretty good speedup compared to a sparse direct solution technique. Table 1 shows the speedup for solving (1) if we compare the sparse direct solver SuperLU with IETI-DP. Moreover, IETI-DP is well suited for parallelization. Strong scaling tests confirm the efficiency of the IETI-DP algorithm for larger problems as can be seen from Table 2. These computations were performed using splines of the degree 3 on the complete cross-section of the motor as is shown in Fig. 3.

Table 1. SuperLU vs. IETI-DP.

# dofs	SuperLU	IETI-DP	speedup
72 572	36.0 sec	17.0 sec	2.12
250 844	193.0 sec	69.8 sec	2.77
928 796	1943.0 sec	463.0 sec	4.20
3 570 332	–	1179.0 sec	–

Table 2. Strong scaling with IETI-DP and 3 570 332 dofs.

# cores	1	2	4	8	16	32	64	128
time [sec]	1179	577	325	164	89	43	22	14
rate	–	2.04	1.78	1.98	1.84	2.07	1.95	1.57

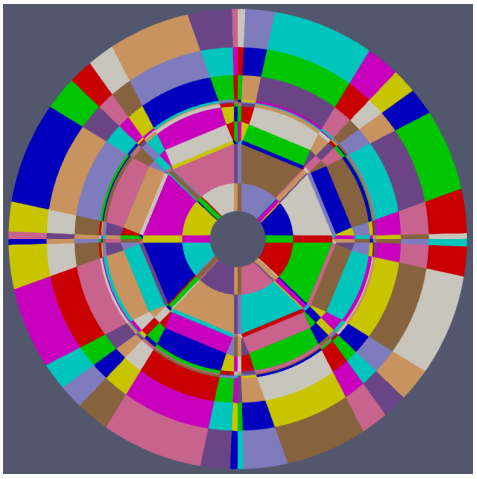

Fig. 3. Full cross section of the motor consisting of 372 patches was used as computational domain Ω for the tests with IETI-DP.

Acknowledgement. This work was supported by the Austrian Science Fund (FWF) via the grants NFN S117-03 and the DK W1214-04. We also acknowledge the permission to use the Photo in Fig. 1 (left) taken by the Linz Center of Mechatronics (LCM). The motor was produced by Hanning Elektro-Werke GmbH & Co KG.

References

1. P. Gangl. *Sensitivity-Based Topology and Shape Optimization with Application to Electrical Machines*. PhD thesis, Johannes Kepler University Linz, 2016.
2. P. Gangl, U. Langer, A. Laurain, H. Meftahi, and K. Sturm. Shape optimization of an electric motor subject to nonlinear magnetostatics. *SIAM Journal on Scientific Computing*, 37(6):B1002–B1025, 2015.
3. C. Hofer and U. Langer. Dual-primal isogeometric tearing and interconnecting solvers for multipatch dG-IgA equations. *Comput. Methods Appl. Mech. Engrg.*, 316:2–21, 2017.
4. R. Schneckenleitner. Isogeometrical Analysis based Shape Optimization. Master thesis, Johannes Kepler University Linz, 2017.

Quasi-Schur Transformation for the Stable Compact Modeling of Piezoelectric Energy Harvester Devices

Siyang Hu[1,2], Chengdong Yuan[1,2], and Tamara Bechtold[1,2]

[1] Jade University of Applied Sciences, Department of Engineering, Friedrich-Paffrath-Str. 101, Wilhelmshaven 26389, Germany.
siyang.hu@jade-hs.de, chengdong.yuan@jade-hs.de, tamara.bechtold@jade-hs.de.
[2] University of Rostock, Institute for Electronic Appliances and Circuits, Albert-Einstein-Str. 2, Rostock 18059, Germany.

Summary. 'Schur after MOR' method has proved successful in obtaining stable reduced piezoelectric device models and is already used in industry. Yet, it is still mathematically unproven. This contribution delivers 'the missing piece of the jigsaw': We show that the involved quasi-Schur transformation indeed does re-stabilize the aforementioned models efficiently.

1 Introduction

Model and simulation-driven development has become state of the art lately due to the increasing capacity of today's computers. However, even the power of modern computers fails to cope with always faster growing demands of the industry. To overcome this issue, the methodology of model order reduction (MOR) has been introduced. MOR significantly reduces the computational effort required for e.g. system-level simulations by replacing the original high-dimensional model with a lower dimensional but still accurate surrogate. Novel MOR methods are mostly interpolation-based and perform well when applied to single-physical-domain models. However, for models involving coupled physical domains, we regularly encounter difficulties in preserving the stable input/output behavior of the original system.

In [2], the authors introduce different approaches to solve the stability issue for the piezoelectric models. However, except for 'MOR after Schur' in [3], none of those methods have been mathematically proven yet. In this contribution, we considered the 'Schur after MOR' approach, as it proved effective in a number of industrial applications. Furthermore, this approach turns to be significantly more efficient than 'MOR after Schur', and its improved successor 'MOR after Implicit Schur', introduced in [3], since the Schur transformation does not have to be performed on the full scale system matrices.

2 Piezoelectric Energy Harvesters

Piezoelectric energy harvesters transform environmental mechanical vibration into electrical energy using the piezoelectric effect. Mechanical part of finite element model reads:

$$\mathbf{M_{11}}\ddot{\mathbf{x}}_\mathbf{1} + \mathbf{D_{11}}\dot{\mathbf{x}}_\mathbf{1} + \mathbf{K_{11}}\mathbf{x_1} = \mathbf{b_1}u, \tag{1}$$

where $\mathbf{M_{11}}, \mathbf{K_{11}} \in \mathbb{R}^{n\times n}$ are symmetric positive definite (s.p.d.) and respectively the mass and stiffness matrices. $\mathbf{D_{11}} = \alpha\mathbf{M_{11}} + \beta\mathbf{K_{11}}, \alpha, \beta \in \mathbb{R}$ is the damping matrix and $\mathbf{x_1}$ is the vector of nodal displacements. The electrical part reads:

$$\mathbf{K_{22}}\mathbf{x_2} = \mathbf{b_2}u, \tag{2}$$

with $\mathbf{K_{22}} \in \mathbb{R}^{k\times k}$ the electrical conductivity matrix, which is symmetric negative definite (s.n.d.) and

$$||\lambda_{\max}(\mathbf{K_{22}})|| \ll ||\lambda_{\min}(\mathbf{K_{11}})|| \tag{3}$$

holds for the respective eigenvalues. $\mathbf{x_2}$ is a vector of nodal electrical potentials. Both physical domains are coupled via piezoelectric patches, which transform stress into electric potential. Thus, we have piezoelectric coupling in $\mathbf{K_{12}} \in \mathbb{R}^{n\times k}$, such that:

$$\Sigma = \begin{cases} \underbrace{\begin{bmatrix}\mathbf{M_{11}} & 0\\ 0 & 0\end{bmatrix}}_{\mathbf{M}}\begin{bmatrix}\ddot{\mathbf{x}}_\mathbf{1}\\ \ddot{\mathbf{x}}_\mathbf{2}\end{bmatrix} + \underbrace{\begin{bmatrix}\mathbf{D_{11}} & 0\\ 0 & 0\end{bmatrix}}_{\mathbf{D}}\begin{bmatrix}\dot{\mathbf{x}}_\mathbf{1}\\ \dot{\mathbf{x}}_\mathbf{2}\end{bmatrix} + \underbrace{\begin{bmatrix}\mathbf{K_{11}} & \mathbf{K_{12}}\\ \mathbf{K_{12}^T} & \mathbf{K_{22}}\end{bmatrix}}_{\mathbf{K}}\begin{bmatrix}\mathbf{x_1}\\ \mathbf{x_2}\end{bmatrix} = \underbrace{\begin{bmatrix}\mathbf{b_1}\\ \mathbf{b_2}\end{bmatrix}}_{\mathbf{b}}u \\ y = \mathbf{c^T}\begin{bmatrix}\mathbf{x_1}\\ \mathbf{x_2}\end{bmatrix}\end{cases}. \tag{4}$$

The input u corresponds to the displacement imposed to the harvester structure with input vector $\mathbf{b} \in \mathbb{R}^{n+k}$ chosen accordingly. The total electrical potential is gathered via output vector $\mathbf{c} \in \mathbb{R}^{n+k}$ in the output y.

3 Schur after MOR

This section briefly reassembles the method introduced in [2]. For a survey on general MOR methods for this class of models, please refer to [1].

'Schur after MOR' method stabilizes unstable reduced order models:

$$\Sigma_r = \begin{cases} \mathbf{M_r}\ddot{\mathbf{x}}_\mathbf{r} + \mathbf{D_r}\dot{\mathbf{x}}_\mathbf{r} + \mathbf{K_r}\mathbf{x_r} = \mathbf{b_r}u \\ y = \mathbf{c_r^T}\mathbf{x_r}\end{cases}, \tag{5}$$

obtained by projective MOR: $\mathbf{V^T \Sigma V}$, where:

$$\begin{aligned} \{\mathbf{M_r}, \mathbf{D_r}, \mathbf{K_r}\} &= \mathbf{V^T}\{\mathbf{M}, \mathbf{D}, \mathbf{K}\}\mathbf{V}, \\ \mathbf{b_r} = \mathbf{V^T b} \quad &\text{and} \quad \mathbf{c_r^T} = \mathbf{c^T V}. \end{aligned} \tag{6}$$

$\mathbf{V} \in \mathbb{R}^{n+k \times p}, p \ll n+k$, is chosen as a orthonormal basis of the p-dimensional second-order input Krylov subspace:

$$\mathscr{K}_p(-\mathbf{K^{-1}M}, -\mathbf{K^{-1}D}, -\mathbf{K^{-1}b}). \tag{7}$$

The stabilization is achieved by performing a quasi-Schur Transformation on Σ_r, where Σ_r is approximated by differential algebraic equations (DAEs) system before being Schur transformed. The approximation involves an eigen-transformation $\widetilde{\Sigma}_r = \mathbf{T^T} \Sigma_r \mathbf{T}$, where $\mathbf{T}$ is a sorted orthonormal eigenbasis of the matrix $\mathbf{M}$, such that its entries $\widetilde{m}_{r,ii} \geq \widetilde{m}_{r,jj}$ for all $i > j$. In the next step, we neglect the subspaces in which the differential equations are quasi-algebraic, i.e. we set $\widetilde{m}_{r,ii} = 0$ for all $i \geq I, I \in [1, p]$ and $\widetilde{m}_{r,(I-1)(I-1)} \gg \widetilde{m}_{r,II}$. Thereby, we obtain a reduced order DAE system, which can be Schur transformed.

Theorem 1. *The quasi-Schur Transformation stabilizes the reduced model Σ_r.*

Proof. As $\mathbf{M_{11}}$ is s.p.d., $\mathbf{M_r}$ has to be symmetric positive semi-definite as well. Furthermore, $\mathbf{K_r}$ must have negative eigenvalues. Otherwise, Σ_r is stable according to [5].

Since $\mathbf{M}$ and $\mathbf{K}$ can obviously be simultaneously diagonalized (e.g. with eigenbasis of $\mathbf{K^{-1}M}$), the system domain can be represented as a direct sum of eigenspaces, i.e.:

$$\lambda(\mathbf{K_r}) = \sum_i \nu_i \lambda(\mathbf{K})_i, \quad \sum_i \nu_i = 1, \tag{8}$$

hold for all eigenvalues of $\mathbf{K_r}$. Now, given (3) and let $P,N \subset \{1,...,n+k\}$ set of indices corresponding to the positive and negative eigenvalues of $\mathbf{K}$, (8) can only be negative if $\sum_{i \in P} \nu_i \ll \sum_{i \in N} \nu_i$. That is to say, given the structure of Σ, the subspaces of the reduced system corresponding to these negative eigenvalues is dominated by the electric domain. These subspaces must obviously also be quasi-algebraic, as $\lambda(\mathbf{M_r}) = \sum_{i \in P} \nu_i \lambda(\mathbf{M})_i$.

Finally, when $\widetilde{\Sigma}_r$ is Schur transformed, we have:

$$\widetilde{\mathbf{K}}_\mathbf{s} = \widetilde{\mathbf{K}}_{\mathbf{r},(\mathbf{1:I},\mathbf{1:I})} - \widetilde{\mathbf{K}}_{\mathbf{r},(\mathbf{1:I},\mathbf{I:p})} \widetilde{\mathbf{K}}^{-\mathbf{1}}_{\mathbf{r},(\mathbf{I:p},\mathbf{I:p})} \widetilde{\mathbf{K}}_{\mathbf{r},(\mathbf{I:p},\mathbf{1:I})} \tag{9}$$

which is s.p.d as $\widetilde{\mathbf{K}}_{\mathbf{r},(\mathbf{1:I},\mathbf{1:I})}$ is s.p.d. and $\widetilde{\mathbf{K}}^{-\mathbf{1}}_{\mathbf{r},(\mathbf{I:p},\mathbf{I:p})}$ s.n.d. That makes the quasi-Schur Transformed system stable according to [5].

Remark 1. In industrial software, the quasi-Schur Transformation introduced in [2] is actually modified [4]. The index I is obtained by $\widehat{\mathbf{K}}_\mathbf{r} = \mathbf{T_K^T K_r T_K}$ and then setting I such that $\widehat{K}_{r,ii} < 0$ for all $i \geq I$. This equivalent criteria is easier to implement and more robust.

4 Numerical Experiments

We have performed 'Schur after MOR' on the original micro-mechanical model form [2] as well as on a novel frequency tuneable piezoelectric energy harvester introduced in [3] and have reliably obtained stable reduced models. Furthermore, we have found the considered (quasi-algebraic) subspaces to coinside even when taking numeric errors into account.

Table 1 shows the computation times[1] of 'Schur after MOR' compared to 'MOR after Implicit Schur' from [3] for the reduction of the tuneable harvester model with 24643 degrees of freedom.

Reduced Order	Schur after MOR	MOR after impl. Schur
30	36.98s	52.85s
90	41.48s	57.24s
240	57.42s	71.11s

Table 1. Computation time of 'Schur after MOR' vs. 'Schur after impl. MOR'.

5 Conclusion and Outlook

In this work, we have given a mathematical proof that quasi-Schur Transformation applied to reduced models of piezoelectric energy harvesters obtained by projective MOR stabilizes the models.

Further, we have found 'Schur after MOR' reliable in generating stable reduced models in this specific use-case and have shown the efficiency of it compared to 'MOR after Implicit Schur' ($\sim$30% decrease of computation time).

In the next step, one can compare quasi-Schur Transformation with conventional stabilizing method, e.g. by simply removing the unstable part of the system.

References

1. P. Benner and T. Stykel. Model order reduction for differential-algebraic equations: a survey. In *Surveys in Differential-Algebraic Equations IV*, pages 107–160. Springer, 2017.
2. M. Kudryavtsev et al. Computationally efficient and stable order reduction methods for a large-scale model of mems piezoelectric energy harvester. *Microelectronics Reliability*, 55(5):747–757, 2015.
3. S. Hu et al. Stable reduced order modeling of piezoelectric energy harvesting modules using implicit schur complement. *Microelectronics Reliability*, 85:148 – 155, 2018.
4. E. B. Rudnyi. MOR for ANSYS. *System-Level Modeling of MEMS*, pages 425–438, 2013.
5. S. B. Salimbahrami. *Structure preserving order reduction of large scale second order models*. PhD thesis, Technische Universität München, 2005.

[1] On Intel® Core™ i5-7600 CPU@3.5GHz, 32GB RAM

Load Snapshot Based Nonlinear-Input Model Order Reduction of a Thermal Human Tissue Model

Onkar Jadhav[1], Evgenii Rudnyi[2], and Tamara Bechtold[3]

[1] Institute of Electronic Appliances and Circuits, University of Rostock, Rostock, Germany
[2] CADFEM GmbH, Germany
[3] Department of Engineering, Jade University of Applied Sciences, Wilhelmshaven, Germany
tamara.bechtold@jade-hs.de

Summary. In this work, a compact model of a miniaturized thermoelectric generator for powering the electrically active implants, embedded into a human tissue is presented. As heat generation by blood perfusion is a temperature dependent effect, the resulting finite element model has a nonlinear input term. To overcome this difficulty, we linearize the load vector by snapshotting prior to applying mathematical model order reduction.

1 Introduction

Implantable medical devices are used to provide medical treatments and support the diagnosis [1]. Currently, the electrical energy for implantable biomedical devices is provided by integrated batteries which have certain energy storage capacity and chemical side effects. As human body is a bountiful source of thermal energy, harvesting this energy to power biomedical implants will increase their lifetime and safety than conventional devices. In this work, we

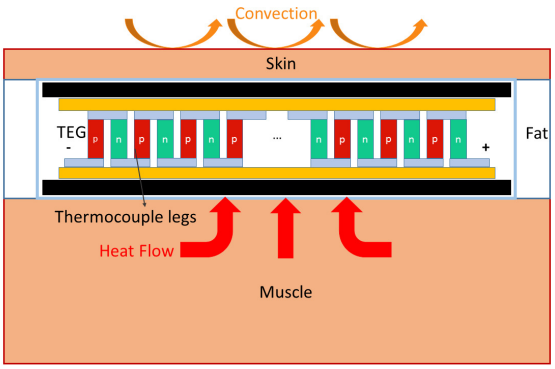

Fig. 1. Schematic of a thermoelectric generator embedded in the fat layer; tissue model as suggested in [2]

.

present the model of a thermoelectric generator (TEG) embedded into a simple three layer tissue structure composed of muscle, fat and skin (See Fig. 1). It shall convert thermal into electrical energy and so power the medical implants. To enable an efficient transient simulation and parameter studies, we apply mathematical model order reduction (MOR) technique, which provides compact but accurate thermal model of a human TEG. As MOR is proven to work well for linear thermal models [3], we have to linearize the temperature dependent perfusion heat generation rate. In the approach presented here, the load snapshots are obtained at discrete time intervals and weighted to obtain a single linearized load for the model to be reduced, difference from [4] where, the time consuming singular value decomposition (SVD) of the snapshots is performed for another thermal system with temperature-dependent input vector.

2 Model Description

The heat conduction in the human tissue can be described by the bio-heat equation of Pennes [5]:

$$\rho c \frac{\partial T}{\partial t} = \nabla \kappa \nabla T + Q_b + Q_m, \tag{1}$$

where, $Q_b = \rho_b c_b \omega_b (T_a - T(\bar{r},t))$ and Q_m are perfusion and metabolic heat generation rates, respectively, ρ, c, κ are the density, specific heat and thermal conductivity of the three tissue types, ρ_b, c_b denote the thermal properties of blood and ω_b is a measure of perfusion. $T(\bar{r},t)$ is the resulting temperature distribution and $T_a = 37°\mathrm{C}$, is the temperature of arterial blood. The spatial discretization of (1), via e. g. finite elements leads to a system of n ordinary differential equations with non-linear input:

$$\sum_n \begin{cases} E \cdot \dot{T}(t) = A \cdot T(t) + Q(T) \\ y(t) = C \cdot T(t), \end{cases} \tag{2}$$

where, $A, E \in R^{n \times n}$ are the global heat conductivity and heat capacity matrices, $Q(T) \in R^{n \times 1}$ is the temperature-dependent load vector and $C \in R^{p \times n}$ is the output matrix. n is the dimension of the system and p is the number of user defined outputs.

3 Methodology

As the finite element method discretizes the domain into e finite-elements and n nodes, $Q(T)$ can be lin-

earized as:

$$q = \rho_b c_b \omega_b (T_a - T_e(t)) + Q_m, \tag{3}$$

where, $T_e(t)$ is the vector of average temperatures per each finite-element e distributed over n nodes. We construct a snapshot matrix $X \in R^{n \times s}$ at s points in time (t_s), which columns are comprised of linearized heat generation vectors, q_i:

$$X = [q_1 \quad q_2 \quad q_3 \quad \dots \quad q_s]_{n \times s}, \tag{4}$$

The final load vector $\bar{Q}$, is obtained by taking the weighted average of these snapshots:

$$\bar{Q} = \sum_{i=1}^{s} w_i q_i, \tag{5}$$

where, w_i denote the weights, which still have to be defined. After applying the block-Arnoldi algorithm [6] to (2), we obtain the reduced order model:

$$\sum_r \begin{cases} E_r \cdot \dot{z}(t) = A_r \cdot z(t) + \bar{Q}_r \\ y(t) = C_r \cdot z(t), \end{cases} \tag{6}$$

where, $E_r = V^T E V$, $A_r = V^T A V$, $\bar{Q}_r = V^T \bar{Q}$, $C_r = CV$ and $V \in R^{n \times r}$ is a projection matrix with $r \ll n$.

4 Results

Figure 2 shows the study carried out for the selection of optimal weights. The snapshots are distributed

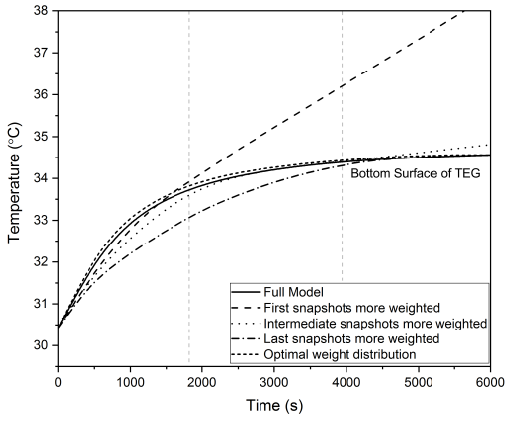

Fig. 2. Temperature Result comparison between full and reduced model at the bottom surfaces of TEG with different weighing of snapshots.

into three groups; separated by the dashed lines. As expected, the time domain in which, we weigh the snapshots strongly, shows the better match between the full and the reduced model. Based on this outcome, optimal weights are selected. Initial state was considered from the steady state thermal simulation

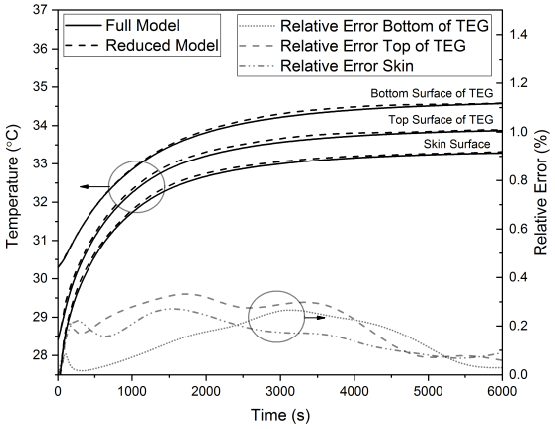

Fig. 3. Result comparison between full and reduced model at the top and bottom surfaces of TEG and skin surface.

with heat transfer coefficient of 20 $\mathrm{W/m^2/K}$ and ambient temperature of 15 °C. Transient thermal simulation was performed with final heat transfer coefficient of 5 $\mathrm{W/m^2/K}$. Figure 3 shows the result comparison between the full model of order 127,944 and reduced model of order 30. With optimal weights, an excellent match is obtained.

5 Conclusion

In this paper, a new approach is presented to consider a nonlinear-input for model order reduction in thermal field problem. We have linearized the temperature dependent load vector, which allows the use of Krylov subspace based MOR. In future the linearization procedure will be investigated in more details.

References

1. Kerley, R. and Huang, X. and Ha, D.S. *Energy Harvesting from the Human Body and Powering up Implant Devices*, pages 147-180. Springer Netherlands, 2016.
2. Yang, Y. and Wei, X. and Liu, J. Suitability of a thermoelectric power generator for implantable medical electronic devices. *Journal of Physics D: Applied Physics*, 40(18):5790-5800, 2007.
3. Bechtold, T. and Rudnyi, E. and Korvink, J.G. Fast Simulation of Electro-Thermal MEMS: Efficient Dynamic Compact Models. Springer Verlag, Heidelberg, Series: MEMS and Microtechnology, 2006.
4. Rother, S. Load Snapshot Decomposition to Consider Heat Radiation in Thermal Model Order Reduction. *9th Vienna International Conference on Mathematical Modelling*, 2018.
5. Pennes, H. Analysis of Tissue and Arterial Blood Temperatures in the Resting Human Forearm. *Journal of Applied Physiology*, 1(2):93-122, 1948.
6. Freund, R. Krylov-subspace methods for reduced-order modeling in circuit simulation. *Journal of Computational and Applied Mathematics*, 123(1-2):395-421, 2000.

A Thermal Extension of Tellinen's Scalar Hysteresis Model

Jan Kühn, Andreas Bartel, and Piotr Putek

Bergische Universität Wuppertal, Gaußstraße 20, D-42119 Wuppertal, Germany
{kuehn,bartel,putek}@math.uni-wuppertal.de

Summary. First, a rough outline of Tellinen's scalar magnetic hysteresis model is presented. Special emphasis is laid upon the ideas and the realization. Second, these ideas are taken up and are extended w.r.t. thermal behavior. In the end, a temperature dependent scalar magnetic hysteresis model is derived and discussed.

1 Introduction and Motivation

In some situations, the thermal behavior of ferromagnetic material is a very important issue. Research shows a significant change of magnetic properties for increased temperature [1]. Several magnetic hysteresis models exist, but only some of them were extended to a temperature dependence (e.g. [2,3]). As far as we know, Tellinen's model [5] was not one of them. In comparison to other models, Tellinen's model is easy to understand, easy to implement and cheap to compute. Nevertheless, its simulation results are still competitive [4]. Another advantage of this model is its frugality w.r.t. the input parameters. We aim at retaining these properties within our thermal extension.

2 Tellinen's Hysteresis Model

In [5], a scalar magnetic hysteresis model is introduced. It is derived from phenomenological considerations and is based on the limiting hysteresis curves as sole input, which can be derived from measurements.

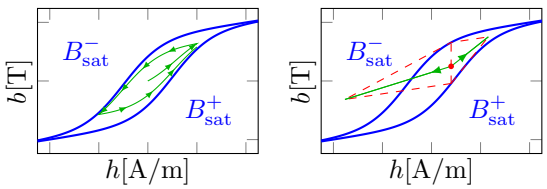

Fig. 1. a) Example of a limiting hysteresis curve (blue) and the resulting path starting from the origin (green).
b) Idea of Tellinen's model: limiting hysteresis curves B^+_{sat} and B^-_{sat} are in blue, the working point (h,b) in red and the resulting direction of change, i.e., $\frac{db}{dh}$, in green.

Input data. If a material is polarized strong enough, say magnetic field strength $h < 0$, it will be fully magnetically saturated. Then, increasing h results in a material specific relation between h and the magnetic flux density b, the saturation curve $B^+_{\mathrm{sat}}(h)$. The C^1-function $B^+_{\mathrm{sat}}(h)$ is the sole input of Tellinen's model, since the saturation curve for the opposite polarization is assumed to be given by $B^-_{\mathrm{sat}}(h) := -B^+_{\mathrm{sat}}(-h)$, see Fig. 1. It is assumed that it holds,

$$B^+_{\mathrm{sat}}(h) < B^-_{\mathrm{sat}}(h)\,, \quad \lim_{|h|\to\infty} B^-_{\mathrm{sat}}(h) - B^+_{\mathrm{sat}}(h) = 0, \quad (1)$$

i.e., B^+_{sat}, B^-_{sat} form a closed loop, see Fig. 1. Moreover, the derivative shall be bounded from below by μ_0

$$\tfrac{d}{dh}B^+_{\mathrm{sat}}(h) \geq \mu_0 > 0\,, \quad \lim_{|h|\to\infty} \tfrac{d}{dh}B^+_{\mathrm{sat}}(h) = \mu_0\,. \quad (2)$$

Due to (2), it is a model for ferromagnetic materials.
Realization. Now, Tellinen's model linearly interpolates the limiting saturation curves B^+_{sat} and B^-_{sat} at intermediate points in a particular way. To this end, let

$$I = \left\{(h,b) \in \mathbb{R}^2 \,\middle|\, B^+_{\mathrm{sat}}(h) \leq b \leq B^-_{\mathrm{sat}}(h)\right\} \quad (3)$$

denote the set of possible states. For any $(h,b) \in I$, the relative position between the boundaries is given by

$$\lambda = \frac{B^-_{\mathrm{sat}}(h) - b}{B^-_{\mathrm{sat}}(h) - B^+_{\mathrm{sat}}(h)} \in [0,1]. \quad (4)$$

For an increasing h, the derivative of b is defined by

$$\tfrac{db}{dh} = \lambda \tfrac{dB^+_{\mathrm{sat}}(h)}{dh} + (1-\lambda)\mu_0 \quad (5)$$

and for a decreasing h by

$$\tfrac{db}{dh} = \lambda\mu_0 + (1-\lambda)\tfrac{dB^-_{\mathrm{sat}}(h)}{dh}. \quad (6)$$

A physical motivation is given in [5]. By construction, the model respects the boundaries B^+_{sat} and B^-_{sat}, that is, an analytical solution (h,b), starting at $(h_0,b_0) \in I$ and calculated by (5) and (6), stays within I.

3 Thermal Extension of Hysteresis

Analogously to Tellinen's model, we describe the thermal extension via partial derivatives for the increasing and decreasing values. The behavior on the saturation surfaces is physically motivated and all intermediate points are approximated by linear interpolation.

Input data. A C^1-function $b = B^+_{\mathrm{sat}}(h,T)$ is needed that describes the saturation surface of b for a given field strength h and temperature T. Analogously to (1), (2) and (3), we define and assume

$$\frac{\partial}{\partial h}B^+_{\mathrm{sat}}(h,T) \geq \mu_0\,, \quad \lim_{|h|\to\infty}\frac{\partial}{\partial h}B^+_{\mathrm{sat}}(h,T) = \mu_0\,,$$
$$B^+_{\mathrm{sat}}(h,T) < B^-_{\mathrm{sat}}(h,T) := -B^+_{\mathrm{sat}}(-h,T)\,,$$
$$\lim_{|h|\to\infty} B^-_{\mathrm{sat}}(h,T) - B^+_{\mathrm{sat}}(h,T) = 0\,,$$
$$I_{\mathrm{T}} = \left\{(h,b,T)\in\mathbb{R}^3 \,\middle|\, B^+_{\mathrm{sat}}(h,T) \leq b \leq B^-_{\mathrm{sat}}(h,T)\right\}.$$

Physical motivation and modeling. The given, limiting $B^+_{\mathrm{sat}}(h,T)$ could be derived from measurements. For an increasing temperature, it can be argued that the system gains energy and therefore its state can be changed. Hence, in this case, the thermal extension tries to follow B^+_{sat} and B^-_{sat} as good as possible by using linear interpolation. Reducing the temperature of the material is equivalent to reducing its energy. Thus, the state of the material is frozen, whenever possible. But the working point (h,b,T) has to stay in I_{T}.
Computation. For $(h,b,T)\in I_{\mathrm{T}}$, the linear interpolation coefficient λ is given by (4) and the partial derivatives w.r.t. h by (5) and (6), where $B^{\pm}_{\mathrm{sat}}(h)$ is replaced by $B^{\pm}_{\mathrm{sat}}(h,T)$. For an increasing temperature change, i.e., $\partial T > 0$, this model assigns $b = b(h,T)$ using

$$\frac{\partial b}{\partial T} = \lambda\frac{\partial}{\partial T}B^+_{\mathrm{sat}}(h,T) + (1-\lambda)\frac{\partial}{\partial T}B^-_{\mathrm{sat}}(h,T) \quad (7)$$

and for a decreasing temperature change, i.e., $\partial T < 0$,

$$\begin{aligned}\tfrac{\partial b}{\partial T} =& \lambda\min\left(\tfrac{\partial}{\partial T}B^+_{\mathrm{sat}}(h,T),0\right) \\ &+ (1-\lambda)\max\left(\tfrac{\partial}{\partial T}B^-_{\mathrm{sat}}(h,T),0\right).\end{aligned} \quad (8)$$

See also Fig. 2. Eq. (8) respects $(h,b,T)\in I_{\mathrm{T}}$ by substituting the derivatives of B^+_{sat}, B^-_{sat} by zero, only if it is possible. Otherwise, measured values are used.
Properties. The definitions of the partial derivatives (7), (8) ensure that we stay in I_{T}, if solved analytically. In general, the thermal extension is non-reversible. Let assume h to be constant. Starting from (T_0,b_0), the temperature is increased to T_1 using (7). Then, T is decreased back to T_0 by (8). This yields the reversal point (T_1,b_1) and the endpoint (T_0,b_2). Generally, $b_0 \neq b_2$ holds, see Fig. 2. There exists exactly one stable loop, such that $b_0 = b_2$ holds, or all loops are stable. Every non-stable loop converges to the stable loop, if the temperature varies iteratively from T_0 to T_1 and back. In the special case of $h = 0$, this leads to a complete depolarization, i.e., b tends to zero. The boundaries $B^+_{\mathrm{sat}}(h,T)$, $B^-_{\mathrm{sat}}(h,T)$ are, in general, not monotone w.r.t. T. At first, an increase of the temperature may result in an increase of the magnetic saturation, but then, a decrease is observed (e.g. NdFeB [1]). So, a curvy shape as in Fig. 2 is possible, which emphasizes the necessity of a thermal model.

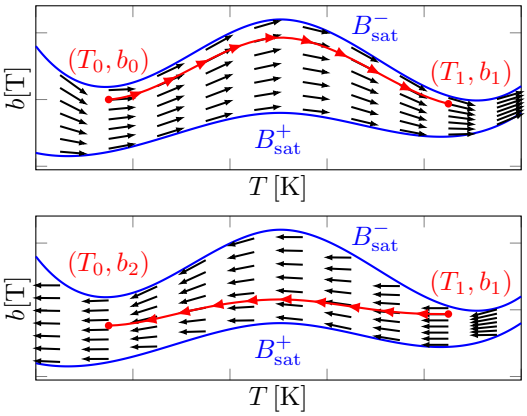

Fig. 2. Limiting saturation functions $B^+_{\mathrm{sat}}(h,T)$ and $B^-_{\mathrm{sat}}(h,T)$, for fixed h, are in blue. The arrows represent the assigned values of $\frac{\partial b}{\partial T}$ for an increase (upper plot) and decrease (lower plot) of the temperature T. The solution $b(h,T)|_{h=\text{const.}}$ for an increase of the temperature from T_0 to T_1 and decrease back to T_0 is shown is red.

Simulation. Our next step is to embed this extended model into a magnetic field simulation. Currently, we investigate an adjustment step after each time step of the magnetic field and temperature simulation. In this step, a modification of b with (7) and (8) is carried out. In particular, this yields the red curves in Fig. 2.

4 Conclusion

A scalar magnetic hysteresis model with temperature dependence was defined based on Tellinen's model. The objective of an easy understanding and implementation is fulfilled. A comparison to other thermal models is still pending and is part of further research.

References

1. M. Ghezelbash, S.M.R. Darbani, A.E. Majd, and A. Ghasemi. Temperature dependence of magnetic hysteresis loop of ndfeb with uniaxial anisotropy by libs technique. *J. Supercond. Nov. Magn.*, 30(7):1893–1898, 2017.
2. A. Raghunathan, Y. Melikhov, J.E. Snyder, and D.C. Jiles. Theoretical model of temperature dependence of hysteresis based on mean field theory. *IEEE Trans. on Magn.*, 46(6):1507–1510, 2010.
3. F. Sixdenier, O. Messal, A. Hilal, C. Martin, M.A. Raulet, and R. Scorretti. Temperature-dependent extension of a static hysteresis model. *IEEE Trans. Magn.*, 52(3):1–4, 2016.
4. S. Steentjes, K. Hameyer, D. Dolinar, and M. Petrun. Iron-loss and magnetic hysteresis under arbitrary waveforms in no electrical steel: A comparative study of hysteresis models. *IEEE Trans. Ind. Electron.*, 64(3):2511–2521, 2017.
5. J. Tellinen. A simple scalar model for magnetic hysteresis. *IEEE Trans. Magn.*, 34(4):2200–2206, 1998.

Optimized Schwarz methods for Helmholtz problems in a closed domain

Nicolas Marsic and Herbert De Gersem

Institut für Theorie Elektromagnetischer Felder, Technische Universität Darmstadt, Germany
{marsic,degersem}@temf.tu-darmstadt.de

Summary. In the last few years, many efforts have been made in developing optimized Schwarz methods for solving the Helmholtz equation. However, to the best of our knowledge, only open domains were considered. This abstract presents an analysis of the Schwarz method for closed geometries, *i.e.* resonators, and shows the limitations of state-of-the-art schemes designed for open problems.

1 Introduction

It is well known that large-scale time-harmonic wave problems are hard to solve. This is explained by two factors: *i)* the low convergence rate of iterative solvers, which comes from the oscillatory nature of the problem [3]; *ii)* the memory scaling limitations of direct solvers, which comes from the fill-in effect [4]. Domain decomposition methods are among the best candidates for tackling time-harmonic wave problems. Basically, these techniques couple direct and iterative strategies by: *i)* dividing the original problem into (potentially overlapping) small sub-problems amenable to direct solvers; *ii)* combining the sub-problems with an iterative approach.

One of the most famous domain decomposition method is the Schwarz algorithm. In recent years, many developments were made in optimizing this technique for Helmholtz problems [1–3]. However, to best of our knowledge, state-of-the-art optimized Schwarz methods for time-harmonic wave problems always assume an outgoing wave boundary condition. While this assumption is satisfied by a large number of applications (*e.g.* in scattering problems), it does not cover the field of resonant cavity design.

In this abstract, we propose to analyze the behavior of state-of-the-art optimized Schwarz methods for the Helmholtz equation, when they are applied to a closed geometry, and to highlight the major problem appearing in this context.

2 The non-overlapping Schwarz algorithm

Let us consider the following time-harmonic wave problem:

$$\begin{cases} \operatorname{div}\mathbf{grad}\, p + k^2 p = f & \text{on } \Omega, \\ p = 0 & \text{on } \Gamma, \end{cases}$$

where p is the unknown function, g a known source term, k the wavenumber, Ω the closed domain depicted in Fig. 1 and Γ its boundary. This problem can be solved by splitting the domain in two (or more) non-overlapping subdomains Ω_0 and Ω_1, and by using the following iterative scheme (indexed by n):

$$\begin{cases} \operatorname{div}\mathbf{grad}\, p_i^{n+1} + k^2 p_i^{n+1} = f & \text{on } \Omega_i, \\ \mathbf{n}_i \cdot \mathbf{grad}\, p_i^{n+1} + \mathscr{S}(p_i^{n+1}) = g_{ij} & \text{on } \Sigma_i, \\ p_i^{n+1} = 0 & \text{on } \Gamma, \end{cases}$$

where

- $\mathscr{S}$ is the so-called transmission operator of the optimized Schwarz algorithm;
- $i \in \{0,1\}$ and $j \in \{1,0\}$ for this two subdomains example;
- p_i^n is the solution of the iterative procedure at iteration n and on domain Ω_i;
- Σ_i designates the artificial boundary introduced in Ω_i by the splitting, as depicted in Fig. 1
- $\mathbf{n}_i$ refers to the outwardly oriented unit vector normal to Σ_i;

and with

$$g_{ij} = -\mathbf{n}_j \cdot \mathbf{grad}\, p_j^n + \mathscr{S}(p_j^n).$$

Once the Schwarz algorithm has converged, the solution p of the original problem is recovered by concatenating the solutions p_0 and p_1.

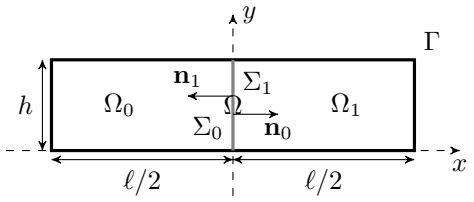

Fig. 1. Domain Ω.

It can be shown that the convergence rate of this numerical scheme is governed by the transmission operator $\mathscr{S}$, which is optimally the Dirichlet to Neumann map of the problem on Σ_i. Unfortunately, this optimal operator[1] cannot be used in practice, since

[1] Which in our case would lead to a convergence in two iterations.

it is non-local. Therefore, the design of an optimized Schwarz method relies on finding an accurate local approximation of the optimal operator $\mathscr{S}$.

3 Transmission operators

In the case of an open problem, it can be shown [3] that the optimal operator $\mathscr{S}$ is given by the symbol

$$\lambda_{\text{open}}(s) = \mathrm{i}\sqrt{k^2 - s^2},$$

which can be approximated by:
i) the constant value [2]

$$\lambda_{\text{open}}^{\text{const}} \approx \mathrm{i}k;$$

ii) a second order polynomial [3]

$$\lambda_{\text{open}}^{\text{poly}}(s) \approx a + bs;$$

iii) a rational Padé approximation [1]

$$\lambda_{\text{open}}^{\text{padé}}(s) \approx C_0 + \sum_{p=1}^{N_p} \frac{A_p s^2}{1 + B_p s^2};$$

where a, b, C_0, A_p and B_p are (possibly complex) constants coming from the polynomial and rational approximations.

In the case of the closed problem described in section 2, the aforementioned optimal transmission condition (and hence its localized approximations) is unfortunately not valid anymore. We showed that for closed domains with homogeneous Dirichlet boundary conditions, the symbol $\lambda_{\text{close}}(s)$ of the optimal operator writes:

$$\lambda_{\text{close}}(s) = \sqrt{k^2 - s^2}\cot\left(\sqrt{k^2 - s^2}\,\frac{\ell}{2}\right),$$

where ℓ the characteristic length of Ω as depicted in Fig. 1. In order to create a local approximation of this optimal symbol, many approaches can be followed.

4 Open transmission conditions for closed problems

In this work, we investigated the effectiveness of the following approximation:

$$\lambda_{\text{close}} \approx \lambda_{\text{open}},$$

this choice being motivated by the pragmatical argument that local approximations of λ_{open} are already implemented in finite element frameworks such as `GetDP`[2] or `FreeFEM++`[3]. In particular, we showed that the convergence radius $\rho(s)$ of the fixed-point Schwarz scheme, presented in section 2, writes:

$$\rho(s) = \begin{cases} 1 & \text{if } s^2 \leq k^2, \\ \exp\left[-\ell\sqrt{s^2 - k^2}\right] & \text{if } s^2 \geq k^2. \end{cases}$$

In other words, the convergence of the Schwarz algorithm is jeopardised by the propagating modes of the transmission condition. It is also worth noticing that when using the local approximations of λ_{open} (presented in section 3) the situation cannot be improved: modes such that $s^2 \leq k^2$ will lead to a stagnation or a divergence of the scheme, as showed in Fig. 2.

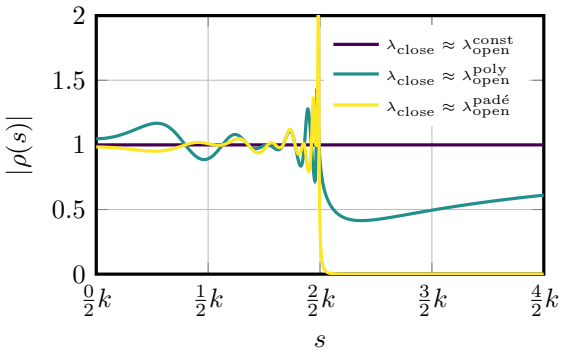

Fig. 2. Modulus of the convergence radius $\rho(s)$.

5 Rational approximation of λ_{close}

Of course, a more effective solution is to directly approximate $\lambda_{\text{close}}(s)$, and a rational approximation seems appropriate and is currently investigated.

References

1. Y. Boubendir, X. Antoine, and C. Geuzaine. A quasi-optimal non-overlapping domain decomposition algorithm for the Helmholtz equation. *Journal of Computational Physics*, 231(2):262–280, 2012.
2. B. Després. *Méthodes de décomposition de domaine pour les problèmes de propagation d'ondes en régime harmonique: le théorème de Borg pour l'équation de Hill vectorielle*. PhD thesis, Université de Paris IX, France, 1991.
3. M. J. Gander, F. Magoulès, and F. Nataf. Optimized Schwarz methods without overlap for the Helmholtz equation. *SIAM Journal on Scientific Computing*, 24(1):38–60, 2002.
4. J-Y. L'Excellent. *Multifrontal methods: parallelism, memory usage and numerical aspects*. Habilitation à diriger des recherches, École Normale Supérieure de Lyon, France, 2012.

[2] `getdp.info`
[3] `www.freefem.org`

A hydrodynamic model for 2D-3D electron transport in silicon devices

Giovanni Mascali[1] and Vittorio Romano[2]

[1] Università della Calabria, INFN-Gruppo c. Cosenza, Member of the INdAM research group GNFM, Dipartimento di Matematica ed Informatica, Rende 87036, Italia g.mascali@unical.it,
[2] Università di Catania, Member of the INdAM research group GNFM, Dipartimento di Matematica ed Informatica, Catania 95125, Italia romano@dmi.unict.it

Summary. The paper presents a hydrodynamic model for electron transport in a MOSFET channel. One of the main results is that the source terms due to all the principal scattering mechanisms of the 2D and 3D electrons are computed, which is extremely important, for example, for a correct determination of the electron mobility. In particular we consider the anisotropy of the scattering of the 2D electrons with the acoustic phonons, the scattering with the remote surface optical (SO) phonons of SiO_2 and that with surface roughness and impurities, this latter is considered also for the 3D electrons. Moreover, we furnish an expression for the part of the collision operator involving transitions from 2D electrons to 3D ones and vice versa, proving that the total number of electrons is conserved, as physically required.

1 Description of the model

In Metal Oxide Field Effect Transistors (MOSFETs), when the channel length is of the order of tents of nanometers, it is necessary to consider quantum effects for a correct description of the charge transport. In fact, large electric fields normal to the Si-SiO_2 interface causes the formation of potential wells, whose effect is that of confining charge carriers to a region close to the interface. Carriers are therefore free to move parallel to the interface, but are tightly confined in the direction normal to it. This confinement leads to quantized energy levels (see Figs. 1, 2).

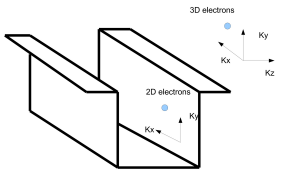

Fig. 1. Schematic representation of electron confinement in the z–direction due to a potential barrier

In order to reduce the computational burden, it is convenient to divide electrons in two populations: 3D

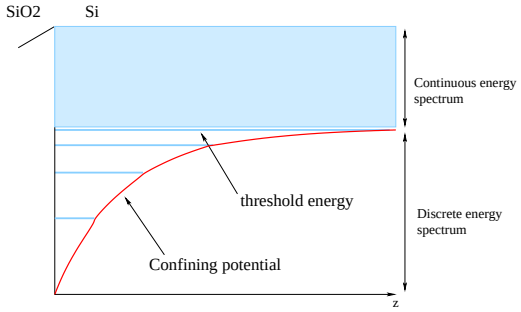

Fig. 2. Energy spectrum.

electrons, which are free to move in all the directions and 2D electrons that are confined in a plane. Near the silicon/oxide interface the two populations coexist, while in the remaining part of the device only the 3D component needs to be considered because quantum effects can be neglected there. It is possible to make a decomposition also in the momentum space, and consider electrons with energy higher than a suitable threshold value as 3D.

One of the main issues in the construction of a macroscopic model is to take into account the most important scattering mechanisms, in particular those which bring electrons from the 2D population to 3D one. Here, we propose a suitable adaptation to the macroscopic case of an approach introduced by Fischetti and Laux in the context of a Monte Carlo simulation [1]. We also prove that the proposed collision operators conserve the total number of electrons.

All the main scattering mechanisms are considered, among which those of electrons with the acoustic and non polar optical phonons, and those with the interface modes and impurities including the screening effects. For the acoustic scattering, the anisotropy effects are taken into account. The calculation of the 2D electrons energy levels is made using the effective mass approximation, and it is also assumed that the potential barrier is large enough that the envelope wave functions vanish at the Si/insulator interface and at the other boundary of the quantum region.

The 2D electrons are described by a Schrodinger–Poisson system coupled to a set of macroscopic transport equations for each subband population [2]. The

3D electrons are described by a macroscopic system of transport equations.

References

1. Fischetti, M. V. and Laux, S. E. 1993 *Monte Carlo study of electron transport in silicon inversion layers*. Phys. Rev. B, 48, 2244–2274.
2. Camiola, V. D., Mascali, G., and Romano, V. 2013 *Simulation of a double-gate MOSFET by a non-parabolic energy-transport model for semiconductors based on the maximum entropy principle*. Mathematical and Computer Modelling, 58, 321–343.

Direct simulation Monte Carlo of the Wigner transport equation

Orazio Muscato

Università degli Studi di Catania, Dipartimento di Matematica e Informatica orazio.muscato@unict.it,

Summary. The Wigner transport equation is solved by Direct Simulation Monte Carlo, based on the generation and annihilation of signed particles. In this framework, stochastic algorithms are derived using the theory of pure jump processes with a general state space. Numerical experiments on benchmark test cases are shown.

1 Introduction

The continuous scaling down of semiconductor devices is nowadays at a point, where active lengths are of the order of only a few tens of nanometers. Effects such as particle tunneling through source-to-drain potential profiles are now highly relevant and cannot be ignored. From this perspective, only full quantum models are capable of describing the appropriate physics. A well-known model is the Wigner equation which can be augmented by a Boltzmann-like collision operator accounting for the process of decoherence. The Wigner equation writes [5]:

$$\frac{\partial f_W}{\partial t} + \frac{\hbar}{m^*} k \cdot \nabla_x f_W = \mathcal{Q}(f_W) \tag{1}$$

$$\mathcal{Q}(f_W) = \int V_W(x, k-k') f_W(x,k')\, dk' \tag{2}$$

$$V_W(x,k) = \frac{1}{i\hbar(2\pi)^d} \times \tag{3}$$

$$\int dx'\, e^{-ik\cdot x'} \left[V\left(x + \frac{x'}{2}\right) - V\left(x - \frac{x'}{2}\right) \right] \tag{4}$$

where V_W is the Wigner potential, and $V(x)$ is the potential energy. The Wigner potential is a non-local potential operator which is responsible of the quantum transport, it is real-valued, and anti-symmetric with respect to k. The numerical solution of the Wigner equation can be obtained using high-order finite difference solvers [6]. To avoid discretization problems, particle Monte Carlo (MC) methods can be used (see [2] for a review), despite the large computational times. In the realm of the MC methods, the *Signed particle Monte Carlo approach* [4] seems to be the most promising, because it can be understood in a probabilistic framework [3]. In fact, the quantum evolution term (2) can be interpreted as a scattering mechanism where a new pair of particle, with real-valued opposite weight, is added to the system.

The main result is that appropriate functionals of this stochastic process satisfy a weak form of the Wigner equation. Moreover, this approach has certain advantages compared to other derivations. In particular, it suggests a variety of new algorithms as well as some of the algorithms previously considered in the literature. However, one should note that the grow of signed particles is exponential therefore showing the necessity for an annihilation process. Such process can be implemented by exploiting the fact that two particles with opposite signs and in the same phase-space cell have a total contribution to the Wigner function equal to zero (as they cancel out due to their opposite signs).

2 Simulation results

As benchmark, we have considered a one dimensional potential barrier with rectangular and gaussian shapes. The initial condition is a gaussian wavepacket. Since for pure states the Wigner and Schrödinger equations are completely equivalent, in figure 1 we have compared the MC mean density with that obtained using a high-order deterministic Schrödinger equation solver [1]. The agreement between the two mean densities is very good.

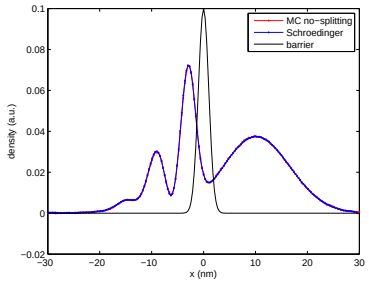

Fig. 1. The mean density versus position at simulation time 20 fsec.

Moreover a Resonant Tunneling Diode can be studied using this methodology and simulations results will shown during the conference.

References

1. S.A. Chin and C.R. Chen. Fourth order gradient symplectic integrator methods for solving the time-dependent schrödinger equation. *J. Chem. Phys.*, 114:7338–7341, 2001.
2. H. Kosina. Wigner function approach to nano device simulation. *Int. J. Comp. Scien. Engineer.*, 2(3-4):100–118, 2006.
3. O. Muscato and W. Wagner. A class of stochastic algorithms for the wigner equation. *SIAM J. Sci. Comput.*, 38(3):A1483–A1507, 2016.
4. M. Nedjalkov, H. Kosina, S. Selberherr, C. Ringhofer, and D. K. Ferry. Unified particle approach to Wigner-Boltzmann transport in small semiconductor devices. *Phys. Rev. B*, 70:115319, 2004.
5. D. Querlioz and P. Dollfus. *The Wigner Monte Carlo method for nanoelectronic devices*. Wiley, 2010.
6. S. Shao, T. Lu, and W. Cai. Adaptive conservative cell average spectral element methods for transient Wigner equation in quantum transport. *Comm. Comput. Phys.*, 9(3):711–739, 2011.

Simulation of double gate graphene field effect tansistors

Giovanni Nastasi[1] and Vittorio Romano[2]

[1] Department of Mathematics and Computer Science, Università degli Studi di Catania viale Andrea Doria 6, 95125 Catania, Italy g.nastasi@unict.it ,
[2] Department of Mathematics and Computer Science, Università degli Studi di Catania viale Andrea Doria 6, 95125 Catania, Italy romano@dmi.unict.it

Summary. Double gate graphene field effects transistors are simulated in the nanoscale case. The model is based on a system of drift-diffusion equations for electrons and holes. The numerical method is based on the Scharfettel and Gummel scheme. A special treatment of the Poisson equation is adopted for taking into account the charge in the graphene sheet. The characteristic curves for fixed gate voltages and for fixed sousrce drain voltage have been obtained.

1 Introduction

In the last years an increasing interest has been devoted to graphene field effect transistors (GFETs) as potential candidates for high-speed analog electronics, where transistor current gain is more important than ratio current ON/current OFF. Several type of GFET will be studied and optimized: top-gated graphene based transistor, obtained synthesizing graphene on silicon oxide wafer, and double gate GFETs.

For the simulation of charge transport in graphene, some simple drift-diffusion models are available in the literature. Recently, more accurate hydrodynamical models have been formulated [1–3] by exploiting the maximum entropy principle. Another approach is to get mobility models by simulations based on deterministic solutions of the semiclassical Boltzmann equation for electrons in graphene by using discontinuous Galerkin (DG) method or based on Monte Carlo simulations [4, 5].

Here we compare the results of the simulations for top-gated and double gate GFETs obtained with the above mentioned models. In particular, the characteristic curves will be studied.

2 Mathematical model

The mathematical model we adopt to simulate the charge transport in graphene is the bipolar drift-diffusion in 1D case,

$$\frac{\partial n}{\partial t} - \frac{1}{e}\frac{\partial}{\partial x}\left(\mu_n k_B T_L \frac{\partial n}{\partial x} - en\mu_n \frac{\partial \phi}{\partial x}\right) = 0,$$
$$\frac{\partial p}{\partial t} + \frac{1}{e}\frac{\partial}{\partial x}\left(-\mu_p k_B T_L \frac{\partial p}{\partial x} - ep\mu_p \frac{\partial \phi}{\partial x}\right) = 0,$$

where $n(t,x)$, $p(t,x)$ are the graphene electron density and hole density respectively, e is the positive elementary charge, k_B is the Boltzmann constant, T_L is the lattice temperature (kept constant), $\mu_n(x)$ and $\mu_p(x)$ are the mobility models for electrons and holes respectively and $\phi(x,y)$ is the electric potential. We adopt the mobility model proposed in ref. [6] given by

$$\mu_s(x) = \frac{v_s}{[1+(v_s E/v_{sat})^\gamma]^{1/\gamma}},$$

where $E = |\partial\phi/\partial x|$ is the absolute value of the x-component of the electric field, v_{sat} is the saturation velocity (we take the value 0.2 μm/ps), $\gamma \approx 2$ and

$$v_s(x) = \frac{\mu_0}{(1+s/n_{ref})^\alpha},$$

where $\mu_0 = 0.4650$ μm^2/V ps is the low field mobility, $n_{ref} = 1.1\times 10^5$ μm^{-2} and $\alpha = 2.2$. The symbol s indicates the carrier density: $s = n$ for electrons and $s = p$ for holes.

The 2D Poisson equation for the electric potential reads

$$\nabla\cdot(\varepsilon\nabla\phi) = h(x,y),$$

where

$$h(x,y) = \begin{cases} e(n(x)-p(x))/t_{gr} & \text{if} \quad y = y_{gr} \\ 0 & \text{if} \quad y \neq y_{gr} \end{cases}$$

being y_{gr} the y-coordinate of the graphene sheet (see Fig. 1), and ε is given by

$$\varepsilon(x,y) = \begin{cases} \varepsilon_{gr} & \text{if} \quad y = y_{gr} \\ \varepsilon_{ox} & \text{if} \quad y \neq y_{gr} \end{cases}$$

where ε_{gr} and ε_{ox} are the dielectric constants of the graphene and oxide respectively.

3 Numerical results

Here some preliminary results are plotted. The devices is depicted in Fig. 1. The length is 100 nm. The width of the lower oxide (SiO_2) is 10 nm while those of the upper oxide (SiO_2) is 5 nm. The source and drain contacts are long 25 nm. The two gate potential

are set as equal. At the metallic contacts the total voltage including the work function is considered equal to 0.25 V. Indeed it depends on the specific material the contacts are made of. In Fig. 2 the shape of the electrical potential is plotted when the gate-source potential is 0.3 V and the source-drain-potential is 0.4 V. The Fig. 3 shows the characteristic curve current versus gate voltage with source drain voltage equal to 0.2 V while Fig. 4 shows the current versus source drain voltage for several values of the gate voltage. Note that above the inversion voltage (0.25 V) the majority carriers are the electrons while below the inversion voltage the majority carriers are the holes. The behavior of the current is very different from the traditional semiconductors like Si or GaAs on account of the zero gap in the energy band. The major issue is the difficulty of fixing the off state which require an accurate calibration of the voltage.

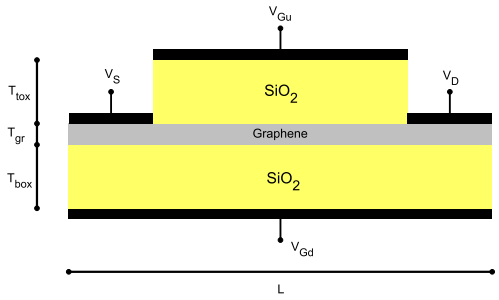

Fig. 1. Schematic representation of a GFET.

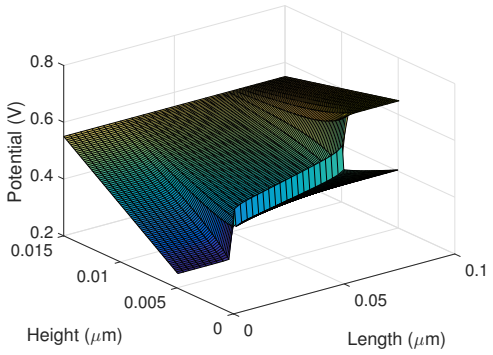

Fig. 2. Electrostatic potential when the gate-source potential is 0.3 V and the source-drain-potential is 0.4 V.

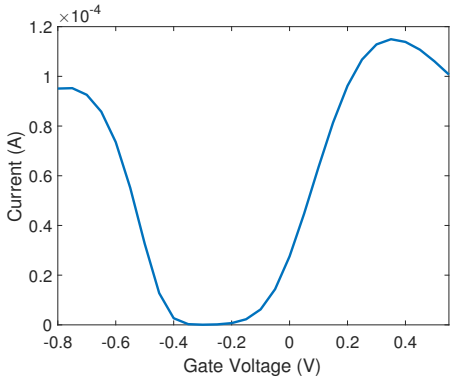

Fig. 3. Current versus gate voltage with source drain voltage equal to 0.2V.

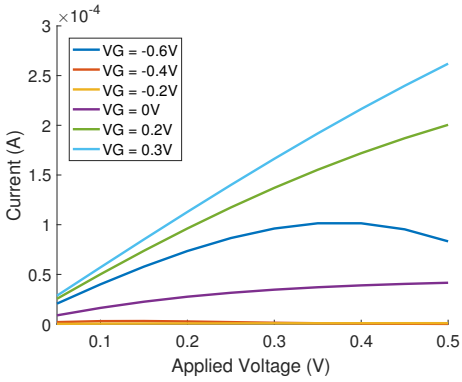

Fig. 4. Current versus source drain voltage for several values of the gate voltage.

References

1. V. D. Camiola, and V. Romano, *Hydrodynamical model for charge transport in graphene*, Journal of Statistical Physics 157, 1114–1137 (2014).
2. G. Mascali, V. Romano, *Charge Transport in graphene including thermal effects*, SIAM J. Appl. Mathematics 77, 593–613 (2017).
3. L. Luca, V. Romano, *Comparing linear and nonlinear hydrodynamical models for charge transport in graphene based on the Maximum Entropy Principle*, International Journal of Non-Linear Mechanics (2018).
4. V. Romano, A. Majorana, M. Coco, *DSMC method consistent with the Pauli exclusion principle and comparison with deterministic solutions for charge transport in graphene*, J. Comp. Physics 302, 267–284 (2015).
5. M. Coco, A. Majorana, V. Romano, *Cross validation of discontinuous Galerkin method and Monte Carlo simulations of charge transport in graphene on substrate*, Ricerche Mat. 66, 201–220 (2016).
6. V. E. Dorgan, M.-H. Bae, E. Pop, *Mobility and saturation velocity in graphene on SiO_2*, Appl. Phys. Lett. 97, 082112 (2010).

Semiconductor Optimization, Model Hierarchies & Asymptotic Analysis

René Pinnau[1]

TU Kaiserslautern, Department of Mathematics, 67663 Kaiserslautern, Germany, pinnau@mathematik.uni-kl.de

Summary. We present an overview of optimization models for semiconductor devices. In particular, we are going to focus on the asymptotic model hierarchy and how it can be exploited to speed-up the design cycle by tailored optimization algorithms. Further, we present analytical results which show how the different optimization problems are connected in the asymptotic limit.

1 Introduction

During the last decade there was an increasing demand for tailored optimization algorithms in the field of optimal semiconductor design (see, e.g., [1, 3, 5] and the references therein), which are now also used for the doping optimization of optoelectronic devices [4].

Due to the variety of semiconductor devices there are various models used for the appropriate device simulation and thus also for their optimization. An overview of the classical semiconductor model hierarchy is given in Figure 1. They range from the mesoscopic Boltzmann equation (c.f. [2] for an optimization approach) to the well-understood drift diffusion model.

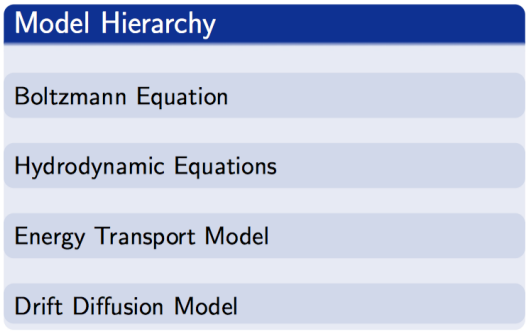

Fig. 1. Hierarchy of semiconductor models

The shrinking device sizes demand even for the usage of quantum models, which were also already used for optimization purposes (see [1] and the references therein).

Here, we are planning to give an overview on the numerical algorithms developed so far, as well as on some analytical results for the asymptotic analysis of semiconductor optimization models.

2 Numerical Semiconductor Optimization

The overall goal for the design of tailored optimization algorithms is that the numerical effort should be in the range of approximately ten forward simulations. Hence, black-box optimization cannot be used, since they normally scale with the number of design variables. To get around this problem, one needs to rely on methods for PDE constrained optimization which provide the necessary derivative information using the adjoint variables.

Such descent algorithms are meanwhile available for the various models in the hierarchy. They perform well and give satisfactory results. Available are first order algorithms as well as second order ones, which can be used for the optimization of doping profiles, e.g., in the on-state and/or the off-state of the device [1], the identification of parameters from measurements or other inverse problems, like LBIC.

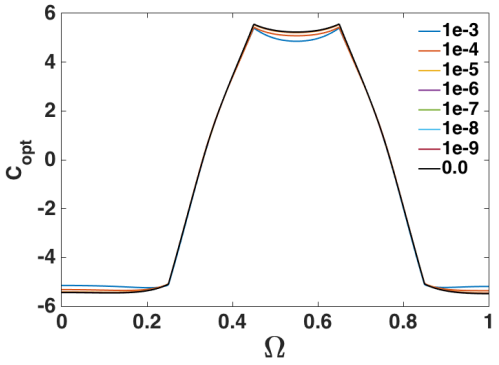

Fig. 2. Optimized Doping Profiles

Further, the convergence for more complex models can be accelerated by the usage of the so-called space-mapping technique, which also allows for an elegant coupling of optimization algorithms and commercial software packages. Here, one needs only evaluations of the more complex model, while the optimization loop is implemented for the simpler set of equations (see [3] and the references therein).

3 Asymptotic Analysis for Semiconductor Optimization Models

The very promising performance of the space-mapping technique suggests that there should be also an asymptotic connection of the semiconductor optimization models, which is already well established for the forward models.

The main challenge is here that the optimal solutions are in general not unique, such that one can only expect weak convergence in the spirit of Γ–convergence.

This shall be exemplified for the optimization of the nonlinear Poisson problem:

$$\min_{(V,C)} J(V,C), \quad \text{where}$$

$$J(V,C) = \frac{1}{2}\|n(V) - n_d\|_{L^2} + \frac{1}{2}\|p(V) - p_d\|_{L^2} + \frac{\gamma}{2}\|\nabla(C - \bar{C})\|_{L^2}$$

subject to

$$e_\lambda(V,C) := -\lambda^2 \Delta V - n(V) + p(V) + C = 0.$$

Here, the solutions depend on the scaled Debye length λ and it is a priori not clear if they will converge in the quasi-neutral limit. But exploiting a priori estimates, the concept of Γ–convergence and the equi-coercivity of the functionals one can prove the the convergence of minima and minimizers (for details see [5]). Hence, one gets an analogous results as for the quasi-neutral limit for the forward problem, which is summarized in Figure 3.

$$\begin{array}{ccc} (V_\lambda, C_\lambda) = \arg\min_{(V,C)} J(V,C) & \text{subject to} & e_\lambda(V_\lambda, C_\lambda) = 0 \\ \Big\downarrow \Gamma & & \Big\downarrow {\scriptstyle L^r,\ r \in [1,\infty)} \\ (V_0, C_0) = \arg\min_{(V,C)} J(V,C) & \text{subject to} & e_0(V_0, C_0) = 0 \end{array} \qquad \lambda \to 0$$

Fig. 3. Convergence diagramm

The analytical results are also confirmed by numerical simulations, which are depicted in Figure 4, where one can nicely observe the convergence of the optimized potentials V_λ in the limit $\lambda \to 0$.

These ideas were also extended to the semi-classical limit in an optimization problem for the quantum drift diffusion model, where one can also prove the convergence of minima and minimizers [1].

Acknowledgement. I would like to thank my coauthors for their valuable collaboration during the last years.

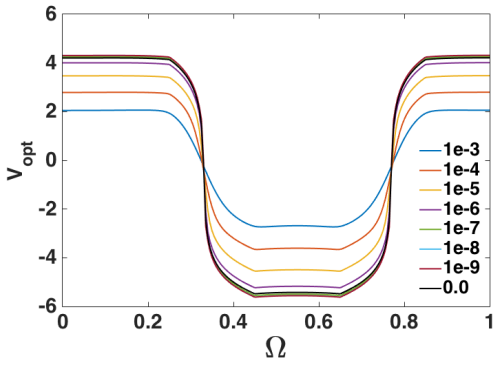

Fig. 4. Optimal potential V_λ for various values of λ

References

1. M. Burger, R. Pinnau, M. Fouego, and S. Rau. Optimal Control of Self-Consistent Classical and Quantum Particle Systems. In Trends in PDE Constrained Optimization (Vol. 165, pp. 455470). Birkhäuser, Cham, 2014.
2. Y. Cheng, I. Gamba, and K. Ren. Recovering doping profiles in semiconductor devices with the BoltzmannPoisson model. Journal of Computational Physics, 230(9), 3391-3412, 2011.
3. C.R .Drago, R. Pinnau. Optimal dopant profiling based on energy-transport semiconductor models. Mathematical Models and Methods in Applied Sciences, 18(02), 195-214, 2008.
4. D. Peschka, N. Rotundo, and M. Thomas. Doping optimization for optoelectronic devices. Optical and Quantum Electronics, 50(3), 63, 2017.
5. R. Pinnau, C. Totzeck, and O. Tse The quasi-neutral limit in optimal semiconductor design. SIAM Journal on Control and Optimization, 55(4), 2603-2635, 2017.

Frequency-domain integrals for stability preservation in model order reduction

Roland Pulch

Institut für Mathematik und Informatik, Universität Greifswald, Walther-Rathenau-Str. 47, D-17489 Greifswald, Germany.
roland.pulch@uni-greifswald.de

Summary. We examine projection-based model order reduction of Galerkin-type for linear dynamical systems. A transformation of the original system guarantees that any reduced system inherits asymptotic stability. The transformation matrix satisfies high-dimensional Lyapunov equations. We develop a frequency-domain approach, where the solution of the Lyapunov equations represents a matrix-valued integral. Consequently, quadrature methods yield approximations in numerical computations.

1 Projection-based Model Order Reduction

We consider linear time-invariant dynamical systems

$$\begin{aligned} \mathbf{E}\dot{\mathbf{x}}(t) &= \mathbf{A}\mathbf{x}(t) + \mathbf{B}\mathbf{u}(t) \\ \mathbf{y}(t) &= \mathbf{C}\mathbf{x}(t) \end{aligned} \tag{1}$$

with matrices $\mathbf{A}, \mathbf{E} \in \mathbb{R}^{n\times n}$, $\mathbf{B} \in \mathbb{R}^{n\times n_{\text{in}}}$, $\mathbf{C} \in \mathbb{R}^{n_{\text{out}}\times n}$. The state variables $\mathbf{x} : I \to \mathbb{R}^n$, the inputs $\mathbf{u} : I \to \mathbb{R}^{n_{\text{in}}}$ and the outputs $\mathbf{y} : I \to \mathbb{R}^{n_{\text{out}}}$ represent functions on a time interval $I = [t_0, t_{\text{end}}]$. Let the mass matrix $\mathbf{E}$ be non-singular, while generalisations to descriptor systems with a singular mass matrix are possible. We assume that the linear dynamical system (1) is asymptotically stable, i.e., all eigenvalues of the matrix pencil $\lambda\mathbf{E} - \mathbf{A}$ exhibit a negative real part.

The aim of model order reduction (MOR) is to construct a linear time-invariant dynamical system

$$\begin{aligned} \bar{\mathbf{E}}\dot{\bar{\mathbf{x}}}(t) &= \bar{\mathbf{A}}\bar{\mathbf{x}}(t) + \bar{\mathbf{B}}\mathbf{u}(t) \\ \bar{\mathbf{y}}(t) &= \bar{\mathbf{C}}\bar{\mathbf{x}}(t) \end{aligned} \tag{2}$$

with matrices $\bar{\mathbf{A}}, \bar{\mathbf{E}} \in \mathbb{R}^{r\times r}$, $\bar{\mathbf{B}} \in \mathbb{R}^{r\times n_{\text{in}}}$, $\bar{\mathbf{C}} \in \mathbb{R}^{n_{\text{out}}\times r}$ of much lower dimension $r \ll n$. Yet the outputs of (1) and (2) should agree, i.e., $\mathbf{y}(t) \approx \bar{\mathbf{y}}(t)$ for all $t \in I$.

In projection-based MOR, each approach determines two projection matrices $\mathbf{V}, \mathbf{W} \in \mathbb{R}^{n\times r}$ of full rank. We assume that $\mathbf{V}$ is an orthogonal matrix satisfying $\mathbf{V}^\top\mathbf{V} = \mathbf{I}_r$ with the identity matrix. The reduced matrices within the system (2) read as

$$\bar{\mathbf{A}} = \mathbf{W}^\top\mathbf{A}\mathbf{V},\ \bar{\mathbf{B}} = \mathbf{W}^\top\mathbf{B},\ \bar{\mathbf{C}} = \mathbf{C}\mathbf{V},\ \bar{\mathbf{E}} = \mathbf{W}^\top\mathbf{E}\mathbf{V}. \tag{3}$$

A Galerkin-type projection-based MOR is characterised by the choice $\mathbf{W} = \mathbf{V}$ in (3), where just an appropriate matrix $\mathbf{V}$ has to be determined. Well-known Galerkin techniques are, for example, the one-sided Arnoldi method and proper orthogonal decomposition (POD), see [1].

2 Stability Preservation

In many MOR methods, the reduced system (2) may be unstable, although the original system (1) is asymptotically stable. Several special techniques were constructed, which guarantee a stable reduced system.

If the matrix $\mathbf{E}$ is symmetric positive definite and the matrix $\mathbf{A}$ is dissipative ($\mathbf{A} + \mathbf{A}^\top$ is negative definite), then any Galerkin-type method yields an asymptotically stable system (2). Otherwise, the system (1) can be transformed to an equivalent system satisfying these properties, see [2,4].

The involved transformation matrix $\mathbf{M} \in \mathbb{R}^{n\times n}$ is symmetric positive definite and solves the generalised Lyapunov equation

$$\mathbf{A}^\top\mathbf{M}\mathbf{E} + \mathbf{E}^\top\mathbf{M}\mathbf{A} + \mathbf{F} = \mathbf{0}. \tag{4}$$

Any symmetric positive definite matrix $\mathbf{F}$ yields an admissible matrix $\mathbf{M}$. A reduction of the transformed system is equivalent to (3) with $\mathbf{W} = \mathbf{M}\mathbf{V}$, see [5].

A direct solution of (4) is not possible for high dimensions n due to a huge computational effort $O(n^3)$. Iterative techniques often produce low-rank factorisations

$$\mathbf{M} \approx \tilde{\mathbf{M}} = \mathbf{Z}\mathbf{Z}^\top \quad \text{with} \quad \mathbf{Z} \in \mathbb{R}^{n\times k} \tag{5}$$

and $k \ll n$. However, the approximation $\tilde{\mathbf{M}}$ is a singular matrix, which causes problems, cf. [5]. Furthermore, iterative methods like the ADI algorithm, for example, require a low-rank factorisation

$$\mathbf{F} = \mathbf{G}\mathbf{G}^\top \quad \text{with} \quad \mathbf{G} \in \mathbb{R}^{n\times \ell} \tag{6}$$

satisfying $\ell \ll n$, where $\mathbf{F}$ becomes just semi-definite.

3 Frequency-Domain Approach

Due to Parseval's theorem, we write the solution of the (generalised) Lyapunov equations (4) with (6) as matrix-valued integrals in the frequency-domain. It holds that

$$\mathbf{M} = \frac{1}{2\pi}\int_{-\infty}^{+\infty} \mathbf{S}(\omega)^{-1}\mathbf{G}\mathbf{G}^\top\mathbf{S}(\omega)^{-\mathrm{H}}\,\mathrm{d}\omega \tag{7}$$

including the matrix

$$\mathbf{S}(\omega) = \mathrm{i}\omega\mathbf{E}^\top - \mathbf{A}^\top \in \mathbb{C}^{n\times n}, \quad \mathrm{i} = \sqrt{-1}. \quad (8)$$

Phillips and Silveira [3] apply a quadrature rule with positive weights to compute an approximation of the integral (7). This approach yields a factorisation (5) of rank $k = q\ell$, where q is the number of nodes in the quadrature.

Alternatively, our idea is to apply the identity matrix $\mathbf{F} = \mathbf{I}_n$ in (4), which owns the trivial (high-rank) factorisation $\mathbf{F} = \mathbf{I}_n\mathbf{I}_n^\top$ ($\mathbf{G} = \mathbf{I}_n$) in (6). We assume large sparse matrices $\mathbf{A}, \mathbf{E}$. Thus the matrix (8) inherits this sparseness. However, the inverse matrices are dense in (7) and we never compute them explicitly. Since we do not need the matrix $\mathbf{M}$ but the matrix-vector product $\mathbf{MV}$, the integral (7) simplifies to

$$\mathbf{MV} = \frac{1}{\pi}\mathrm{Re}\left[\int_0^{+\infty} \mathbf{S}(\omega)^{-1}\mathbf{S}(\omega)^{-\mathrm{H}}\mathbf{V}\,\mathrm{d}\omega\right]. \quad (9)$$

Each evaluation of the integrand requires to solve complex-valued linear systems, where r right-hand sides appear with identical coefficient matrices. We investigate the efficient numerical solution of the linear systems in this context. Furthermore, the performance of quadrature rules is discussed.

4 Numerical Results for Test Example

In [7], a benchmark is a thermal model for a micro-thruster unit. A spatial discretisation of the heat transfer partial differential equation yields a linear dynamical system (1). The state space dimension is $n = 4257$. The number of inputs and outputs represents $n_{\mathrm{in}} = 1$ and $n_{\mathrm{out}} = 7$, respectively. This system is asymptotically stable with a spectral abscissa about -0.0013. The mass matrix $\mathbf{E}$ is diagonal with positive elements, whereas the matrix $\mathbf{A}$ is not dissipative.

We use the one-sided Arnoldi algorithm with a single real expansion point to generate reduced systems (2) via matrices (3). The reduced systems of dimension $r = 1, 2, \ldots, 100$ are arranged for the conventional choice $\mathbf{W} = \mathbf{V}$ as well as the transformed formulation $\mathbf{W} = \mathbf{MV}$ with (9). We compute the matrix-valued integrals (9) by an adaptive quadrature, see [6].

Figure 1 illustrates the spectral abscissa of the matrix pencils in the reduced systems. In the conventional technique, the spectral abscissa is larger than zero for 11 cases in the range $20 < r < 50$, i.e., stability is lost. Alternatively, the MOR using (9) always achieves a spectral abscissa below zero with a maximum about -0.0012 for all $r = 1, 2, \ldots, 100$.

For comparison, we calculate errors of the MORs based on the transfer functions H of the linear dynamical systems. Therein, we restrict the analysis to the first output of this benchmark. The relative error between full-order model and reduced-order model reads as $\varepsilon = \|H_{\mathrm{FOM}} - H_{\mathrm{ROM}}\|_{\mathscr{H}_2} / \|H_{\mathrm{FOM}}\|_{\mathscr{H}_2}$ using the $\mathscr{H}_2$-norm, see [1]. Figure 2 depicts the errors ε for the different reduced dimensions. We recognise that the application of the stabilisation technique does not deteriorate the MOR. Moreover, a smaller error often appears for lower dimensions.

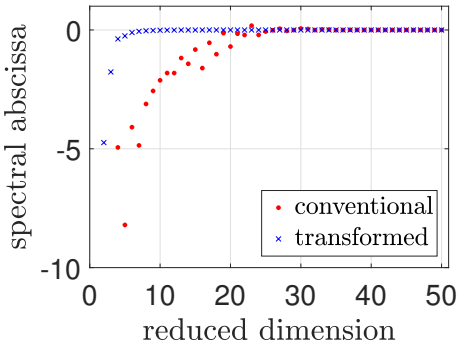

Fig. 1. Spectral abscissa of matrix pencils in reduced-order models for conventional system and transformed system.

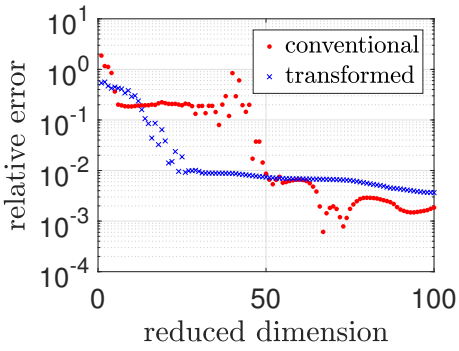

Fig. 2. Relative errors in $\mathscr{H}_2$-norm for MOR of conventional system and transformed system.

References

1. A.C. Antoulas. *Approximation of Large-Scale Dynamical Systems*. SIAM, Philadelphia, 2005.
2. R. Castañé Selga, B. Lohmann, and R. Eid. Stability preservation in projection-based model order reduction of large scale systems. *Eur. J. Control*, 18:122–132, 2012.
3. J.R. Phillips and L.M. Silveira. Poor man's TBR: A simple model reduction scheme. *IEEE Trans. Comput.-Aided Design Integr. Circuits Syst.*, 24:43–55, 2005.
4. S. Prajna. POD model reduction with stability guarantee. In *Proceedings of 42nd IEEE Conference on Decision and Control*, pp. 5254–5258, 2003.
5. R. Pulch. Stability preservation in Galerkin-type projection-based model order reduction. arXiv:1711.02912, 2017.
6. L.F. Shampine. Vectorized adaptive quadrature in MATLAB. *J. Comput. Appl. Math.*, 211:131–140, 2008.
7. MOR Wiki, `morwiki.mpi-magdeburg.mpg.de` online document, cited May 14, 2018.

Shape optimization of a permanent magnet synchronous machine under probabilistic constraints

Piotr Putek, E.Jan.W. ter Maten, and Michael Günther

Bergische Universität Wuppertal, Gaußstraße 20, D-42119 Wuppertal, Germany
{putek,termaten,guenther}@math.uni-wuppertal.de

Summary. This paper proposes a robust and reliability-based shape optimization method to find the optimal design of a permanent magnet (PM) synchronous machine. Specifically, a design of rotor poles and stator teeth are subjected to the shape optimization under manufacturing tolerances / imperfections and probabilistic constraints. In a forward problem, certain parameters are assumed to be random. This affects also a shape optimization problem, which is formulated in terms of a tracking-type robust cost functional and which is constrained by probabilistic constraints in order to attain a new desired, robust, design. The gradient is evaluated using the material derivative and the stochastic collocation method. In the end, to illustrate our approach, we provide the optimization results for a 2D model of the PM machine.

1 Introduction

With the rapid development of the performance of PM synchronous machines, they have become the main type of driving motors for electric vehicles due to such advantages as high efficiency in the whole working region and good dynamic performance.

Compared with the conventional surface-mounted PM synchronous machine, the ECPSM[1] has a wider speed range, because of the field-weakening and better output torque characteristics [3]. However, it typically suffers from the considerable high level of the cogging torque, which causes the undesired torque and speed ripples, and acoustic noise and vibrations.

Yet, as a result of manufacturing processes, a design of electric machines is strongly affected by the uncertainties in both, the geometrical and material parameters [5]. Thus, to provide the reliable simulations, a mathematical model with random input data needs to be considered [4]. This implies the use of the reliability analysis and the robust framework for a design assessment in order to investigate the risk of failure and variability of the output performance functions.

In our paper, we formulate the shape optimization in terms of both concepts. Therefore, we combine the reliability-based and the robust approach for a design of the ECPSM in order to attain its new topology, which meets both considered criteria.

[1] The Electrically Controlled Permanent Magnet Excited Synchronous Machine was investigated within the scientific project under grant no. N510 508040, Poland.

2 Stochastic Forward problem

Let a mathematical model be described by the nonlinear Poisson equation with q random input data $\mathbf{p}(\boldsymbol{\xi})$ in a two dimensional setting $\mathbf{x} \in D \subset \mathbb{R}^2$ with Lipschitz boundaries $\partial D \in C^2$. Then, for a magnetic vector potential $A = (0,0,u)$ and $\chi := (\mathbf{x}, \boldsymbol{\xi}) \in D \times \Gamma$, the weak form reads as: find $u \in V_\rho$ such that

$$\big(\nu(|\nabla u(\chi)|^2)\nabla u(\chi), \nabla\varphi(\chi)\big) = (f, \varphi(\chi)) \qquad (1)$$

for all $\varphi \in V_\rho$ with $V_\rho = L^2\left(H_0^1(\mathrm{D})\right) \otimes L^2_\rho(\Gamma)$. The function f is given by $f(\chi) = J(\chi) + \nu_{\mathrm{PM}}(\chi)\nabla\cdot\mathbf{M}(\chi)$, where J, $\mathbf{M}(\chi)$ and $\nu_{\mathrm{PM}}(\chi)$ denote the current density, the magnetization and the reluctivity of the PM, respectively. A random vector $\boldsymbol{\xi} = (\xi_1, \ldots, \xi_q)^\top$ is defined on some probability space $(\Gamma, \mathscr{B}^q, \rho d\mathbb{P})$ with Γ the image of the joint probabilistic density function ρ, $\mathscr{B}^q$ the q-dimensional Borel space and $\rho d\mathbb{P}$ a probabilistic measure, respectively.

The stochastic reluctivity model incl. the soft iron material $\nu(\mathbf{x}) : D \times \mathbb{R}_0^+ \to \mathbb{R}^+$ is given by [4]

$$\nu(\chi) = \begin{cases} \nu_{\mathrm{Fe}}(\mathbf{x}, |\nabla u(\chi)|^2)(1+\delta_1\xi_1) & \text{for } \mathbf{x} \in D_{\mathrm{rot}}, \\ \nu_{\mathrm{Fe}}(\mathbf{x}, |\nabla u(\chi)|^2)(1+\delta_1\xi_2) & \text{for } \mathbf{x} \in D_{\mathrm{sta}}, \\ \nu_0(\mathbf{x})(1+\delta_2\xi_3) & \text{for } \mathbf{x} \in D_{\mathrm{air}}, \\ \nu_{\mathrm{PM}}(\mathbf{x})(1+\delta_3\xi_4) & \text{for } \mathbf{x} \in D_{\mathrm{PM}}, \end{cases} \qquad (2)$$

with vaccum reluctivity ν_0 and the computational domain $D = D_{\mathrm{air}} \cup D_{\mathrm{PM}} \cup D_{\mathrm{rot}} \cup D_{\mathrm{sta}}$ composed of the area of air, the region of the PM and the iron domain for a rotor and a stator, respectively. We also consider $\mathbf{M}(\chi) = b_r(1+\delta_5\xi_5)\mathbf{T}(\mathbf{x})$, where b_r is the remanence flux density and $\mathbf{T}(\mathbf{x})$ denotes the magnetization direction. Scalings in (2) are $\delta_{1-4} = 0.15$ and $\delta_5 = 0.1$.

2.1 Reliability and Robustness Analysis

We use the First-Order Reliability Method (FORM) [7] to evaluate the reliability criteria.After transforming the selected random variables $\mathbf{r} \subset \mathbf{p}$ into the standard normal space by $\boldsymbol{\xi}_r = \mathbf{T}_{\xi_r}(\mathbf{r})$, the reliability index β is found by solving the constraint optimization problem

$$\beta^* = \min_{\boldsymbol{\xi}_r} \ \beta(\boldsymbol{\xi}_r) = \sqrt{(\boldsymbol{\xi}_r{}^\top \boldsymbol{\xi}_r)}$$
$$\text{s.t.} \quad g(\boldsymbol{\xi}_r, \cdot) = 0,$$

where $g(\boldsymbol{\xi}_r,\cdot)$ is a limit state function. The failure probability is approximated by $\mathbb{P}[g_k(\Omega,u(\cdot))\leq 0]\approx \Phi(-\beta)$, where $\Phi(\cdot)$ is the standard normal cumulative distribution function. In consequence, the resulting normalized vector $\boldsymbol{\xi}_r^*$ is used to modify the random vector $\mathbf{r}^*$, which influences the uncertainty quantification of a model (1). To this end, we model $\mathbf{p}(\boldsymbol{\xi})$ = $[\nu_{\text{Fe}}^{\text{sta}}(\xi_1),\ \nu_{\text{Fe}}^{\text{rot}}(\xi_2),\ \nu_{\text{air}}(\xi_3),\ \nu_{\text{PM}}^{*}(\xi_4),\ b_r^{*}(\xi_5)]$ using $\boldsymbol{\xi}$ as in (2). Then, under some assumptions [6], the polynomial chaos-based response surface model of u is given by

$$u(\mathbf{x};\mathbf{p}) \doteq \sum_{i=0}^{N} \alpha_i(\mathbf{x})\Psi_i(\mathbf{p}), \tag{3}$$

with a priori unknown coefficients α_i and corresponding basis polynomials Ψ_i with $\mathbb{E}[\Psi_i\Psi_j]=\delta_{ij}$, where $\mathbb{E}$ denotes the expected value. To calculate α_i, we combine a pseudo-spectral approach with the Stroud quadrature formula of order 3 [4, 6]. Finally, the statistical moments are approximated by

$$\mathbb{E}[u(\mathbf{x};\mathbf{p})] \doteq \alpha_0(\mathbf{x}), \mathrm{Var}[u(\mathbf{x};\mathbf{p})] \doteq \sum_{i=1}^{N} |\alpha_i(\mathbf{x})|^2, \tag{4}$$

assuming $\Psi_0 = 1$.

Similarly to the reliability-based topology method [2], the proposed algorithm does not contain the nested robust and reliability loops. For simplicity, we consider as the limit state function $f_{\text{PM}}(\boldsymbol{x}_c) = \nu_{\text{PM}}(\chi)\nabla\cdot \mathbf{M}(\chi)$ and the target reliability index $\beta_t = 3.8$, which corresponds to the failure probability $P_f = 10^{-4}$.

3 Shape Optimization Problem

For the cost functional with $\Omega = \Omega_{\text{PM}} \cup D_{\text{rot}} \cup D_{\text{sta}}$, defined in terms of the magnetic energy,

$$F(\Omega,u(\chi)) = \frac{1}{2}\int_D \nu|\nabla u(\chi)|^2 d\mathbf{x}, \tag{5}$$

the shape optimization problem is formulated as

$$\inf_{\Omega}\ \mathbb{E}\big[F(\Omega,u(\cdot))\big] + \iota\sqrt{\mathrm{Var}\big[F(\Omega,u(\cdot))\big]} \tag{6a}$$

$$\text{s.t.}\quad \beta(\cdot)\geq\beta_t, \tag{6b}$$

$$u \text{ satisfies (1)}, \tag{6c}$$

with $\iota = 3$. To solve the problem (6a)–(6c), we use the sensitivity-based algorithm [4]. The shape derivative of (6a) is given by

$$d\mathscr{J}(\Omega,u(\cdot)) = \big([\nu(|\nabla u(\cdot)|^2)-\nu_0]\nabla u(\cdot)\, V_{n_1}, \nabla\lambda(\cdot)\big)_{\partial D_1} - \big(\upsilon(\cdot)_{\text{PM}}\mathbf{M}(\cdot)V_{n_2}, \nabla\lambda(\cdot)\big)_{\partial D_2},$$

with $D_1 = D_{\text{rot}}\cup D_{\text{sta}}$ and $D_2 = D_{\text{PM}}$. Under some regularity conditions w.r.t. $F(\Omega,u(\cdot))$, an adjoint variable $\lambda\in V_\rho$ is the solution of the dual problem for $\phi\in V_\rho$

$$a(\lambda,\phi) = (d\mathbb{E}\big[F(\Omega,u(\cdot))\big] + \iota d\sqrt{\mathrm{Var}\big[F(\Omega,u(\cdot))\big]}, \phi),$$

where a bilinear form $a(\lambda,\phi)$ has been derived in [1].

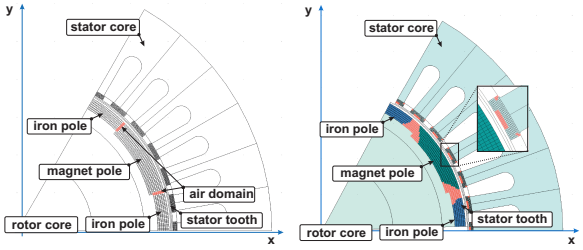

(a) initial configuration (b) optimal configuration

Fig. 1: ECPSM topology.

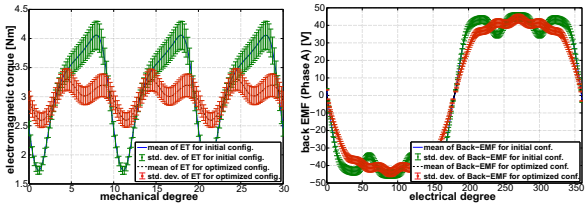

(a) electromagnetic torque (b) back electromotive force

Fig. 2: Statistical moments for ET and back EMF.

4 Conclusion

We integrated the reliability analysis and the robust framework to accomplish a new design of the ECPSM, shown in Fig. 1, which is resistant to input variations and satisfies safety criteria. This resulted in a decrease of statistical moments for the ET and the back EMF, depicted on Figs. 2b and 2, by 5%/7% and 21%/23% in *rms* sense, respectively.

References

1. I. Cimrák. Material and shape derivative method for quasi-linear elliptic systems with applications in inverse electromagnetic interface problems. *SIAM J. Numer. Anal.*, 50(3):1086–1110, 2012.
2. G. Kharmanda, N. Olhoff, A. Mohamed, and M. Lemaire. Reliability-based topology optimization. *Struct. Multidisc. Optim.*, 26(5):295–307, 2004.
3. P. Putek, P. Paplicki, and R. Paka. Low cogging torque design of permanent magnet machine using modified multi-level set method with total variation regularization. *IEEE Trans. on Magn.*, 50(2):657–660, 2014.
4. P. Putek, E.J.W. ter Maten, M. Günther, and J.K. Sykulski. Variance-based robust optimization of a permanent magnet synchronous machine. *IEEE Trans. on Magn.*, 54(3):1–4, 2018.
5. P. Sergeant, G. Crevecoeur, L. Dupré, and A. Van den Bossche. Characterization and optimization of a permanent magnet synchronous machine. *COMPEL*, 28(2):272–285, 2009.
6. D. Xiu. *Numerical methods for stochastic computations: A spectral method approach*. Princeton University Press, United States, 7 2010.
7. Y.G. Zhao and T. Ono. A general procedure for first/second-order reliability method (form/sorm). *Structural Safety*, 21(2):95 – 112, 1999.

Analysis and Numerical Solution of Piecewise Smooth Differential Algebraic Equations for Power Electronic Circuit Simulation

Jeroen Tant and Johan Driesen

KU Leuven - Energyville, Dept. Electrical Engineering, 3000 Leuven, Belgium
jeroen.tant@esat.kuleuven.be, johan.driesen@esat.kuleuven.be

Summary. Differential algebraic equations with piecewise smooth and possibly discontinuous equations are discussed. In power electronic circuit simulation, such equations result from modeling power semiconductor devices as controlled switches, as ideal diodes, or with piecewise smooth characteristics. With the ultimate goal of developing a piecewise smooth circuit simulation tool, this paper presents initial results on theoretical and numerical solution approaches and discusses the associated difficulties.

1 Introduction

One of the currently applied approaches for power electronic circuit simulation is to model power devices as ideal switches or with piecewise linear models [2,7,9]. Example tools include PSIM and PLECS. Such tools handle ideal switch events and transitions between segments of piecewise defined equations as non-smooth modifications of the circuit equations. A common solution technique is to advance the simulation with a numerical integration method until a switch event is encountered, rollback the solution with interpolation to the moment of switching, and modify the circuit equations accordingly after switching before continuing the simulation. There is usually only limited support for smooth nonlinear equations.

Another approach is to use compact behavioral semiconductor device models [5] in conventional circuit simulation tools such as SPICE or SABER. The highly nonlinear equations of such models are usually also piecewise defined, but they are made sufficiently smooth at transitions between segments to avoid convergence problems. Small simulation steps are needed to track switch transitions accurately and ensure convergence.

In this paper, the combination of both approaches is considered in the proposed framework of piecewise smooth differential algebraic equations (PWS DAEs).

2 Piecewise Smooth Differential Algebraic Equations

We consider DAEs of the semi-explicit form

$$\begin{aligned} \dot{\mathbf{x}} &= \mathbf{z}, \\ 0 &= g(\mathbf{x},\mathbf{y},\mathbf{z},\mathbf{u},\mathbf{v},\mathbf{w},\min(\mathbf{u},\mathbf{v}),\varphi(\mathbf{w})), \end{aligned} \tag{1}$$

where $\mathbf{x}$ are the dynamic variables and $\mathbf{y}$, $\mathbf{z}$, $\mathbf{u}$, $\mathbf{v}$, $\mathbf{w}$ are the algebraic variables, g is a smooth function, $\min(\mathbf{u},\mathbf{v})$ is the element-wise continuous piecewise defined minimum value operator

$$\min(u_i,v_i) = \begin{cases} u_i, & u_i \le v_i, \\ v_i, & u_i > v_i, \end{cases} \tag{2}$$

and $\varphi(\mathbf{w})$ is the element-wise discontinuous step function

$$\varphi(w_i) \in \begin{cases} \{0\}, & w_i < 0, \\ \{0,1\}, & w_i = 0, \\ \{1\}, & w_i > 0. \end{cases} \tag{3}$$

Following the ideas of [4], the introduction of the minimum value operator allows to model almost any continuous piecewise smooth function. The discontinuous step operator is introduced to enable the modeling of controlled switches.

Compared to classical piecewise smooth dynamical systems and ODEs with a discontinuous right hand side [1,3], the circuit DAE equations do not have to be reformed to an ODE representation. Compared to hybrid DAEs [8], the possible transitions between modes do not have to be enumerated. Compared to switched DAEs [6], the switch instants are implicitly determined and do not have to be known in advance. The full paper will discuss local solutions in the sense of Carathéodory, and continuous and discontinuous boundary crossings of the non-smooth operator modes. One of the associated difficulties is that the DAE index structure can change at such boundary crossings. Some examples are shown in Fig. 1.

3 Solution Approach

The numerical solution approach, to be discussed in the full paper, follows the block diagram of Fig. 2. At each boundary crossing of a discontinuous step operator, a new valid mode for all non-smooth operators must be determined and the algebraic variables must be reinitialized. This mode-selection and reinitialization problem involves solving static subsystems of piecewise smooth continuous equations, for which piecewise linearization techniques are explored [4]. The discontinuous operators are assumed to posses

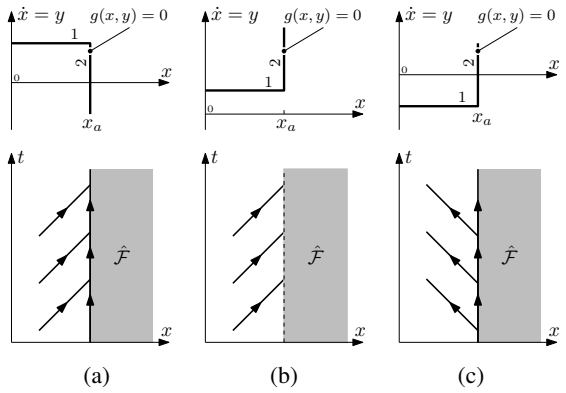

Fig. 1: Examples of PWS DAEs with forbidden region $\hat{\mathcal{F}}$. There is a unique local solution for $x_0 = x_a$ in (a), no solution for $x_0 = x_a$ in (b), and two local solutions for $x_0 = x_a$ in (c).

a specific structure so that they can be resolved sequentially. Once a valid operating mode is found, the equations can be solved as a regular smooth DAE with a numerical integration method until a boundary crossing event is encountered. An example solution is shown in Fig. 3.

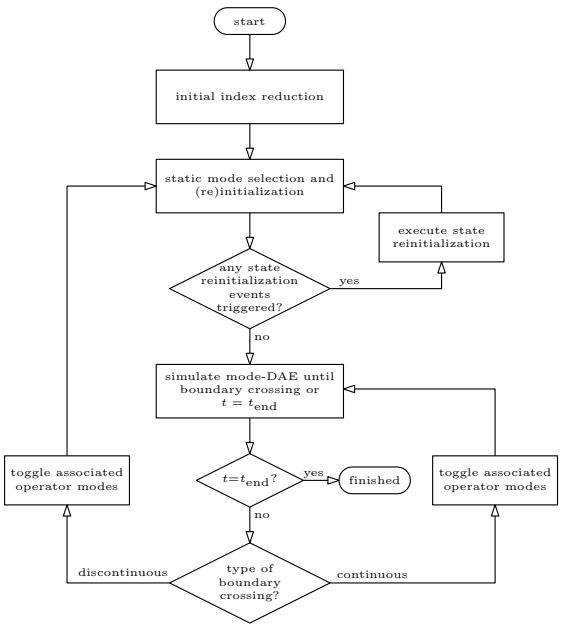

Fig. 2: Flowchart of the solution approach

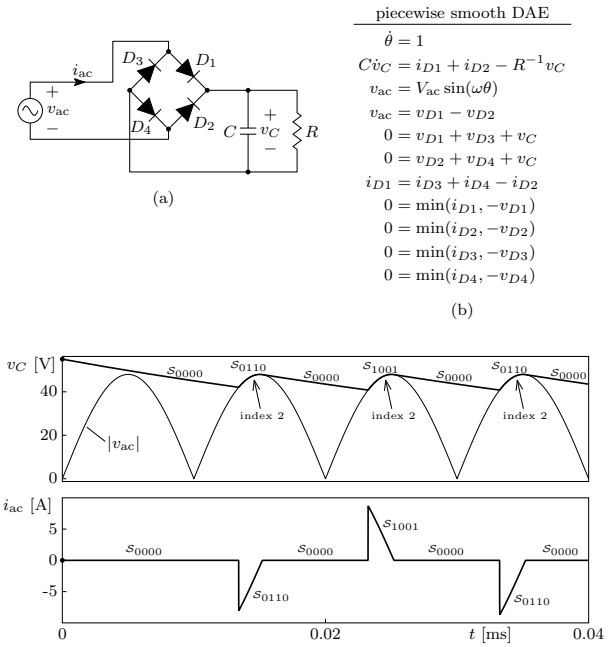

Fig. 3: Example of an ideal bridge rectifier (a) with piecewise smooth DAE (b) and waveform solution in (c).

References

1. Jorge Cortés. Discontinuous dynamical systems. *IEEE Control Syst. Mag.*, 28(3):36–73, 2008.
2. B. De Kelper, L. A. Dessaint, K. Al-Haddad, and H. Nakra. A comprehensive approach to fixed-step simulation of switched circuits. *IEEE Trans. Power Electron.*, 17(2):216–224, March 2002.
3. Carmina Georgescu, Bernard Brogliato, and Vincent Acary. Switching, relay and complementarity systems: A tutorial on their well-posedness and relationships. *Phys. D Nonlinear Phenom.*, 241(22):1985–2002, 2012.
4. Andreas Griewank. On stable piecewise linearization and generalized algorithmic differentiation. *Optim. Methods Softw.*, 28(6):1139–1178, 2013.
5. Rainer Kraus and H. J. Mattausch. Status and trends of power semiconductor device models for circuit simulation. *IEEE Trans. Power Electron.*, 13(3):452–465, May 1998.
6. Daniel Liberzon and Stephan Trenn. Switched nonlinear differential algebraic equations: Solution theory, lyapunov functions, and stability. *Automatica*, 48(5):954–963, 2012.
7. D. Maksimovic, A. M. Stankovic, V. J. Thottuvelil, and G. C. Verghese. Modeling and simulation of power electronic converters. *Proc. IEEE*, 89(6):898–912, June 2001.
8. Volker Mehrmann and Lena Wunderlich. Hybrid systems of differential-algebraic equations - analysis and numerical solution. *J. Process Control*, 19(8):1218–1228, 2009.
9. N Mohan, W P Robbins, T. M. Undeland, and R. Nilssen. Simulation of power electronic and motion control systems-an overview. *Proc. IEEE*, 82(8):1287–1302, 1994.

An Unbiased Hybrid Importance Sampling Monte Carlo Approach for Yield estimation in Electronic Circuit Design

A.K. Tyagi[1], X. Jonsson[2], T.G.J. Beelen[1], and W.H.A. Schilders[1]

[1] Department of Mathematics and Computer Science, Eindhoven University of Technology, Eindhoven (NL)
{a.k.tyagi, t.g.j.beelen, w.h.a.schilders}@tue.nl
[2] Mentor, A Siemens Business, Grenoble (FR) xavier_jonsson@mentor.com

Summary. Yield of an Integrated Circuit (IC) is commonly expressed as the fraction (in %) of working chips over all manufactured chips and often interpreted as the failure probability of its analog blocks. We consider the Importance Sampling Monte Carlo (ISMC) as a reference method for estimating tail probabilities. For situations where only a limited number of simulations is allowed, ISMC remains unattractive. In this case, we propose an unbiased hybrid Monte Carlo approach that provides a fast estimation of the probability. Hereby we use a combination of a surrogate model, ISMC technique and the stratified sampling.

Keywords: IC Design, Yield, Rare Events, Monte Carlo, Surrogate Model, Importance Sampling, Stratification

1 Introduction

Yield of an Integrated Circuit (IC) is commonly expressed as the fraction (in %) of working chips over all manufactured chips and often interpreted as the failure probability of its analog blocks such as memory bitcells, standard cells and analog IPs. To ensure a circuit will not degrade the yield of the IC, very low failure probabilities of $p_{\text{fail}} = 10^{-10}$ are needed.

When we estimate the probability of failure, it is done with some fixed environmental parameters (such as temperature, supply voltage and process corners). They can cause a lot of complexity. For instance, the failure probability must be computed for a large range of working temperatures. The complexity grows exponentially when the other dimensions are combined. For complex systems one usually can only afford a limited number (say, hundreds) of simulations, and therefore standard Monte Carlo (MC) method is not directly applicable and a variance reduction Importance Sampling (IS) technique remains unattractive. Then an effective hybrid ISMC (HISMC) approach is introduced in [3]. Here we propose an Unbiased-HISMC (UHISMC) approach which is identical to HISMC in the exploration but different in the estimation phase where we use the controlled stratified sampling as in [2].

2 Importance Sampling MC Technique

Let $\mathbf{X} \in \mathbb{R}^d$ be the input vector of the circuit under study and $\mathbf{x}$ a realization of $\mathbf{X}$, with probability density function $g(\mathbf{x})$, and let $H(\mathbf{X})$ be the corresponding response of the circuit. In importance sampling (IS) we sample from another distribution (from which the rare-events are generated) rather than the original. Let $g^{\boldsymbol{\theta}}(\mathbf{x})$ be the IS density function parameterized by its mean $\boldsymbol{\theta} \in \mathbb{R}^d$. Then the failure probability $p_{\text{fail}} = \mathbb{P}(H(\mathbf{X}) \geq \gamma)$ of the circuit is defined as

$$\begin{aligned} p_{\text{fail}} &= \mathbb{E}_g\left[\mathbb{1}_{(H(\mathbf{X})\geq\gamma)}\right] = \int \mathbb{1}_{(H(\mathbf{x})\geq\gamma)} g(\mathbf{x}) d\mathbf{x} \qquad (1)\\ &= \int \mathbb{1}_{(H(\mathbf{x})\geq\gamma)} \frac{g(\mathbf{x})}{g^{\boldsymbol{\theta}}(\mathbf{x})} g^{\boldsymbol{\theta}}(\mathbf{x}) d\mathbf{x} \\ &= \mathbb{E}_{g^{\boldsymbol{\theta}}}\left[\mathbb{1}_{(H(\mathbf{X}^{\boldsymbol{\theta}})\geq\gamma)} \frac{g(\mathbf{X}^{\boldsymbol{\theta}})}{g^{\boldsymbol{\theta}}(\mathbf{X}^{\boldsymbol{\theta}})}\right] \end{aligned}$$

where subscript g means that the expectation is taken with respect to the pdf $g(\mathbf{x})$, γ is a given failure threshold and $\mathbb{1}_{\{H(\mathbf{X})\geq\gamma\}}$ is an indicator function being 1 if $H(\mathbf{X}) \geq \gamma$, 0 otherwise.

Assuming $g(\mathbf{x})$ is standard Gaussian, we use $g^{\boldsymbol{\theta}}(\mathbf{x}) = g(\mathbf{x} - \boldsymbol{\theta})$ as in [1]. Then, the ISMC estimator of (1) can be computed by

$$\hat{p}_{\text{fail}}^{\text{IS}} = \frac{1}{N} \sum_{j=1}^{N} J(\mathbf{X}_j) \qquad (2)$$

where $J(\mathbf{X}) = \mathbb{1}_{(H(\mathbf{X}+\boldsymbol{\theta})\geq\gamma)}\, e^{-\boldsymbol{\theta}\mathbf{X} - \frac{|\boldsymbol{\theta}|^2}{2}}$, $\mathbf{X}_j$'s are N independent and identically random vectors distributed from the density $g(\mathbf{x})$ and $\boldsymbol{\theta}$ is unknown but that can be estimated by minimizing the variance $\text{Var}_{g^{\boldsymbol{\theta}}}[J(\mathbf{X})]$. For details we refer to [1, 3, 4].

3 Unbiased Hybrid Importance Sampling Monte Carlo Approach

In this section we propose a surrogate-based UHISMC approach. We use the IS technique and split it into two phases, the exploration and the estimation phase. In the exploration phase we estimate the mean-shift $\boldsymbol{\theta}$ by using a surrogate-based multi-level mean-shift

approach. For details, see [3, 4]. In the estimation phase we estimate the failure probability p_{fail} with the known $\boldsymbol{\theta}$ (from exploration phase). Moreover, we use a so called controlled stratified sampling (CSS) technique proposed in [2].

We partition the input space $\mathbb{R}^d$ into I mutually exclusive and exhaustive regions $D_1,\ldots,D_I$ called strata. To use stratified sampling we must know how to sample in each D_i. To this end we use a surrogate model to find the strata $D_i = \{\mathbf{X} : \hat{h}_{\rho_{i-1}} < \widehat{H}(\mathbf{X}) \leq \hat{h}_{\rho_i}\}$ where $\widehat{H}(\mathbf{X})$ is a surrogate prediction and $\hat{h}_{\rho_{i-1}}$ and $\hat{h}_{\rho_i}$ are quantiles $\widehat{H}(\mathbf{X})$ computed for $0 \leq \rho_{i-1} < \rho_i < 1$. Further, we sample in each stratum using an accept/reject criterion. The rough idea is to generate many realizations of a r.v. $\mathbf{X} \sim g(\mathbf{x})$, to evaluate the corresponding surrogate responses $\widehat{H}(\mathbf{X}^*)$ and to accept/reject the realizations depending on the responses $\widehat{H}(\mathbf{X}^*)$. The simulator response $H(\mathbf{X}^*)$ is then computed with the accepted realizations.

Let N be the total number of simulations from the simulator. We fix an allocation $N_1,\ldots,N_m$ of positive integers with $\sum_{i=1}^m N_i = N$. For each stratum i, we generate many realizations of the r.v. $\mathbf{X} \sim g(\mathbf{x})$ and accept N_i realizations $\left(\mathbf{X}_j^{(i)}\right)_{j=1,\ldots,N_j}$ among them such that the model predictions $\hat{H}\left(\mathbf{X}_j^{(i)} + \boldsymbol{\theta}\right)$ lie in the interval $(h_{\rho_{i-1}}, h_{\rho_j}]$. The true response $H\left(\mathbf{X}_j^{(i)} + \boldsymbol{\theta}\right)$ is computed for the accepted realizations. The conditional probability $P_i = \left\{\mathbb{E}_g\left[J(\mathbf{X}^{(i)})\right] : \mathbf{X}^{(i)} \in D_i\right\}$ is estimated for each i:

$$\hat{P}_i = \frac{1}{N_i}\sum_{j=1}^{N_i} J(\mathbf{X}_j^{(i)}) \tag{3a}$$

with the conditional variance of $\hat{P}_i$

$$\mathrm{Var}(\hat{P}_i) = \frac{\mathrm{Var}\left(J(\mathbf{X}_j^{(i)})\right)}{N_i} = \frac{\sigma_i^2}{N_i} \tag{3b}$$

Finally, the Importance Sampling Controlled Stratified (ISCS) probability estimator of p_{fail} is given by:

$$\hat{p}_{fail}^{ISCS} = \sum_{i=1}^{m} w_i \hat{P}_i \tag{4}$$

with $w_i = \mathbb{P}(\mathbf{X} \in D_i)$. For an optimal mean-shift $\boldsymbol{\theta}$, the estimator $\hat{p}_{fail}^{ISCS}$ is unbiased and follows the central limit theorem.

4 Results

Here, we present the results of a realistic circuit "VCO" with 1500 stochastic input parameters and scalar response 'oscillation frequency'. Our goal is to estimate the probability for the oscillation frequency to be larger than the given threshold $\gamma = 1900$.

Table 1. VCO: ISMC Versus HISMC Probability Estimation

Method	$\hat{p}_{fail}$	CV(%)	MSE	**#Runs**
ISMC	$\mathbf{1.10 \times 10^{-10}}$	**8.14**	2.34×10^{-23}	12000
UHISMC	$\mathbf{1.09 \times 10^{-10}}$	**6.16**	1.47×10^{-23}	2978

In Table 1, we compare the results for ISMC and UHISMC. '$\hat{p}_{fail}$', 'CV' and '#Runs' are the estimated probability, coefficient of variation and number of runs. They are the average of 100 experiments of per method. 'MSE' is the mean squared error $\left(\sum_{i=1}^{100}(\hat{p}_{fail\,i} - \hat{p}_{fail}^{ref})^2\right)$ where $\hat{p}_{fail}^{ref}$ refers to a reference probability computed with ISMC for a very small coefficient of variation. The efficiency of the UHISMC method with respect to the ISMC is computed as

$$\begin{aligned}\mathrm{Eff}(\mathrm{ISMC},\mathrm{UHISMC}) &= \frac{(\mathrm{MSE}\times\#\mathrm{Runs})\text{ in ISMC}}{(\mathrm{MSE}\times\#\mathrm{Runs})\text{ in UHISMC}} \\ &= \frac{2.34\times10^{-23}\times 12000}{1.47\times10^{-23}\times 2978} \approx 7\end{aligned}$$

So, ISMC requires about 7 times more simulations than UHISMC to achieve the same accuracy. Thus, UHISMC is preferred.

5 Conclusion

From the results above we can conclude that UHISMC is more efficient than ISMC. Moreover, UHISMC provides an unbiased estimator and follows the central limit theorem. Thus UHISMC is preferred over ISMC.

Acknowledgement. The first author is grateful to the financial support from the Marie Curie Action.

References

1. L. Ciampolini, J.-C. Lafont, F. T. Drissi, J.-P. Morin, D. Turgis, X. Jonsson, C. Descléves and J. Nguyen. Efficient yield estimation through generalized importance sampling with application to NBL-assisted SRAM bitcells. *Proceedings of the 35th International Conference on Computer-Aided Design*, Article No. 89, 2016.
2. C. Cannamela, J. Garnier and B. Iooss. Controlled Stratification for Quantile Estimation. *The Annals of Aplied Statistics*, 2(4):1554–580, 2008.
3. A.K. Tyagi, X.Jonsson, T.G.J. Beelen and W.H.A. Schilders. Hybrid Importance Sampling Monte Carlo Approach for Yield Estimation in Circuit Design. *Submitted to the Journal of Mathematics in Industry*, (Springer Open), January 2, 2018.
4. A.K. Tyagi, X.Jonsson, T.G.J. Beelen and W.H.A. Schilders. Speeding Up Rare Event Simulations Using Kriging Models. *In Proceedings of IEEE 21st Workshop on Signal and Power Integrity (SPI)*, IEEE, 2017.

Electromagnetic stimulation chambers for cartilage regeneration

Julius Zimmermann and Ursula van Rienen

Institute of General Electrical Engineering, University of Rostock, A.-Einstein-Str. 2, D-18059 Rostock
julius.zimmermann@uni-rostock.de, ursula.van-rienen@uni-rostock.de

Summary. Electromagnetic (EM) stimulation has been identified as a tool to enhance cartilage regeneration. It is a major goal to understand the influence of the applied EM fields on the cartilage cells, i.e. chondrocytes. We present ideas to compute the EM fields inside commonly used stimulation chambers and cells embedded in those chambers to shed light on the mechanisms leading to cell growth and eventually cartilage regeneration.

1 Introduction

In an ageing society, many people suffer from weak hyaline cartilage. Eventually, it leads to osteoarthritis, which is a painful disease. In the last years, the treatment of weakened cartilage tissue by electromagnetic fields awoke interest [8]. In general, there exist two options for tissue stimulation: direct stimulation, where the electrodes are in contact with the tissue, and capacitive coupling, where the electrodes are insulated. For the sake of biocompatibility, capacitive coupling is currently favored by medical researchers as no electrochemical reactions appear at the electrodes. Since the biological processes are mainly driven by the cells that maintain the tissue, the effect of the EM fields on them needs to be elucidated.

2 Theory

In case of low-frequency fields with negligible magnetic induction, the time-harmonic fields can be calculated by using the electro-quasistatic (EQS) approximation of Maxwell's equations. Since the EQS field is curl-free it may be determined from the Laplace equation via the scalar potential Φ:

$$\nabla\left(\left(\mathrm{i}\omega\varepsilon(\mathbf{r},\omega)+\sigma(\mathbf{r},\omega)\right)\nabla\Phi(\mathbf{r})\right)=0\ , \qquad (1)$$

where ω is the angular frequency, ε the permittivity and σ the conductivity. In general, the dielectric parameters ε and σ are material- and frequency-dependent properties. Since data for chondrocytes from the hyaline articular cartilage does not exist, the parameters for costal chondrocytes were taken from [6] and the frequency dependence was neglected in this preliminary study. The parameters are summarized in Table 1.

It has been shown that for cells the electric behaviour of the membrane can be described by the so-called impedance boundary condition [5]. In this case, the current density in the membrane consists only of the normal component, which is given by

$$j_n=\frac{(\sigma_\mathrm{m}+\mathrm{i}\omega\varepsilon_\mathrm{m}\varepsilon_0)\Delta\Phi}{d_\mathrm{m}}\ , \qquad (2)$$

where σ_m is the membrane conductivity, ε_m is its permittivity, $\Delta\Phi$ is the potential difference of its outer and inner surface and d_m is its thickness.

Table 1. Dielectric parameters for costal chondrocytes [6] and capacitively-coupled chamber [7].

	medium	membrane	cytoplasm
ε_r	80	59.05	60
$\sigma\,[\mathrm{Sm}^{-1}]$	1.5	$6.895\cdot10^{-5}$	0.16

3 Geometries and Modelling

An exemplary stimulation chamber is depicted in Fig. 1. This geometry can be fully discretized including a membrane of 5 nm, as described in [7]. For that, we used COMSOL Multiphysics (Version 5.3). By exploiting (2), the number of degrees of freedom can be reduced from 2,176,318 to 26,933. However, the usage of the boundary conditions turns out to be only justified if the conductivity of the membrane is large in comparison to that of the electrode's dielectric coating and small to that of the bulk medium.

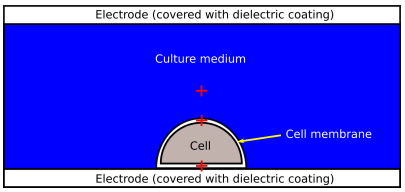

Fig. 1. Typical set up for a capacitive-coupling stimulation chamber [7].

4 Results

As a first approach, the study of Taghian *et al.* [7] was adapted. After introducing the parameters measured for chondrocytes, the observed induced membrane potential was remarkably different from the values previously reported. A main reason is that in comparison to [7] a non-zero membrane conductivity is imposed, which has a crucial effect (see Fig. 2). For low or even zero membrane conductivity a potential difference is already induced at low frequencies [7].

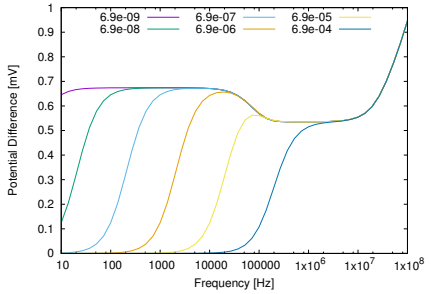

Fig. 2. Potential difference $\Delta\Phi$ for various values of the membrane conductivity σ_m for the chamber shown in Fig. 1.

In addition, a 3D model, where the cell is not in close contact with the substrate, shows a similar behaviour. However, the induced potential differences are smaller than previously and increase only at higher frequencies.

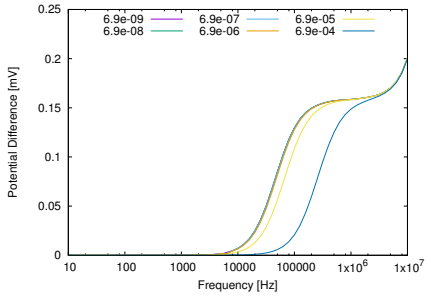

Fig. 3. Potential difference $\Delta\Phi$ at the membrane apex for different values of σ_m for a spherical cell placed in a 3D model of the chamber shown in Fig. 1.

The effect at 60 kHz is of paramount interest as this frequency has been used in experiments already [2]. Following [4], the power input can be estimated for a 5 nm membrane to be around 48 kWm^{-3} for the parameters given in Table 1. This yields a maximal temperature increase in the membrane during a 60 s treatment of around 1.3 K assuming thermal properties for fat [3], building the major component of membranes, and neglecting heat flow.

5 Discussion

The obtained results suggest that a potential difference along the cell membrane is induced from a certain frequency on, which depends on the membrane conductivity as well as on the cell shape. With regard to the low values (less than a mV), it is an open question whether the induced membrane potential is sufficient to trigger e.g. voltage-gated channels. Regarding the long exposure times up to some hours [2], a temperature increase in the cell membrane could be crucial.

6 Outlook

The simulations will be applied on stimulation chambers developed by cooperation partners in the CRC 1270 ELAINE. Moreover, multiphysics models involving e.g. heat transfer are to be developed. The implementation of an open-source solution that relies on a SALOME - GMSH - FEniCS workflow for CAD, meshing and solving (1) is planned [1].

Acknowledgement. This research was supported by the DFG (German Research Foundation) Collaborative Research Centre 1270 ELAINE.

References

1. B. E. Abali. *Computational Reality: Solving Nonlinear and Coupled Problems in Continuum Mechanics*. Number 55 in Advanced Structured Materials. Springer, Singapore, 2017.
2. C.T. Brighton, W. Wang, and C.C. Clark. The effect of electrical fields on gene and protein expression in human osteoarthritic cartilage explants. *J. Bone Joint Surg. Am.*, 90:833–848, 2008.
3. P.A. Hasgall et al. IT'IS Database for thermal and electromagnetic parameters of biological tissues - Version 3.0. https://www.itis.ethz.ch/virtual-population/tissue-properties/overview/. accessed on 09.05.2018.
4. T. Kotnik and D. Miklavčič. Theoretical evaluation of the distributed power dissipation in biological cells exposed to electric field. *Bioelectromagnetics*, 21:385–394, 2000.
5. G. Pucihar, T. Kotnik, B. Valič, and D. Miklavčič. Numerical determination of transmembrane voltage induced on irregularly shaped cells. *Ann Biomed Eng*, 34(4):642–652, 2006.
6. M. W. Stacey, A. C. Sabuncu, and A. Beskok. Dielectric characterization of costal cartilage chondrocytes. *BBA - General Subjects*, 1840(1):146–152, 2014.
7. T. Taghian, D. A. Narmoneva, and A. B. Kogan. Modulation of cell function by electric field: a high-resolution analysis. *J. Royal Soc. Interface*, 12(107):20150153–20150153, 2015.
8. G. Thrivikraman, S. K. Boda, and B. Basu. Unraveling the mechanistic effects of electric field stimulation towards directing stem cell fate and function: A tissue engineering perspective. *Biomaterials*, 150:60–86, 2018.

Part IV

Abstracts of Poster Session

On a Bloch-type model with electron–phonon interactions: modeling and numerical simulations

B. Bidégaray-Fesquet[1], C. Jourdana[1], and K. Keita[2]

[1] Univ. Grenoble Alpes, CNRS, Grenoble INP[†], LJK, 38000 Grenoble, France
[†] Institute of Engineering Univ. Grenoble Alpes
brigitte.bidegaray@univ-grenoble-alpes.fr,
clement.jourdana@univ-grenoble-alpes.fr
[2] Univ. Jean Lorougnon Guédé (UJLoG), 2 BP V 25 DALOA 12, Ivory Coast keitakole96@gmail.com

Summary. In this work, we discuss how to take into account electron–phonon interactions in a Bloch type model for the description of quantum dots. The model consists in coupling an equation on the density matrix with a set of equations on quantities called phonon-assisted densities, one for each phonon mode. At a first look, the scattering terms introduce a relaxation behaviour. After a description of the model, we discuss how to discretize efficiently this non-linear coupling in view of numerical simulations.

1 Bloch model

1.1 Quantum dot description

Quantum dots are usually described using electrons and holes. As detailed in [1], we prefer a conduction and valence electron description, where valence electrons can be seen as an absence of holes in a valence band. Due to the 3D confinement, energy levels are quantized for each species of electrons and can be indexed by integers. We denote respectively $(\varepsilon_j^c)_{j\in\mathscr{J}^c}$ and $(\varepsilon_j^v)_{j\in\mathscr{J}^v}$ the conduction and valence energy levels.

To describe the time evolution of the energy level occupations, we define a global density matrix by

$$\rho = \begin{pmatrix} \rho^c & \rho^{cv} \\ \rho^{vc} & \rho^v \end{pmatrix}.$$

ρ^c and ρ^v are respectively the conduction and valence densities. Their diagonal terms, called populations, are the occupation probabilities and their off-diagonal terms, called coherences, describe the intra-band transitions. Finally, ρ^{cv} and $\rho^{vc} = \rho^{cv^*}$ (A^* denoting the Hermitian matrix of a matrix A) describe the inter-band transitions.

The time-evolution of ρ can be driven by a free electron Hamiltonian associated to electron level energies and the interaction with an electromagnetic wave (see e.g. [1] for details):

$$i\hbar\partial_t\rho = [E_0 + \mathbf{E}\cdot\mathbf{M}, \rho], \tag{1}$$

where $[A,B]$ denotes the commutator $AB-BA$, $E_0 = \mathrm{diag}(\{\varepsilon_j^c\},\{\varepsilon_j^v\})$, $\mathbf{M}$ is the dipolar moment matrix (a matrix that can be expressed in terms of the wave functions associated to each energy level) and $\mathbf{E}$ is a time-dependent electric field.

To study the interaction of the quantum dot with an electromagnetic field, equation (1) can be coupled with Maxwell equations:

$$\partial_t\mathbf{E} = c^2\,\mathrm{curl}\,\mathbf{B} - \mu_0 c^2\mathbf{J}, \tag{2}$$
$$\partial_t\mathbf{B} = -\,\mathrm{curl}\,\mathbf{E}, \tag{3}$$

$\mathbf{B}$ being the magnetic field, c the speed of light in free space and μ_0 the vacuum permeability. The coupling is expressed via the current density $\mathbf{J}$ which is given by

$$\mathbf{J} = n_a\,\mathrm{Tr}(\mathbf{M}\partial_t\rho)$$

where n_a is the quantum dot volume density.

Equation (1) is a Liouville equation and it confers a certain number of properties to the solution that have already been extensively studied in the literature. Here, we focus on the addition of electron–phonon (e–ph) interactions in such a model.

1.2 Electron–phonon Hamiltonian

As in [2] where the addition of Coulomb interactions is discussed, the starting point is to use field quantification to write an e–ph Hamiltonian. We write it in the form $H^{c-ph}+H^{v-ph}$. It implies that e–ph interactions cannot lead the electron to change species. In this work, only polar coupling to optical phonons is considered since it usually leads to the fastest dynamics in low excitation regime. The corresponding Frölich interaction Hamiltonian is given by (see e.g. [4]):

$$H^{c-ph} = \int_{\mathscr{B}} \sum_{\alpha,\alpha'\in\mathscr{J}^c} G^c_{\mathbf{q},\alpha,\alpha'} c^\dagger_\alpha \left(b_{\mathbf{q}} + b^\dagger_{-\mathbf{q}}\right) c_{\alpha'}\mathrm{d}\mathbf{q} \tag{4}$$

$$H^{v-ph} = \int_{\mathscr{B}} \sum_{\alpha,\alpha'\in\mathscr{J}^v} G^v_{\mathbf{q},\alpha,\alpha'} v^\dagger_\alpha \left(b_{\mathbf{q}} + b^\dagger_{-\mathbf{q}}\right) v_{\alpha'}\mathrm{d}\mathbf{q} \tag{5}$$

$c_j^\dagger$ and c_j (resp. $v_j^\dagger$ and v_j) are creation and annihilation operators for conduction (resp. valence) electrons and $b_{\mathbf{q}}^\dagger$ and $b_{\mathbf{q}}$ are those for phonons, where the phonon mode $\mathbf{q}$ belongs to the Brillouin zone $\mathscr{B}$ of

the underlying crystal. For $e \in \{c,v\}$, $G^e_{\mathbf{q}}$ is a matrix whose coefficients are expressed in terms of the wave functions associated to each energy level:

$$G^e_{\mathbf{q},\alpha,\alpha'} = \mathscr{E}_{\mathbf{q}} \int \psi^{e*}_{\alpha}(\mathbf{r}) \exp(i\mathbf{q}\cdot\mathbf{r}) \psi^{e}_{\alpha'}(\mathbf{r}) \mathrm{d}\mathbf{r},$$

$\mathscr{E}_{\mathbf{q}}$ being the Frölich constant [4] defined such that $G^{e*}_{\mathbf{q}} = G^e_{-\mathbf{q}}$. Finally, optical phonons are almost dispersionless and for simplicity a constant phonon energy $E_{\mathbf{q}}$ will be assumed in the sequel.

1.3 Phonon-assisted densities and time evolution

As in [3], we introduce phonon-assisted density matrices

$$S_{\mathbf{q}} = \begin{pmatrix} S^{cc}_{\mathbf{q}} & S^{cv}_{\mathbf{q}} \\ S^{vc}_{\mathbf{q}} & S^{vv}_{\mathbf{q}} \end{pmatrix}$$

where $S^{ef}_{\mathbf{q},\alpha,\alpha'} = \left\langle f^{\dagger}_{\alpha'} b_{\mathbf{q}} e_{\alpha} \right\rangle$, $e,f \in \{c,v\}$. Then, the time evolution of the density matrix due to e–ph interaction can be cast in a very compact form as

$$i\hbar\partial_t \rho|_{e-ph} = \int_{\mathscr{B}} [G_{\mathbf{q}}, S_{\mathbf{q}} + S^*_{-\mathbf{q}}] \mathrm{d}\mathbf{q} \equiv P(S). \qquad (6)$$

where we have introduced the notations

$$G_{\mathbf{q}} = \begin{pmatrix} G^c_{\mathbf{q}} & 0 \\ 0 & G^v_{\mathbf{q}} \end{pmatrix} \text{ and } S = \{S_{\mathbf{q}},\ \mathbf{q} \in \mathscr{B}\}.$$

$P(S)^* = -P(S)$ independently of the structure of S. Therefore ρ, which is initially Hermitian, remains Hermitian through time evolution via (6). This equation is also trace preserving since the right-hand side is a combination of trace-free commutators.

To close the system, we now look for the time evolution of phonon-assisted densities. After making explicit the commutators between the e–ph interaction Hamiltonian and other Hamiltonians involved in the system and using the Wick theorem to approximate the means involving four operators, we finally obtain, for each $\mathbf{q} \in \mathscr{B}$, the following equation

$$\begin{aligned} i\hbar\partial_t S_{\mathbf{q}}|_{e-ph} &= E_{\mathbf{q}} S_{\mathbf{q}} + \frac{1}{2}\{G^*_{\mathbf{q}}, \rho\} + (\frac{1}{2} + n_{\mathbf{q}})[G^*_{\mathbf{q}}, \rho] \\ &\quad + C(\rho, G^*_{\mathbf{q}}) \equiv E_{\mathbf{q}} S_{\mathbf{q}} + Q(\rho). \end{aligned} \qquad (7)$$

$\{A,B\}$ denotes the skew-commutator $AB+BA$, $n_{\mathbf{q}}$ is the phonon density expressed in terms of the phonon energy $E_{\mathbf{q}}$ by the Bose–Einstein statistics, and $C(\rho, G^*_{\mathbf{q}})$ is a non-linear term expressed as

$$C(\rho, G^*_{\mathbf{q}}) = -\widetilde{\rho} G^*_{\mathbf{q}} \widetilde{\rho} + \mathrm{Tr}(G^*_{\mathbf{q}} \widetilde{\rho}) \widetilde{\rho}$$

where $\widetilde{\rho} = \rho \begin{pmatrix} I^c & 0 \\ 0 & -I^v \end{pmatrix}$, I^c and I^v being the identity matrices for the conduction and valence spaces.

To summarize, introducing the e–ph interaction in the Bloch equation (1) leads to the system

$$i\hbar\partial_t \rho = [E_0 + \mathbf{E}\cdot\mathbf{M}, \rho] + P(S), \qquad (8)$$

$$i\hbar\partial_t S_{\mathbf{q}} = E_{\mathbf{q}} S_{\mathbf{q}} + [E_0 + \mathbf{E}\cdot\mathbf{M}, S_{\mathbf{q}}] + Q(\rho). \qquad (9)$$

2 Numerical simulations

For simulations, we consider a collection of quantum dots which are scattered in a one dimensional space and interact not directly but through the interaction with the electromagnetic field. So, densities depend on time and space and the e–ph Bloch model (8-9) is coupled with Maxwell equations (2-3).

First, we introduce a discretization of phonon modes using N_q points. The integral over $\mathbf{q}$ in (6) is approximated by a simple quadrature formula and consequently the global phonon-assisted density S is computed solving N_q independent equations (9).

A finite difference Yee scheme is used for Maxwell equations. Equations (8-9) are discretized working on a staggered grid in time and each equation is solved using a Strang splitting procedure. For instance, the three different terms in the right hand side of (9) are solved separately. Each term is computed exactly using matrix exponential formulas. The advantage of this splitting is that it numerically preserves positiveness for each equation.

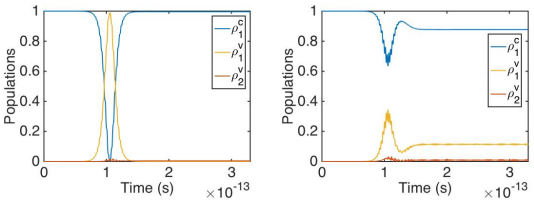

Fig. 1. Time evolution of populations for a three energy level case (Left: without e-ph; Right: with e-ph ($N_q = 100$)).

As preliminary result, we present in Fig.1 a three-level test case with a single conduction level and two valence levels (see Fig.1(b) in [2] for more details). An electromagnetic pulse propagates to the dots. Its center frequency ω_0 corresponds to the energy between the conduction level and the first valence level whereas the two valence levels are far apart enough (transition energy equal to $2\hbar\omega_0$). A consequence is that a Self-Induced Transparency (SIT) is observed without e-ph interactions (left picture). For that case, e-ph interactions destroy the SIT phenomenon (right picture).

References

1. B. Bidégaray-Fesquet. Positiveness and Pauli exception principle in raw Bloch equations for quantum boxes. *Annals of Physics*, 325(10):2090 – 2102, 2010.
2. B. Bidégaray-Fesquet and K. Keita. A nonlinear Bloch model for Coulomb interaction in quantum dots. *Journal of Mathematical Physics*, 55(2):021501, 2014.
3. E. Gehrig and O. Hess. Mesoscopic spatiotemporal theory for quantum-dot lasers. *Phys. Rev. A*, 65(033804):1–16, 2002.
4. H. Haug and S.W. Koch. *Quantum theory of the optical and electronic properties of semiconductors*. World Scientific, fifth edition, 2009.

Recent developments in Liouville ensemble optimal control problems

Alfio Borzì[1]

Institut für Mathematik, Universität Würzburg, Emil-Fischer-Strasse 30, 97074 Würzburg, Germany
alfio.borzi@mathematik.uni-wuerzburg.de,

Summary. This contribution is devoted to a discussion of recent developments in the field of ensemble optimal control problems, which were originally proposed by R.W. Brockett with the aim to construct a general and robust control framework that applies to problems involving a large number of identical subsystems such as multiple spin systems in NMR, multi-particle systems, flocks, and multi-agent models. Applications with mass transportation problems, queueing problems, and pedestrian avoidance problems are presented.

1 Ensemble optimal control problems

The formulation and study of optimal control of ensembles governed by differential equations have been recently proposed by R.W. Brockett [8, 10] with the aim to construct a general and robust control framework that applies to problems involving a large number of identical subsystems such as multiple spin systems in NMR, multi-particle systems, flocks, and multi-agent models. However, this framework applies equally well to control a single dynamical system with uncertainty in the initial conditions that are only known in the sense of a statistical distribution.

Central to the formulation of ensemble control with deterministic evolving systems is the Liouville equation, which is a linear hyperbolic partial differential equation. On the other hand, in the case of Itō stochastic models, Brockett's ensemble control requires to consider Fokker-Planck equations, which are parabolic convection-diffusion equations.

In both cases, ensemble optimal control problems consider cost functionals that include tracking of ensembles and different control costs that are motivated by different modelling requirements.

1.1 The deterministic case

In order to illustrate the formulation of ensemble control, in the case of deterministic evolution models, consider the following optimal control problem

$$\min j(x,u) := \int_0^T \left(\theta(x(t)) + \kappa(u(t))\right) dt + \varphi(x(T)) \tag{1}$$

$$\text{s.t.} \quad \dot{x}(t) = a(t,x(t);u(t)), \qquad x(0) = x_0, \tag{2}$$

where 's.t.' stands for 'subject to', and θ, κ and φ are continuous convex functions of their arguments. The optimal control function u is sought in the following set of admissible controls

$$U_{ad} := \left\{ u \in L^\infty(0,T) \;\middle|\; u^a \le u(t) \le u^b \, a.e. [0,T] \right\}.$$

In this problem, $a(t,x;u)$ denotes the controlled dynamics and x represents the state of the system. The purpose of the control is to minimize a function of the state trajectory given in terms of θ, while putting minimal effort by minimizing the costs given in terms of κ.

Now, in order to strike a balance between the desired performance of the system and the cost of implementing an effective control, the ensemble control strategy considers a density of initial conditions, and therefore ensemble of trajectories, with the aim to achieve robustness, while choosing control costs that promote control functions that allow easier implementation. This approach leads to the formulation of the following ensemble optimal control problem

$$\min_{u\in U_{ad}} J(\rho,u) := \int_0^T \int_{\mathbb{R}^d} \theta(x)\,\rho(x,t)\,dxdt + \int_{\mathbb{R}^d} \varphi(x)\,\rho(x,T)\,dx + \int_0^T \kappa(u(t))\,dt \tag{3}$$

$$\text{s.t.} \quad \partial_t \rho + \operatorname{div}\big(a(t,x;u)\,\rho\big) = 0, \qquad \rho_{|t=0} = \rho_0. \tag{4}$$

In this formulation, the initial density $\rho_0 \ge 0$ represents the probability distribution of the initial condition x_0 in (1) - (2), and thus it models the known uncertainty on the initial data. Alternatively, ρ_0 represents the material density distribution at $t = 0$. Then the solution to the Liouville equation (4), denoted with ρ, represents the probability density function of the system's trajectory or the evolving material density, respectively.

2 Review of work

The notion of Liouville-based ensemble control was proposed by R.W. Brockett in [8], and further developed in [9, 10], while considering the problem of trade-off between the complexity of implementing a

control strategy and the performance of the control system. On the other hand and independently, it has been recognized that the framework of optimal control of Liouville models is natural to investigate transportation problems. In this case, we refer to the work of [15] and [16]. Ensemble control has similarity with stochastic control problems, and in this case more results are available starting from [2]. In this case, the system's trajectories are stochastic, and depending on the class of stochastic processes, different Fokker-Planck equations (replacing the Liouville equation (4)) represent the evolution model of the probability density function of the process. For Itō processes, we refer to, e.g., [3, 4], and to [11, 17] for transport application. In the case where the Itō process is also subject to jumps see [14]. For piecewise-deterministic Markov processes, we refer to [5, 19]. A case with subdiffusion dynamics is discussed in [6].

We remark that the study of ensemble control in [7] has shown a connection between optimal control of Fokker-Planck equations with suitably choosen ensemble cost functionals and the Hamilton-Jacobi-Bellman control framework.

3 Ongoing research

The research on ensemble optimal control problems is very active and focuses on different theoretical and numerical issues concerning the governing models and the structure of the optimal control problems. In the case of (3) - (4), one has to deal with the theory of Liouville equations with variable coefficients and even discontinuous (bang-bang) control functions. This study relies on the fundamental works [1] and [13] and many others. From the optimization point of view, one has to deal with recent developments in optimal control theory with non-smooth cost functionals; see [12] and references therein. Further, the ensemble control approach can successfully accommodate problems of crowd modelling as in [17] and avoidance as in [18] where a Fokker-Planck Nash game is considered.

Acknowledgement. This work was supported by the National Group of Mathematical Physics (GNFM-INdAM).

References

1. L. Ambrosio and G. Crippa, *Continuity equations and ODE flows with non-smooth velocity*, Proc. Roy. Soc. Edinburgh Sect. A, 144 (2014), pp. 1191–1244.
2. M. Annunziato and A. Borzì, *Optimal control of probability density functions of stochastic processes*, Mathematical Modelling and Analysis. Matematinis Modeliavimis ir Analizė. The Baltic Journal on Mathematical Applications, Numerical Analysis and Differential Equations, 15 (2010), pp. 393–407.
3. M. Annunziato and A. Borzì, *A Fokker-Planck control framework for multidimensional stochastic processes*, Journal of Computational and Applied Mathematics, 237 (2013), pp. 487–507.
4. M. Annunziato and A. Borzì, *Fokker-Planck-Based Control of a Two-Level Open Quantum System*, Math. Models and Meth. in Appl. Sci. (M3AS), 23 (2013), 2039–2064.
5. M. Annunziato and A. Borzì, *Optimal control of a class of piecewise deterministic processes*, European Journal of Applied Mathematics, 25 (2014), pp. 1–25.
6. M. Annunziato, A. Borzì, M. Magdziarz, A. Weron, *A fractional Fokker-Planck control framework for subdiffusion processes*, Optimal Contr. Appl. and Meth. Vol. 37 (2016), 290–304.
7. M. Annunziato, A. Borzì, F. Nobile, and R. Tempone, *On the connection between the Hamilton-Jacobi-Bellman and the Fokker-Planck control frameworks*, Applied Mathematics, 5 (2014), 2476–2484.
8. W. Brockett, *Minimum attention control*, in Decision and Control, 1997., Proceedings of the 36th IEEE Conference on, vol. 3, IEEE, 1997, pp. 2628–2632.
9. R. W. Brockett, *Optimal control of the Liouville equation*, in Proceedings of the International Conference on Complex Geometry and Related Fields, vol. 39 of AMS/IP Stud. Adv. Math., Amer. Math. Soc., Providence, RI, 2007, pp. 23–35.
10. R. Brockett, *Notes on the Control of the Liouville Equation*, in Control of Partial Differential Equations, Springer, 2012, pp. 101–129.
11. G. Carlier and J. Salomon, *A monotonic algorithm for the optimal control of the Fokker-Planck equation*, in 47TH IEEE CONFERENCE ON DECISION AND CONTROL, 2008 (CDC 2008), IEEE Conference on Decision and Control, 2008, pp. 269–273.
12. G. Ciaramella and A. Borzì, *Quantum optimal control problems with a sparsity cost functional*, Numerical Functional Analysis and Optimization, 37 (2016), pp. 938–965.
13. R. J. DiPerna and P.-L. Lions, *Ordinary differential equations, transport theory and Sobolev spaces*, Invent. Math., 98 (1989), pp. 511–547.
14. B. Gaviraghi, A. Schindele, M. Annunziato, and A. Borzì, *On optimal sparse-control problems governed by jump-diffusion processes*, Applied Mathematics, 7 (2016), pp. 1978–2004.
15. N. Pogodaev, *Optimal control of continuity equations*, Nonlinear Differential Equations and Applications NoDEA, 23 (2016), p. 21.
16. S. Roy and A. Borzì, *Numerical investigation of a class of Liouville control problems*, Journal of Scientific Computing, 73 (2017), pp. 178–202.
17. S. Roy, M. Annunziato, and A. Borzì, *A Fokker-Planck feedback control-constrained approach for modelling crowd motion*, Journal of Computational and Theoretical Transport, 45 (2016), pp. 442–458.
18. S. Roy, A. Borzì, A. Habbal, *Pedestrian motion modelled by Fokker - Planck Nash games*, Royal Society open science, 4: 170648, 2017.
19. V. Thalhofer, M. Annunziato, and A. Borzì, *Stochastic modelling and control of antibiotic subtilin production*, Journal of Mathematical Biology, 73 (2016), pp. 727–749.

Lie symmetry analysis and symmetry reductions of a generalized family of third-order partial differential equations

M.S. Bruzón[1], R. de la Rosa[1], M.L. Gandarias[1], and R. Tracinà[2]

[1] Departamento de Matemáticas, Universidad de Cádiz, Campus de Puerto Real, 11510 Cádiz, Spain
m.bruzon@uca.es, rafael.delarosa@uca.es , marialuz.gandarias@uca.es
[2] Dipartimento di Matematica e Informatica, Università di Catania, Viale A. Doria 6, Catania 95125, Italy
tracina@dmi.unict.it

Summary. This work is devoted to make a full analysis of a generalized family of third-order partial differential equations from the point of view of symmetry reductions. The class considered broadens out many other well-known equations as the KdV equation, the Burgers equation or the Gardner equation. The use of solvable symmetry algebras allow us to reduce this class to first-order nonlinear ODEs. Furthermore, symmetry groups are used to determine a reduction of the class to a quadrature. Finally, exact solutions are obtained.

The study of integrable equations which model real-world phenomena have drawn the attention of numerous researchers in the last years. Nevertheless, in the early period of development of integrability theory, most of the PDEs considered were constant-coefficient ones. The issue lies in the fact that variable-coefficient models describe nonlinear phenomena more realistically that constant-coefficient models.

Gandarias and Bruzón [4] considered the generalized third-order variable-coefficient equation given by

$$u_t = (g(u))_{xxx} + (f(u))_x, \tag{1}$$

where $f(u)$ and $g(u)$ are arbitrary functions satisfying $f_u \neq 0$, $g_u \neq 0$. They obtained the point symmetries admitted by equation (1). Moreover, they determined the subclasses of family (1) which are self-adjoint and quasi self-adjoint. Then, by using a general theorem on conservation laws which does not require the existence of a classical Lagrangian, they found conservation laws for some equations belonging to class (1).

In this work, we consider a generalization of equation (1) which is given by

$$u_t = (g(u))_{xxx} + (f(u))_x + h(u)u_{xx}, \tag{2}$$

where $h(u)$ is an arbitrary function of u. This class generalizes many well-known equations as the Korteweg-de Vries equation, the Burgers equation and the Gardner equation, among others.

The symmetry group of a partial differential equation (PDE) is the largest transformation group which acts on dependent and independent variables of the equation in a manner that it maps solutions of the equation into other solutions. Symmetry groups have several well-known applications. Among them, we highlight local symmetries admitted by a PDE are useful for obtaining invariant solutions [2, 5]. The fundamental basis of this technique is that, when a differential equation is invariant under a Lie group of transformations, a reduction transformation exists. Furthermore, symmetry groups can also be used to determine conservation laws, obtain exact solutions or the construction of maps between equivalent equations of the same family [1, 3, 6–8].

For equation (2), a one-parameter Lie group of transformations is a transformation depending on the parameter ε

$$\begin{aligned} \hat{t}(t,x,u;\varepsilon) &= t + \varepsilon\,\tau(t,x,u) + O(\varepsilon^2), \\ \hat{x}(t,x,u;\varepsilon) &= x + \varepsilon\,\xi(t,x,u) + O(\varepsilon^2), \\ \hat{u}(t,x,u;\varepsilon) &= u + \varepsilon\,\eta(t,x,u) + O(\varepsilon^2), \end{aligned} \tag{3}$$

such that its third extension leaves equation (2) invariant [6].

The Lie group of transformations is known when the components $\tau(t,x,u)$, $\xi(t,x,u)$, and $\eta(t,x,u)$ are determined. These components are also the coordinates of the infinitesimal symmetry generator.

By using infinitesimal symmetries, it is well known that a PDE with two independent variables can be reduced to an ordinary differential equation (ODE). This reduction procedure can be performed taking into account the characteristic system

$$\frac{dt}{\tau} = \frac{dx}{\xi} = \frac{du}{\eta}.$$

The solutions of the characteristic system provide a similarity variable z, and a similarity solution $h(z)$. By substituting these new variables into equation (2) we obtain a third-order nonlinear ODE for $h(z)$.

However, it is not always evident how to solve the ODEs obtained. In fact, not all third-order non-

linear ODEs can be solved in explicit form. One alternative is to prove if the third-order nonlinear ODE inherits a three-dimensional solvable Lie group from equation (2). In this way, equation (2) can be reduced to quadrature. We recall that the necessary condition for equation (2) can be reduced to quadrature is that the initial reduction comes from a point symmetry belonging to a four-dimensional solvable Lie group. Following reference [1], $\mathscr{A}^k$ is a k-dimensional solvable Lie algebra if there exists a chain of subalgebras $\mathscr{A}^{(1)} \subset \mathscr{A}^{(2)} \subset \ldots \subset \mathscr{A}^{(k-1)} \subset \mathscr{A}^{(k)} = \mathscr{A}^k$, with $\mathscr{A}^{(m)}$ a m-dimensional Lie algebra, being $\mathscr{A}^{(m-1)}$ an ideal of $\mathscr{A}^{(m)}$, $m = 1,2,\ldots,k$. An equivalent formulation of this result more fitting for reducing differential equations using symmetries is $\mathscr{A} \supset \mathscr{A}^{(1)} \supset \mathscr{A}^{(2)} \supset \ldots \supset \mathscr{A}^{(k)} \supset \mathscr{A}^{(k+1)} = 0$, where $\mathscr{A}^{(m)} = \left[\mathscr{A}^{(m-1)}, \mathscr{A}^{(m-1)}\right]$, $m = 1,2,\ldots,k \leq \dim \mathscr{A}$.

In this work, we will perform a classification of the point symmetries admitted by equation (2). Then, we will determine the most general symmetry Lie algebra that the equation admits depending on the form of the arbitrary functions $f(u)$, $g(u)$ and $h(u)$. From the maximal Lie algebras, we will determine the three and four-dimensional solvable symmetry algebras of equation (2). This allows us to transform the third-order nonlinear PDE (2) into first-order nonlinear ODEs. Furthermore, in some cases it is possible to obtain exact group-invariant solutions by using the solvable symmetry groups which yields a reduction of equation (2) to a quadrature. Finally, we will show exact solutions of equation (2).

Acknowledgement. R. Tracinà acknowledges Università di Catania for financial support, *Metodi gruppali e umbrali per modelli di diffusione e trasporto*. M.S. Bruzón, R. de la Rosa and M.L. Gandarias acknowledge the financial support from Junta de Andalucía group FQM-201, Universidad de Cádiz. M.S. Bruzón and M.L. Gandarias also acknowledge the support of DGICYT project MTM2009-11875 with the participation of FEDER. R. de la Rosa also expresses his sincere gratitude to the Plan Propio de Investigación de la Universidad de Cádiz.

References

1. G.W. Bluman and S.C. Anco. *Symmetry and integration methods for differential equations*. Springer-Verlag, 2002.
2. R. de la Rosa and M.S. Bruzón. Symmetry reductions of a generalized Kuramoto-Sivashinsky equation via equivalence transformations. *Commun. Nonlinear Sci. Numer. Simulat.* 63:12–20, 2018.
3. I.L. Freire and A.C. Faleiros. Lie point symmetries and some group invariant solutions of the quasilinear equation involving the infinity Laplacian. *Nonlinear Anal. TMA* 74:3478–3486, 2011.
4. M.L. Gandarias and M.S. Bruzón. Conservation laws for a class of quasi self-adjoint third order equations. *Appl. Math. Comput.* 219:668–678, 2012.
5. S. Kontogiorgis and C. Sophocleous. Group classification of systems of diffusion equations. *Math. Meth. Appl. Sci.* 40:1746–1756, 2017.
6. P.J. Olver. *Applications of Lie groups to differential equations*. Springer-Verlag, 1986.
7. L.V. Ovsyannikov. *Group analysis of differential equations*. Academic, New York, 1982.
8. R. Tracinà, M.S. Bruzón, M.L. Gandarias and M. Torrisi. Nonlinear self-adjointness, conservation laws, exact solutions of a system of dispersive evolution equations. *Commun. Nonlinear Sci. Numer. Simulat.* 19:3036–43, 2014.

MD-FEM Force Field Simulations of Particle Subjected to Dielectrophoresis Interactions

M. Cascio[1,2,*], G. Falci[1,2], S. F. Lombardo[1],
I. Deretzis[1] and A. La Magna[1],
[1]CNR-IMM, Catania, Italy
[2]Department of Physics and Astronomy and INFN, University of Catania, Italy
[*]michele.cascio@ct.infn.it

Keywords: *MD-FEM, electromechanical particles, dielectrophoresis*

Particles with sizes that range from sub-micrometers to about 1 millimeter and with particular electrical and/or magnetic properties, experience mechanical forces and torques when they are subjected to electromagnetic fields (this type of particles are called "electromechanical particles").

The theoretical study of this large class of complex systems is possible thanks to the development of real-system models and numerical simulations of the stable (multi-particle) configurations and their dynamics.

One of the phenomena that affect electromechanical particles is the dielectrophoresis (DEP)[1, 2].

A branch of emerging application relates to controlled manipulation of particles dispersed in colloidal solutions (i.e. biological particles such as cells or DNA), since the strong selectivity of the response depends on the particle volume, shape and composition [3]. Application fields of dielectrophoresis include cell partitioning/isolation for the capture/separations without the use of biomarkers [4].

This contribution focuses on the theoretical study of the dynamics of micro-sized spherical biological particles suspended in a colloidal solution, which are subjected to dielectrophoresis in the presence of non-homogeneous and non-uniform variable electric fields.

Most DEP models in the literature are based on particles in the diluted solution limit [5]; in this case the forces are calculated using an approximate method (standard DEP). The electric field is applied through the electrodes present in a microfluidic channel in which the colloidal solution flows. Particle manipulation and characterization using DEP is generally performed in a confined region near the electrodes, so that the interaction between the particle and the surrounding walls can be significant. In this work, we present numerical simulations of the movement of MDA-MB-231 tumor cells near electrodes edges; we run a more detailed study, with a non-approximate calculation of the dielectrophoretic force: DEP forces are estimated by integrating the Maxwell tensor [6]; it leads to an overall DEP force independent of the complex dielectric permittivity of the particles and suspending medium and depends only on the type of boundaries (conductive or isolating) and on the ratio between the particle and electrode dimensions.

The dynamics is simulated by techniques borrowed from Molecular Dynamics (MD): our goal is to first evaluate the forces acting on electromechanical particles starting from the initial configuration of the system (position of the particles, geometry of the electrodes, electrical potentials applied), and then calculate the dynamics of the particles through the integration of the equations of motion using MD-like techniques. The Coupled MD-FEM study of particles' kinetics consists of a loop with the following steps: initial positions of the particles; calculation of forces; calculation of acceleration; integration of the equations of motion; new positions. We use the numerical integration technique called Verlet Method. The coupled MD-FEM algorithm and its implementation in the FEniCS environment are presented. Realistic simulated cases will be discussed, showing also the difficulties of the methodic implementation in 3D domains.

We carry out simulations of the movement of MDA-MB-231 tumor cells near the electrode edges, based both on the standard DEP theory and on the non approximate theoretical model (MST). We find that, in the case of standard DEP, the cells experience an attractive force that traps them near the electrodes, while in the case of the MST-DEP force, the cells also form chains due to dipole-dipole interactions and some escape from the attraction of the electrodes.

Our work shows the potential of coupled MD-FEM study of electromechanical particles.

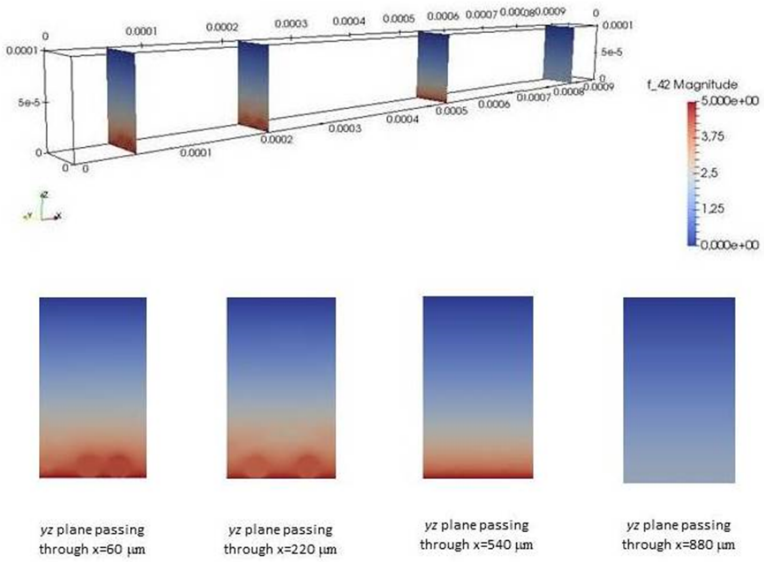

Figure 1: Self consistent solution of the complex Poisson equation

References

[1] P. R. C. Gascoyne, J. Noshari, T. J. Anderson, F. F. Becker, *Electrophoresis* **30**, 1388 (2009)

[2] Dho-Hyoung Lee, Chengjie Yu, Papazoglou E., Bakhtier F., Hongseok M., *Electrophoresis* **32**, 2298-2306 (2011)

[3] B. Cetin and D. Li, *Electrophoresis* **32**, 2410 (2011)

[4] M. P. Huges, *Electrophoresis* **23**, 2569 (2002)

[5] O. E. Nicotra, A. La Magna, S. Coffa, *Appl. Phys. Lett.* **95**, 073702 (2009)

[6] M. Camarda, S. Scalese and A. La Magna, *Electrophoresis* **36**, 13961404 (2015)

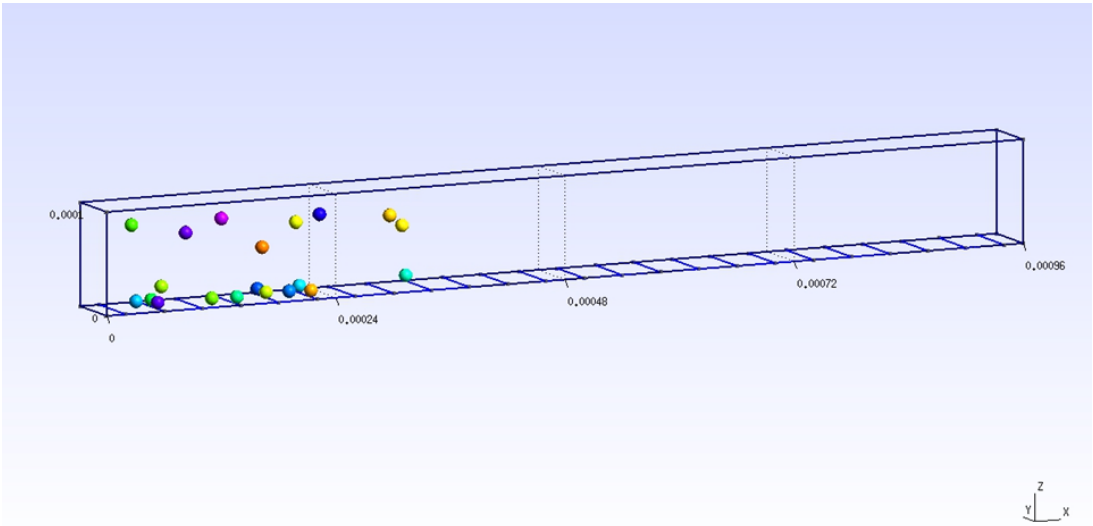

Figure 2: MST-DEP configuration after 0.6s of simulated evolution. In the presence of the DEP force calculated by the Maxwell Stress Tensor, the cells are attracted by the electrodes and form chains due to dipole-dipole interactions; some cells escape the attraction of the electrodes.

Fast transient simulation of RCc* circuits with dense capacitive coupling

N. T. K. Dang[1], J. M. L. Maubach[1], J. Rommes[2], P. Bolcato[2], and W. H. A. Schilders[1]

[1] Department of Mathematics and Computer Sciences, Eindhoven University of Technology, 5612 AZ Eindhoven, The Netherlands t.k.n.dang@tue.nl, J.M.L.Maubach@tue.nl, w.h.a.schilders@TUE.nl

[2] Mentor Graphics, 110 Blaise Pascal, 38330 Joost_Rommes@mentor.com, pascal_bolcato@mentor.com

Summary. The main motivation of this work is lying in the acceleration of transient simulation of Analog Mixed Signal circuits. As in the electronics industry, smaller and faster electronic devices have been always demanded, leading to challenging problems in the Electronic Design Automation industry. Full device-parasitic transient simulations of realistic circuits are time consuming or even infeasible due to a huge number of electrical devices and unavoidable parasitics. In this paper, we introduce a novel technique to address the problem. The technique activates/inactives coupling capacitances at each time step, therefore, giving faster transient simulation.

$\star$ Resistors, coupling capacitors

1 Introduction

Very Large Scale Integrated circuits contain numerous tiny electronic devices placed in a small flat piece of semiconductor material. In every new generation, smaller-size transistors and denser electronic devices significantly cause parasitic electromagnetic effects in transistors and interconnects to be more apparent. Simulation of such parasitic networks is too costly or unattainable. With the purpose of speedup and (or) enabling transient simulation of AMS[1] circuits, reduced models are sought for the parasitics. Well-known MOR[2]methods to deal with these large networks are Krylov subspaces [4], balanced truncation methods [8], and elimination methods [6]. However, existing MOR methods can produce dense reduced models that become more expensive to simulate than the original systems. Moreover, for multi-terminal networks MOR is inefficient because of generating dense models such as when using PRIMA [4], and/or large reduced models. Recently, ReduceR [7], SparseRC [3] and TurboMOR-RC [5] are presented to share the common goals: creating sparse reduced models and working efficiently with multi-terminal networks. In the present study, we work on an innovative method where the sparsity, efficiency, and accuracy of the method for multi-terminal networks are of great concern.

In the new approach, for each time step of transient simulation coupling capacitors between nets are selected to be active/inactive results in sparser capacitance matrix in some time steps, thus providing faster transient simulation. For some initial experiments, described below, the method gives promising results.

[1] Analog Mixed Signal

[2] Model Order Reduction

2 Problem formulation and the method

Time-domain circuit simulation

The time-domain transient behaviour of a given circuit is described by the following formulation:

$$\mathbf{f}(\mathbf{x}) = \mathbf{C}\mathbf{x}'(t) + \mathbf{G}\mathbf{x}(t) + \mathbf{H}g(\mathbf{x}(t)) - \mathbf{B}\mathbf{u}(t) = \mathbf{0} \quad (1)$$

where:

- MNA [1] matrices $\mathbf{G}, \mathbf{C} \in \mathbb{R}^{N\times N}$ are symmetric, semi-positive definite, corresponding to the conductivities and capacitances, respectively;
- $\mathbf{x} \in \mathbb{R}^N$ denotes the node voltages;
- $\mathbf{u} \in \mathbb{R}^M$ is the current or voltage source and $\mathbf{B} \in \mathbb{R}^{N\times M}$ is the incidence matrix;
- g is a vector of nonlinear functions, and $\mathbf{H}$ is a matrix with entries in $0, \pm 1$.

The nonlinear system of equations (1) is usually solved for a given initial condition $\mathbf{x}(t_0) := \mathbf{x}_0$ where $\mathbf{x}_0$ is obtained by solving the DC solution:

$$\mathbf{f}_0(\mathbf{x}) = \mathbf{G}\mathbf{x} + \mathbf{H}g(\mathbf{x}) - \mathbf{B}\mathbf{u}_0 = \mathbf{0}. \quad (2)$$

Equations (2) and (1) are solved numerically by using a nonlinear iterative method such as Newton$'$s method. At each Newton iteration, a linearized problem is solved to update the approximation:

$$\mathbf{x}^{(k+1)} = \mathbf{x}^{(k)} - \mathbf{J}_\mathbf{f}^{-1}\mathbf{f}(\mathbf{x}^{(k)}), \quad (3)$$

where $\mathbb{R}^{N\times N} \ni \mathbf{J}_\mathbf{f} = \frac{\partial \mathbf{f}}{\partial \mathbf{x}}\big|_{\mathbf{x}=\mathbf{x}^{(k)}}$ is the Jacobian matrix of $\mathbf{f}(\mathbf{x})$, $\mathbf{J}_g \in \mathbb{R}^{N\times N}$, and $\mathbf{J}_g(\mathbf{x}^{(k)}) = \frac{\partial g}{\partial \mathbf{x}}\big|_{\mathbf{x}=\mathbf{x}^{(k)}}$ is the Jacobian matrix of $g(\mathbf{x})$.
For time domain simulation, from the initial condition the DAE system in (1) is discretized into a set of nonlinear algebraic equations by a numerical integration method (Backward Euler, Trapezoidal). Then iterative Newton$'$s algorithm is applied at each time point t_i and finally linear solvers are used to solve linearized set of equations.

Most of the computation at time is spent in assembling the derivative matrix $\mathbf{J}(\mathbf{x}^{(k)})$ and in solving system with it [2]. Therefore, reducing sparsity of contributed matrices of the system would help to accelerate transient simulation.

The SelectC method

The current passing through a capacitor c_{ij} between V_i and V_j (direction $V_i \to V_j$) is

$$i_c = c_{ij} \times \frac{d(V_i - V_j)}{dt} \tag{4}$$

$$\approx c_{ij} \times \left(\frac{V_i(t_{n+1}) - V_i(t_n)}{t_{n+1} - t_n} - \frac{V_j(t_{n+1}) - V_j(t_n)}{t_{n+1} - t_n} \right). \tag{5}$$

When the current i_C is negligible i.e. approximate to 0, then c_{ij} is said to be inactive and can be removed from the capacitance matrix.
In other words, SelectC is the method of selecting active/inactive coupling capacitors based on the currents going through them. The inactive capacitors are coupling capacitors whose node voltages barely change from the previous time step to the current one. At the current time step, the active capacitances will be kept while the inactive capacitances are removed from the capacitance matrix of the system matrix. To make sure the voltage derivative part is minor and the i_c value is not affected by the c_{ij} value, the possibly inactive capacitors c_{ij} to be removed should have capacitance smaller than to be chosen constant τ_{cap}. Eventually, a capacitance is removed if

$$\begin{cases} c_{ij} \le \tau_{cap} \\ c_{ij} \times \left(\dfrac{V_i(t_{n+1}) - V_i(t_n)}{t_{n+1} - t_n} - \dfrac{V_j(t_{n+1}) - V_j(t_n)}{t_{n+1} - t_n} \right) \le \tau_{sel} \end{cases} \tag{6}$$

SelectC can be seen as eliminating small currents passing through capacitors by eliminating capacitors, thus reduces the number of capacitors. At a certain time step, SelectC eliminates inactive capacitors, which is essential for preserving accuracy.

Table 1. Numerical results of SelectC, removing c_{ij} if c_{ij} meets (6)

Netlist	τ_{cap}	τ_{sel}	Type	Avg#C	Sim. Time (s)	Error
1. N = 18,927	-	-	Orig.	168,309	619	-
	1e-14	1e-8	SelectC	15,090	105	1.2e-03
			Red. rate	91%	5.9X	
		1e-4	SelectC	17,756	88.5	6.1e-02
			Red. rate	89.5%	7X	
2. N = 6,887	-	-	Orig.	14,161	53	-
	1e-14	1e-8	SelectC	2,102	23	6.2e-04
			Red. rate	85%	2.3X	
		1e-4	SelectC	611	11.6	1.2e-01
			Red. rate	94.7%	4.6X	

3 Numerical results

We focus on SelectC applied to matrix $\mathbf{C}$ of the linear system $\mathbf{Cx}' + \mathbf{Gx} = \mathbf{Bu}(t)$, where $\mathbf{G}, \mathbf{C}$ are large industrially relevant matrices. The sparsity of the resulting matrices greatly contributes to faster transient simulation time, as can be seen in Table 1. SelectC can reduce about 90% of average density of the original $\mathbf{C}$ leading to faster transient simulation time up to the factor of six (netlist 1). The error is acceptable with maximum absolute error less than 2% for $\tau_{sel} = 1e-8$.

4 Conclusions and outlook

The new technique provides faster transient simulations of RCc networks up to the factor of six. The method works nicely with stable signals, for instance trapezoidal, pulse and/or square signals. To be investigated are the reliability and automatic detection/generation of the method (more precisely, given an error tolerance, which value of τ_{sel} and τ_{cap} we should choose, and vice versa).

Acknowledgement. This work was supported by the Marie Curie Initial Training Networks (project ASIVA14)

References

1. F. N. Najm. *Circuit Simulation*. ISBN 978-0-470-53871-5, Wiley, New Jersey, 2010.
2. P. Li. Foundations and Trends in Electronic Design Automation. *Parallel Circuit Simulation: A Historical Perspective and Recent Developments*. Vol.5,No.4,2011.
3. R. Ionutiu, J. Rommes, W. H. A. Schilders. SparseRC: Sparsity preserving model reduction for RC circuits with many terminals *IEEE Trans. Comput.-Aided Des.*, vol. 30, no. 12, pp. 1828-1841, Dec. 2011.
4. A. Odabasioglu, M. Celik, and L. Pileggi, PRIMA: Passive reduced-order interconnect macromodeling algorithm, *IEEE Trans. Comput.-Aided Des. Integr. Circuits Syst.*, vol. 17, no. 8, pp. 645654, Aug. 1998.
5. D. Oyaro and P. Triverio. TurboMOR-RC: An effficient model order reduction technique for RC networks with many ports. *IEEE Trans. Comput.-Aided Des. Integr. Circuits Syst.*, vol. 35, no. 10, pp. 16951706, Oct 2016.
6. B. N. Sheehan. Realizable reduction of RC networks. *IEEE Trans. Comput.-Aided Design Integr. Circuit Syst.*, vol. 26, no. 8, pp. 1393–1407, Aug. 2007.
7. J. Rommes and W. H. A. Schilders. Efficient methods for large resistor networks. *IEEE Trans. Comput.-Aided Design Integr. Circuit Syst.*, vol. 29, 2010.
8. T. Reis and T. Stykel. PABTEC: Passivity-preserving balanced truncation for electrical circuits. IEEE Trans. Comput.-Aided Des., vol. 29, no. 9, pp. 1354-1367, Sep. 2010.

Energy transport mediated by phonons at the nanoscale in complex device structures

Ioannis Deretzis , Karim Huet, Salvatore. Francesco Lombardo, and Antonino La Magna

CNR-IMM, Catania, Italy; SCREEN-LASSE Paris, France ioannis.deretzis@imm.cnr.it, karim.huet@screen-lasse.com, antonino.lamagna@imm.cnr.it

Summary. We present a computation tool developed for the simulation of localized heating and eventual melting processes. The code is designed to efficiently simulate 3D structures with TCAD capabilities for the design of the system. Thermal transport in critical regions (intermediate and large Knudsen number) is ruled by advanced models (order reductions of the Boltzmann transport equation) whilst in regions with small Knudsen number is ruled by the conventional Fourier law. Heating can be also evaluated by means of self consistent solutions of the Maxwell equations where optical constants are functions of the local average phonons' energy (temperature in quasi-equilibrium conditions). A preliminary calibration is provided for given materials/phases. Applications of the simulations to realistic cases will be discussed and compared with experimental data in order to demonstrate the potentiality of the method.

1 Introduction

Ultra localized annealing techniques, using laser sources, are necessary where heating processes need nanoscale resolution for a plethora of applications in the nanotechnology field. In nano-electronics laser irradiation is invoked as ideal heating technique for 3D vertical integration. Indeed, due to its low in-depth thermal diffusion, laser anneal is nowadays widely applied as a post-fabrication annealing step to activate isolated doped regions with a null or strongly reduced heating of the other zones of the devices.

Anyhow, the application of such techniques is often hindered by the difficulties in the process control and understanding. Indeed, LA process is highly influenced by the interaction between electromagnetic (e.m.) field and complex device structures. In order to correctly design processes and control experiments accurate modelling is needed, especially when the reference systems are complex 3D systems made by objects with size in the nm range made of different materials.

Models of laser annealing process have been developed by our team for particular limited applications and implemented in academic or commercial package [1–4]. However, several limitations remain (see e.g. discussion in Ref. [5]) in the previous modeling approach for the general application in future devices, characterized by complex structures with nm wide elements made of different materials/phases. Moreover, for nanoscale size of the devices the process conditions often fall in a regime where Fourier law is questionable and the heat propagation should be studied and simulated in term of phonon transport.

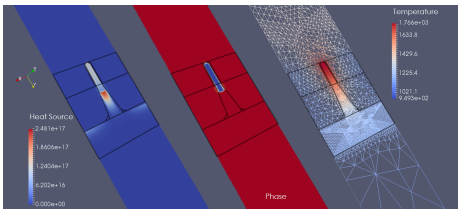

Fig. 1. Simulation example of the Laser Annealing process in a FINFET device structure, from left to right the heat sources, the phase (liquid phase in blue, solid one in red) and temperature. Is also shown the mesh used. The correlation between phase and heat source in the figure demonstrates the role of self-consistency in the simulation.

2 Methods and computational tool

In the paper we present an extension of our tool for the simulation of laser annealing process(named LIAB: LASSE Innovation Application Booster) aiming to consider correction to the Fourier law for phonon mediated transport of irradiation energy. The original LIAB solver simulates a complex self-consistent problem in 1D, 2D and 3D systems, where the heating is evaluated by mean of the time harmonic solution of the Maxwell equations and the source term in the heat equation is

$$S_{laser}(t,\mathbf{r}) = \frac{\varepsilon''}{2\rho}|\mathbf{E}_{t-h}|^2 \qquad (1)$$

Where ε'' is the imaginary part of the complex dielectric constant $\varepsilon^{''} = \varepsilon^{'} + j\varepsilon^{''}$ of the material and $\mathbf{E}_{t-h}$ is the time harmonic electric field $\mathbf{E} = \mathbf{E}_{t-h} \times exp(-j\omega t + \phi)$. The self consistency derives from the dependence of the optical constant on the temperature field (varying in the range 300-2000K), the phases and the alloy fraction(see fig.1).

The main features of the LIAB package include the following:

- Versatile Graphical User Interface for the structure design, the material assignment and the simulation analysis;
- Interface with the FEniCS solver for the automatic generation of the mesh and the runtime control;
- Many materials calibration (optical and thermal properties and mass transport) as a function of temperature and phases;
- Efficient coupling with Electromagnetic Simulation for the self-consistent source estimate (i.e. power dissipation) in nano-structured topographies;
- Experimental validation in nanostructured samples;
- Multiple-dopant models simulating dopant atoms redistribution including diffusion solubility and segregation;
- Alloy model e.g. SiGe (where melting point depends on the alloy fraction);
- Multiple phases (e.g. amorphous, liquid, crystal).

In the LIAB extension we includes corrections for the thermal transport in critical regions (characterized by intermediate and large Knudsen number). The advanced models implemented in these regions are based on order reductions of the Boltzmann transport equation of the phonons, whilst in regions with small Knudsen number is ruled by the conventional Fourier law. Alternative numerical solutions of the full problem are presented where: a) Discontinuous Galerkin method are applied for the full problem with a single evolving average energy field or b) Continuous Galerkin formulation is used for the the fields related to the different orders of the corrections. In both case jump like solutions appear at the boundaries between materials and/or between thermostats and device.

Some application cases will be discussed in order to demonstrate the potentiality of the package. Possible future extension will be outlined in the framework of the development LIAB project.

References

1. A. La Magna, P. Alippi, V. Privitera, G. Fortunato, M. Camalleri, B. Svensson *Journal of Applied Physics* **95**, 4806 (2004)
2. A. La Magna, P. Alippi, V. Privitera, G. Fortunato *Applied Physics Letters* **86**, 4738 (2005)
3. K. Huet, G. Fisicaro, J. Venturini, H. Besaucle, A. La Magna *Applied Physics Letters* **95**, 231901 (2009)
4. G. Fisicaro, K. Huet, R. Negru,M. Hackenberg, P. Pichler, N. Taleb, A. La Magna *Phys. Rev. Lett.* **110**, 117801 (2013)
5. S.F. Lombardo, F. Cristiano, G. Fisicaro, G. Fortunato, M.G. Grimaldi, G. Impellizzeri, M. Italia, A. Marino, R. Milazzo, E. Napolitani, V. Privitera, A. La Magna *Mat. Sci. Semi. Proc* **62**, 80 (2017)

Method of Moments Formulation for Magnetic and Conductive Wires in a Time-harmonic Magnetic Field

Luca Giussani[1], Massimo Bechis[2], Carlo de Falco[3], and Luca Di Rienzo[1]

[1] Dipartimento di Elettronica, Informazione e Bioingegneria, Politecnico di Milano, Milan 20133, Italy
luca.giussani@polimi.it, luca.dirienzo@polimi.it
[2] Prysmian S.p.A., Milan 20126, Italy massimo.bechis@prysmiangroup.com
[3] MOX – Modeling and Scientific Computing, Dipartimento di Matematica, Politecnico di Milano, Milan 20133, Italy
carlo.defalco@polimi.it

Summary. The finite element method presents severe limitations when applied to geometries containing many thin wires in magnetodynamic problems. We propose an integral formulation for an array of wires in a three-dimensional magneto-quasi-static field able to reduce the computational burden of finite element simulations.

1 Introduction

Magnetic and conductive wires are present in many electrical engineering applications. For example, the armor of a high voltage AC submarine cable is composed of iron wires (Fig. 1).

When analyzing these problems by means of the finite element method (FEM), it is necessary to discretize the wires into fine elements in order to consider hysteresis and eddy current phenomena. Moreover, FEM requires to discretize not only the wires, but also the air which surrounds them, and to introduce an artificial boundary to the computational domain. For inherently 3D geometries that cannot be reduced to 2D, this requires the introduction of a large number of degrees of freedom.

This paper proposes an alternative approach, based on the magnetostatic method of moments (MoM) [1]. The advantages of this method are that only the magnetic material parts are discretized, and that there is no need either to discretize the air domain, or to introduce fictitious computational boundaries and associated boundary conditions.

2 Method of Moments Formulation

For simplicity we present our formulation for the case of a single wire. The extension to the case of multiple wires is straightforward. We suppose that the wire is made of a conductive and magnetizable material of uniform conductivity σ and relative magnetic permeability μ_r. The wire has a length L and a circular cross-section of radius r and could be arbitrarily curved in space. We denote by $\Gamma(s)$, $s \in [0,L]$ its centerline and by Ω its volume.

We suppose that the wire is subject to a known external magnetic field $\mathbf{B}_0 = \mathbf{B}_0(\mathbf{x})$. As a first step we suppose that $\mathbf{B}_0$ is a static field. The effect of $\mathbf{B}_0$ is to magnetize the wire. The magnetization $\mathbf{M}$ along the wire in turn produces a magnetic field $\mathbf{B}_M$, given by [3]

$$\mathbf{B}_M(\mathbf{x};\mathbf{M}) = \frac{\mu_0}{4\pi}\int_{\partial\Omega}(\mathbf{n}\times\mathbf{M})(\mathbf{x}')\times\frac{\mathbf{x}-\mathbf{x}'}{|\mathbf{x}-\mathbf{x}'|^3}\,da'. \quad (1)$$

The total magnetostatic field $\mathbf{B}(\mathbf{x})$ at a generic physical point $\mathbf{x}$ can thus be written as the sum of the background field $\mathbf{B}_0(\mathbf{x})$ and the reaction field $\mathbf{B}_M(\mathbf{x};\mathbf{M})$ produced by the wire magnetization:

$$\mathbf{B}(\mathbf{x}) = \mathbf{B}_0(\mathbf{x}) + \mathbf{B}_M(\mathbf{x};\mathbf{M}). \quad (2)$$

To obtain an equation for the unknown magnetization $\mathbf{M}$ we combine (2) with the constitutive equation of the wire material. In the case of a linearly magnetizable material, it is given by [3]

$$\mathbf{M}(\mathbf{x}) = \frac{1}{\mu_0}\left(1-\frac{1}{\mu_r}\right)\mathbf{B}(\mathbf{x}). \quad (3)$$

Combining (2) with (3), we obtain the desired equation for the unknown magnetization $\mathbf{M}$

$$\mathbf{M}(\mathbf{x}) - \frac{\alpha}{\mu_0}\mathbf{B}_M(\mathbf{x};\mathbf{M}) = \frac{\alpha}{\mu_0}\mathbf{B}_0(\mathbf{x}), \quad (4)$$

where $\mathbf{B}_M(\mathbf{x};\mathbf{M})$ is given by (1), and, for ease of notation, we have put $\alpha = 1 - 1/\mu_r$.

The fundamental hypothesis that allows to simplify (4) is that the wire is sufficiently thin. Under this hypothesis, the background field $\mathbf{B}_0$ and the magnetization $\mathbf{M}$ can vary appreciably along the wire, but are almost constant over its cross-sections. Therefore the values of these quantities over a cross-section $\Sigma(s)$ are approximately equal to the values at the center $\Gamma(s)$ of the cross-section.

We can then transform the surface integral equation (4) into a line integral equation

$$\mathbf{M}(s) - \frac{\alpha}{\mu_0}\mathbf{B}_M(s;\mathbf{M}) = \frac{\alpha}{\mu_0}\mathbf{B}_0(s), \quad s \in [0,L]. \quad (5)$$

Equation (5) represents a magnetostatic formulation. We now extend the applicability of the formulation to the case of a time-harmonic external field $\mathbf{B}_0(\mathbf{x},t) = \mathbf{B}_0(\mathbf{x})\exp(\mathrm{i}\omega t)$. An $\exp(\mathrm{i}\omega t)$ time dependence is assumed for the field quantities and suppressed from now on.

An alternating magnetic field $\mathbf{B}_0$ besides magnetizing the wire as in the static case also induces an alternating electric current $\mathbf{J}$ inside the conductive wire.

Thus, in the time-harmonic case an additional contribution $\mathbf{B}_J(\mathbf{x})$ must be included into (2), obtaining

$$\mathbf{B}(\mathbf{x}) = \mathbf{B}_0(\mathbf{x}) + \mathbf{B}_M(\mathbf{x};\mathbf{M}) + \mathbf{B}_J(\mathbf{x};\mathbf{J}). \qquad (6)$$

Under the hypothesis that the wires are open-circuit, the average of $\mathbf{J}$ over any cross-section is zero. Therefore the volume current density $\mathbf{J}$ can be modeled as a linear distribution of magnetic dipoles along the centerline Γ of the wire. In other words, the effect of the eddy currents $\mathbf{J}$ can be modeled as an additional source of magnetization.

Therefore we can define an effective linear distribution of magnetization $\mathbf{M}^*(s)$ along the centerline Γ, which takes into account both the magnetization $\mathbf{M}$, already analyzed in the static case, and the eddy current density $\mathbf{J}$. The magnetic field produced by $\mathbf{M}$ and by $\mathbf{J}$ can thus be computed through (1), as long as we substitute $\mathbf{M}$ with $\mathbf{M}^*$.

So we can express the magnetic field $\mathbf{B}(\mathbf{x})$ at a generic point $\mathbf{x}$ as a function of the line quantity $\mathbf{M}^*(s)$:

$$\mathbf{B}(\mathbf{x}) = \mathbf{B}_0(\mathbf{x}) + \mathbf{B}_M(\mathbf{x};\mathbf{M}^*), \qquad (7)$$

with $\mathbf{B}_M$ given by (1).

To obtain a line-integral formulation, it only remains to specify the analogue of (3) for the time-harmonic case. In [2] it is shown that the effective magnetization $\mathbf{M}^*$ is related to the magnetic field $\mathbf{B}$ through

$$\mathbf{M}^*(s) = \frac{1}{\mu_0}[\mathbf{K}](s)\mathbf{B}(s), \qquad (8)$$

where $[\mathbf{K}](s)$ is a tensor that takes into account the different behavior of $\mathbf{J}$ in the direction parallel to the wire and in the direction perpendicular to the wire respectively.

Finally, combining (7) and (8), we obtain the equation for the effective magnetization $\mathbf{M}^*(s)$:

$$\mathbf{M}^*(s) - \frac{1}{\mu_0}[\mathbf{K}](s)\mathbf{B}_M(s;\mathbf{M}^*) = \frac{1}{\mu_0}[\mathbf{K}](s)\mathbf{B}_0(s). \qquad (9)$$

Once (9) is solved, the computed $\mathbf{M}^*(s)$ can be used in the post-processing phase to compute the magnetic field $\mathbf{B}(\mathbf{x})$ at a generic physical point $\mathbf{x}$ by means of (7).

3 Results and Conclusions

The proposed method is applied to the case of a cable structure consisting of three helically twisted conductors carrying a system of three-phase currents of intensity $I = 800\,\mathrm{A}$, and shielded by 95 closely spaced cylindrical wires made of ferromagnetic material (Fig. 1). The relative magnetic permeability of the wires is $\mu_r = 300\exp(-\mathrm{i}\pi/3)$ and their conductivity is $\sigma = 4.808\times10^6\,\mathrm{S/m}$.

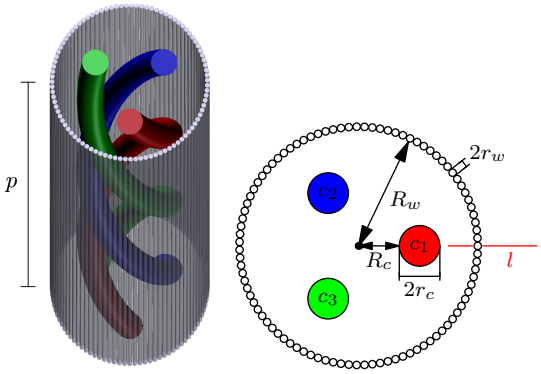

Fig. 1. Geometry for the test case: $R_c = 57.8\,\mathrm{mm}$, $R_w = 110\,\mathrm{mm}$, $r_c = 19.2\,\mathrm{mm}$, $r_w = 3.50\,\mathrm{mm}$, $p = 3000\,\mathrm{mm}$.

As it can be seen in Fig. 2, the results obtained with the proposed method are in very good agreement with the results of FEM simulations. The advantage of the proposed method lies in the reduction in computational requirements, compared to FEM simulations, both in terms of memory occupation and time of computation.

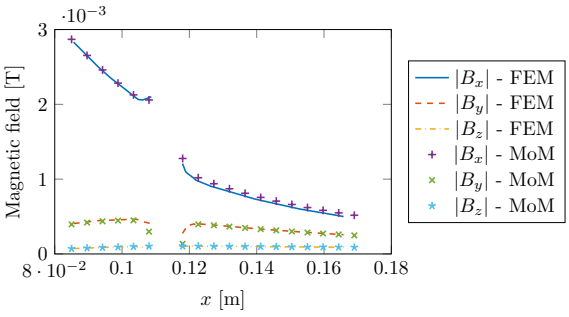

Fig. 2. Magnetic field intensity along line l (Fig. 1). Comparison between proposed method (MoM) and FEM.

References

1. O. Chadebec, J. L. Coulomb, and F. Janet. A review of magnetostatic moment method. *IEEE Transactions on Magnetics*, 42(4):515–520, April 2006.
2. L. Giussani, M. Bechis, C. de Falco, and L. Di Rienzo. An integral formulation for an array of wires in a 3d magneto-quasi-static field. *IEEE Transactions on Magnetics*. To be published.
3. J. D. Jackson. *Classical Electrodynamics*. Wiley, third edition, 1998.

Gappy-POD versus DEIM reduced-order model of a non-linear magnetodynamic problem

MD Rokibul Hasan[1], Laurent Montier[2], Thomas Henneron[2], and Ruth V. Sabariego[1]

[1] Dept. Electrical Engineering (ESAT), EnergyVille, KU Leuven, Belgium
rokib.hasan@esat.kuleuven.be, ruth.sabariego@kuleuven.be
[2] Laboratoire d'Electrotechnique et d'Electronique de Puissance, Arts et Metiers ParisTech, France
laurent.montier@ensam.eu, thomas.henneron@univ-lille1.fr

Summary. The finite element (FE) model of a non-linear eddy-current problem is reduced by enriching the discrete interpolation method (DEIM) with a gappy proper orthogonal decomposition (G-POD). Particular attention is paid to robustness and stability with an optimal computational cost.

Introduction

The finite element method (FEM) allows to accurately model electromagnetic devices accounting for eddy currents and nonlinearities. It may be extremely expensive, though. The discrete empirical interpolation (DEIM) [1] combined with the proper orthogonal decomposition (POD) [2] can provide a reduced-order model (ROM) which is computationally efficient and stable for non-linear magnetostatic problems [3].

In nonlinear magnetodynamic problems, the DEIM-POD approach leads to instability, i.e. wrong simulation results for particular choices of interpolants [3]. The gappy (G-) POD method [4] is a POD variant that seems to ensure stability in case of non-linear eddy current problems. An error indicator is proposed and analized in [5].

In this digest, we aim at comparing the DEIM-POD and G-POD when reducing the FE model of a single-phase power transformer.

1 MOR of a nonlinear magnetodynamic problem

The FE element discretisation of the magnetodynamic vector potential formulation with N basis functions leads to the time-dependent system:

$$A\,\partial_t x(t) + B(x(t))\,x(t) = c(t)\,, \qquad (1)$$

with $x \in \mathbb{R}^{N\times 1}$ the unknowns, A and $B \in \mathbb{R}^{N\times N}$ the coefficients, and $c \in \mathbb{R}^{N\times 1}$ the source. The nonlinear material properties are embedded in $B(x)$. The time discretization of (1), with e.g. a backward Euler scheme, reads

$$[A_{\Delta t} + B(x_k)]\,x_k = A_{\Delta t}x_{k-1} + c_k\,, \qquad (2)$$

with $A_{\Delta t} = \frac{A}{\Delta t}$ and $\Delta t = t_k - t_{k-1}$ the time step. Subscript k indicates the instant t_k at which the vectors are evaluated, e.g. $x_k = x(t_k)$. The solution of (2) can be obtained by means of a Newton-Raphson scheme.

Proper Orthogonal Decomposition

Applying the POD to (2), we can write [2, 3]

$$[A^r_{\Delta t} + B^r(x^r_k)]\,x^r_k = A^r_{\Delta t}x^r_{k-1} + c^r_k\,, \qquad (3)$$

with $A^r_{\Delta t} = \Psi^T A_{\Delta t}\Psi$, $B^r(x^r_k) = \Psi^T B(\Psi x^r_k)\Psi$, and $c^r_k = \Psi^T c_k$. Ψ is an orthonormal projection operator obtained by getting the SVD of the snapshot matrix $S = [x_1, \ldots, x_L] = \mathcal{U}\Sigma\mathcal{V}^T$ and truncating $\mathcal{U}$, i.e. keeping the M first columns that correspond to singular values in Σ larger than a prescribed error ε, $\Psi = \mathcal{U}^r$ [6].

The solution vector x_k is approximated by $x^r_k \in \mathbb{R}^{M\times 1}$ within a reduced subspace spanned by $\Psi \in \mathbb{R}^{N\times M}$, $M \ll N$, i.e. $x_k \approx \Psi x^r_k$.

The nonlinear term in (3) reads

$$B^r(x^r_k) = \underbrace{\Psi^T}_{M\times N}\ \underbrace{B(\Psi x^r_k)}_{N\times N}\ \underbrace{\Psi}_{N\times M}\,. \qquad (4)$$

It requires the computationally expensive evaluation of $B(\Psi x^r_k)$ as x^r_k is reprojected to the full dimensional space.

Discrete Empirical Interpolation Method

The DEIM [1] allows approximating the term $B(\Psi x^r_k)\Psi x^r_k$ by means of an orthogonal projection operator $\mathcal{W}$, which is generated by applying the SVD to the nonlinear snapshot matrix $S_{nl} = [B(x_1)x_1, \ldots, B(x_L)x_L] = \mathcal{U}_{nl}\Sigma_{nl}\mathcal{V}^T_{nl}$, and selecting the D_e columns of $\mathcal{U}_{nl}$ that correspond to error ε_{nl}, $\mathcal{W} = \mathcal{U}^r_{nl}$. A greedy algorithm [1] is then used for selecting some interpolation indexes and construct matrix $\mathcal{P} = [e_{p_1}, \ldots, e_{p_{D_e}}] \in \mathbb{R}^{N\times D_e}$, where e_j is the j-th column of the identity matrix. The expensive term in (4) becomes

$$B(\Psi x^r_k)\Psi x^r_k \approx \mathcal{W}(\mathcal{P}^T\mathcal{W})^{-1}\mathcal{P}^T B(\mathcal{P}^T\Psi x^r_k)\Psi x^r_k. \qquad (5)$$

Therefore, the reduced non-linear matrix $B^r(x^r_k)$ can be approximated by

$$B^r(x_k^r) \approx \underbrace{\Psi^T \mathcal{W}(\mathcal{P}^T\mathcal{W})^{-1}}_{M \times D_e} \underbrace{\mathcal{P}^T B(\Psi x_k^r)\Psi}_{D_e \times M}, \quad (6)$$

that does not depend on the full system order N any more, as we need only D_e components to evaluate the nonlinear matrix B.

Gappy Proper Orthogonal Decomposition

We propose a procedure similar to the G-POD [4]. It consists in enriching the number of selected DEIM components, $\tilde{\mathcal{P}} = [e_{p_1}, \ldots, e_{p_{D_g}}] \in \mathbb{R}^{N \times D_g}$, $D_g > D_e$, while keeping the original DEIM operator $\mathcal{W} = \mathcal{U}_{\mathrm{NL}}{}^r \in \mathbb{R}^{N \times D_e}$. The nonlinear term becomes

$$B(\Psi x_k^r)\Psi x_k^r \approx \underbrace{\mathcal{W}(\tilde{\mathcal{P}}^T\mathcal{W})^\dagger}_{N \times D_g} \underbrace{\tilde{\mathcal{P}}^T B(\Psi x_k^r)}_{D_g \times N} \Psi x_k^r \,. \quad (7)$$

where the $\dagger$ denotes the pseudo-inverse. If $D_g = D_e$, then we have just the DEIM approach. An error indicator per instant t_k can be introduced:

$$\alpha = (\tilde{\mathcal{P}}^T\mathcal{W})^\dagger \tilde{\mathcal{P}}^T B(\Psi x_k^r)\Psi x_k^r. \quad (8)$$

The norm of α should decrease for stability [5].

2 Single-phase power transformer

By way of illustration we consider a single-phase power transformer in no load operation and with sinusoidal current supply at the primary (5 A peak, $f = 50$ Hz). The primary and secondary copper coils (358 and 206 turns) are wound on a nonlinear conducting core ($\sigma = 3.72\,10^3$ S/m, $\nu = 100 + 10e^{2|b|^2}$ m/H). Time-stepping simulations are carried out with time step $\Delta t = T/60$, period T. We compare the DEIM-POD and G-POD-POD results to the *Full* FE reference.

We construct the RO models from 85 time steps (28 ms). The POD truncation for an error of $\epsilon = 10^{-6}$ is $M = 25$. This POD set is used for the DEIM with $D_e = 25$ and $D_e = 30$. The L_2-relative errors (%) with regard to the *Full* model is acceptable for $D_e = 25$ but not for $D_e = 30$, see Table 2. The result becomes clearly wrong when increasing D_e, see joule losses in Fig. 1. This unexpected behaviour corroborates the instability of the approach. Note that $|\alpha|$ with $D_e = 30$ oscillates and increases with the number of basis and the number of TS, which indicates divergence.

Using the error indicator $|\alpha|$, we select the number of DEIM bases D_e to construct the G-POD model. E.g., the joule loss curve in Fig. 1 diverges at 18 ms (54 TS) and for that number of TS, $|\alpha|$ presents a minimum at $D_e = 24$. For the sake of fair comparison, we take $D_g = 30$, so that we have the same number we had with pure DEIM. One observes that G-POD allows stabilizing the DEIM models.

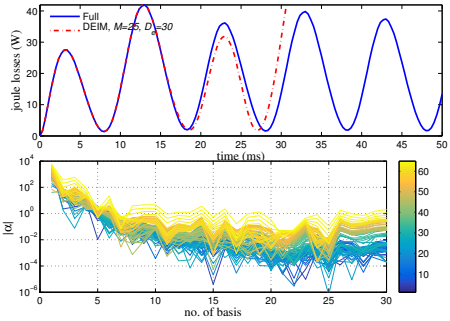

Fig. 1. Joule losses (up) and error indicator α (down) for DEIM with 85 TS (28 ms), $D_e = 30$. Scale: blue to yellow (initial to final TS).

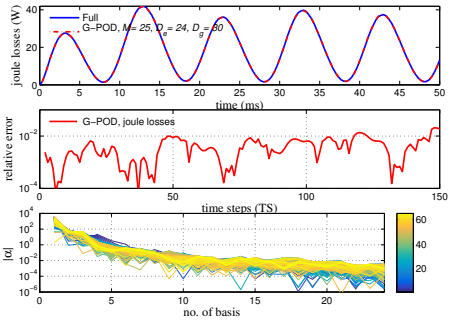

Fig. 2. Joule losses (up), relative error (middle) and error indicator α (down) for G-POD with 85 TS (28 ms), $D_e = 24$, $D_g = 30$. Scale: blue (initial TS) to dark yellow (final TS).

Table 1. L_2-relative errors on the joule losses

DEIM		G-POD		
D_e	L_2-error %	D_e	D_g	L_2-error %
25	1.57	22	25	0.38
30	diverge	24	30	0.44

References

1. S. Chaturantabut, D.C. Sorensen. Nonlinear model reduction via discrete empirical interpolation. *SIAM J. Sci. Comp.*, 32(5):2737–2764, 2010.
2. D. Schmidthausler, M. Clemens. Low-order electroquasistatic field simulations based on proper orthogonal decomposition. *IEEE Trans. Mag.*, 48(2):567–570, 2012.
3. L. Montier, T. Henneron, S. Clénet, B. Goursaud. Robust model order reduction of an electrical machine at startup through reduction error estimation. *Int. J. Numer. Model.*, 31(2):1–9, 2018.
4. R. Everson, L. Sirovich. Karhunen–Loeve procedure for gappy data. *Journal of the Optical Society A*, 12(8):1657–1664, 1995.
5. MD R. Hasan, L. Montier, T. Henneron, R.V. Sabariego. Stabilised reduced-order model of a non-linear eddy current problem by a Gappy-POD approach. submitted to *IEEE Trans. Mag.*, 2018.
6. Y. Sato, H. Igarashi. Model reduction of three-dimensional eddy current problems based on the method of snapshots. *IEEE Trans. Magn.*, 49(5):1697–1700, 2013.

Monte Carlo Simulation of Electron-electron Interactions in Bulk Silicon

Guillermo Indalecio[1,2] and Hans Kosina[2]

[1] CITIUS, University of Santiago de Compostela, 15782, Spain guillermo.indalecio@usc.es
[2] Institute for Microelectronics, TU Wien, 1060, Vienna, Austria kosina@iue.tuwien.ac.at

Summary. We have developed a novel Monte Carlo (MC) algorithm to solve the semiconductor Boltzmann equation in the presence of electron-electron scattering (EES). It is well known that the scattering operator for EES is nonlinear in the single-particle distribution function. Numerical solution methods of the resulting nonlinear equation are usually based on more or less severe approximations. In terms of the pair distribution function, however, the scattering operator is linear. We formulate a kinetic equation for the pair distribution function and related MC algorithms for its numerical solution. Assuming a spatially homogeneous system we derived a two-particle MC algorithm for the stationary problem and an ensemble MC algorithm for the transient problem. Both algorithms were implemented and tested for bulk silicon. As a transient problem we analyzed the mixing of a hot and a cold carrier ensemble. The energy of the hot ensemble relaxes faster with EES switched on. The cold ensemble is temporarily heated by the energy transferred from the hot ensemble. Switching on the electric field rapidly is known to result in an velocity overshoot [1]. We observe that EES enhances the overshoot. The stationary algorithm was used to calculate the energy distribution functions at different field strengths.

1 Introduction

It is commonly accepted that EES alters the high-energy tail of the energy distribution function in a semiconductor device [2]. Since physical models of hot carrier degradation rely on accurate distribution functions as an input it is important to model EES carefully [4]. In this work we present results of a novel treatment of EES that avoids several of the commonly made approximations.

2 Theory

In the Boltzmann equation (BE), carrier-carrier scattering is described by the following, nonlinear integral operator.

$$Q[f](\boldsymbol{k}_1,t) = \int dk_1'\, dk_2'\, dk_2\, S(\boldsymbol{k}_1,\boldsymbol{k}_2;\boldsymbol{k}_1',\boldsymbol{k}_2') \times \left[f(\boldsymbol{k}_1',t)f(\boldsymbol{k}_2',t) - f(\boldsymbol{k}_1,t)f(\boldsymbol{k}_2,t)\right]$$

Here, f is the single-particle distribution function. Integration is over all initial states ($\boldsymbol{k}_2$) and final states ($\boldsymbol{k}_2'$) of the partner electron and all final states ($\boldsymbol{k}_1'$) of the sample electron. Replacing the product of the distribution functions by the two-particle distribution function g

$$f(\boldsymbol{k}_1,t)f(\boldsymbol{k}_2,t) \rightarrow g(\boldsymbol{k}_1,\boldsymbol{k}_2,t),$$

gives a linear scattering operator.

$$Q[g](\boldsymbol{k}_1,\boldsymbol{k}_2,t) = \int dk_1'\, dk_2'\, S(\boldsymbol{k}_1,\boldsymbol{k}_2;\boldsymbol{k}_1',\boldsymbol{k}_2') \times \left[g(\boldsymbol{k}_1',\boldsymbol{k}_2',t) - g(\boldsymbol{k}_1,\boldsymbol{k}_2,t)\right]$$

A Boltzmann-like kinetic equation is derived for the two-particle distribution function g, which is posed in the six-dimensional momentum space $(\boldsymbol{k}_1,\boldsymbol{k}_2)$. This equation is linear and can be transformed into an integral equation of the form

$$g(x) = \int g(x')\, K(x',x)\, \mathrm{d}x' + g_0(x)$$
$$x \equiv (\boldsymbol{k}_1,\boldsymbol{k}_2,t)$$

In this work, we solve this integral equation by a Monte Carlo method [3].

3 Results and Discussion

In the following simulations we are assuming an electron concentration of 10^{19} cm^{-3}, and a lattice temperature of 300 K.

Fig. 1 shows how an ensemble of hot electrons gets cooled down when interacting with the phonons of the crystal lattice and additionally with an electron ensemble at lattice temperature. The mean energy of the hot electrons relaxes faster when EES is present. The mean energy of the cold electrons is temporarily increased by the energy transfer from the hot carriers. Averages are calculated by sampling the two ensembles at equidistant time steps. The number of particle pairs simulated is $2 \cdot 10^4$.

Another application of the transient MC algorithm is the study of the response of the carriers to an abrupt change in the electric field. At 1 ps a field step of 50 kV/cm has been applied. Fig. 2 shows that EES enhances the velocity overshoot and gives a faster rise of

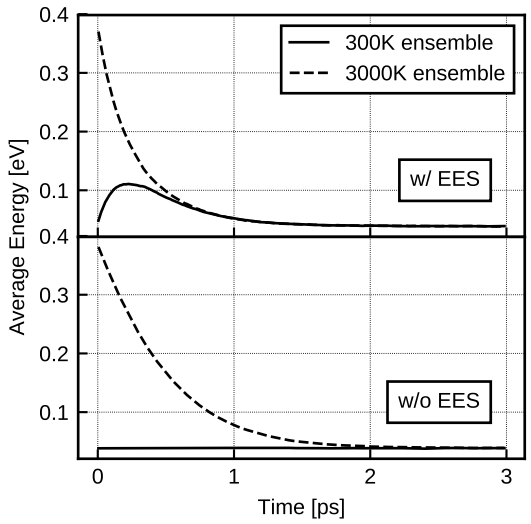

Fig. 1. Relaxation of the mean energy is affected by EES. The initial two-particle distribution function assumed consists of a hot ensemble at 3000K and a cold ensemble at 300K.

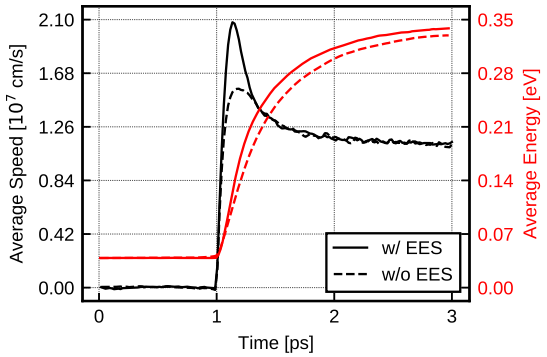

Fig. 2. Velocity overshoot (left, black) and energy transient (right, red) after applying an electric field step of 50 kV/cm at 1 ps.

the mean energy towards the stationary value. Again, in the simulation we sampled an ensemble of $2 \cdot 10^4$ particle pairs at equidistant time steps.

Finally, we apply the stationary MC algorithm to calculate the momentum distribution functions at different field strengths. In accordance with thermodynamics, in equilibrium a Maxwellian distribution is obtained in our simulations. EES has no effect on the equilibrium distribution, see Fig. 3. With an electric field applied there is a noticeable difference for a lattice temperature of 77 K. With EES the non-equilibrium distribution is wider.

4 Conclusions

We have developed a two-particle Monte Carlo algorithm for the solution of a two-particle kinetic equation that includes electron-electron scattering.

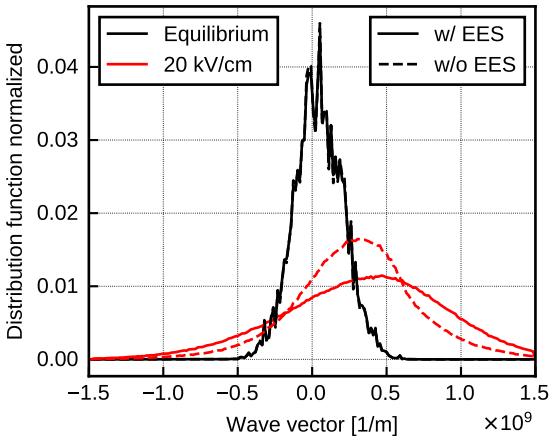

Fig. 3. Momentum distribution functions at equilibrium and at 20 kV/cm, lattice temperature 77 K.

We demonstrate the impact of electron-electron scattering on the transient relaxation of an ensemble of hot carriers, on the veloicty overshoot in the presence of a field step, and on the shape the momentum distribution function.

Acknowledgement. The work of G. Indalecio was supported by the Programa de Axudas a Etapa Posdoutoral da Xunta de Galicia under grant number 2017/077.

References

1. G. Baccarani and M.R. Wordeman. An investigation of steady-state velocity overshoot in silicon. *Solid-State Electronics*, 28(4):407 – 416, 1985.
2. P. A. Childs and C. C. C. Leung. A one-dimensional solution of the Boltzmann transport equation including electron-electron interactions. *Journal of Applied Physics*, 79:222, 1996.
3. H. Kosina, M. Nedjalkov, and S. Selberherr. Theory of the Monte Carlo method for semiconductor device simulation. *IEEE Transactions on Electron Devices*, 47(10):1898–1908, 2000.
4. S. E. Rauch, G. La Rosa, and F. J. Guarin. Role of e-e scattering in the enhancement of channel hot carrier degradation of deep-submicron NMOSFETs at high v_{GS} conditions. *IEEE Transactions on Device and Materials Reliability*, 1(2):113–119, 2001.

Computational characterization of a composite ceramic layer for a millimeter wave heat exchanger

Petra Kumi[1], Jonathan S. Venne[1], Vadim V. Yakovlev[1], Martin S. Hilario[2], Brad W. Hoff[2], and Ian M. Rittersdorf[3]

[1] Worcester Polytechnic Institute, 100 Institute Rd., Worcester, MA 01609, USA vadim@wpi.edu
[2] Air Force Research Laboratory, Kirtland AFB, Albuquerque, NM 87117, USA brad.hoff@us.af.mil
[3] Naval Research Laboratory, Washington, DC 20375, USA ian.rittersdorf@nrl.navy.mil

Summary. Electromagnetic and electromagnetic-thermal coupled problems are solved by the FDTD technique for an AlN:Mo ceramic layer irradiated by a millimeter-wave plane wave. Computation uses experimental data on temperature-dependent complex permittivity, specific heat, and thermal conductivity. Non-uniformity of patterns of dissipated power and temperature is quantified via standard-deviation-based metrics, and the composition of the ceramic material producing the highest levels of heating uniformity and total dissipated power is determined.

1 Introduction

Electromagnetic (EM) heating is employed in applications in food engineering, chemistry, materials science, etc. EM heat exchangers (HE) have been introduced as core elements of solar energy collectors, power beaming applications, and microwave thermal thrusters. A fundamental understanding of the interactions of the millimeter-wave (MMW) EM field with a ceramic material is necessary for effectively utilizing EM energy in controllably heating the material and transferring heat to fluid flowing through neighboring channels [1, 2]. In this paper, we study the process of MMW heating of a rectangular block of an AlN:Mo composite by the means of EM and EM-thermal modeling and characterize the ceramic material in terms of homogeneity of heating and total absorbed power.

2 Computational Scenario & Input Data

A MMW HE under development involves ceramic tiles with a metal baseplate attached to their back surfaces, and the adjacent channels with fluid flow (Fig. 1(a)). To help design a physical prototype, we use a computer model dealing with a ceramic block irradiated by a plane wave (Fig. 1(b)). Due to dielectric losses in the material, a 3D temperature field is induced inside the block. The goal is to find a composition of the ceramic material that leads to a uniform heat distribution under applicable requirements.

The considered parameters affecting the heating pattern are the EM and thermal material parameters: dielectric constant ε', loss factor ε'', specific heat C_p,

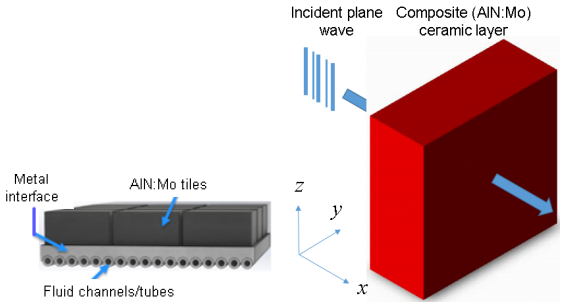

(a) (b)

Fig. 1. Concept of a MMW HE (a) and 3D view of the considered computational scenario (b).

and thermal conductivity k. We consider a set of AlN samples with Mo doping; by varying the percent Mo in the AlN:Mo composite, both the EM and thermal parameters can be significantly changed.

Temperature characteristics of the dielectric constant and loss factor were obtained experimentally with the use of a dedicated apparatus [3]: ε' and ε'' were measured at 95 GHz for temperatures up to $\sim$600 ^{o}C for several samples of AlN with concentrations of Mo doping from 0.25 to 4%. The characteristics turned out to be approximately linearly dependent on T, so ε' and ε'' at temperatures up to 1000 ^{o}C were determined by linear extrapolation. Temperature characteristics of C_p and k were measured for Mo = 4% from room temperature to $\sim$1000 ^{o}C, and they were assumed to be similar to those for lower concentrations of Mo.

3 Computational Techniques

The approaches used in studying the process of MMW heating of the AlN:Mo blocks are based on (*i*) EM and (*ii*) EM-thermal (coupled) models. Both solve the related problems by a 3D finite-difference time-domain (FDTD) technique as it is implemented in the solver *QuickWave* [4].

In the first approach, we compute patterns of EM power (P_d) dissipated in the composite due to dielectric losses. In the second, the EM and thermal solvers are coupled through experimental data on temperature-

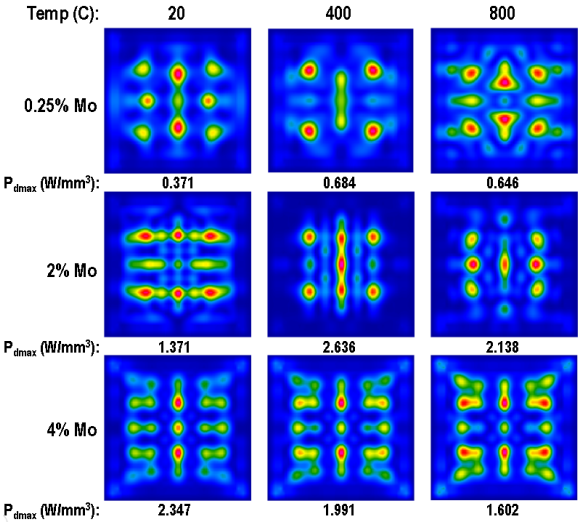

Fig. 2. Patterns of dissipated power on the back surface of the AlN:Mo blocks with 0.25, 2, 4% of Mo at 20, 400, 800 ^{o}C; maximum value of P_d is shown under each pattern.

dependent material parameters. While (*ii*) allows for mimicing time evolutions of the T fields, (*i*) produces patterns identical to corresponding temperature distributions in the absence of thermal conductivity.

Profiles of the P_d field are quantitatively characterized by a non-uniformity metric λ introduced as

$$\lambda = \sigma/\mu, \tag{1}$$

where σ is the standard deviation of the P_d values in all FDTD cells in the sample from the average value, and μ is their mean; the lower λ, the more uniform a pattern. For the T fields varying in time, the metric depends on the initial state of the process:

$$\lambda = \frac{\sqrt{\sigma^2 - \sigma_0^2}}{\bar{T} - \bar{T}_0}, \tag{2}$$

where $\sigma(\sigma_0)$ is the standard deviation of the final (initial) temperature in all FDTD cells from the final (initial) average temperature, and $\bar{T}(\bar{T}_0)$ is the final (initial) average temperature. For 2D patterns, computation of λ is based on the values of P_d and T in a particular layer of cells, while for 3D patterns, λ is found using the values in the cells from everty layer.

The process of MMW heating is characterized by parameters λ_T as the average of values of λ and P_{dt} as the average of total power dissipated in the ceramic material; both λ_T and P_{dt} are computed for a set of T values in the temperature range. The goal of this computational study is to find the percent Mo that leads to the lowest possible value of λ_T and highest possible value of P_{dt}.

4 Results & Discussion

The dimensions of the AlN:Mo composite in the considered scenario are 5×5×2 mm, and the power of the

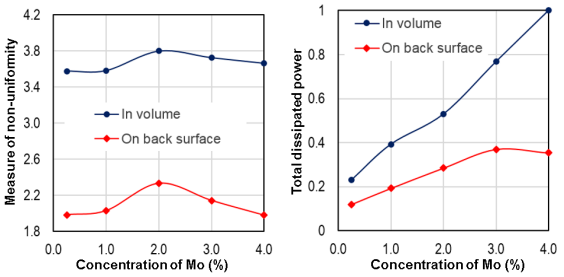

(a) (b)

Fig. 3. Measure of non-uniformity of heating of an AlN:Mo block λ_T (a) and total dissipated power P_dt (normalized to unity) (b) as functions of concentration of Mo.

incident field is 1 W. The material is irradiated by the plane wave at 95 GHz. Patterns of P_d are computed for five percentages of Mo in the interval 0.25 $\leq$ Mo $\leq$ 4.0% and six values of T in the interval 20 $\leq T \leq$ 1,000 ^{o}C. For each point, the sample was assigned with corresponding values of ε' and ε''. Patterns of P_d on the back of the block are shown in Fig. 2. The non-uniformity and energy efficiency of each heating are characterized by the graphs in Fig. 3.

While all the materials are heated quite non-uniformly, the composites with less than 1% and with 4% of Mo are characterized by lower values of λ_T compared to other materials. In terms of homogeneity, the ceramics with Mo $\leq$ 1% appear attractive, but in terms of dissipated power the composites with Mo $\geq$ 3% look preferable as they absorb almost twice as much as the materials with Mo $\leq$ 1%.

Analysis of the heating process by technique (*ii*) reveals more spread heating patterns due to the effect of thermal conductivity. Application of technique (*i*) illustrated in this paper is still meaningful as it leads to best heating patterns prior to heat diffusion and sets terms for optimization. Being computationally more expensive, (*ii*) could be used after (*i*) to look for an optimal material in the domain suggested by (*i*).

Acknowledgement. This work was supported by Leidos, Inc./AFRL, Grant No P010200226.

References

1. B.W. Hoff, M.S. Hilario, *et al*. Millimeter wave interactions with high temperature materials and their applications to power beaming. *Proc. 52nd IMPI Microwave Power Symp., Long Beach, CA, June 2018,* pp. 82-83.
2. A.A. Mohekar, J.M. Gaone, *et al*. A 2D coupled electromagnetic, thermal and fluid flow model: application to layered microwave heat exchangers. *IEEE MTT-S Intern. Microwave Symp. Dig., Philadelphia, PA, June 2018,* pp. 1389-1392.
3. M.S. Hilario, B.W. Hoff, *et al*. W-band free-space dielectric material property measurement techniques for beamed energy applications. *Proc. 53rd AIAA Aerospace Sciences Meeting, Kissimmee, FL, January 2015,*
4. *QuickWave,* QWED Sp. z o. o., http://www.qwed.eu/.

Quantum corrected Hydrodynamic Models for Charge Transport in Graphene

Liliana Luca[1] and Vittorio Romano[2]

[1] Department of Mathematics and Computer Science, Università degli Studi di Catania viale Andrea Doria 6, 95125 Catania, Italy liliana.luca@unict.it ,
[2] Department of Mathematics and Computer Science, Università degli Studi di Catania viale Andrea Doria 6, 95125 Catania, Italy romano@dmi.unict.it

Abstract A quantum hydrodynamic model for charge transport in graphene is derived from a moment expansion of the Wigner-Boltzmann equation. The needed closure relations are obtained by adding to the semiclassical ones quantum corrections based on the equilibrium Wigner function. The latter is obtained from the Bloch equation by taking into account the appropriate energy band of graphene. Numerical solutions of this model are currently under investigation. The semiclassical counterpart has been formulated in [1, 2] by exploiting the Maximum Entropy Principle (MEP).

1 Introduction

Quantum semiconductor devices are playing an increasingly important role in advanced microelectronic applications, including multiple-state logic and memory devices. Therefore in the modeling and simulations of semiconductor devices (like MOSFET and RTD) in ultra-small size (say nano-size) in a strong electric field, the effects of quantum mechanics have to be taken into account. Graphene, consisting of an isolated single atomic layer of graphite, is an ideal candidate for quantum devices. To take into account quantum phenomena, the semiclassical Boltzmann equation is not enough to describe charge transport. As a starting point for deriving of the quantum corrections to the semiclassical model, we consider the Wigner equation. In this work we present the formulation of quantum hydrodynamic models for charge transport in graphene which consist of the semiclassical models developed in [3, 4], augmented with $\hbar^2$ order corrections obtained by the scaling of high field and collision dominated regime [5].

2 Wigner equation

In the proximity of the Dirac points K (K'), which are the vertices of the Brillouin zone, by choosing in the $\mathbf{k}$-space a reference frame centered in the considered Dirac point, the energy dispersion relation can be considered approximately linear with respect to the modulus of the wave-vector $\mathbf{k}$. It is not clear if a small gap between the conduction and the valence band exists. Therefore we adopt the following regularization

$$\mathscr{E}(\mathbf{k}) = \pm v_F \sqrt{a^2 + p^2},$$

where $p = \hbar|\mathbf{k}|$, $v_F \simeq 1 \times 10^6$ cm/s is the Fermi velocity, $\hbar$ is the reduced Planck's constant. The upper sign refers to the conduction band while the lower one refers to the valence band. a is a small parameter related to the nearest-neighbour hopping energy [6]. To derive a transport equation, we introduce the single electron Wigner quasi-distribution $w(\mathbf{x}, p, t)$, depending on the position $\mathbf{x}$, momentum p and time t. Evolution is governed by the *Wigner-Poisson* system for w and the electrostatic potential V

$$\frac{\partial w(\mathbf{x},p,t)}{\partial t} + S[\mathscr{E}]w(\mathbf{x},p,t) - q\theta[\mathscr{E}]w(\mathbf{x},p,t) = C[w],$$
$$\nabla\cdot(\varepsilon\nabla V) = -q(N_D - n),$$

where q is the elementary (positive) charge, N_D is donor carrier concentration, $C[w]$ is the collision term representing the electron-phonon scattering while $S[\mathscr{E}]$ and $\theta[\mathscr{E}]$ represent the pseudo-differential operators

$$S[\mathscr{E}]w(\mathbf{x},p,t) = \frac{i}{\hbar(2\pi)^2}\int_{\mathbb{R}^2_{\mathbf{x}'}\times\mathbb{R}^2_{\mathbf{v}}} [\mathscr{E}(p+\frac{\hbar}{2}\mathbf{v},t) + - \mathscr{E}(p-\frac{\hbar}{2}\mathbf{v},t)]w(\mathbf{x}',p,t)e^{-i(\mathbf{x}'-\mathbf{x})\cdot\mathbf{v}}d\mathbf{x}'d\mathbf{v},$$

$$\theta[\mathscr{E}]w(\mathbf{x},p,t) = \frac{i}{\hbar(2\pi)^2}\int_{\mathbb{R}^2_{p'}\times\mathbb{R}^2_{\eta}} [V(\mathbf{x}+\frac{\hbar}{2}\eta,t) + - V(\mathbf{x}-\frac{\hbar}{2}\eta,t)]w(\mathbf{x},p',t)e^{i(p'-p)\cdot\eta}dp'd\eta.$$

In the semiclassical limit $\hbar \to 0$, the Wigner equation reduces to Boltzmann one.

3 Equilibrium Wigner function

If we denote the density matrix at equilibrium by $\rho_{eq}(\mathbf{r},\mathbf{s},\beta)$, it satisfies the Bloch equation

$$\frac{\partial\rho_{eq}(\mathbf{r},\mathbf{s},\beta)}{\partial\beta} = -\frac{1}{2}[H_{\mathbf{r}}\rho_{eq}(\mathbf{r},\mathbf{s},\beta) + H_{\mathbf{s}}\rho_{eq}(\mathbf{r},\mathbf{s},\beta)].$$

Applying the Fourier transform to the Bloch equation, we get

$$\frac{\partial w_{eq}(\mathbf{x},\mathbf{p},\beta)}{\partial\beta} = -\frac{1}{2}\left\{\frac{1}{(2\pi)^2}\int_{\mathbb{R}^2_{\mathbf{x}'}\times\mathbb{R}^2_{\mathbf{v}}}\mathscr{E}\left(\mathbf{p}+\frac{\hbar}{2}v\right)+\mathscr{E}\left(\mathbf{p}-\frac{\hbar}{2}v\right)w_{eq}(\mathbf{x}',\mathbf{p},\beta)e^{-i(\mathbf{x}'-\mathbf{x})\cdot v}d\mathbf{x}'dv-\right.$$

$$\left.-\frac{q}{(2\pi)^2}\int_{\mathbb{R}^2_{\mathbf{p}'}\times\mathbb{R}^2_{\eta}}V\left(\mathbf{x}+\frac{\hbar}{2}\eta\right)+V\left(\mathbf{x}-\frac{\hbar}{2}\eta\right)w_{eq}(\mathbf{x},\mathbf{p}',\beta)e^{i(\mathbf{p}'-\mathbf{p})\cdot\eta}d\mathbf{p}'d\eta\right\},$$

where $w_{eq}(\mathbf{x},\mathbf{p},\beta)$ is the equilibrium Wigner function. We looked for solution of the type

$$w_{eq}(\mathbf{x},\mathbf{p},\beta) = w_{eq}^{(0)}(\mathbf{x},\mathbf{p},\beta)+\hbar^2 w_{eq}^{(1)}(\mathbf{x},\mathbf{p},\beta).$$

After some algebra we get the equilibrium Wigner function

$$w_{eq}(\mathbf{x},p,\beta) = \exp(qV(\mathbf{x})\beta)\exp(-\beta\mathscr{E}(p))\left\{1+\frac{q\beta^2\hbar^2}{8}\frac{\partial^2\mathscr{E}(p)}{\partial p_i\partial p_j}\frac{\partial^2 V(\mathbf{x})}{\partial x_i\partial x_j}+\right.$$

$$\left.+\frac{\beta^3\hbar^2}{24}\left[q^2\frac{\partial^2\mathscr{E}(p)}{\partial p_i\partial p_j}\frac{\partial V(\mathbf{x})}{\partial x_i}\frac{\partial V(\mathbf{x})}{\partial x_j}-q\frac{\partial^2 V(\mathbf{x})}{\partial x_i\partial x_j}v_i v_j\right]\right\}+o(\hbar^2).$$

4 Quantum hydrodynamic model

Supposing the expansion

$$w = w^{(0)}+\hbar^2 w^{(1)}+O(\hbar^4)$$

holds and by proceeding formally, as $\hbar\longrightarrow 0$ the Wigner equation gives the semiclassical Boltzmann equation. Therefore we identify $w^{(0)}(\mathbf{x},p,t)$ with the semiclassical distribution which has been approximated in [1, 2] with the maximum entropy principle estimator $w^{(0)}(\mathbf{x},p,t)\approx f_{MEP}(\mathbf{x},p,t)$.

At first order in $\hbar^2$ one finds

$$\frac{\partial w^{(1)}(\mathbf{x},p,t)}{\partial t}+\mathbf{v}\cdot\nabla_{\mathbf{x}}w^{(1)}(\mathbf{x},p,t)-\frac{1}{24}\frac{\partial^3\mathscr{E}(p)}{\partial p_i\partial p_j\partial p_k}\frac{\partial^3 w^{(0)}(\mathbf{x},p,t)}{\partial x_i\partial x_j\partial x_k}+$$

$$+q\nabla_{\mathbf{x}}V(\mathbf{x})\nabla_p w^{(1)}(\mathbf{x},p,t)-\frac{q}{24}\frac{\partial^3 V(\mathbf{x})}{\partial x_i\partial x_j\partial x_k}\frac{\partial^3 w^{(0)}(\mathbf{x},p,t)}{\partial p_i\partial p_j\partial p_k}=\mathscr{C}[w^{(1)}]$$

Hereafter, suppose $w^{(1)} = w_{eq}^{(1)}$.

As an example, consider a 6-Moment Model based on the following moments

$$\frac{2}{(2\pi\hbar)^2}\int_{\mathbb{R}^2} w(\mathbf{x},p,t)dp = n(\mathbf{x},t) \quad \text{density},$$

$$\frac{2}{(2\pi\hbar)^2}\int_{\mathbb{R}^2} w(\mathbf{x},p,t)\mathscr{E}(p)dp = n(\mathbf{x},t)W \quad \text{energy density},$$

$$\frac{2}{(2\pi\hbar)^2}\int_{\mathbb{R}^2} w(\mathbf{x},p,t)\mathbf{v}(p)dp = n(\mathbf{x},t)\mathbf{V} \quad \text{linear momentum density},$$

$$\frac{2}{(2\pi\hbar)^2}\int_{\mathbb{R}^2} w(\mathbf{x},p,t)\mathscr{E}(p)\mathbf{v}(p)dp = n(\mathbf{x},t)\mathbf{S} \quad \text{energy-flux density}.$$

The corresponding evolution equations are given by [1]

$$\frac{\partial}{\partial t}n(\mathbf{x},t)+\frac{\partial}{\partial x_i}\left(n(\mathbf{x},t)V_i-\frac{\hbar^2}{24}\frac{\partial^2\left(n(\mathbf{x},t)F_{ijk}^{(0)}\right)}{\partial x_j\partial x_k}\right)=0, \tag{1}$$

$$\frac{\partial}{\partial t}\left(n(\mathbf{x},t)W\right)+\frac{\partial}{\partial x_i}\left(n(\mathbf{x},t)S_i-\frac{\hbar^2}{24}\frac{\partial^2\left(n(\mathbf{x},t)F_{ijk}^{(1)}\right)}{\partial x_j\partial x_k}\right)-q\frac{\partial}{\partial x_i}V(\mathbf{x})\cdot n(\mathbf{x},t)V_i+$$

$$+\frac{q\hbar^2}{24}\frac{\partial^3 V(\mathbf{x})}{\partial x_i\partial x_j\partial x_k}n(\mathbf{x},t)F_{ijk}^{(0)}=C_W[w^{(0)}], \tag{2}$$

$$\frac{\partial}{\partial t}\left(n(\mathbf{x},t)V_i\right)+\frac{\partial}{\partial x_j}\left(n(\mathbf{x},t)T_{ij}^{(0)}-\frac{\hbar^2}{24}\frac{\partial^2\left(n(\mathbf{x},t)G_{ijkl}^{(0)}\right)}{\partial x_k\partial x_l}\right)-q\frac{\partial}{\partial x_j}V(\mathbf{x})\cdot n(\mathbf{x},t)H_{ij}^{(0)}+$$

$$+\frac{q\hbar^2}{24}\frac{\partial^3 V(\mathbf{x})}{\partial x_j\partial x_k\partial x_l}n(\mathbf{x},t)L_{ijkl}^{(0)}=C_{V_i}[w^{(0)}], \tag{3}$$

$$\frac{\partial}{\partial t}\left(n(\mathbf{x},t)S_i\right)+\frac{\partial}{\partial x_j}\left(n(\mathbf{x},t)T_{ij}^{(1)}-\frac{\hbar^2}{24}\frac{\partial^2\left(n(\mathbf{x},t)G_{ijkl}^{(1)}\right)}{\partial x_k\partial x_l}\right)-q\frac{\partial}{\partial x_j}V(\mathbf{x})\cdot n(\mathbf{x},t)V_j\cdot n(\mathbf{x},t)H_{ij}^{(1)}+$$

$$+\frac{q\hbar^2}{24}\frac{\partial^3 V(\mathbf{x})}{\partial x_j\partial x_k\partial x_l}n(\mathbf{x},t)L_{ijkl}^{(1)}=C_{S_i}[w^{(0)}] \tag{4}$$

where V_i and S_i are the significant components of macroscopic velocity $\mathbf{V}$ and energy-flux $\mathbf{S}$ respectively.

All the additional fields are expressed as integrals involving $w^{(0)}$ and $w^{(1)}$. Regarding the production terms, they are given by the sum of contributions arising from the different types of phonon scattering. Explicit closure relations have been obtained and numerical simulations are under current investigation.

References

1. L. Luca, V. Romano, *Comparing linear and nonlinear hydrodynamical models for charge transport in graphene based on the Maximum Entropy Principle*, International Journal of Non-Linear Mechanics (2018).
2. L. Luca, V. Romano, *Hydrodynamical models for charge transport in graphene based on the Maximum Entropy Principle: The case of moments based on energy powers*, Atti della Accademia Peloritana dei Pericolanti (2018).
3. V.D. Camiola, and V. Romano, *Hydrodynamical model for charge transport in graphene*, Journal of Statistical Physics **157** 114-1137 (2014).
4. G. Mascali, V. Romano, *Charge Transport in graphene including thermal effects*, SIAM J. Appl. Mathematics (2017), 77: 593-613.
5. V. Romano, *Quantum corrections to the semiclassical hydrodynamical model of semiconductors based on the maximum entropy principle*, Journal of Mathematical Physics 48, 123504 (2007).
6. A. H. Castro Neto, F. Guinea, N. M. R. Peres, K. S. Novoselov, A. K. Geim, *The electronic properties of graphene*, Rev. Modern Phys. **81**, 109 (2009).
7. E. T. Jaynes, *Information Theory and Statistical Mechanics*, Phys. Rev. **106** 620 (1957).

[1] Einstein's summation convention is used

Simulation of short time current tests of industrial devices

Jörg Ostrowski[1], Michael Gatzsche[2], and Bogusław Samul[3]

[1] ABB Switzerland Ltd., Corporate Research joerg.ostrowski@ch.abb.com
[2] ABB Switzerland Ltd., GIS Development michael.gatzsche@ch.abb.com
[3] ABB Poland Ltd., Corporate Research boguslaw.samul@pl.abb.com

Summary. In this contribution we show that simulations are capable to predict possible failures of realistic devices of the power grid during short time current tests. We quantitatively compare transient 2-way coupled electro-thermal FEM calculations with lab results of GIS earthing switches. We also investigate the importance of modeling geometrical details, and the sensitivity of the computations with respect to electric contact resistances (ECRs) at interfaces. It can be concluded that products can reliably be designed by using such simulations, if the ECRs are known in advance.

1 Introduction

Devices in the power grid have to be able to carry large short-time currents (STC) in order to guarantee reliable supply of electricity. STCs can be caused by short-circuits in the grid. They are typically one order of magnitude higher than normal operating currents and last up to 3 s. This results in fast transient temperature rise and causes intensive thermal load of all components. The capability to withstand STC has to be proven by short-time withstand current type tests, see [1]. Simulations reduce the number of costly and time-intensive STC lab tests and increase the product understanding. The goal of electro-thermal STC simulations is to calculate the transient temperature distribution and to evaluate if the temperature stays below certain limits (e. g. melting temperature). The most important phenomena that have to be considered for an electro-thermal simulation of a STC test are:

- Ohmic losses in the volume of the device
- Temperature dependence of the el. conductivity
- Ohmic losses due to ECRs at interfaces
- Heat conduction inside of the device

Heat exchange with the environment is of minor importance, due to the short duration. Phase transitions also don't have to be modelled, because a test is passed only if melting temperature isn't reached.

2 Simulation method

The simulation is carried out by using a transient two-way coupled electro-thermal method, see Fig. 1. This is necessary because of the temperature dependence of the electrical conductivity, see Fig. 2. The exchange of information (P, T) is triggered when the temperature change locally exceeds $100K$. It is not necessary to use a transient electromagnetic solver, because the time-constant for the applied $50Hz$ current is way smaller than the time-constant of the heating processes. On the electromagnetic side we use an $\mathbf{A}-$

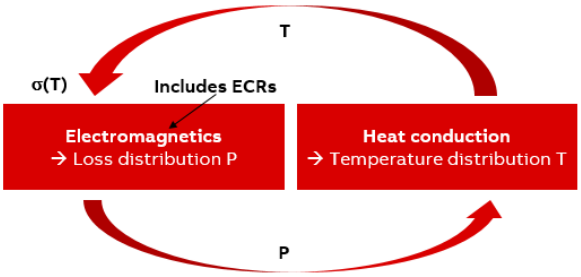

Fig. 1. Two-way-coupled simulation

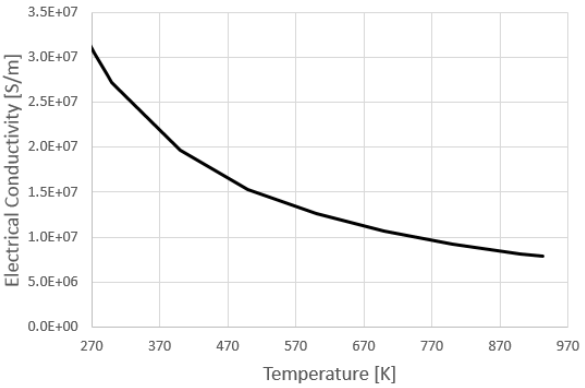

Fig. 2. T-dependence of electrical conductivity of the used Aluminum alloy

φ-based FEM solver of the time-harmonic Maxwell equations, see [2]. The ECRs are therein modelled as discontinuities of the scalar electric potential, that correspond to constant contact resistances. So we did not use elaborate temperature dependent models for the ECRs as e.g. described in [3], [4]. Physically this temperature independent ECR is the simplest representation of a contact for which the increasing material resistivity during heat-up is compensated by a decrease of the total resistance due to a larger contact area caused by material softening. Note that the in-

clusion of the ECRs are mandatory, because of their large contribution to the losses, see Fig. 3.

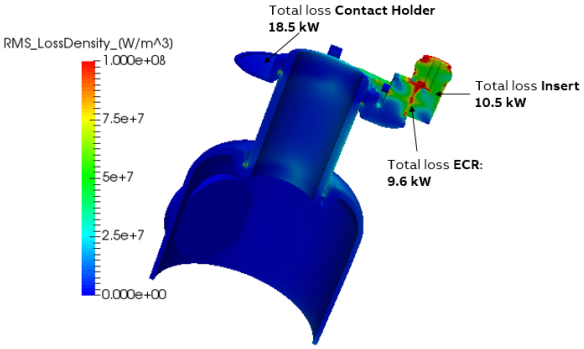

Fig. 3. Power loss density distribution and total losses of the constituting parts.

A standard transient heat conduction FEM solver is used on the thermal side. The heat exchange with the environment is taken into consideration by simple heat exchange coefficients. The entire simulation method is embedded into CAD and the solvers run on a large computer cluster. This enables product designers to carry out simulations of realistic devices.

3 Comparison lab results v.s. simulations

Two different designs of an earthing switch of an ABB[1] gas insulated switchgear (GIS) was tested in the laboratory. A smaller design A and a bigger design B. STC tests with $I_{rms} = 63kA/80kA$ were carried out on design A. This design passed the $63kA$ test. It also passed an $80kA$ test of $2sec$, but failed an $80kA$ test of $2.5sec$. The second design B passed both tests with $I_{rms} = 80kA/90kA$ of $3sec$. The figures 4 and 5 show simulation results of the temperatures. The simulations reproduce very well the experimental results of failure or pass. Melting temperature is reached after $1.8sec$ for design A with $80kA$ applied. This is shortly before the experimental failure between $2.0 - 2.5sec$. That is not wrong, because contacts do not immediately fail when melting temperature is reached [5]. The applicable standard [6] even allows *light welding of contacts* to pass the STC type test.

4 Sensitivity analysis

We tested if

- geometrical details like bolts are of importance,
- and what influence a change in the electrical contact resistance has on the temperature.

[1] www.abb.com

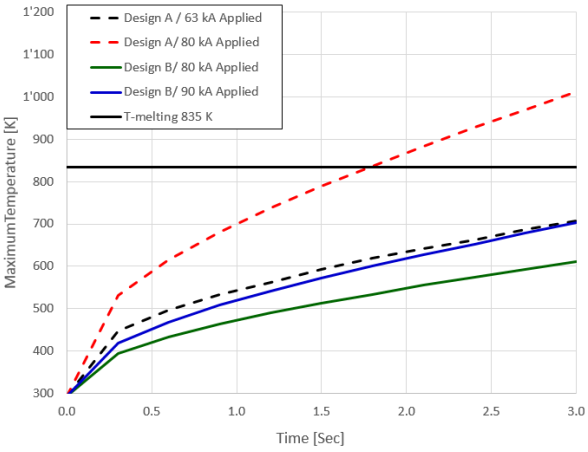

Fig. 4. Maximum of the temperature over time

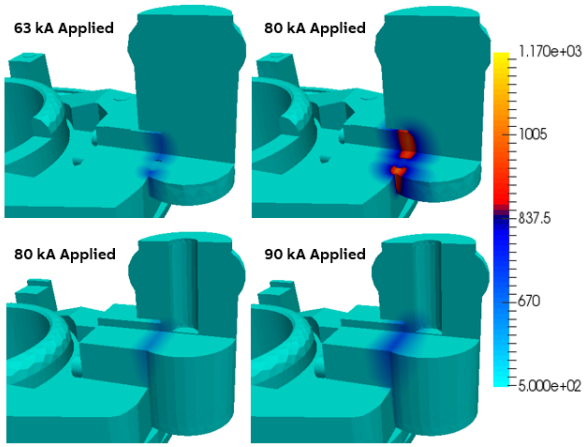

Fig. 5. Design A in upper two pictures, design B in lower two pictures. Two orthogonal cutting planes through hottest area. Temperature after 3 seconds on same scale. Melting temperature is $835K$.

It turned out that details like bolts cannot be neglected and that is of key importance to know the ECRs in advance. These results will be shown at the conference.

References

1. IEC 62271-1, Ed. 2.0 High-voltage switchgear and controlgear: Common specifications for alternating current switchgear and controlgear.
2. C. Winkelmann, R. Casagrande, R. Hiptmair, P.-T. Müller, J. Ostrowski, and T. Werder Schläpfer. Electro-Thermal Simulations with Skin-Layers and Contacts. *SCEE 2016*, Springer, Math. in Industry, vol 28., 2018
3. R. Holm. Electric contacts handbook. *Springer, 1958.*
4. T. Israel, M. Gatzsche, S. Schlegel, S. Großmann, T. Kufner and G. Freudiger. The Impact of Short Circuits on Contact Elements in High Power Applications. *2017 IEEE Holm Conference on Electrical Contacts*
5. Vinaricky. Elektrische Kontakte, Werkstoffe und Anwendungen. Springer 2002
6. IEC 62271-102: 2018, HV switchgear and controlgear: Alternating current disconnectors and earthing switches

A PARALLEL ALGORITHM FOR MULTIPHYSICS ANALYSIS OF RF-MEMS SWITCHES

Mihai Popescu, Second Daniel Ioan, Third Gabriela Ciuprina, Fourth Sorin Lup, and Ruxandra Barbulescu

Politehnica University of Bucharest, Spl. Independentei 313, 060042, Bucharest, Romania mihai.popescu@upb.ro

Summary. The main objective of this paper is to develop a parallel algorithm in order to reduce the computational time required to solve coupled multiphysics problems that arise in the RF-MEMS switches. A coupled electrostatic/liniar-elastic analysis is performed allowing consequent model order reduction to be carried out efficiently. The parallel algorithm uses the domain decomposition technique. It is based on a weak formulation and implemented with FreeFem++ and MPI. The results are compared with COMSOL simulations - strong formulation and parallel solver.

1 General

In the latest time, RF-MEMS switches had an important evolution, driven by their huge economic and practical potential. This justifies the importance of related research topics that have as a final target the correct and effective modeling required for designers of advanced Micro and Nano-electronic systems.

Modeling has two main objectives. The first is to obtain, through numerical simulation, the parameters describing switching behavior of the devices, or when they do not move and have to conduct an RF signal. The second objective is to extract an equivalent electric circuit (reduced order model - ROM) which, approximates the behavior of the studied device. For the first objective, the simulation must be done using a reasonable computational effort, whereas for the second objective the extracted reduced model must have the lowest possible order that would still preserve an acceptable accuracy and its essential characteristics. The contribution of this paper is focused on the multiphysics part of first modeling objective.

2 The Physical Model

The physical model involves a coupled electrostatic/ elasto-static field formulation. A constant voltage is applied on the actuation electrode with respect to the elastic membrane, which is grounded. If the applied voltage is greater than a certain value, due to the electrostatic force, the membrane will drop on the electrode closing the switch. The highest voltage that still doesn't close the switch is called the static pull-in voltage (Vpi). In our previous research, we focused on the extraction of a ROM able to predict with an acceptable accuracy the value of Vpi. The success of the reduction algorithm depends on the accuracy of the static simulation which involves using high-density discretization grids. This leads to significant computation times especially for complicated geometric structures. In this paper, we aim to investigate how we can decrease the computational cost by using high performance computing techniques but without reducing accuracy.

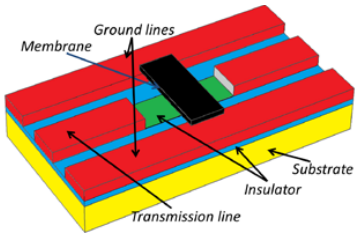

Fig. 1. The conceptual model of the simple bridge RF-MEMS

3 The Mathematical Model

Because of the symmetry of the device we can use only a half of the 2D model (see Fig. 2). According to the physical description, we can distinguish two main computational domains: the electrostatic one represented by the thin dielectric which lays over the fixed actuation electrode (Ω_1) together with the surrounding air gap (Ω_2) and the structural-elastic domain (Ω_3) represented by the elastic membrane (bridge). The electrostatic problem implies solving the Laplace equation for the electrical potential V in the domains Ω_1 and Ω_2:

$$\Delta V = 0 \text{ in } \Omega_1 \text{ and } \Omega_2, \tag{1}$$

with Dirichlet boundary conditions on the electrode ($\partial\Omega_{11}$) and bridge ($\partial\Omega_{23}$) surfaces:

$$V = V_a \text{ on } \partial\Omega_{11},\ V = 0 \text{ on } \partial\Omega_{23}, \tag{2}$$

and Neumann boundary conditions on the rest of the boundary of the electrostatic domain:

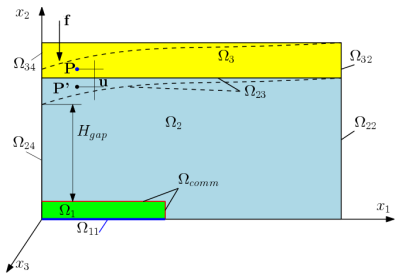

Fig. 2. The computational domains used by the mathematical model

$$\frac{\partial V}{\partial n} = 0 \text{ on } \partial\Omega_{22} \cap \partial\Omega_{24}. \quad (3)$$

For the structural - elastic domain one can write the principle of virtual displacements:

$$\int_{\Omega_3} \mathbf{f}\delta\mathbf{u}\,d\Omega + \int_{\partial\Omega_{32}} \mathbf{t}\delta\mathbf{u}\,ds = \int_{\Omega_3} \sigma\,\delta\varepsilon\,d\Omega \quad (4)$$

which leads to finding the displacement $\mathbf{u} \in H^2(\Omega_3)$ by solving the weak form of the elasticity equation:

$$\int_{\Omega_3} (2\mu\varepsilon(\mathbf{u})\cdot\varepsilon(\psi) + \lambda\nabla\mathbf{u}\nabla\psi)\,dx = \int_{\Omega_3} \psi\mathbf{f}\,dx \quad (5)$$

for the applied force $\mathbf{f} \in L^2(\Omega_3)$ and any $\psi \in H_0^1(\Omega_3)$. $[\varepsilon]$ and $[\sigma]$ are the strain and stress tensors. The boundary conditions taken into account are:

$$\mathbf{u} = 0 \text{ on } \partial\Omega_{32},\ \sigma\mathbf{n} = \mathbf{t} \text{ on } \partial\Omega_{34} \quad (6)$$

4 The Algorithm

For our case, the algorithm uses 3 paralleled processors (called P_i). Each of them is taking care of one of the domains Ω_i. For the electrostatic problem, a Schwartz decomposition algorithm is used by solving (1)-(2) on each domain Ω_1 and Ω_2, with the additional boundary conditions:

$$V_1|_{\partial\Omega_{12}} = V_2|_{\partial\Omega_{12}} = V_c \quad (7)$$

Starting with $V_c = 0$, each of P_1 and P_2 solves (1)-(2) until (7) becomes true within an imposed accuracy. Different mesh refinement degrees can be used for the two domains, which is good, taking into account that Ω_1 needs a much finer mesh than Ω_2. P_3 takes care of the elasticity problem defined on Ω_3. P_2 will finally provide the electrostatic force which acts on the Ω_3 bridge. On the other hand, P_3 will provide the displacement needed to re-iterate the electrostatic problem with a modified mesh, according to the new bridge position. It has to be remarked that only Ω_2 and Ω_3 are re-meshed during the process. Only during the first iteration P_3 waits after P_1 and P_2 to finish - in order to get the first displacement. In the rest of the time

Table 1. Flow chart of the parallel algorithm

Step	P_1	P_2	P_3
S1	read V_a		
S2	mesh Ω_1	mesh Ω_2	mesh Ω_3
S3	compute V_1	compute V_2	if first iter. wait for **f**
S4	broadcast V_1	broadcast V_2	get **f**
S5	wait for another iter. or STOP flag	if $(V_1 - V_2) > err$ goto S3	compute **u**
S6		broadcast V_c	if $(\mathbf{u} > H_{gap})$break
S7		compute **f**	if err(**u**) ok
S8			return **u**; STOP
S9		broadcast **f**	else
S10		wait for **u**	broadcast **u**
S11		get **u**	remesh Ω_3
S12		remesh Ω_2	re-iterate from S4
S13		re-iterate with P1 starting from S2	

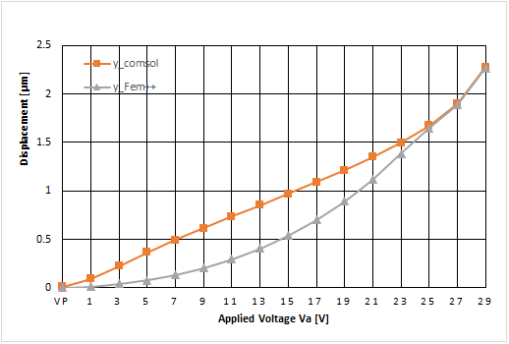

Fig. 3. Comparison of the displacement w.r.t. applied voltage

all solvers will run independently. However certain waiting times are needed for data synchronization and transfer. The above mentioned algorithm was implemented with the highly adaptable mathematical software package FreeFem++. Its efficiency was proven by comparing it with the performance of a very popular professional multiphisycs software package: Comsol Multiphysics. Using FreeFem++ capabilities, our parallel algorithm could be implemented and tested in a very efficient manner on an 8 core I7 Intel processor.

References

1. G.M. Rebeiz. *RF MEMS switches: status of the technology, in transducers*. Wiley, New York, 1973.
2. A.S. Lup et al Parametric reduced order models in static multiphysics analysis of MEMS switches. *10th International Symposium ATEE.*, 513–518, 2017.
3. Hecht, F. New development in freefem++. *Journal of Numerical Mathematics.*, 20(3-4):251–166, 2018.
4. J. Qian, G. Li, and F. De Flavis A parametric model of mems capacitive switch operating at microwave frequencies. *Microwave Symposium Digest. 2000 MTT-S IEEE.*, 1229–1323, 2000.

Model order reduction for dynamic thermal models of LED packages

W.H.A. Schilders[1] and S. Lungten[1]

TU Eindhoven, The Netherlands w.h.a.schilders@tue.nl, sangye30@gmail.com

Summary. Thermal management is one of the key issues arising in designing light-emitting diode (LED) based luminaire products. Dynamic compact thermal models (DCTMs) are required to predict the thermal behaviour of LED packages fast and accurately in system level simulations. The European Delphi4LED consortium aims to develop multi-domain (electrical-thermal-optical) compact models. One of its targets is to develop a methodology to extract DCTMs that can handle multiple heat sources of LEDs.

This presentation focuses on the implementation of Krylov subspace based model order reduction (MOR) methods [5] in extracting DCTMs for LEDs. Various techniques for generating DCTMs exist in the literature, for instance, see [1–4, 6]. Most of them focus on the extraction of DCTMs using thermal RC-network optimization techniques. MOR methodologies based on Krylov subspaces are capable of handling MIMO (multi-input-multi-output) dynamical systems. Hence, such methodologies are suitable for LEDs with multiple heat sources and multiple dies. The approach of MOR consists of semi-discretising the system of partial differential equations (PDEs) describing the physics of LED packages in the spatial domain using a 3D CFD tool such as FloTHERM, leading to a system of ordinary differential equations (ODEs) in the time domain. This can then be handled by several MOR techniques, and reduced to obtain acceptable compact model representations of the behaviour.

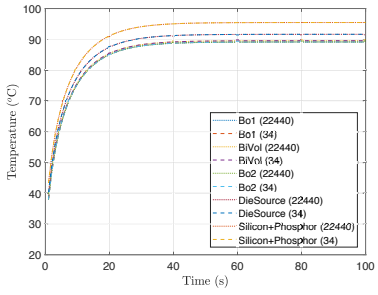

Fig. 1. Transient solutions of the single-die LED package for five different outputs comparing the full-order (n=22,440) model with the reduced-order (r=34) model.

The temperature plots for five outputs from a single-die LED comparing the full-order model with the reduced-order model is shown in Figure 1. The simulation was performed for 100 time steps with a uniform step size $\Delta t = 1s$ in $0, 100$ where the model was at an initial constant temperature of 25°C at $t = 0$. The CPU time spent on solving the full-order model is $14s$, while the time spent on solving the reduced-order model is $1s$. An excellent match is noted for each output as shown in Figures 1 and 2.

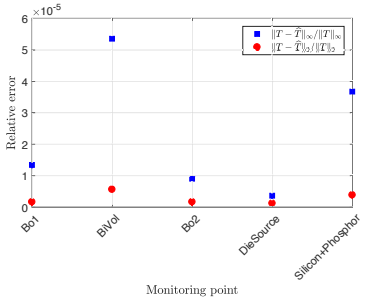

Fig. 2. Relative errors of the temperatures

The results presented in this paper show that the extraction of DCTMs using iterative rational Krylov is highly accurate for a set of benchmark problems developed within the Delphi4LED project.

References

1. T. Bechtold, E.B. Rudnyi and J.G. Korvink. *Fast simulation of electro-thermal MEMS: efficient dynamic compact models*. Springer Science Business Media, 2006.
2. L. Codecasa, D. D'Amore and P. Maffezzoni. *"An Arnoldi based thermal network reduction method for electro-thermal analysis"*. IEEE Transactions on Components and Packaging Technologies, vol. 26, no. 1, pp. 186–192, 2003.
3. L. Codecasa, V. d'Alessandro, A. Magnani, N. Rinaldi and P.J. Zampardi. *"Fast novel thermal analysis simulation tool for integrated circuits (FANTASTIC)"*. Thermal Investigations of ICs and Systems (THERMINIC), 20th International Workshop, Greenwich, London, UK, pp. 1–6, 2014.
4. L. Codecasa. *"Compact models of dynamic thermal networks with many heat sources"*. IEEE Transactions on Components and Packaging Technologies, vol. 10, no. 4, pp. 653–659, 2007.
5. W.H.A. Schilders, H.A. van der Vorst and J. Rommes. *Model order reduction: theory, research aspects and applications*, vol. 13. Berlin, Germany: Springer, 2008.
6. D. Schweitzer. *"Generation of multisource dynamic compact thermal models by RC-network optimization"*. Semiconductor Thermal Measurement and Management Symposium (SEMI-THERM), 29th Annual IEEE, Orlando, FL, pp. 116–123, 2013.

Potential and application of DFT method to understand physical properties of emerging materials

Luis Villamagua[1] and Manuela Carini[2]

[1] Grupo de Fisicoquímica de Materiales, Sección de Fisicoquímica y Matemáticas, Universidad Técnica Particular de Loja, Apartado 11-01-608, Loja, Ecuador, lmvillamagua@uptl.edu.ec
[2] Department of Environmental and Chemical Engineering, University of Calabria, 87036 Arcavacata di Rende (CS), Italy, manuela.carini@unical.it

Summary. In this work, we describe the potential of the computational modeling method, known as density functional theory (DFT), to investigate the physical properties of emerging materials of industrial interest. In particular, we report results obtained by the application of the DFT method to transparent conductive oxides (SnO_2 and ZnO), alternative semiconductors (graphene) and ferroelectric ceramic materials ($BaTiO_3$).

1 Potential of DFT method

A plethora of emerging materials are currently under the magnifying lens of the Industry for their electronic, optical and mechanical applications. In this scenario, it is crucial to understand the physical properties of these emerging materials in reasonable time. In spite of the considerable amount of efforts put to delve into physical and chemical properties of such materials from the experimental standpoints [1], there is still a long way to go until their fundamental characteristics are properly understood [2]. Experimentalist can only claim their findings until where their apparatus (precision) allows them, often resorting to analogies to discuss and infer about the behavior of their samples at the fundamental scale. This is where computational models, and particularly the density functional theory (DFT) methods, play an important role and have its stronghold [3]. This method is an alternative (variational) procedure to the solution of Schrödinger's equation, where the functional of electronic energy is minimized with respect to electronic density, allows one to compute the electronic structure of atoms, molecules, and crystals [3–5].Furthermore, the reason for its popularity stems from a good balance between reasonable and useful accuracy (e.g., bond lengths, vibrational frequencies, elastic constants are calculated with errors of less than a few percent), speed, lower computational cost, and computational efficiency [5]. Accordingly, DFT methods have already been established as a valuable research tool both in the independent applications and as a complement of experimental investigations. Nevertheless, the basic difficulty is that an exact solution to this problem by means of a direct solution of the Schrödinger equation, either in its numerical, variational or perturbation theory versions, is nowadays out of the reach of even the most advanced supercomputers [5]. It is for this reason that alternative ways for handling the quantum-mechanical many-body problem have been vigorously pursued during the last few years by mathematicians, quantum chemists and condensed matter physicists. The traditional methods to compute the electronic structure of matter, in particular the Hartree-Fock theory, are based purely on the multielectronic wavefunction [6]. Although this resolution of the Schrödinger equation allows one to describe the exact behavior of small systems, its prediction capacity is limited by the fact that its equations are too complex to solve even numerically. The DFT reformulates the problem to be able to obtain, for example, the energy and the electronic distribution of the ground state, working with the functional of the electronic density instead of the wavefunction. An advantage is that the density is a much simpler quantity than the wavefunction and therefore easier to calculate, and in practice much more complex systems can be studied: the wavefunction of a system of N electrons depends on N variables, whereas electronic density only depends on 3 variables (x, y, z). An important disadvantage is that, except for the simplest cases, the functional that relates this density to the energy of the system is unknown. In practice (in the majority of DFT calculations), the functionals used are the ones that have proven to give good results, resulting often in a semi empirical method.

2 Application of DFT method to emerging materials

In the last five years, we have used the DFT method, as it is implemented in the Vienna ab initio package (VASP) code [7], to delve into structural, electrical, magnetic, and optical properties of many TCO materials. Since the majority of properties and newly discovered physical effects in the oxides occur due to the presence of different type of point defects, the main research was dedicated to quantum-chemical studies of different point defects (e.g., vacancies, interstitials,

Frenkel defects, Schottky defects, antisites, Fig. 1), complemented with the doping and codoping of crystals with different elements (e.g. H, N, Al, Mg, F, Nb, etc.). The study has been carried out in the following materials: (i) zinc oxide (ZnO); (ii) rutile and anatase of titanium dioxide (TiO_2); (iii) tin dioxide (SnO_2); (iv) chromium oxide (α-Cr_2O_3); (v) strontium titanate ($SrTiO_3$); and graphene. A big deal of unexplained effects and phenomena in these crystals have been revealed by our group recently: (a) reproduce both intrinsic n-type as well as p-type conductivity in concordance to results observed in real samples of SnO_2 material [2] , (b) the H atoms has been proposed as the alternative way to attain n-type electrical conductivity in SnO_2 and ZnO [8, 9], (c) we explored the changes endured by energy gap (E_G) of semiconducting (armchair) graphene nanoribbons (AGNRs) when Stone-Wales (SW) defects were placed inside their lattices [10], (d) study the adsorption of an ethanol molecule on the $BaTiO_3$ (001) surface [11]. These and many other results are proving the potential of DFT methods over the years.

In the present work we propose to delineate the changes experienced by the above-mentioned materials when different defects are included within their lattice. The results will be investigated in terms of the density of state (DOS) pattern (Fig. 2) (e.g. type of conductivity and number of free carriers), the electron localization function (ELF) graphs (charge localization), and Bader charge analysis (e.g. the structural organization of atoms). Specifically, by taking a close look at the Fermi level (dotted vertical line in the DOS) within the DOS pattern, one can find the type of conductivity the material has acquired. Moreover, asymmetry in the α and β spin, in the DOS, indicate that magnetic properties have been acquired by the material, as in (Fig. 2). Partial contributions are analyzed to understand, from a chemical point of view, the rise of the changes endured by the crystallographic lattice. This along with the Bader Charge analysis allows us to provide a clear description about the nature of the atomic movements and therefore the final geometry of the crystal

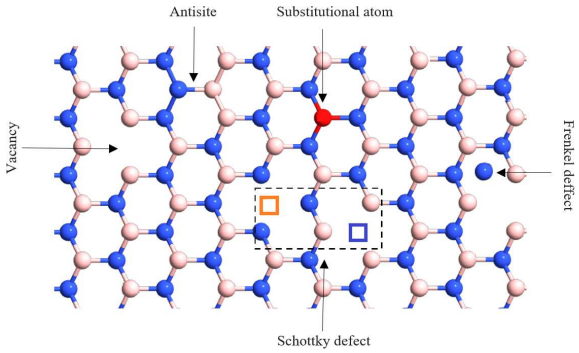

Fig. 1. Schematic illustration of defects in a compound solid, using boron nitride as an example.

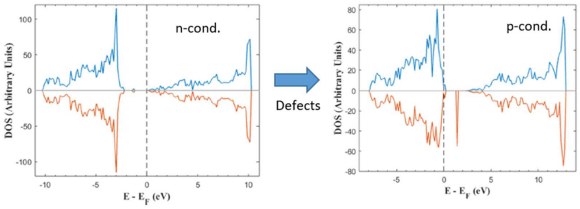

Fig. 2. At the left side, total DOS of a pure SnO_2 lattice. The Fermi level (dotted vertical line) within the energy gap indicates that the lattice has acquired n-type conductivity. At the rigth side, total DOS of N and Al codoped SnO_2 lattice. The position of the Fermi inside the valence band indicates that the material has acquired p-type conductivity.

References

1. Kumar, A., and Zhou, C.. The race to replace tin-doped indium oxide: which material will win?. *ACS nano*, 4(1):11-14, 2010.
2. Villamagua, L., Stashans, A., Lee, P. M., Liu, Y. S., Liu, C. Y., and Carini, M.. Change in the electrical conductivity of SnO2 crystal from n-type to p-type conductivity. *Chemical Physics*, 452:71-77, 2015.
3. Cohen, A. J., Mori-Snchez, P., and Yang, W.. Challenges for density functional theory. *Chemical Reviews*, 112(1):289-320, 2011.
4. Kaduk, B., Kowalczyk, T., and Van Voorhis, T. Constrained density functional theory. *Chemical Reviews*, 112(1):321-370, 2011.
5. Kryachko, E. S., and Ludea, E. V.. Density functional theory: Foundations reviewed. *Physics Reports*, 544(2):123-239, 2014.
6. Kittel, C.. *Quantum theory of solids*. Wiley, 1987.
7. Sholl, D., and Steckel, J. A.. *Density functional theory: a practical introduction*. Wiley, 2011.
8. Marcillo, F., Villamagua, L.,and Stashans, A.. Analysis of electrical and magnetic properties of zinc oxide: A quantum mechanical study. *International Journal of Modern Physics B*, 31(14):1750111, 2017.
9. Villamagua, L., Stashans, A., Carini, M., and Maldonado, F.. Doping of SnO2 with H atoms: An alternative way to attain n-type conductivity. *AIP Advances*, 6(11):115217, 2016.
10. Villamagua, L., Carini, M., Stashans, A., and Gomez, C. V.. Band gap engineering of graphene through quantum confinement and edge distortions. *Ricerche di Matematica*, 65(2):579-584, 2016.
11. Maldonado, F., Rivera, R., Villamagua, L., and Maldonado, J.. DFT modelling of ethanol on $BaTiO_3$ (001) Surface. *Applied Surface Science*, submitted, 2018.

A fast and parallel approach towards accurate analog simulations

Konrad Waldherr[1], Janos Benk[2], and Georg Denk[1]

[1] Infineon Technologies, Am Campeon 1–15, Neubiberg 85579, Germany konrad.waldherr@infineon.com, georg.denk@infineon.com
[2] benkjanos@gmail.com

Summary. We present an efficient method for fast and accurate analog simulations of integrated circuits in the time domain. Our approach combines and extends concepts from linear algebra and circuit theory in a unifying way. This allows the development of a block diagonal solver which can additionally be accelerated by a partition-bypass strategy. Compared to the state-of-the-art solver KLU the new method leads to significant sequential and parallel speedups, while keeping SPICE-level accuracy.

1 Introduction

In SPICE-like simulators the mathematical formulation of analog circuits is based on the modified nodal analysis (MNA), which seeks for all node voltages and the currents of voltage-defined branches. For time-domain simulations the application of Kirchhoff's current law then leads to a system of differential-algebraic equations of the general form

$$\frac{\mathrm{d}}{\mathrm{d}t}q(x(t)) + f(x(t)) + s(t) = 0. \tag{1}$$

Here q, f, and s are the vectors of charges, resistive currents, and independent stimuli, respectively, whereas x is the vector of unknown MNA voltages and currents. At time point t_k the time derivative of the charge vector is discretized by an implicit time integration method of the form

$$\left.\frac{\mathrm{d}}{\mathrm{d}t}q(x(t))\right|_{t=t_k} = \alpha_k q(x(t_k)) + \beta_k,$$

with a method-specific integration coefficient α_k and a vector β_k of backward data. Applied to Eq. (1) the relation for the unknown $x_k := x(t_k)$ reads

$$r_k(x_k) := \alpha_k q(x_k) + \beta_k + f(x_k) + s(t_k) = 0.$$

The Newton-Raphson method transforms this nonlinear system to a sequence of linear systems which seek for an increment Δx_k to the unknown x_k:

$$\underbrace{\left(\alpha_k \frac{\mathrm{d}q(x_k)}{\mathrm{d}x_k} + \frac{\mathrm{d}f(x_k)}{\mathrm{d}x_k}\right)}_{=:A(x_k)} \Delta x_k = -r_k(x_k). \tag{2}$$

Constructing and solving the linear systems (2) for discrete time points is the computationally dominating task within transient simulations, cf. Fig. 1. For more details we refer to [1].

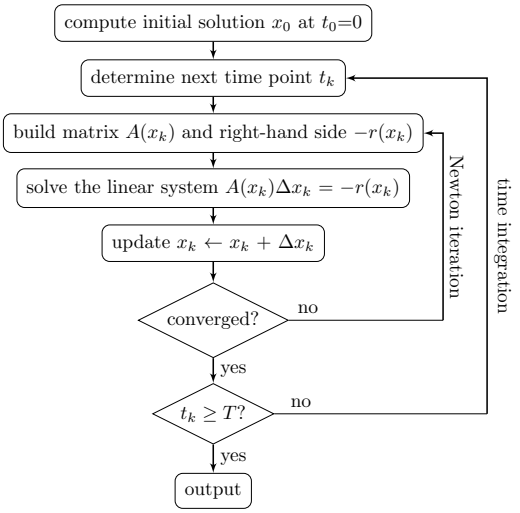

Fig. 1. Transient simulation in the time domain $[0, T]$.

2 BBD solver with partitioning bypass

2.1 Circuit partitioning

The basis of our bordered-block diagonal (BBD) solver is an appropriate circuit partitioner which groups the devices into distinct parts. They are only connected by so-called coupling nodes as sketched in Fig. 2.

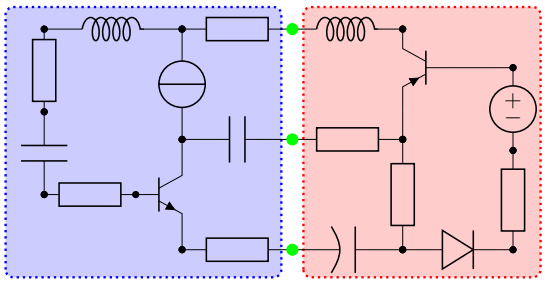

Fig. 2. Splitting of an electrical circuit into a blue and a red partition. The coupling nodes are marked by green bullets.

Splitting into p partitions and reordering the rows and columns accordingly transforms the linear system (2) into the BBD structure with p diagonal partition blocks $A_{i,i}$ and coupling blocks indexed by c.

$$\begin{bmatrix} A_{1,1} & & A_{1,c} \\ & \ddots & \vdots \\ & A_{p,p} & A_{p,c} \\ A_{c,1} & \cdots & A_{c,p} \; A_{c,c} \end{bmatrix} \begin{bmatrix} y_1 \\ \vdots \\ y_p \\ y_c \end{bmatrix} = \begin{bmatrix} b_1 \\ \vdots \\ b_p \\ b_c \end{bmatrix} \tag{3}$$

Our BBD solver is based on a static graph partitioning algorithm according to [2] which minimizes the number of coupling nodes. Additionally we limit the number of to be expected fill-ins in $A_{c,i}$ by a certain threshold, and we ensure that each diagonal block can be solved by static pivoting. Otherwise further nodes are moved to the coupling part.

2.2 Solving the BBD system

By splitting the coupling system into contributions from the individual partitions, $A_{c,c} = A_{c,c}^{(1)} + \ldots + A_{c,c}^{(p)}$ and $b_c = b_c^{(1)} + \ldots + b_c^{(p)}$, the BBD system (3) can be constructed in a parallel partition-based way. The solving of Eq. (3) is based on the solvability of each individual diagonal block, which is assured by the construction of the partitions. Assuming y_c is known, the solution for partition i is $y_i = A_{i,i}^{-1}(b_i - A_{i,c}y_c)$ and can be calculated in parallel for all partitions. The solution of the coupled system is determined by

$$\underbrace{\sum_{i=1}^{p} \overbrace{\left(A_{c,c}^{(i)} - A_{c,i}A_{i,i}^{-1}A_{i,c}\right)}^{=:S_i} y_c}_{=:S} = \underbrace{\sum_{i=1}^{p} \overbrace{\left(b_c^{(i)} - A_{c,i}A_{i,i}^{-1}b_i\right)}^{=:d_i}}_{=:d}.$$

The construction of the partial forward substitutions S_i and d_i can be done partition-wise in a fully parallel way. Thus only the construction and solving of the coupling system $Sy_c = d$ requires a synchronization step and has to be executed sequentially.

2.3 Partition-bypass strategy

The parallel construction and solving of the BBD system already results in substantial speedups. Additional acceleration can be obtained by exploiting the latency in the partitioned circuit, meaning that the activity of an analog circuit is typically concentrated within a few number of partitions. The main idea of our bypass strategy is to reuse the LU-decomposed matrix $A_{i,i}$, the right-hand side evaluation b_i, and the contributions S_i and d_i to the coupling system from the previous Newton iteration, if the bypass criterion is met, cf. Alg. 1.

A partition is being bypassed when the following two conditions are fulfilled: The Newton method has to be converged for all MNA variables associated to the partition, which can be easily checked by monitoring the right-hand side of the BBD system. Additionally, the Newton update must not exit a trust region around the state of the latest full evaluation of the partition. To ensure SPICE-accuracy, we execute one full evaluation per time step, so that partitions can only be bypassed from the second Newton iteration onwards.

Algorithm 1 BBD solver with partition bypass

```
for i = 1,...,p do                          ▷ can be executed in parallel
    if partition i can be bypassed then
        reuse A_{i,i}, b_i, S_i, d_i from the previous iteration
    else
        build partition matrix A_{i,i} and right-hand side b_i
        partial LU decomposition of A_{i,i} to get S_i
        partial forward substitution with b_i to get d_i
build and solve the coupling system S y_c = d
for i = 1,...,p do                          ▷ can be executed in parallel
    partial backward substitution with y_c
```

3 Results and conclusion

We now study the performance of the BBD solver in the frame of Infineon's internal analog simulator. We investigate two layouts, a mid-sized circuit of about 35,000, and a large circuit of about 240,000 semiconductor devices. Fig. 3 illustrates the speedup of our approach compared to the state-of-the-art KLU solver.

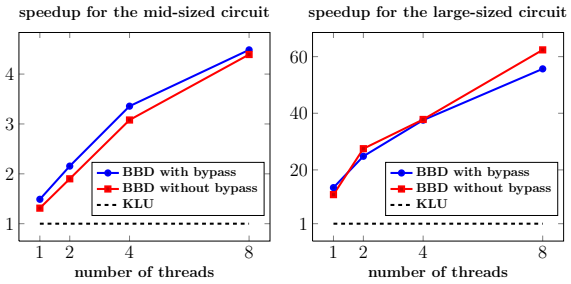

Fig. 3. Speedup of the BBD solver compared to KLU.

Even in sequential mode, the block diagonal structure improves the simulation time, and the partitioning bypass leads to additional acceleration. With enabled multithreading, we gain parallel speedup due to the concurrent execution of the individual partitions.

Altogether, our BBD approach combines and extends existing approaches in an appropriate way and results in an efficient and parallel solver which maintains SPICE-level accuracy.

References

1. J. Benk, G. Denk, and K. Waldherr. A holistic fast and parallel approach for accurate transient simulations of analog circuits. *Journal of Mathematics in Industry*, 7(1), 2017.
2. G. Karypis and V. Kumar. METIS – unstructured graph partitioning and sparse matrix ordering system, version 2.0. Technical report, University of Minnesota, Department of Computer Science, 1995.

Topology and Parametric Design Optimization of a Hall Effect Thruster

Rtimi Youness[1], Maxime Bonnet[1], Frédéric Messine[1], and Carole Hénaux[1]

LAPLACE, Université de Toulouse, CNRS, Toulouse, France rtimi@laplace.univ-tlse.fr, frederic.messine@laplace.univ-tlse.fr carole.henaux@laplace.univ-tlse.fr and maxime.bonnet@etu.enseeiht.fr

Summary. In magneto-static , Topology Optimization (TO) is a tool helping to find a suitable ferromagnetic material space distribution in order to fulfill a specified magnetic objective. TO becomes very interesting when the designer looks for new and unfamiliar structures. Herein, TO is used to design a Hall Effect Thruster (HET). But, the topological solutions are often not feasible. Thus, Parametric Optimization (PO) is then carried out from the topological solution. PO takes into account the manufacturing constraints as well as the non linearity of the ferromagnetic materials.

1 Introduction

The HETs are widely used for satellites electrical propulsion. The 3D structure of a HET is given in the Fig. 1. Since the axisymetry of the HET, its 3D structure is reduced into a 2D one as illustrated in Fig.1. The main idea of a HET is that the propellant is initially ionized and then, expelled thanks to an applied electrical field; for details see [2]. The optimal propulsion is obtained if two specifications are respected:

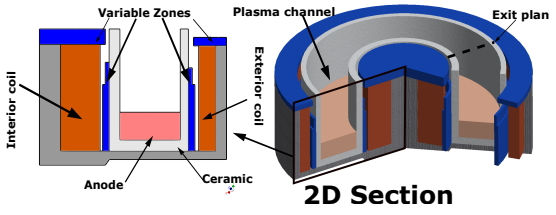

Fig. 1. 3D-2D structure of a standard Hall Effect thruster.

- Radial magnetic field B_0 whose amplitude varies according to a gaussian function along the middle of the plasma channel.
- Horizontal magnetic field at the exit plan.

In order to achieve that, the geometry of the variable regions is designed (Fig.1) and the values of current densities in the coils (Fig.1) are sought.

The design process is done in two steps: -TO that gives the key idea of the variables zones shape; -PO that reshapes the topological design. Besides the variables regions, PO makes it possible to take into account as variables the other iron parts of the HET structure. Moreover, using PO the non linearity of the used ferromagnetic material is addressed.

2 Topology design optimization

In TO the variable regions are meshed as shown in Fig.1 .The topology of those regions is understood as the assignment of either iron or air in each mesh element. Herein, the iron is considered as linear ferromagnetic material and it is identified by its permeability value, whereas the air or void is identified by a permeability equal to 1. In the optimization formulation, the topology of the variable regions is expressed by a scalar vector μ of the permeability values in each mesh element. Thus, the design optimization problem is formulated as follows:

$$(\mathfrak{P}_\mu)\begin{cases} \min\limits_{\mu,J} F_1(\mu,J) = \displaystyle\int_{\Omega_{T_1}} \|\mathbf{B}-B_0\|_2^2\, d\Omega \\ \text{uc :} \\ \quad F_2(\mu,J) = \displaystyle\int_{\Omega_{T_2}} \left\| \arctan\left(\frac{\mathbf{B}_z}{\mathbf{B}_r}\right)\right\|_2^2 d\Omega \le \varepsilon, \end{cases} \tag{1}$$

$$\text{with} \quad -\nabla\times(\nu(\mu)\mathbf{B}) + J = 0, \tag{2}$$

where J denote the vector of the current densities J_1 and J_2 in the internal and external coils (see Fig.1). $\mathbf{B} = (\mathbf{B}_z, \mathbf{B}_r)$ is the magnetic flux density obtained by solving the equation (2) for given μ and J.

Solving $(\mathfrak{P}_\mu)$ is to search J and μ so that the magnetic field $\mathbf{B}$ is the closest to B_0 allover the middle of the channel Ω_{T1} while keeping the flux lines horizontal allover the exit plan region Ω_{T2}. The first main issue in solving $(\mathfrak{P}_\mu)$ is that he cost and the constraint functions are implicitly linked to the design variables J and μ via Maxwell equation (2). This makes the gradient respect to J and μ computationally expensive using classic methods like finite difference estimations. In this work, we developed the adjoint variable method that provides the gradient with very cheap computational cost, [1]. The second issue in solving $(\mathfrak{P}_\mu)$ is that the permeability scalars in μ could take different values between 1 and the iron permeability. This means that the solution could not be feasible if we do not all the composite materials with different permeability values taken by the solution. In order to avoid that, intermediate values of permeability are penalized using SIMP (Solid Isotropic Material with Penalization) method in order to obtain solutions with just two materials: iron and air; for details

see [1]. The topological design found could be seen through Fig.2. The iron regions is those that concentrate the flux lines. The current density in the internal coil is $2.1MA/m^2$ and in the external coil is $1MA/m^2$. It is clear that the topology of the variable regions is

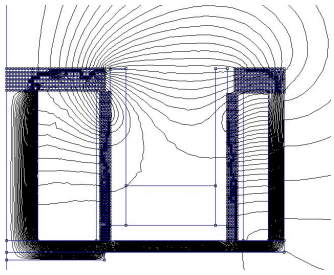

Fig. 2. Topological design solution of the HET.

not a feasible structure. Moreover, the ferromagnetic material is considered as a linear material. To remedy to all this manufacturing issues, we carry out another step of design optimization as detailed in the next section.

3 Parametric optimization adjustment

In order to have a feasible structure the topological solution is slightly modified while making sure that the cost and the constraint values are not strongly impacted. In our application case the structure given in Fig.2 is modified such that we obtain a more feasible one as shown in Fig.3.

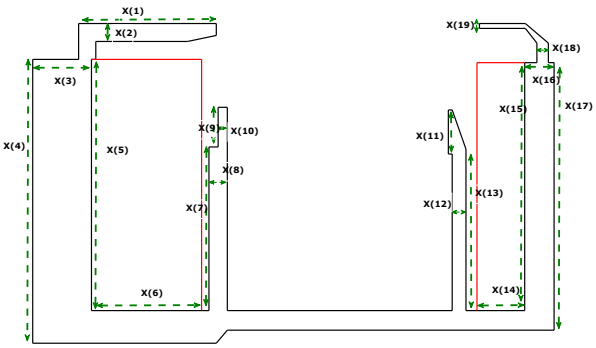

Fig. 3. The main geometry of topological design.

This structure is then parameterized with a vector X of geometrical parameters (see Fig.3). The new structure is designed again in order to offset the cost and the constraint values modifications. For this purpose, we solve a parametric design problem that is the same as $(\mathfrak{P}_\mu)$ but expressed with the geometrical parameters vector X instead t of he topological design variable μ:

$$(\mathfrak{P}_X)\begin{cases} \min\limits_{X,J} F_1(X,J) = \int_{\Omega_{T_1}} \|\mathbf{B}-B_0\|_2^2 \, d\Omega \\ \text{uc :} \\ \quad F_2(X,J) = \int_{\Omega_{T_2}} \left\| \arctan\left(\dfrac{\mathbf{B}_z}{\mathbf{B}_r}\right)\right\|_2^2 d\Omega \leq \varepsilon, \end{cases} \tag{3}$$

Unlike topology optimization, herein a non linear material is assigned to the ferromagnetic structure. The gradient of the cost and the constraint functions respect to the vector of geometrical parameters X are estimated by a finite difference method. It is clear that this could be cpu time consuming. But, in our numerical experiments this is still acceptable for two reasons. First, X length is very small compared to μ, and second, the initial structure is not far away from the optimal structure given that it is based on slight modification of the topological solution. The solution of parametric optimization is given in Fig.4. The obtained magnetic specifications are compared to the required ones in Fig.5.

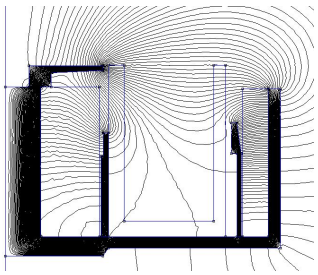

Fig. 4. The final feasible design of the HET.

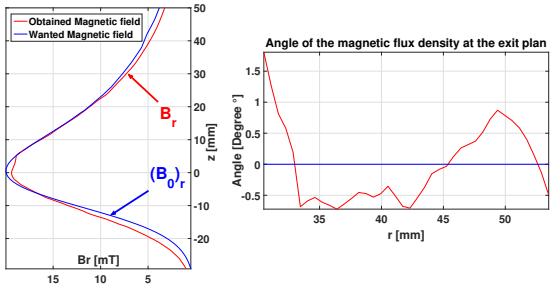

Fig. 5. Magnetic specifications: in blue are the required specifications and in red are the obtained ones.

4 Conclusion

A Complete methodology to design magnetic circuit is presented through the HET application. It consists of: -TO that gives the key idea about how the structure should look like; -PO that reshapes the topology found in order to make it feasible.

References

1. S. Sanogo, F. Messine, C. Henaux and R. Vilamot, *Topology Optimization for Magnetic Circuits dedicated to Electric Propulsion*, IEEE Trans. on Mag: Vol. 50, No. 12, December 2014.
2. A. Rossi, F. Messine, C. Hénaux, *A parametric optimization code based on local algorithms to design magnetic circuits of Hall effect thrusters*, International Journal of Applied Electromagnetics and Mechanics 53 (2017) S153–S165, 2017.